usually uncountable

STUDIES ON DYNAMIC CHARACTERISTICS OF SMALL-SIZED DC MOTOR AND TRANSIENT BEHAVIORS OF MAGNETIC FLUXES IN ITS COMMUTATING ZONE AND SO ON

BY

TSUGUO ANDO

DECEMBER 1985

DEPARTMENT OF ELECTRICAL ENGINEERING

KYOTO UNIVERSITY

STUDIES ON DYNAMIC CHARACTERISTICS OF SMALL-SIZED DC MOTOR AND TRANSIENT BEHAVIORS OF MAGNETIC FLUXES IN ITS COMMUTATING ZONE AND SO ON

英文検討の余地あり.

BY

TSUGUO ANDO

DECEMBER 1985

DEPARTMENT OF ELECTRICAL ENGINEERING

KYOTO UNIVERSITY

ACKNOWLEDGMENTS

The author would like to fully appreciate Professor Juro Umoto of Kyoto University for supervising and completing this thesis. His enthusiastic guidance and continuous encouragement enable the author to accomplish the work.

The author also wishes to express his thanks to Associate Professor Takehisa Hara of Kyoto University and Associate Professor Masaharu Yoshida of Gifu University for their useful discussions concerning the numerical solution of the work.

The author is deeply indebted to Mr. Satoshi Okabayashi of IBM, Japan and Mr. Shinichiro Mori of Nippon Steel Co. for their efforts concerning the work of Part I in this thesis. Concerning the work of Part II, the author is much indebted to Mr. Minoru Takemura of Toshiba Co. and Mr. Kiyoshi Yoshida of Kansai Electric Power Co. for their help in the experiments and the numerical computations.

The author wishes to express his thanks to Associate Professor Motoo Ishikawa, Instructor Yoshitaka Inui, and other members of Professor J. Umoto's Laboratory, Department of Electrical Engineering, Kyoto University, whose encouragement help the author for completing the work.

All numerical computations were performed at the Data Processing Center, Kyoto University, of which the staffs must be appreciated.

ACKNOWLEDGMENTS

The author would like to fully appreciate Professor Juro Umoto of Kyoto University for supervising and completing this thesis. His enthusiastic guidance and continuous encouragement enable the author to accomplish the work.

The author also wishes to express his thanks to Associate Professor Takehisa Hara of Kyoto University and Associate Professor Masaharu Yoshida of Gifu University for their useful discussions concerning the numerical solution of the work.

The author is deeply indebted to Mr. Satoshi Okabayashi of IBM, Japan and Mr. Shinichiro Mori of Nippon Steel Co. for their efforts concerning the work of Part I in this thesis. Concerning the work of Part II, the author is much indebted to Mr. Minoru Takemura of Toshiba Co. and Mr. Kiyoshi Yoshida of Kansai Electric Power Co. for their help in the experiments and the numerical computations.

The author wishes to express his thanks to Associate Professor Motoo Ishikawa, Instructor Yoshitaka Inui, and other members of Professor J. Umoto's Laboratory, Department of Electrical Engineering, Kyoto University, whose encouragement help the author for completing the work.

All numerical computations were performed at the Data Processing Center, Kyoto University, of which the staffs must be appreciated.

1 項欠

PART I

DYNAMIC CHARACTERISTICS OF SMALL-SIZED DC MOTOR CONTROLLED BY THYRISTOR CIRCUITS

CHAPTER 1

GENERAL INTRODUCTION

1.1 Research Trend and Problem

In a direct current(dc) motor, the driving torque is efficiently generated by means of interaction between the main pole flux excited by the field current and the mechanically commutated armature current. Therefore, the dc motor has inherently a superior speed-torque characteristic and a strong starting torque, which can't be obtained by ac motors such as an induction motor and a synchronous one. Also, the rotating speed of the dc motor can be more flexibly controlled than the one of ac motors, because the field current and the armature current can be independently controlled. Thus, dc motors are widely applied to iron manufacturing, electric car, industrial servomotor, etc. which need precise speed control.

There are three types of control methods of the dc motor speed, namely, the field, the armature rheostatic and the armature voltage control methods.[1],[2] The field control method, in which the exciting field current is regulated by changing the resistance or the impressed voltage of the field circuit, has an advantage that the motor speed can be controlled with a small dissipation of the electric power. However, this method can be used only for a limited range of speed control, because the quick regulation of the field current is made impossible by large inductance of the field circuit. Especially, the unstable motor performance may occur in the case where the main pole flux excited by the field current is too small. The rheostatic control method, in which the resistance of the armature circuit is varied, is now seldom used because of the large ohmic power loss. The last voltage control method, in which the large power supply voltage of the armature circuit is regulated, is now used most widely, because by this method the motor speed can be quickly and

stably controlled.

Before about 1960 year, the Ward-Leonard system[1] or the mercury rectifier circuit[3],[4] was mainly used for regulating the voltage supplied to the armature circuit. Ever since the thyristor was put to practical use in 1957, thyristor circuits, by which the supply voltage can efficiently and quickly be regulated, have been applied to the speed control system of the dc motor. Also, the other power semi-conductor devices such as a power transistor, a gate-turned-off thyristor, etc. were improved.[5]-[8]

In addition to the improvement of power semi-conductor devices, the application technique of those was rapidly progressed by the aid of the automatic control theory and the actual analog and digital control systems. Specially, since the digital control circuit was practically used in 1980, the precisely regulated ac supply voltage with variable frequencies, which was impossible of realization in former years, were put to practical use, too. By using the regulated ac supply voltage, at present, the ac machines, such as an induction motor and a synchronous motor, were driven as the fairly precise variable speed machines.[9],[10],[11]

As the speed control techniques of the ac machines are largely improved, the dc motor must be used as the best precise machine in which wide and quick change of the speed is required. While the present dc motor has been controlled fairly well by using the application technique of the thyristor rectifier or the chopper circuit, for the improvement of the control it is necessary to analyse the motor performance exactly.

There are many studies on performances of the dc motor controlled by the thyristor circuits, but they have mostly investigated the performances under the assumption that the fluctuation of the motor speed can be ignored. Namely, Harris,[12] Ishizaki,[13] Nitta[14] and others[4],[15]-[18] analysed firstly the steady performances of the motor controlled by the rectifier circuits under the above assumption. Next, they derived the appearance increase of the armature resistance from the calculated results of the steady speed-torque characteristics,

and so estimated the rough dynamic characteristics by using the appearance increased armature resistance. Also, Parrimelalagan,[19] Ishizaki[20] and others[21]-[25] roughly analysed the steady and the dynamic performances of the motor controlled by the chopper circuit with the above same processes.

Next, the analysis of the motor performances considering the fluctuation of the motor speed, when the motor is controlled by the grid controlled thyratron rectifier circuit, was done by Togino.[26] Also, he presented the transfer function of the motor in the speed control system. However, he failed to introduce the approximate time constant of the transfer function by treating the motor speed periodically controlled by the rectifier circuit as the same as the one continuously controlled by the dc source voltage.

As mentioned above, the theoretical and precise transfer function of the motor, which is effective to analyse the dynamic characteristic of the motor whose rotating speed fluctuates, is yet introduced.

1.2 Purpose and Synopsis of Part I

The recent dc motors are required to be used as the more precise variable speed machines than the ac motors. Those dc motors are mostly controlled by the variable dc voltage regulated by the rectifier or the chopper circuits, in which the thyristors or the other semi-conductor devices are used. However, the theoretical investigation of the performance of the motor controlled by those circuits has not carried out sufficiently well.

In Chapter 2, the author first shows the theoretical method to analyse the dynamic and steady performance characteristics of a separately excited dc motor controlled by the single-phase half-wave thyristor rectifier circuit, in which, to analyse exactly the motor performances, there are considered the periodically interrupted armature current, the fluctuation of the motor speed, the voltage drops on the brushes, the friction torque of the motor with the load, etc.. Next, by

investigating the small fluctuation of the motor speed during the period of one cycle of the ac supply frequency, he introduces approximately the time constant of the motor in the control circuit. Also, transfer and pulse transfer functions of the motor control system are introduced to present the good approximate method, by which the dynamic characteristics can be easily analysed, and it is shown that the dynamic characteristic of the motor can be evaluated by an equivalent first order sampled data system. And the steady and dynamic characteristics are investigated in detail theoretically and experimentally. In this connection, the validity of the presented theoretical method is ascertained by showing the good agreement between the calculated results and the experimental results.

In Chapter 3, first, a theoretical method to analyse the dynamic and steady performances of a separately excited dc motor controlled by a chopper circuit is introduced by using the theory of periodically interrupted electric circuit.[27] In the method, the fluctuation of the motor speed, the friction torque of the motor with a load and the voltage drops on the armature brushes are considered as in Chapter 2. These factors have not been considered by the conventional theory, but they are important for researching the motor performances. Also, as in Chapter 2, transfer and pulse transfer functions of the motor control system are introduced to present an good approximate method of the above precise motor performances. And it is shown that the dynamic characteristics can be evaluated by an equivalent second order sampled data system. Next, the steady and the dynamic characteristics are investigated in detail theoretically and experimentally. In this connection, the author confirms the appropriateness of the theory by showing that the calculated results agree sufficiently well with the experimental results.

CHAPTER 2

DYNAMIC CHARACTERISTICS OF DC MOTOR CONTROLLED BY SINGLE-PHASE HALF-WAVE THYRISTOR RECTIFIER CIRCUIT

2.1 Introduction

A thyristor rectifier circuit is widely used to obtain a adjustable dc voltage from a commercial ac supply voltage. For example, the circuit is often used to drive the dc motor as a precise variable speed machine such as a mill motor, an industrial servo-motor, an electric traction motor, etc.. Therefore, it is necessary to research not only the static characteristics of the motor in the steady state, but also the dynamic ones including the circuit performances in the transient state.

Since the motor speed is efficiently controlled by regulating the armature terminal voltage, many studies on the speed control of the dc motor, of which the armature power is regulated by a thyristor rectifier circuit, were presented.[12]-[18] However, the analysis of the motor performances were mostly carried out under the assumption that the fluctuation of the motor speed is negligible, and the papers that dealt with the dynamic characteristics considering the fluctuation are rarely found. Also, in order to improve still more the control characteristic of the motor, the exact analyses of the dynamic and the steady performances are desired.

In this chapter, first, there is introduced a theoretical method to analyse the dynamic characteristics of a separately excited dc motor controlled by a single-phase half-wave thyristor rectifier circuit, in which the armature current flows interruptedly. Here, though the motor is usually controlled by a polyphase rectifier circuit to reduce the ripples of the armature current and the motor

speed, the armature current sometimes flows interruptedly, when the armature circuit inductance or the motor load is small. Then, the dynamic characteristics of the motor are different from the case of the continuous current. So, the influences of the interrupted current on the motor performance are investigated by using a single-phase half-wave rectifier circuit.

In the analysis, there is considered the fluctuation of the motor speed for one cycle of an ac supply frequency, which has not been considered in the conventional analysis. Also, the effects of the friction torque of the motor with load, the motor brush voltage drop and the added inductance of the armature circuit on the motor characteristics are considered. [28]-[38]

Next, transfer and pulse transfer functions of the motor control system are introduced to present a good approximate method, by which the dynamic characteristics of the motor can be easily analysed. And it is shown that the dynamic characteristics can be obtained by an equivalent first order sampled data system.

Also, the steady and the dynamic characteristics are investigated in detail theoretically and experimentally. In this connection, the appropriateness of the theory is confirmed by ascertaining that the calculated results agree well with the experimental ones.

2.2 Fundamental Theory

2.2.1 Single-phase half-wave rectifier circuit and fundamental equations

Figure 2.1 shows the circuit diagram of a single-phase half-wave thyristor rectifier circuit for the speed control of the separately excited dc motor, where

e : output voltage of rectifier circuit,

E_m : maximum value of ac supply voltage,

i : armature current,

i_f : fixed field current of motor,

n : motor speed,

v_r : input voltage to controller,

$\omega=2\pi f$: angular frequency of ac supply,

f : frequency of ac supply,

L : total inductance of armature circuit,

R : total resistance of armature circuit,

T_h : thyristor.

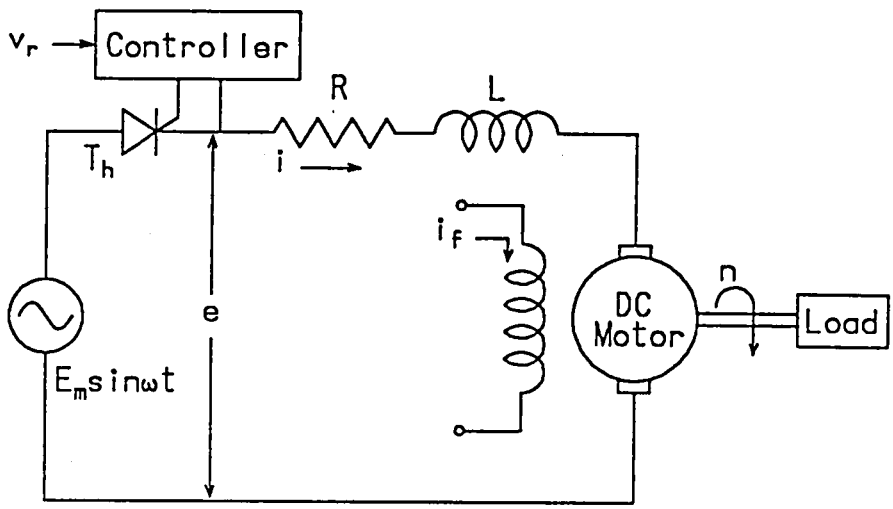

Fig.2.1. Control circuit of separately excited dc motor.

In the figure, the output voltage e is regulated by changing the firing angle of T_h. The firing angle of T_h is changed by v_r. When the motor speed n is fed back to the controller, the motor is more precisely controlled.

Now, there are three types of friction torque to be considered in the analysis of the motor with load, namely, static, Coulomb and viscous friction torque. The static torque Q_s is the one which is needed to rotate a stalled motor. The Coulomb torque Q is the one that is independent of the speed in a rotating motor. The viscous torque is the one which is approximately proportional to the speed n and

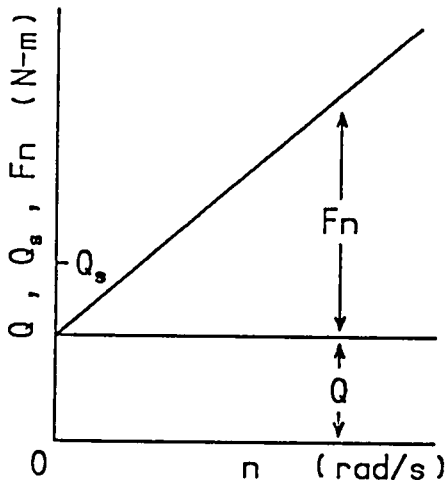

Fig.2.2. Approximate speed-torque characteristic.

expressed by Fn, where F is the viscous friction coefficient. Figure 2.2 illustrates the relation of the friction torque vs. the motor speed n.

The performances of the dc motor in Fig.2.1 can be now analysed by the following fundamental equations:

$$\left.\begin{aligned} e&=Ldi/dt+Ri+K_v n+E_b, \\ K_t i&=Jdn/dt+Fn+Q, \end{aligned}\right\} \qquad (2.1)$$

where

E_b : brush voltage drop including thyristor voltage drop,

J : moment of inertia of motor contained load,

K_t : torque coefficient of motor,

K_v : counter emf coefficient of motor.

In this connection, in the conventional analysis, where the fluctuation of the motor speed and E_b are ignored, the following equations

$$\left.\begin{aligned} e&=Ldi/dt+Ri+K_v N, \\ K_t I_d&=FN+Q, \end{aligned}\right\} \qquad (2.2)$$

where

I_d : average value of i,

N : constant motor speed,

have been used, and by these equations the steady characteristics have been investigated. Also, the dynamic characteristic is approximately evaluated by using those results. In this paper, in order to obtain the precise characteristics, we use the exact equations shown in Eqs. (2.1)

2.2.2 Circuit modes

Let us consider performances of the circuit shown in Fig.2.1. The current i begins to flow at the instant when T_h is turned on by the gate signal generated in the controller, and the driving torque $K_t i$ is added to the motor. The stalled motor begins to rotate when $K_t i$ exceeds Q_s. On the other hand, when i decreases to zero, i is blocked by a reverse blocking characteristic of T_h and the motor rotates by inertia. But when the average value of $K_t i$ is smaller than Q, the motor can't keep rotating and stops.

Therefore, we can divide the circuit performances into the four fundamental modes, which depend on the situations of i and n, as follows:

mode 0 : i is zero and motor is at a standstill,

mode 1 : i is supplied, but motor can't rotate because lack of $K_t i$,

mode 2 : motor is driven by i,

mode 3 : i is blocked and motor is rotated by inertia.

The situations of i and n in each mode and the criteria for the mode transitions are shown in Fig.2.3, where

$I_s=Q_s/K_t$: equivalent constant current of Q_s,

$v=K_v n$: counter emf of motor,

$i_m=i_m(t)$: current i in mode m,

$v_m=v_m(t)$: voltage v in mode m,

t_m : duration of interval of mode m,

m= 0, 1, 2, 3 : mode number.

In Figs.2.1 and 2.3, T_h can be turned on by the gate signal when the following condition

$$e=E_m \sin\alpha \geqq v+E_b. \tag{2.3}$$

where

α : firing angle of T_h,

is satisfied.

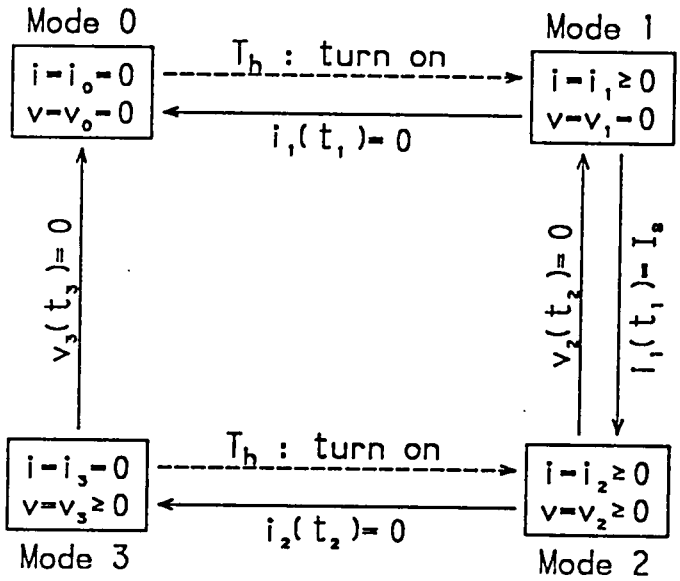

Fig.2.3. Circuit modes.

2.2.3 Electrical equivalent circuit and mode analysis

(1) Equivalent circuit

Although the system performances of the electromechanical system in Fig.2.1 can be analysed by using Eqs. (2.1) and Fig.2.3, in order to simplify the analysis, we use the electrical equivalent circuit of the system. By neglecting a motor armature reaction and a nonlinearity of a circuit parameter, the fundamental equations (2.1) can be transformed to the following electrical ones:

$$\left.\begin{aligned} e&=L di/dt+Ri+v+E_b, \\ i&=C dv/dt+Gv+I_q, \end{aligned}\right\} \tag{2.4}$$

where

$C=J/(K_tK_v)$: equivalent capacitance of J,

$G=F/(K_tK_v)$: equivalent conductance of F,

$I_q=Q/K_t$: equivalent forced current of Q.

From Eqs.(2.4), we can derive the electrical equivalent circuit as shown in Fig.2.4.

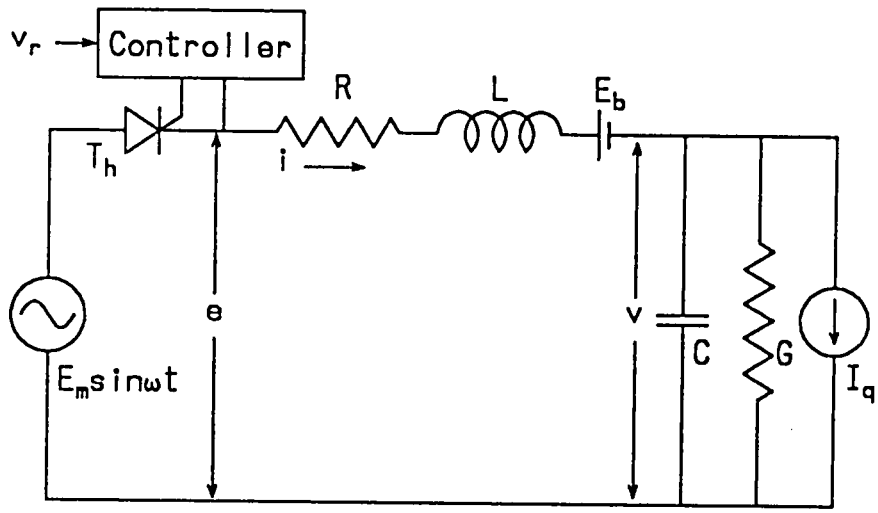

Fig.2.4. Electrical equivalent circuit.

(2) Mode analyses

Let us show the fundamental relations among e, i and v in each mode obtained by the above equivalent circuit.

(i) Mode 0

We can readily arrive at the following equations

$$e=0, \quad i=0, \quad v=0. \tag{2.5}$$

(ii) Mode 1

By assuming that mode 1 starts at the phase angle α_1 and replacing e, i and v by e_1, i_1 and v_1, respectively, Eqs.(2.4) are transformed as follows:

$$\left.\begin{aligned} e_1&=E_m\sin(\omega t+\alpha_1), \\ &=Ldi_1/dt+Ri_1+E_b, \\ v_1&=0. \end{aligned}\right\} \tag{2.6}$$

Solving Eqs. (2.6), we can obtain

$$i_1=\varphi_1(t)+\chi_1(t)i_1^{\circ}, \tag{2.7}$$

where

$$\varphi_1(t)=E_m\{\sin(\omega t+\alpha_1-\delta)-\chi_1(t)\sin(\alpha_1-\delta)\}/(R^2+\omega^2L^2)^{1/2}-E_b\{1-\chi_1(t)\}/R,$$

$$\chi_1(t)=\varepsilon^{-tR/L}, \quad \delta=\tan^{-1}(\omega L/R).$$

i_1° : initial value of i_1, which is determined by value of i at instant when mode transition from mode 0 or 2 occurs.

This mode is kept for the duration t_1, and, of course, t_1 is determined by $i_1=0$ or $i_1=I_s$.

(iii) Mode 2

The circuit equations for this mode are given by Eqs. (2.4), as follows:

$$\left.\begin{aligned} e_2&=E_m\sin(\omega t+\alpha_2)\\ &=Ldi_2/dt+Ri_2+v_2+E_b,\\ i_2&=Cdv_2/dt+Gv_2+I_q, \end{aligned}\right\} \tag{2.8}$$

where

e_2, i_2 and v_2 : e, i and v in this mode, respectively,

α_2 : starting phase angle of this mode.

Solving Eqs. (2.8), we can obtain the following solution in the following matrix notation

$$\begin{bmatrix} i_2\\ v_2 \end{bmatrix}=\begin{bmatrix} \varphi_{21}(t)\\ \varphi_{22}(t) \end{bmatrix}+\begin{bmatrix} \chi_{211}(t) & \chi_{212}(t)\\ \chi_{221}(t) & \chi_{222}(t) \end{bmatrix}\begin{bmatrix} i_2^{\circ}\\ v_2^{\circ} \end{bmatrix} \tag{2.9}$$

where

$$\varphi_{21}(t)=I_m\{\sin(\omega t+\alpha_2+\theta_1-\theta_2)-\chi_{211}(t)\sin(\alpha_2+\theta_1-\theta_2)\}-V_m\chi_{212}(t)\sin(\alpha_2-\theta_2)$$
$$+(I_q-GE_b)\{1-g_3(t)\}/(RG+1)+E_b\chi_{212}(t),$$

$$\varphi_{22}(t)=V_m\{\sin(\omega t+\alpha_2-\theta_2)-g_3(t)\sin(\alpha_2-\theta_2)-\omega g_2(t)\cos(\alpha_2-\theta_2)\}$$
$$-I_q\chi_{221}(t)-(RI_q+E_b)\{1-g_3(t)\}/(RG+1),$$

$$\chi_{211}(t)=g_1(t)-\sigma g_2(t), \qquad \chi_{212}(t)=-g_2(t)/L,$$

$$\chi_{221}(t)=g_2(t)/C, \qquad \chi_{222}(t)=g_1(t)+\sigma g_2(t),$$

$$g_1(t)=\varepsilon^{-\lambda t}\cosh\mu t, \quad g_2(t)=\varepsilon^{-\lambda t}\sinh\mu t/\mu, \quad g_3(t)=g_1(t)+\lambda g_2(t),$$

$I_m=V_m(G^2+\omega^2C^2)^{1/2}$, $V_m=E_m/\{(RG+1-\omega^2LC)^2+\omega^2(LG+CR)^2\}^{1/2}$,

$\theta_1=\tan^{-1}(\omega C/G)$, $\theta_2=\tan^{-1}\{\omega(LG+CR)/(RG+1-\omega^2LC)\}$,

$\lambda=0.5(R/L+G/C)$, $\sigma=0.5(R/L-G/C)$, $\mu=\{\sigma^2-1/(LC)\}^{1/2}$,

$i_2^{+o}=0$ or I_s : initial value of i_2,

v_2^{+o} : initial value of v_2.

The uninterrupted duration t_2 of this mode is determined by $i_2=0$ or $v_2=0$ in accordance with Fig.2.3.

(iv) Mode 3

The circuit equations for this mode are given by

$$\left.\begin{aligned} e_3&=v_3,\\ i_3&=0=Cdv_3/dt+Gv_3+I_q, \end{aligned}\right\} \qquad (2.10)$$

where

e_3, i_3 and v_3 : e, i and v in mode 3.

Solving the above equations, we can get

$$e_3=v_3=\varphi_3(t)+\chi_3(t)v_3^{+o}, \qquad (2.11)$$

where

$\varphi_3=-I_q\{1-\chi_3(t)\}/G$,

$\chi_3=\varepsilon^{-tG/C}$,

v_3^{+o} : initial value of v_3.

The duration t_3 of this mode is determined by the criteria shown in Fig.2.3.

2.2.4 Analysis of circuit performances for one cycle and steady ones

The steady and dynamic characteristics of the electromechanical system in Fig.2.1 can be explained by analysing the circuit performances for any one cycle of the ac source frequency. Referring to Fig.2.3, we can readily think of the following four cases concerning the circuit performances during one cycle:

case 1 : motor doesn't rotate,

case 2 : motor, which stops, begins to rotate,

case 3 : motor rotates continuously,

case 4 : motor, which is rotating, stops.

Figures 2.5 (a) to (d) show the illustrative waveforms of e, i and v for cases 1 to 4, respectively, where

α : firing angle of thyristor T_h,

v^{+o} : initial value of v, when T_h is turned on,

Δv^{+o} : variation of v during any one cycle,

t_m : duration of interval of mode m,

m=0, 1, 2, 3 : mode number.

In addition to Figs.2.5 (a) to (d), we can think of other mode transitions from Fig.2.3. However, these transitions rarely occur and so can be ignored for the analysis of the motor characteristics.

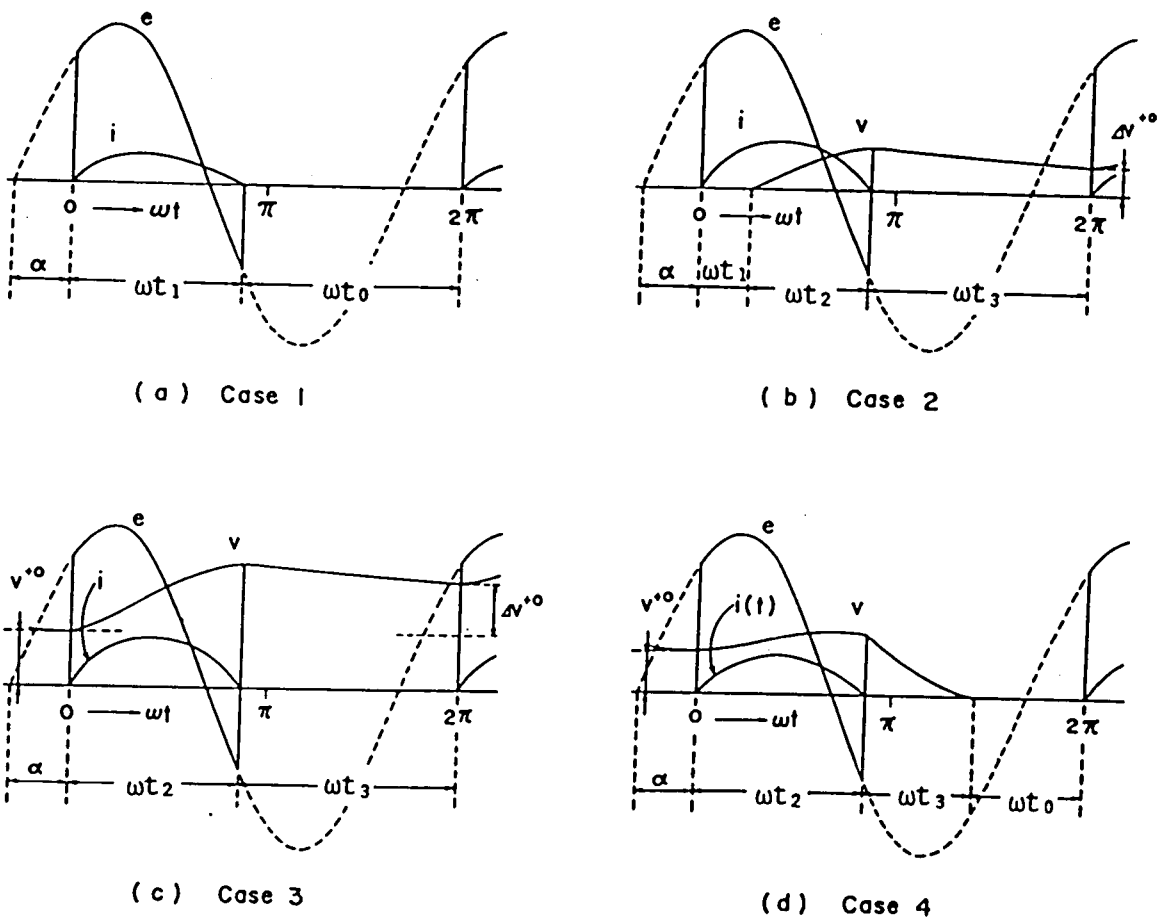

Fig.2.5. Illustrative waveforms of e, i and v in cases 1 to 4.

In this article, let us introduce the method analysing the circuit performances for one cycle in only the case 3 as shown in Fig.2.5(c), which is closely concerned to the dynamic and the steady characteristics of the motor. In this connection, the analyses of the circuit performances in cases 1, 2 and 4 are ignored, because the motor speed is too small to investigate the dynamic characteristics of the dc motor.

The circuit performance in the case 3 is represented by modes 2 and 3, as shown in Fig.2.5(c). In mode 2, $e=e_2$, $i=i_2$ and $v=v_2$ can be obtained by substituting $\alpha_2=\alpha$, $i_2^{+o}=0$ and $v_2^{+o}=v^{+o}$ into Eqs.(2.8) and (2.9). Then, the relation between v^{+o} and t_2 is obtained by putting $i_2=0$ at $t=t_2$, namely

$$\varphi_{21}(t_2)+\chi_{212}(t_2)v^{+o}=0. \tag{2.12}$$

In next mode 3, $v=v_3$ is given by substituting $v_3^{+o}=v_2(t_2)$ in Eq.(2.11). Therefore, the voltage $v=v_3(t_3)$ and the variation Δv^{+o} are given by

$$\left.\begin{aligned} &v_3(t_3)=\varphi_3(t_3)+\chi_3(t_3)\{\varphi_{22}(t_2)+\chi_{222}(t_2)v^{+o}\}, \\ &\Delta v^{+o}=v_3(t_3)-v^{+o}, \end{aligned}\right\} \tag{2.13}$$

where

$$t_2+t_3=\tau,$$

$\tau=2\pi/\omega$: period of ac source frequency,

and $v_3(t_3)$ becomes the initial voltage in the next cycle.

However, when $v^{+o}>E_m\sin\alpha$, the thyristor T_h can't be turned on and the circuit performance is represented by mode 3 only. Accordingly, v_3, t_3 and Δv^{+o} are given by substituting $t_2=0$ and $t_3=\tau$ into Eqs.(2.13). Also, in the case where v_3 reaches to zero in mode 3, as shown in Fig.2.5(d), $v_3=0$ at $t=t_3$ and $\Delta v^{+o}=v^{+o}$ are obtained.

Now, in the steady state where Δv^{+o} becomes zero, the relations among t_2, t_3 and v_∞^{+o} are derived from Eqs.(2.12) and (2.13), as follows:

$$\left.\begin{aligned} &\varphi_3(t_3)+\chi_3(t_3)\varphi_{22}(t_3)+\{\chi_3(t_3)\chi_{222}(t_2)-1\}v_\infty^{+o}=0, \\ &v^{+o}=v_\infty^{+o}=-\varphi_{21}(t_2)/\chi_{212}(t_2), \\ &t_2+t_3=\tau, \end{aligned}\right\} \tag{2.14}$$

where

v_∞^{+o} : initial voltage in steady state.

Also, with respect to the average values E_d, I_d and V_d of e, i and v, the following relations

$$\left.\begin{aligned} E_d &= \frac{E_m}{2\pi}\{\cos\alpha - \cos(\omega t_2+\alpha)\} - \frac{1}{\tau G}\{t_3 I_q + C(v_\infty^{+o} - v_3^{+o}\} \\ &= RI_d + V_d + \frac{t_2}{\tau}E_b, \\ I_d &= GV_d + I_q, \end{aligned}\right\} \qquad (2.15)$$

where

$$E_d = \frac{1}{\tau}\int_0^\tau e\,dt = \frac{1}{\tau}\int_0^{t_2} E_m \sin(\omega t+\alpha)\,dt + \frac{1}{\tau}\int_0^{t_3} v_3\,dt,$$

$$I_d = \frac{1}{\tau}\int_0^\tau i\,dt = \frac{1}{\tau}\int_0^{t_2} i_2\,dt,$$

$$V_d = \frac{1}{\tau}\int_0^\tau v\,dt = \frac{1}{\tau}\int_0^{t_2} v_2\,dt + \frac{1}{\tau}\int_0^{t_3} v_3\,dt,$$

$$v_3^{+o} = \varphi_{22}(t_2) + \chi_{222}(t_2)v_\infty^{+o},$$

are derived from Eqs. (2.8) and (2.10).

2.3 Approximate Method for Analysing Dynamic Performances

The detailed circuit performances of the electromechanical system in Fig.2.1 can be analysed by using the criteria shown in Fig.2.3 and the results of mode analysis given by Eqs. (2.5), (2.7), (2.9) and (2.11). In this section, there is shown an approximate method of the dynamic characteristics in the case 3 where the motor rotates continuously and the circuit performance is represented by modes 2 and 3 in every cycle of the ac source frequency.

2.3.1 Transfer function

When the dc motor is driven by the dc voltage $e=E$, under the assumption that

$J/F \gg L/R$, $E_b=0$ and $I_q=0$, the transfer function $G_d(s)$ of the motor is usually expressed by [39], [40]

$$G_d(s)=\frac{v(s)}{E(s)}=\frac{K_d}{sT_d+1} \tag{2.16}$$

where

$K_d=K_tK_v/(RF+K_tK_v)=1/(RG+1)$: gain,

$T_d=JR/(RF+K_tK_v)=CR/(RG+1)$: time constant of dc motor,

$E(s)$: s-function of E,

$v(s)$: s-function of v,

s : Laplace operator.

Then, the expression of v is easily obtained by the inverse Laplace transformation of $v(s)=G_d(s)E(s)$.

However, since the armature current flows discontinuously in our circuit, the expression of v becomes very complex as described in the previous section. So, let us introduce the approximate method, by which we can easily evaluate v and the dynamic performance of the motor.

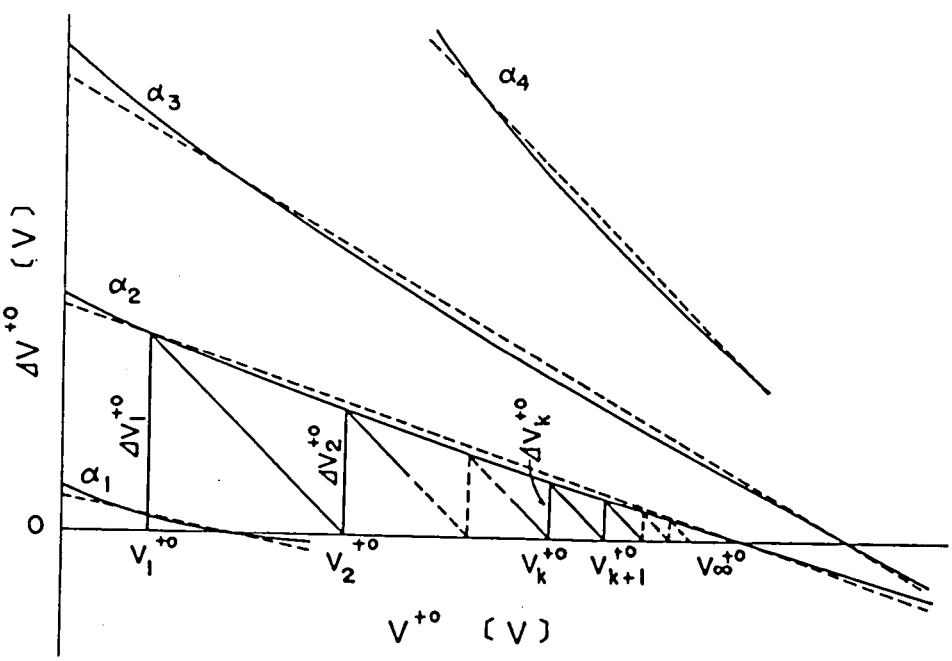

Fig.2.6. Illustrative relation between v^{+o} and Δv^{+o}.

Now, we assume that the relations between the initial value v^{+o} of v and its variation Δv^{+o} during one cycle are represented by the curves as shown in Fig.2.6 for the various firing angles α_1 to α_4.

Next, let us study on the process of the change of v^{+o} in the case where the firing angle is α_2 in Fig.2.6. When we express the initial value and the variation of v^{+o} in the first cycle by v_1^{+o} and Δv_1^{+o}, respectively, the initial voltage v_2^{+o} in the next cycle is given by $v_2^{+o}=v_1^{+o}+\Delta v_1^{+o}$. Repeating a similar treatment, the initial value is finally should arrived at the one v_∞^{+o} in the steady state.

Approximating the $v^{+o}-\Delta v^{+o}$ curves by the dotted straight lines as shown in Fig.2.6, the above mentioned process is simplified and the following linear difference equations

$$\left.\begin{aligned} &v_{k+1}^{+o}=v_k^{+o}+\Delta v_k^{+o}, \\ &\Delta v_k^{+o}=\Delta v_1^{+o}-m(v_k^{+o}-v_1^{+o}), \\ &k=1,2,\ldots\ , \end{aligned}\right\} \tag{2.17}$$

where

$m=-d\Delta v^{+o}/dv^{+o}$,

v_k^{+o} and Δv_k^{+o} : initial value and variation of v in k-th cycle,

are obtained. Solving Eqs. (2.17), we can obtain

$$v_{k+1}^{+o}=v_\infty^{+o}\{1-(1-m)^k\}+v_1^{+o}(1-m)^k, \tag{2.18}$$

where

$v_\infty^{+o}=\lim_{k\to\infty} v_k^{+o}=v_1^{+o}+\Delta v_1^{+o}/m$,

$0<m<2$: convergence condition of v^{+o} when k tends to infinity.

Here, with respect to the value of m, we can find it graphically from the $v^{+o}-\Delta v^{+o}$ curve for a specific firing angle α. However, in the case where the motor rotates continuously as shown in Fig.2.5(c), it is convenient that we look for the value of m in the following manner. As t_2 is the function of $v^{+o}=v_2^{+o}$ as seen in Eq. (2.12), we have

$$m=-d\Delta v^{+o}/dv^{+o}=-(\partial\Delta v^{+o}/\partial t_2)(dt_2/dv^{+o})-\partial\Delta v^{+o}/\partial v^{+o}. \tag{2.19}$$

Calculating $\partial\Delta v^{+o}/\partial t_2$ by using Eqs. (2.14) and (2.15), we can obtain

$\partial \Delta v^{+o}/\partial t_2=\chi_3(\tau-t_2)i_2(t_2)/C=0$. Consequently, m can be expressed as follows:

$$m=-\partial \Delta v^{+o}/\partial v^{+o}=1-\chi_3(\tau-t_2)\chi_{222}(t_2). \tag{2.20}$$

From the exponential functions $\chi_3(\tau-t_2)$ and $\chi_{222}(t_2)$ given in Eqs.(2.9) and (2.11), the condition $0<m<1$ is derived for the usual dc motor, in which $J/F>L/R$ is satisfied. Also, replacing the term $(1-m)$ in Eq.(2.18) by $\exp(-\tau/T_m)$, v_{k+1}^{+o} is rewritten as

$$v_{k+1}^{+o}=v_\infty^{+o}(1-\varepsilon^{-k\tau/T_m})+v_1^{+o}\varepsilon^{-k\tau/T_m}, \tag{2.21}$$

in which T_m is an equivalent time constant of the motor and is given by

$$T_m=-\tau/\log(1-m)=-\tau/\log\{\chi_3(\tau-t_2)\chi_{222}(t_2)\}, \tag{2.22}$$

Consequently, we can see that the initial value v^{+o} changes discretely with the time constant T_m and the period τ. In this connection, there was a paper[26] in which the change of v^{+o} is represented by a continuous function of the time t, but the one should be done by the discrete function as shown in Eq.(2.21).

Next, let us consider the dynamic performance of the motor when α is changed to $\alpha+\Delta\alpha$. In this case, the changes of the values t_2 and t_3 given by Eqs.(2.14) are assumed to be very small for $\Delta\alpha$, and the change of T_m given by Eq.(2.22) can be neglected. The gain K_m of the motor for $\Delta\alpha$ can be obtained by using Eqs.(2.14), as follows:

$$K_m=\Delta v^{+o}/\Delta\alpha\cong\partial v_\infty^{+o}/\partial\alpha+(\partial v_\infty^{+o}/\partial t_2)(dt_2/d\alpha), \tag{2.23}$$

where

$\Delta v^{+o}=\Delta v_\infty^{+o}$: variation of v_∞^{+o} for α due to $\Delta\alpha$.

From Eqs.(2.21) and (2.23), the relation between Δv^{+o} and $\Delta\alpha$ is now expressed by the following transfer function

$$G(s)=\frac{\Delta v^{+o}(s)}{\Delta\alpha(s)}=\frac{K_m}{sT_m+1}, \tag{2.24}$$

where

$\Delta v^{+o}(s)$: s-function of Δv^{+o},

$\Delta\alpha(s)$: s-function of $\Delta\alpha$.

This transfer function $G(s)$ is very useful to analyse the dynamic characteristic of

the motor. Now, the one in Fig.2.1 is evaluated by the equivalent sampled data system, as shown in Fig.2.7, where

Δv : change of voltage v,

Δv^{+o} : change of initial value of v,

Δv_r : change of input voltage v_r,

$\Delta\alpha=K_c\Delta v_r$: change of α,

$H(s)=(1-\varepsilon^{-\tau s})/s$: zeroth order holding circuit,

K_c : gain in controller,

S_s : sampling switch with period τ.

The holding circuit $H(s)$ and the sampling switch S_s are used, because α is periodically given to the rectifier circuit and is kept constant during τ. This sampled data system is easily applied in the case where the motor is driven with the speed feedback. Figure 2.8 shows the equivalent system with the speed feedback, where

$\Delta\alpha=K_c(\Delta v_r-K_b\Delta v^{+o})$,

$\varepsilon=\Delta v_r-K_b\Delta v$: offset,

K_b : gain in feedback circuit.

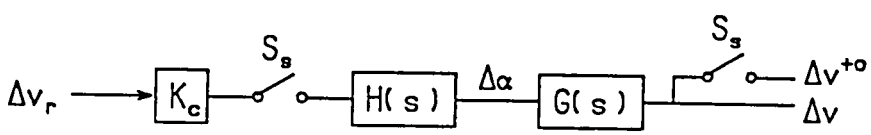

Fig.2.7. Equivalent sampled data system without speed feedback.

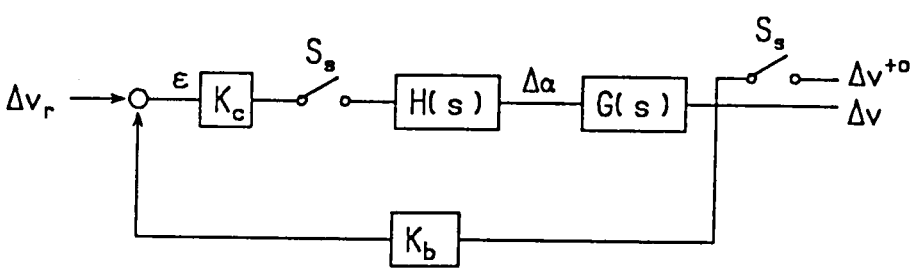

Fig.2.8. Equivalent sampled data system with speed feedback.

2.3.2 Pulse transfer function

To analyse the motor performance by using Fig.2.7 or 2.8, it is convenient to use a pulse transfer function.[41] We first introduce the pulse transfer function of the control system with the speed feedback, as shown in Fig.2.8. The total pulse transfer function $G_t(z)$ is given by

$$G_t(z)=\frac{\Delta v^{+o}(z)}{\Delta v_r(z)}=\frac{K_c HG(z)}{1+K_b K_c HG(z)}=K\frac{1-b}{z-b}, \tag{2.25}$$

where

$HG(z)$: z-function of $H(s)G(s)$,

$\Delta v^{+o}(z)$: z-function of Δv^{+o},

$\Delta v_r(z)$: z-function of Δv_r,

$z=\exp(s\tau)$, $a=\exp(-\tau/T_m)$, $b=a-K_b K_c K_m(1-a)=a(1+K_b K_c K_m)-K_b K_c K_m$,

$K=K_c K_m/(1+K_b K_c K_m)$: total gain,

Here, let us consider the characteristics of the system given by Eqs.(2.25). As the value of K_c increases, K and ε approach closely to $1/K_b$ and zero, respectively. However, b becomes negative and the motor performance becomes oscillatory. Especially, the instability of the motor performance may happen when $|b|<1$. Then, the useful value of K_c is limited. There is another limitation for K_c that the firing angle $\alpha+\Delta\alpha$ of thyristor must satisfy the conditions of $E_m\sin(\alpha+\Delta\alpha)>v^{+o}$ and $0\leq\alpha+\Delta\alpha\leq 180^\circ$, where $\Delta\alpha=K_c\varepsilon$.

The pulse transfer function $G_t(z)$ is useful when we wish to calculate the transient or frequency response of the motor. The transient response can be obtained by reversing the z-function $\Delta v^{+o}(z)=G_t(z)\Delta v_r(z)$ to the time function. On the other hand, when Δv_r is varied sinusoidally with the angular frequency ω_r, the frequency response is derived as follows:

$$G_t(z)=R_e+jI_m, \tag{2.26}$$

where

$z=\exp(j\omega_r\tau)$, $j=\sqrt{-1}$,

$$\Re_e=\frac{K(1-b)(\cos\omega_r\tau-b)}{1-2b\cos\omega_r\tau+b^2} \quad : \text{real part of } G_t(z),$$

$$\Im_m=\frac{K(1-b)\sin\omega_r\tau}{1-2b\cos\omega_r\tau+b^2} \quad : \text{imaginary part of } G_t(z).$$

And the vector trajectory of $G_t(z)$ is plotted by the following circular equation

$$(\Re_e-\frac{bK}{1+b})^2+\Im_m^2=(\frac{K}{1+b})^2. \tag{2.27}$$

Next, in the control system without the feedback, as shown in Fig.2.7, the pulse transfer function and the frequency response are obtained by putting $K_b=0$ into Eqs.(2.25) to (2.27).

2.4 Numerical Calculations and Experimental Results

In the previous sections, we presented a theoretical method, by which we can analyse the dynamic and the steady performances of the motor control circuit in Fig.2.1. So in this section, in order to investigate the appropriateness of our method, let us compare the results of the numerical analysis with the experimental results, and also add some new contributions to the speed control technique of the motor by the thyristor rectifier circuit. Next, when the motor is controlled by the rectifier circuit, some inductance is usually added to the armature circuit to reduce the abrupt change of the armature current, because the abrupt change often gives a bad influence on the commutation characteristics of the motor, such as the commutation spark.[42],[43] Therefore, we also investigate the influence of the inductance on the characteristics of the motor.

2.4.1 Experimental circuit

Figure 2.9 shows the schematic diagram of the experimental circuit, where

g : gate signal for thyristor T_h,

I : ammeter to measure average value I_d of current i,

V : volt meter to measure average value V_d of counter emf v,

v_r : input voltage to controller,

$v_g=v/K_{tg}$: output voltage of T_g,

K_{tg} : voltage coefficient of T_g,

G_e : generator to regulate load of M,

M : supplied dc motor,

R_l : load resistor of G_e,

T_g : tachometer generator,

T_r : transformer.

In the circuit, the firing angle α of T_h is regulated by v_r, and the load of M is adjusted by changing the one R_l of G_e.

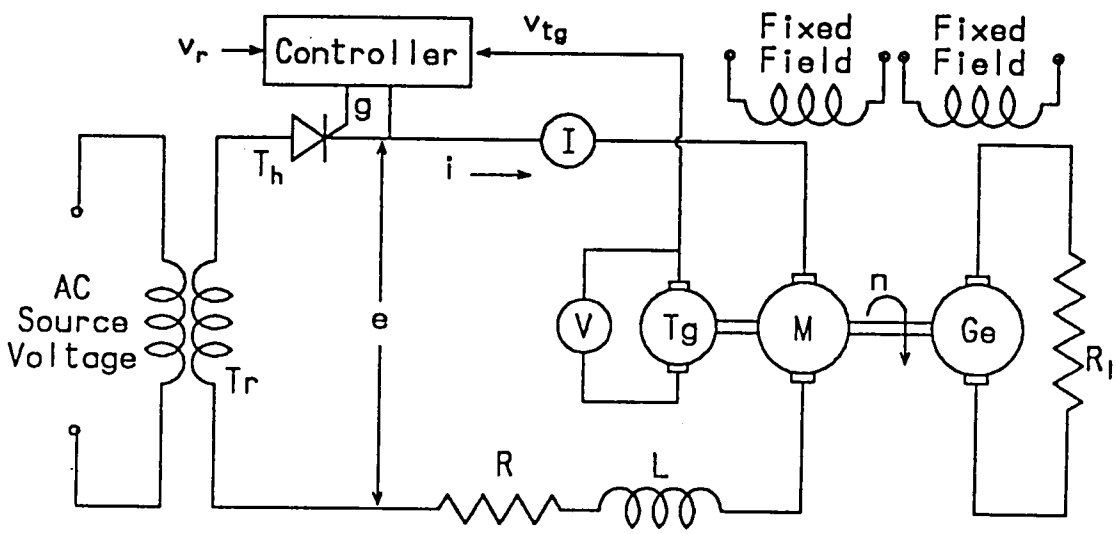

Fig.2.9. Schematic diagram of experimental circuit.

In the controller, there is prepared the linear relation between $E_m\cos\alpha$ and the offset ε, because the term $E_m\cos\alpha$ is involved in the average value E_d of e as shown in Eqs.(2.15). Figure 2.10 shows the operation block diagram of the controller to generate the gate signal g, where

$\varepsilon=v_r-K_b v$: offset,

$E_m \sin\omega t$: ac supply voltage and $\omega=2\pi f$,

e_b : bias voltage for comparator,

e_c : output of comparator, which determines α,

$e_l=K_1\varepsilon$: output of limited amplifier and $0\leqq e_l\leqq e_{lm}$,

e_{lm} : maximum voltage of e_l ,

e_r : output of half-wave rectifier circuit,

$e_{ri}=K_2E_m(\cos\omega t-1)$ for $0\leqq\omega t\leqq\pi$: output of integration circuit,

f : ac source frequency,

K_b and K_{tg} : gains in feedback circuit,

K_1 : gain of limited amplifier,

K_2 : gain in integration circuit.

The gate signal g and the firing angle α are given by e_c, which is obtained by comparing e_b, e_l and e_{ri}. The illustrative waveform of each signal is shown in Fig.2.11. We can now obtained the linear relation between $E_m\cos\alpha$ and e_l as follows:

$$K_2E_m(\cos\alpha-1)=-e_b+e_l, \tag{2.28}$$

where

$e_l=K_1\varepsilon=K_1(v_r-K_b v^{+o})$,

$0\leqq e_l\leqq e_{lm}$,

v^{+o} : value of v at phase angle α.

Figure 2.12 shows the relation between e_l and α in our controller, where e_b=5.4 V and e_{lm}=4.8 V. Now, the gain K_c shown in Figs.2.7 and 2.8 is replaced by

$$K_c=K_1K_\alpha, \tag{2.29}$$

where

$K_\alpha=\Delta\alpha/\Delta e_l$,

Δe_l and $\Delta\alpha$: variations of e_l and α,

in which K_α is evaluated from Fig.2.12.

According to Figs.2.9 to 2.12, we can change the firing angle α by regulating v_r, where $15^\circ\leqq\alpha\leqq140^\circ$. Also, we can drive the motor M with or without the speed

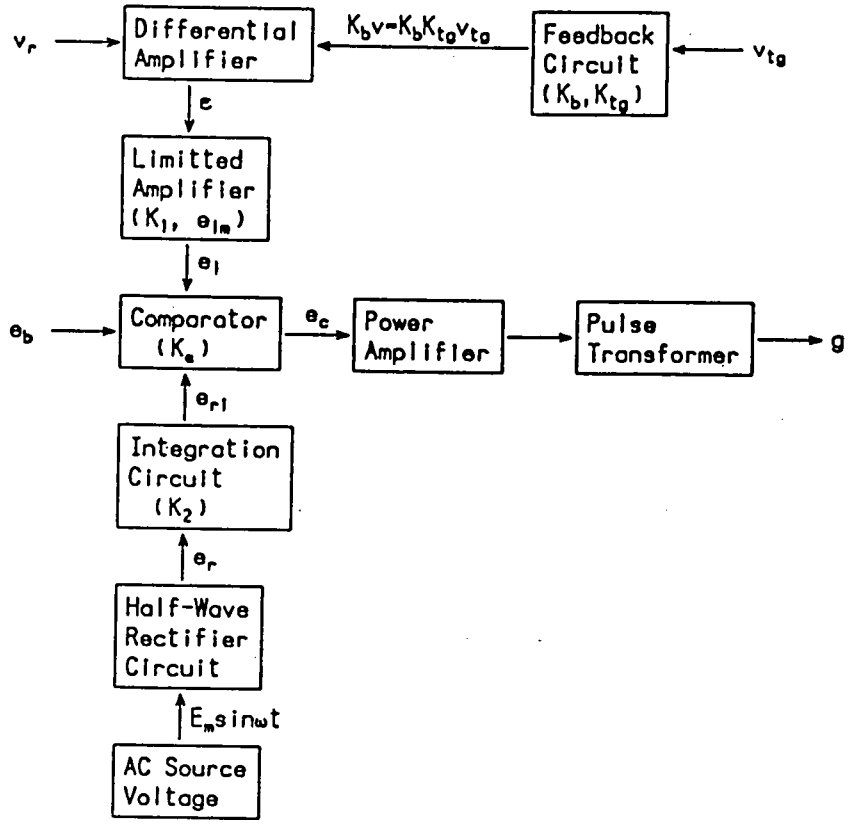

Fig.2.10. Block diagram of controller.

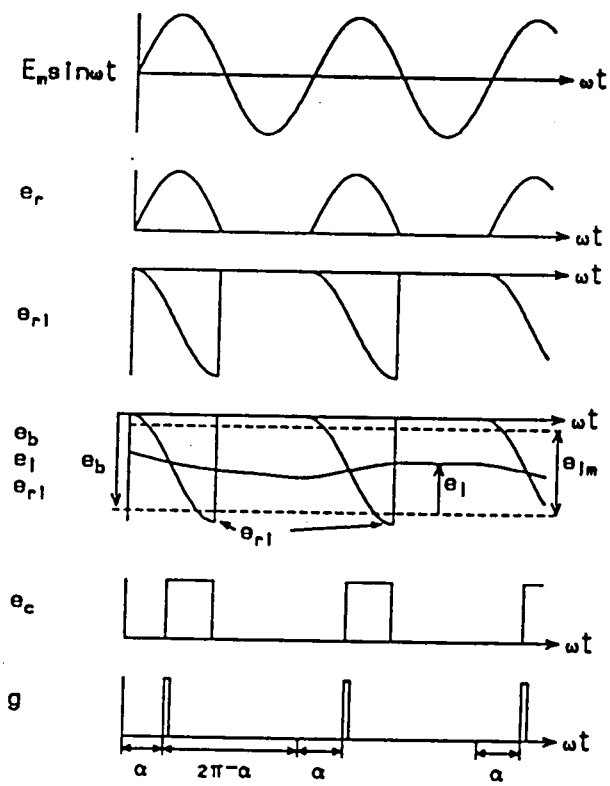

Fig.2.11. Signal waveforms in controller.

feedback by setting $K_b>0$ or $K_b=0$.

Next, Table 2.1 presents the specification of the servomotors which are used for both M and G_e, and Table 2.2 the values of circuit parameters, where we assume that the impedance of the transformer T_r and the forward resistance of T_h are negligible. The actual waveforms of e, i and v are measured with a synchroscope or a photo-recorder.

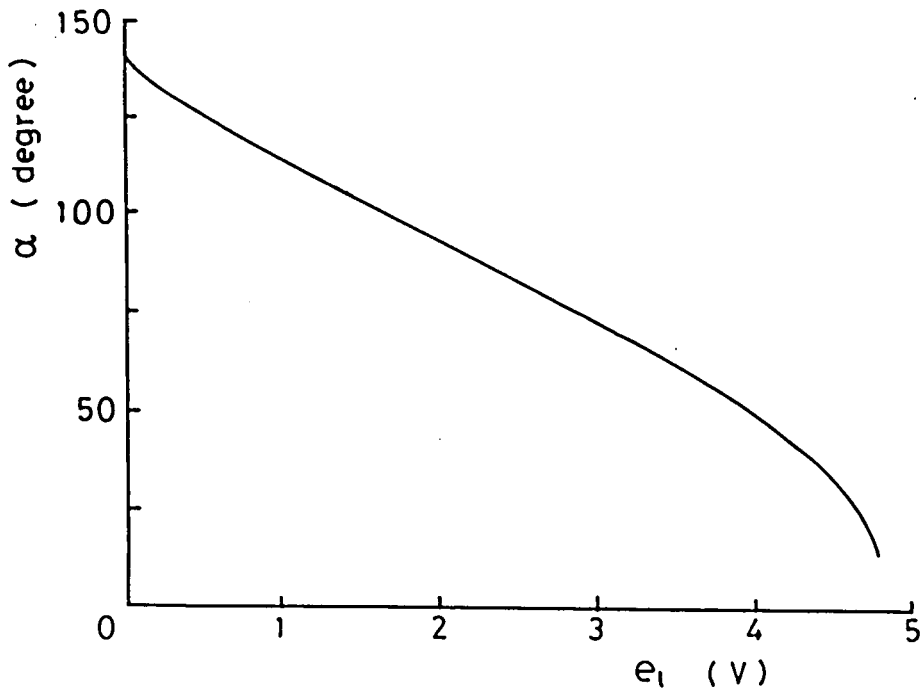

Fig.2.12. Relation between e_t and α.

Table 2.1 Specification of dc motor

Type(maker)	TD13-5 (Sanyo Electric Co.)
Rated power	200 W
Rated voltage	100 V
Rated current	2.7 A
Rated speed	3000 rpm
Rated field current	250 mA

Table 2.2 Circuit paramers

Mechanical parameters		Electric parameters	
J = 0.00214	kg·m	C = 14.0	mF
Qs = 0.263	N·m	Is = 0.672	A
Q = 0.168	N·m	Iq = 0.430	A
F = 0.000364 to 0.0299	N·m·s/rad	G = 2.38 to 195.6	mS
Kv = 0.391	V·s/rad	Em = 141.4	V
Kt = 0.391	N·m/A	f = 60	Hz
Ktg = 5.038		R = 14.1	Ω
		L = 6.3,46.9, 108.7	mH
		Eb = 2.48	V

2.4.2 Steady characteristics[36], [37], [38]

The fundamental characteristics of the motor in the steady state is investigated, where K_b=0 is set in the controller shown in Fig.2.10 and so the motor is driven without the feedback.

(1) Instantaneous waveforms

Figure 2.13 shows the examples of instantaneous waveforms of i and v for α=60° , G=20.9 mS and some values of L, which are calculated by using Eqs. (2.9), (2.11) and (2.14). From the figure, we see that the fluctuation of the motor speed is negligible, because our dc motor has a large value of inertia of moment as shown in Table 2.2. Furthermore, when the value of L increases, the conducting duration of i increases but the peak values of i and v decrease. In Fig.2.13, the experimental results which are measured with a synchroscope are added, too. By comparing the calculated results with the experimental ones, we see that the good agreement is obtained.

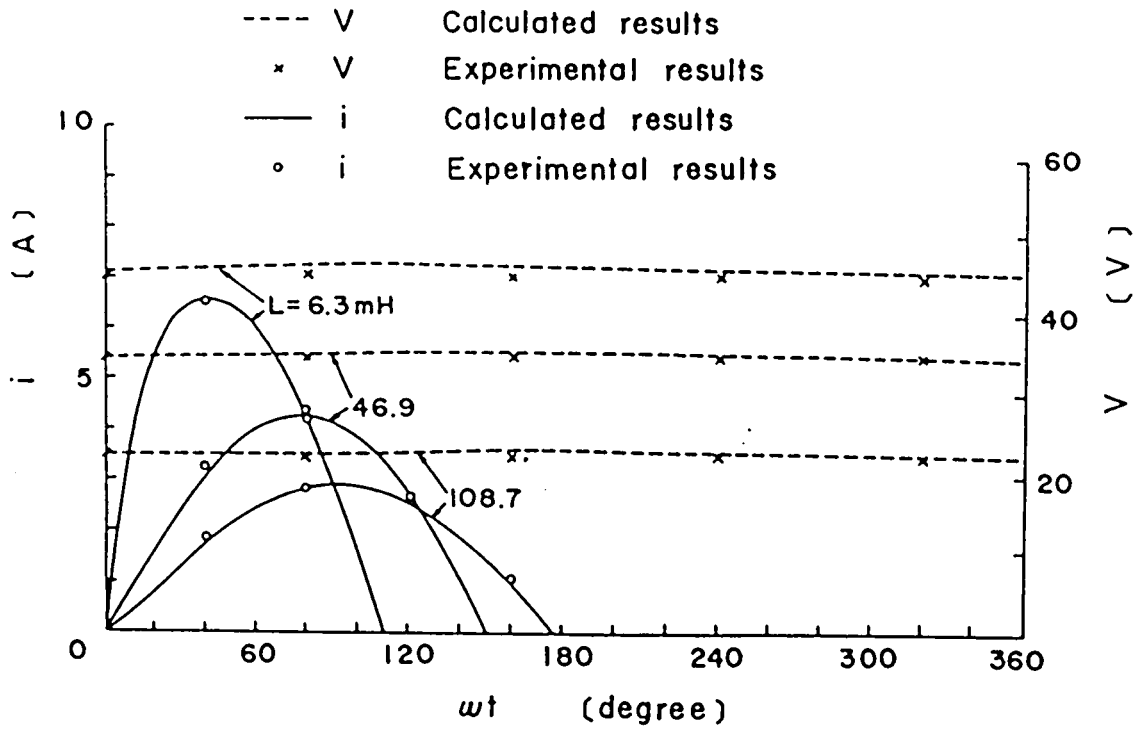

Fig.2.13. Instantaneous waveforms of i and v for G=20.9 mS and α=60° .

(2) Speed-torque characteristics

In Figs.2.14 to 2.16, the calculated I_d–V_d curves, corresponding to the speed-torque characteristic ones, are presented for several values of α and L, and also some experimental results are plotted. The small difference between both results is surmised to be caused by the armature reaction of the motor, the nonlinearities of circuit parameters and the measurement errors. From the figures, we can see that V_d for a specific firing angle decreases steeply according to the increases of I_d and L. We think that this is owing to the ohmic voltage drop RI_d and the large decrease of the terminal voltage E_d in Eqs. (2.15).

Now, the fluctuation of v is very small as shown in Fig.2.13, so we can suppose that the conventional analysis, in which the motor speed is assumed to be constant, is available occasionally in the analysis of the steady characteristics. As it is assumed that v=V_d is constant in the conventional method, so this method is convenient to analyse the relations among V_d, I_d and α. However, the method is not useful to investigate the precise dynamic characteristics of the motor.

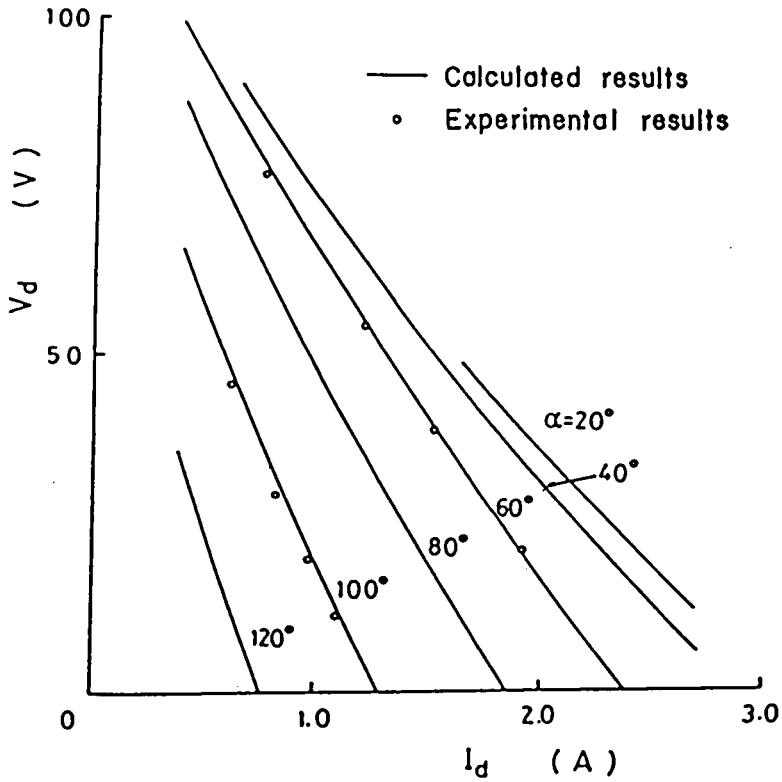

Fig.2.14. Relation between I_d and V_d for L=6.3 mH.

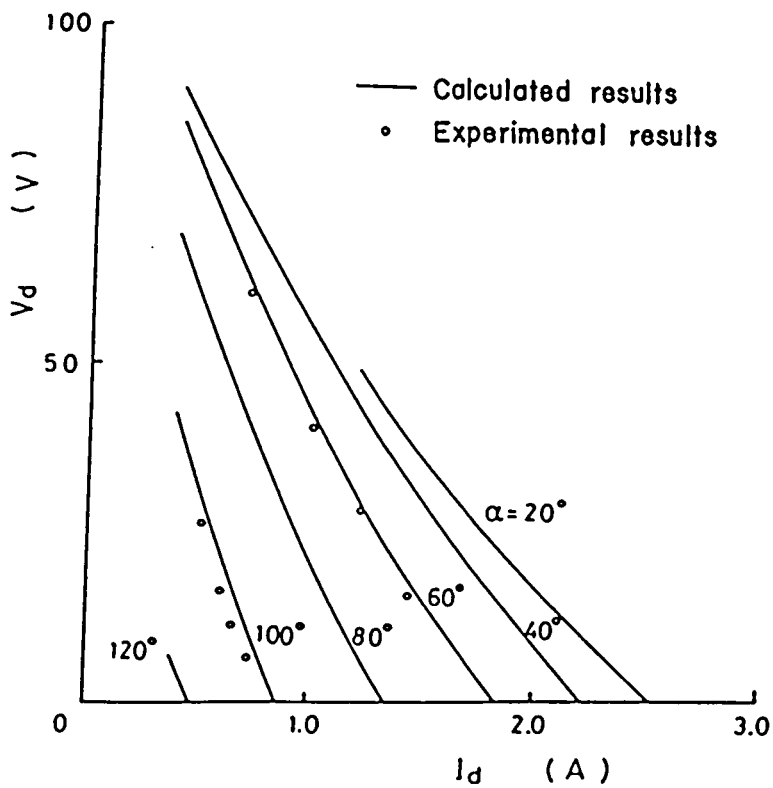

Fig.2.15. Relation between I_d and V_d for L=46.9 mH.

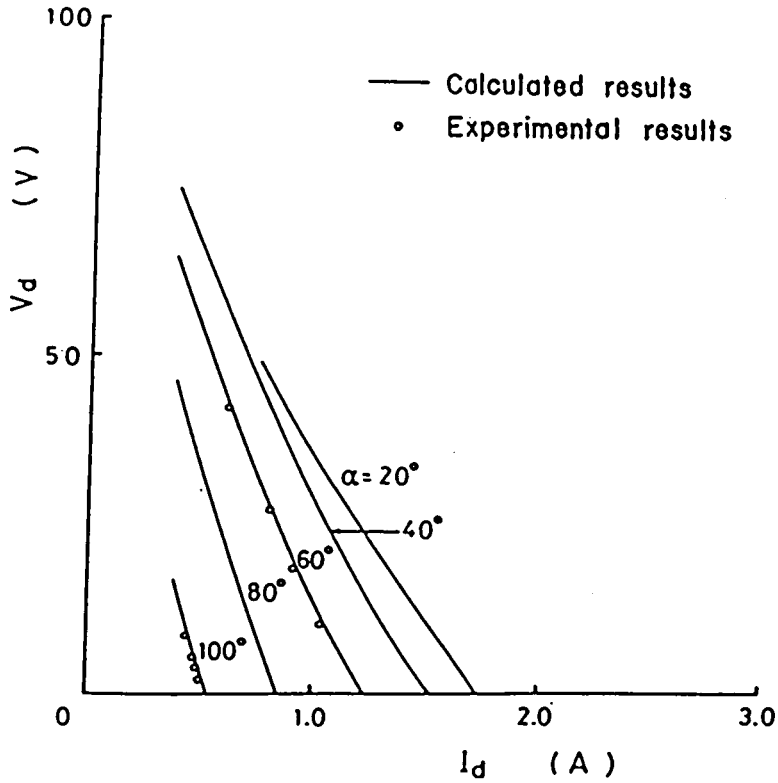

Fig.2.16. Relation between I_d and V_d for L=108.7 mH.

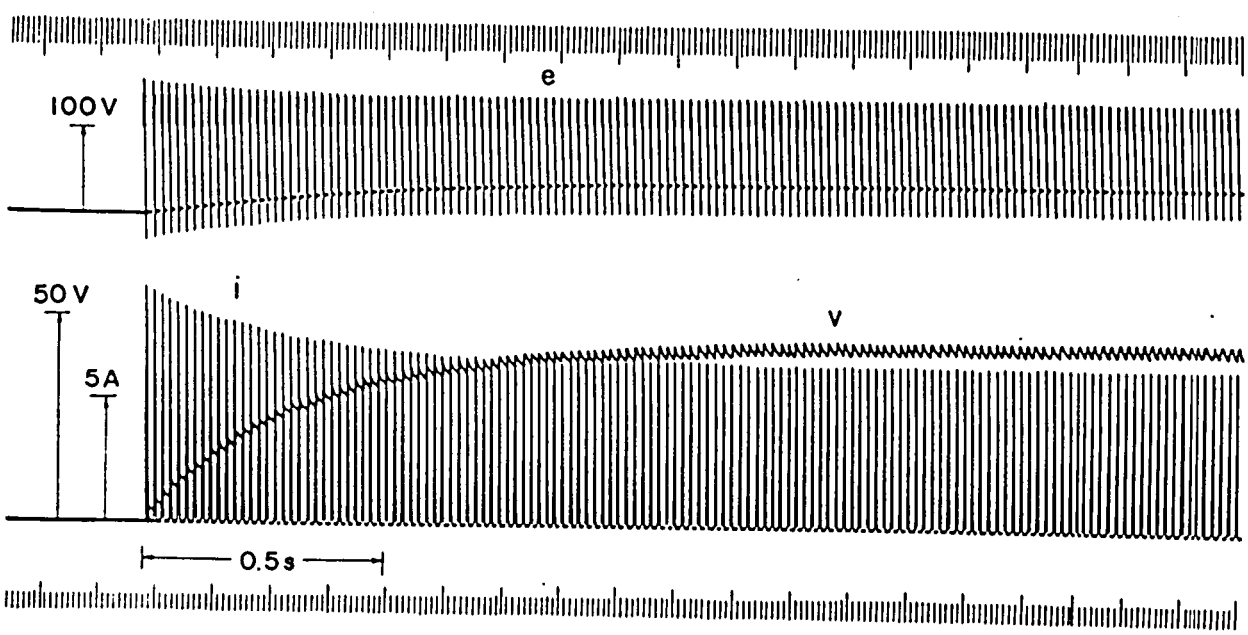

Fig.2.17. Example of oscillogram of transient response for L=6.3 mH, G=20.9 mS, K_b=0 and α=60° .

2.4.3 Transient characteristics[32], [37], [38]

Figure 2.17 shows the representative oscillograms of e, i and v in the transient state, where α=60° , L=6.3 mH, G=20.9 mS and K_b=0.

In Figs.2.18 and 2.19, we plot some examples of the calculated relations between v^{+o} and Δv^{+o} and also some experimental results, which are measured from the oscillograms of v. Comparing the calculated results with the experimental ones, fairly good agreement is obtained.

As described in Article 2.3.1, we can easily see the transient performance of the motor from the characteristic curves in Figs.2.18 and 2.19. In this connection, when v^{+o} exceeds $E_m \sin\alpha$, for example α=20° and v^{+o}>48.4 V in Fig.2.18, the thyristor is not turned on and v^{+o} drops from the right end of the curve for α=20° to the one for α=180° . The curve for α=180° shows the relation in the case where T_h is not turned on and the motor rotates only by its inertia.

As shown in Figs.2.18 and 2.19, it can be seen that the v^{+o}-Δv^{+o} curves are able to be fairly well approximated by the straight lines independently of the values of L, G and α. Then, we can evaluate T_m given by Eq. (2.22). In Fig.2.20, we plot the relation of T_m vs. α for some values of L and G. From the figure, we see that T_m is much influenced by G rather than L, because the mechanical time constant $J/F=C/G$ is much larger than the electric one L/R in our motor. Next, let us compare the value of T_m plotted in Fig.2.20 with the one of T_d given in Eq. (2.16). The former is several times larger than the latter, as, for example 0.63<T_m<1.42 s and T_d=0.191 s for G=2.38 mS or 0.27<T_m<0.51 s and T_d=0.152 s for G=20.9 mS, because there can exist a duration when the armature current is blocked and the motor is decelerated in our rectifier circuit.

In Fig.2.21, we plotted the calculated transient values of v^{+o} for α=60° , which are found by putting the values of T_m obtained from Fig.2.20 into Eq. (2.21), and the experimental ones which are acquired from the oscillograms of v. It is seen that the calculated results agree well with the experimental ones.

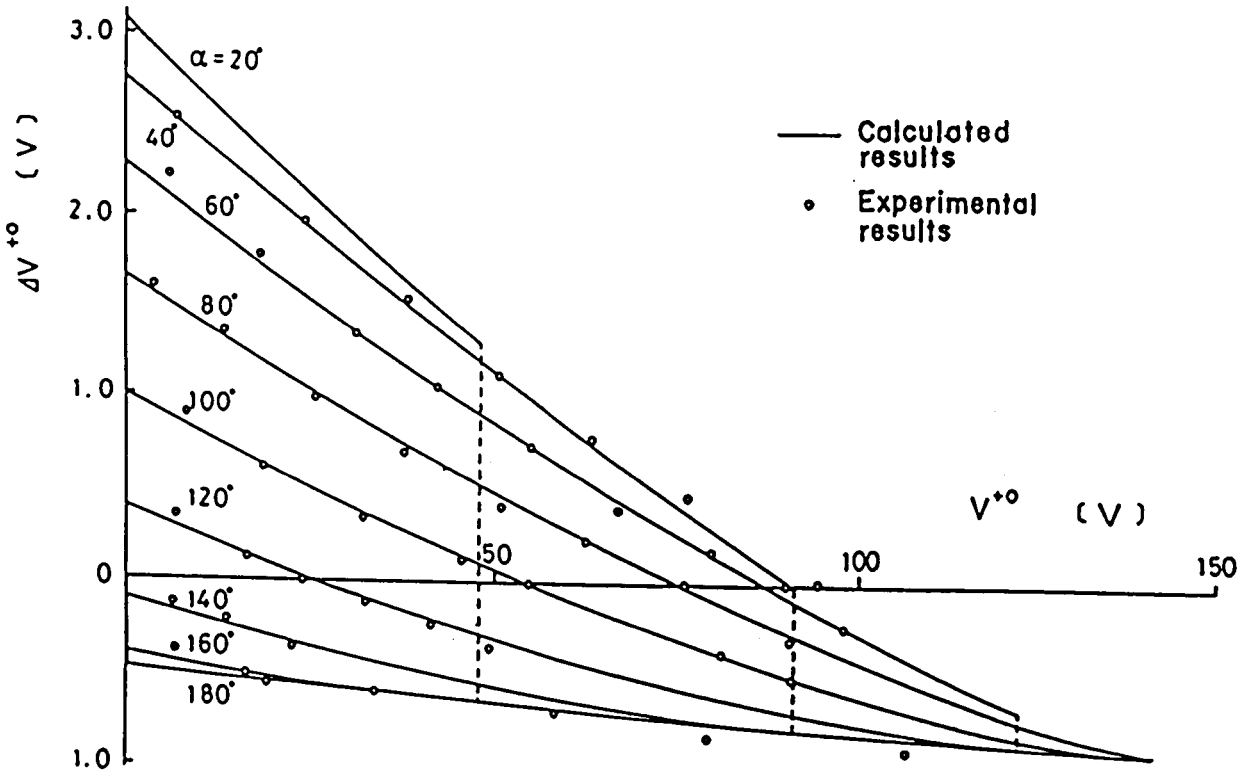

Fig.2.18. Relation between v^{+o} and Δv^{+o} for L=6.3 mH and G=2.38 mS.

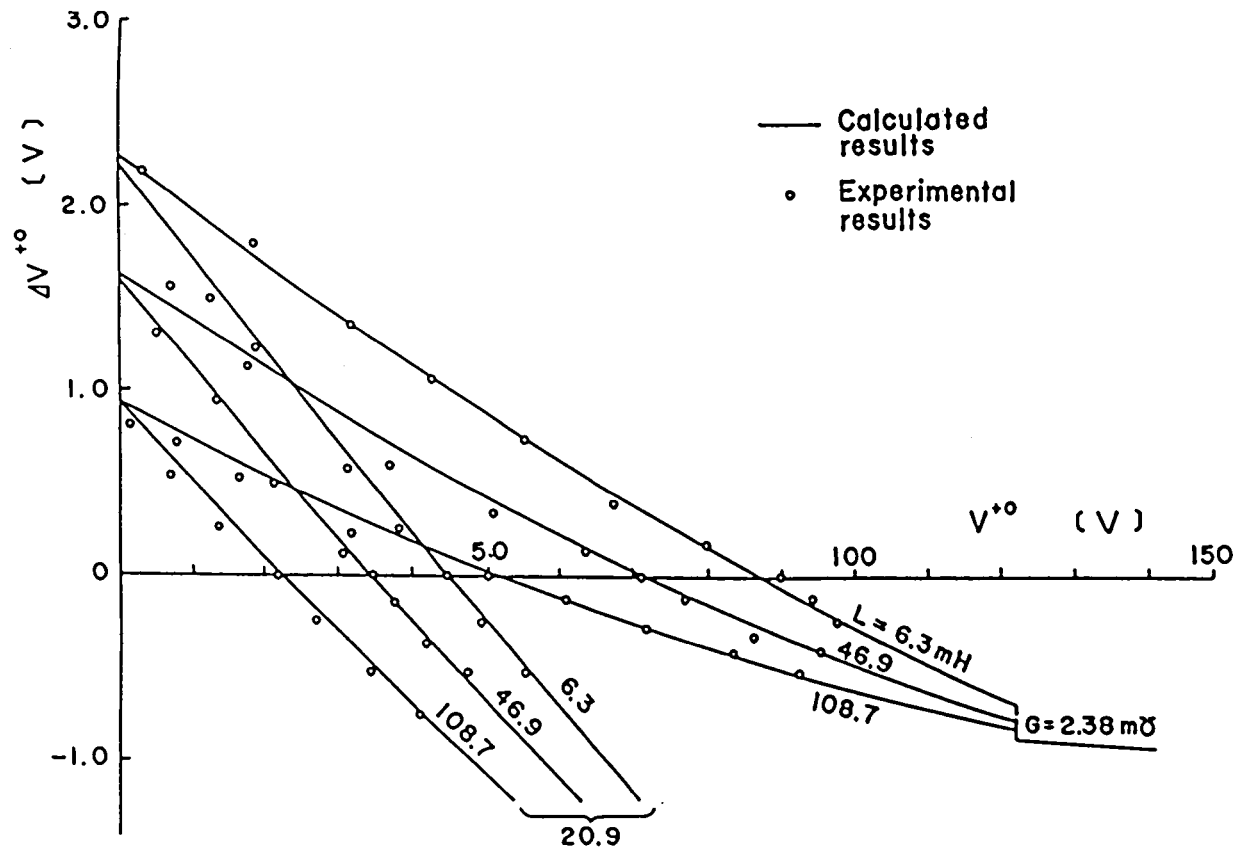

Fig.2.19. Relation between v^{+o} and Δv^{+o} for α=60° .

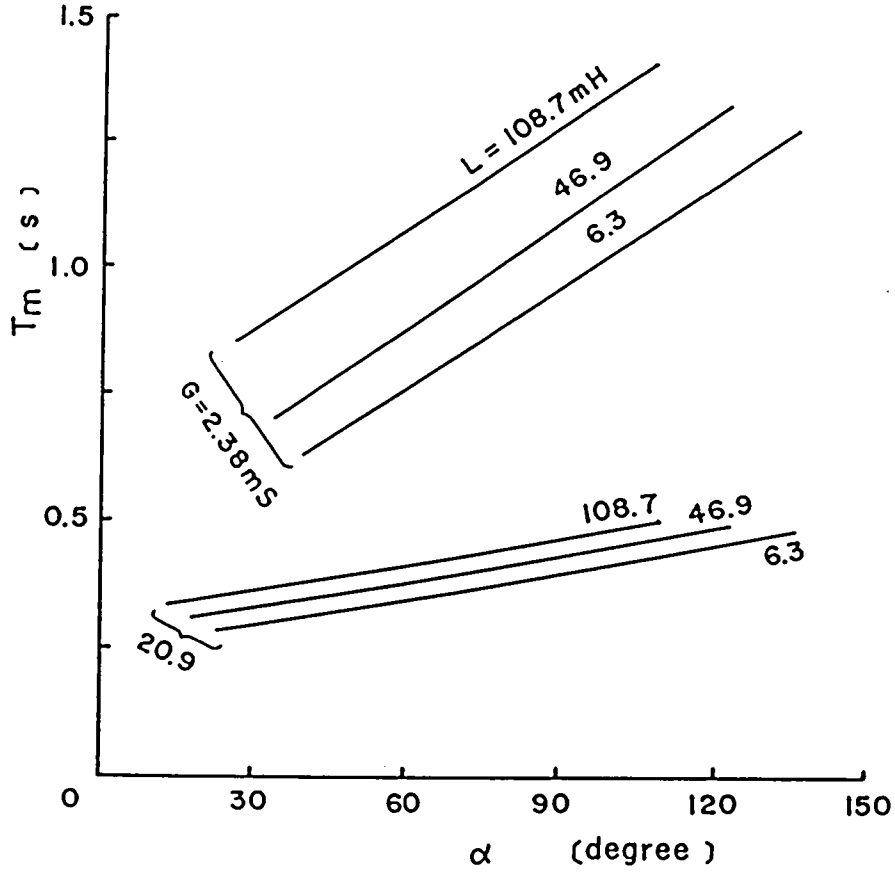

Fig.2.20. Relations between α and T_m.

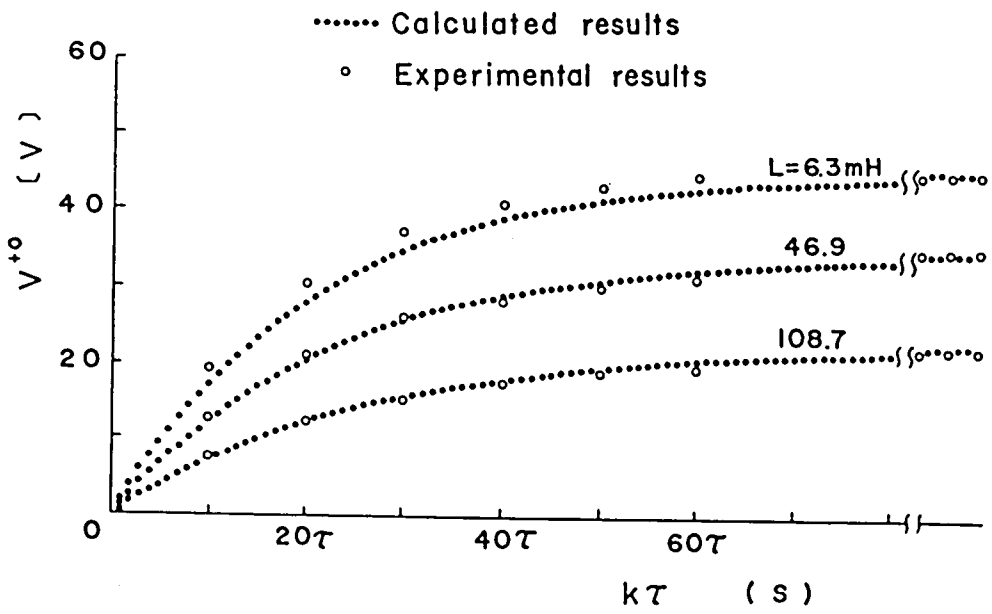

Fig.2.21. Transient response of v^{+o} for G=20.9 mS and α=60°.

2.4.4 Transfer function[31]-[38]

In Figs.2.22 and 2.23, there are plotted the relations of $K_m' = K_\alpha K_m = \Delta v^{+o}/\Delta e_l$, T_m and v_∞^{+o} vs. e_l and α for several values of L and G, which are obtained from Eqs.(2.14), (2.22), (2.23) and (2.29), and Figs.2.12 and 2.20. By using Figs.2.22 and 2.23, we can easily estimate the dynamic characteristic of the motor, such as a frequency response, for the variation of v_r or $e_l = K_l(v_r - K_b v^{+o})$ in the controller.

Next, the term $K_c K_m$ in the pulse transfer function $G_t(z)$ given by Eqs.(2.25) or (2.26) is replaces as

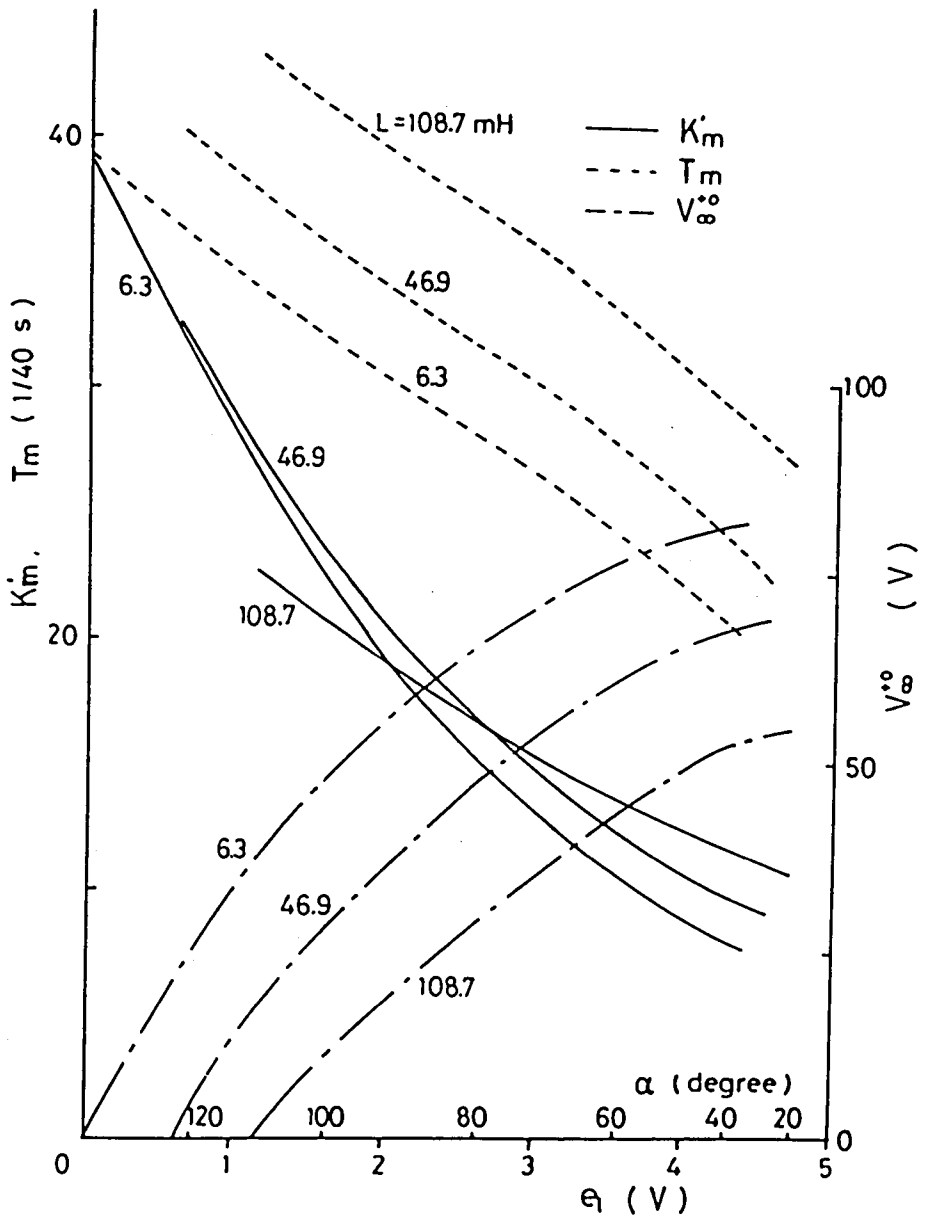

Fig.2.22. Relations of K_m', T_m, v_∞^{+o} and α vs. e_l for G=2.38 mS.

$$K_c K_m = K_1 K_m' , \tag{2.30}$$

where

$$K_c = K_1 K_\alpha ,$$

$$K_m' = K_\alpha K_m .$$

From Fig.2.22, we can see that K_m' and T_m are fairly influenced by e_l, in the case where the motor load, namely the value of G, is small. Thus, we can partially use the block diagram shown in Fig.2.7 or 2.8 and $G_t(z)$ given in Eqs. (2.25) or (2.26), where the parameters K_c, K_m and T_m are assumed to be constants independent of the variation of e_l or α. In order to limit the variation of e_l shown in Eq. (2.28), we set K_1=1.06 in our controller shown in Fig.2.10.

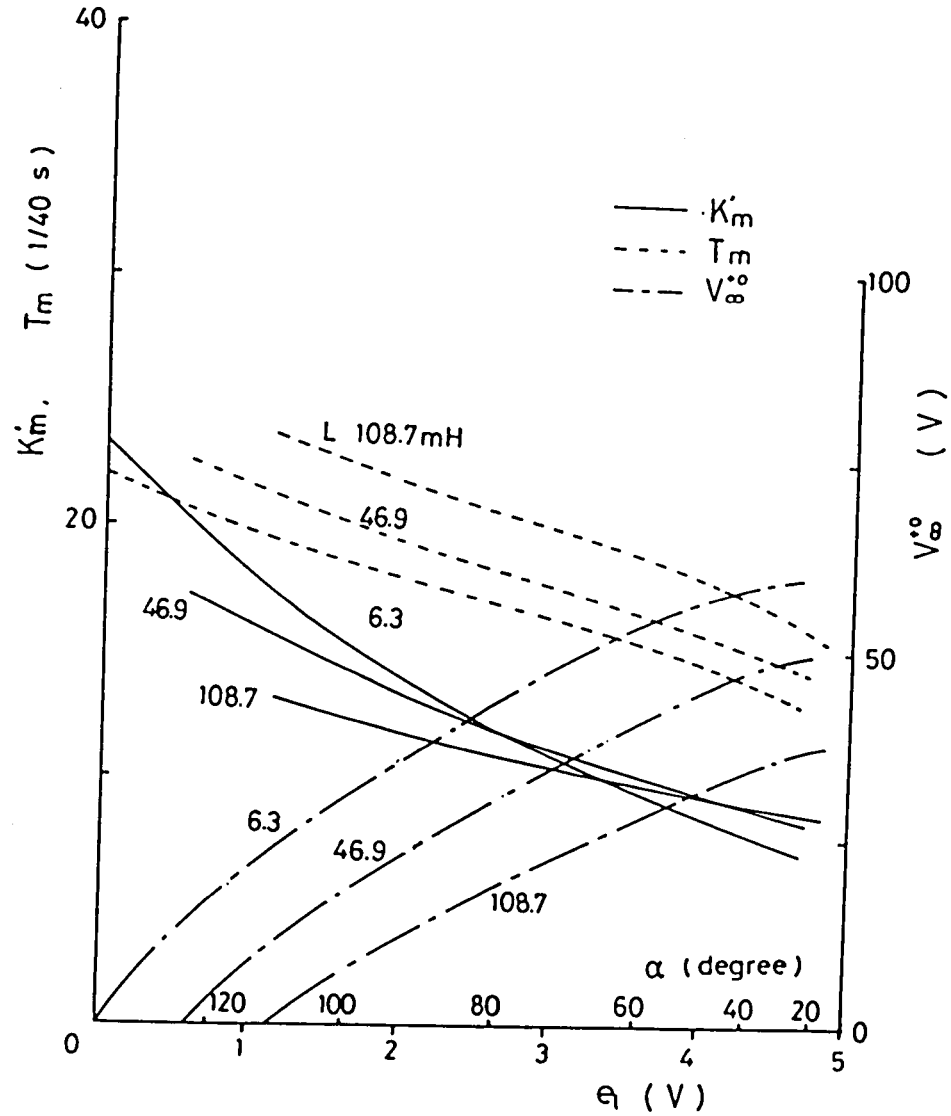

Fig.2.23. Relations of K_m', T_m, v_∞° and α vs. e_l for G=20.9 mS.

2.4.5 Frequency responses [33], [34], [37], [38]

The caluculated frequency responses of the motor for G=20.9 mS and L=6.3 and 108.7 mH are presented in Fig.2.24, where K_b=0 and the motor is driven by a basic firing angle α=80° , which is obtained for e_l=2.6 V, without the feedback. Here, for numerical calculation of the frequency responses by Eqs.(2.26), (2.27) and (2.30), we use the following conditions

$$\left.\begin{aligned} &K_m'=11.9 \text{ and } 10.9, \\ &T_m=0.422 \text{ and } 0.515\ s, \\ &K_l=1.06. \end{aligned}\right\} \qquad (2.31)$$

where most values of these parameters are derived from Fig.2.23. The experiment is made by regulating v_r in Fig.2.9, where we have $v_r=2.45+0.283\sin(2\pi f_r t)$ to prepare $e_l=2.6+0.3\sin(2\pi f_r t)$. Also, the actual frequency responses are measured by using a transfer function analyser.

In Fig.2.24, the gain $(\mathfrak{G}_e^2+\mathfrak{g}_m^2)^{1/2}$ of the pulse transfer function $G_l(z)$ is much decreased for the input frequency f_r>1 Hz, so we can see that the motor can't respond to the abrupt change of v_r. This is caused by the large value of the time constant T_m. Also, by our numerical conditions shown in Eqs.(2.31), the relation $0.96<b=a=\exp(-\tau/T_m)<0.97$ is satisfied, and the relation $bK/(1+b)\fallingdotseq K/2$ is obtained for $6.3\leqq L\leqq 108.7$ mH , where $11.5<K=K_lK_m'<12.7$.

Next, the calculated frequency responses for G=20.9 mS, $\alpha\fallingdotseq 80°$ and L=6.3 and 108.7 mH are shown in Fig.2.25, where the motor is driven with K_b=0.5. The experimental results are obtained by driving the motor, where v_r is regulated to give $e_l=2.6+0.3\sin(2\pi f_r t)$ V. From Fig.2.25, we can see that both loci of the frequency response for L=6.3 and 108.7 mH draw considerably near each other, since b and K in Eq.(2.27) are

$$\left.\begin{aligned} &b=0.717 \text{ and } 0.785, \\ &K=1.73 \text{ and } 1.70, \end{aligned}\right\} \qquad (2.32)$$

for L=6.3 and 108.9 mH, respectively, although the values of K_m and T_m differ as shown in Eqs.(2.31).

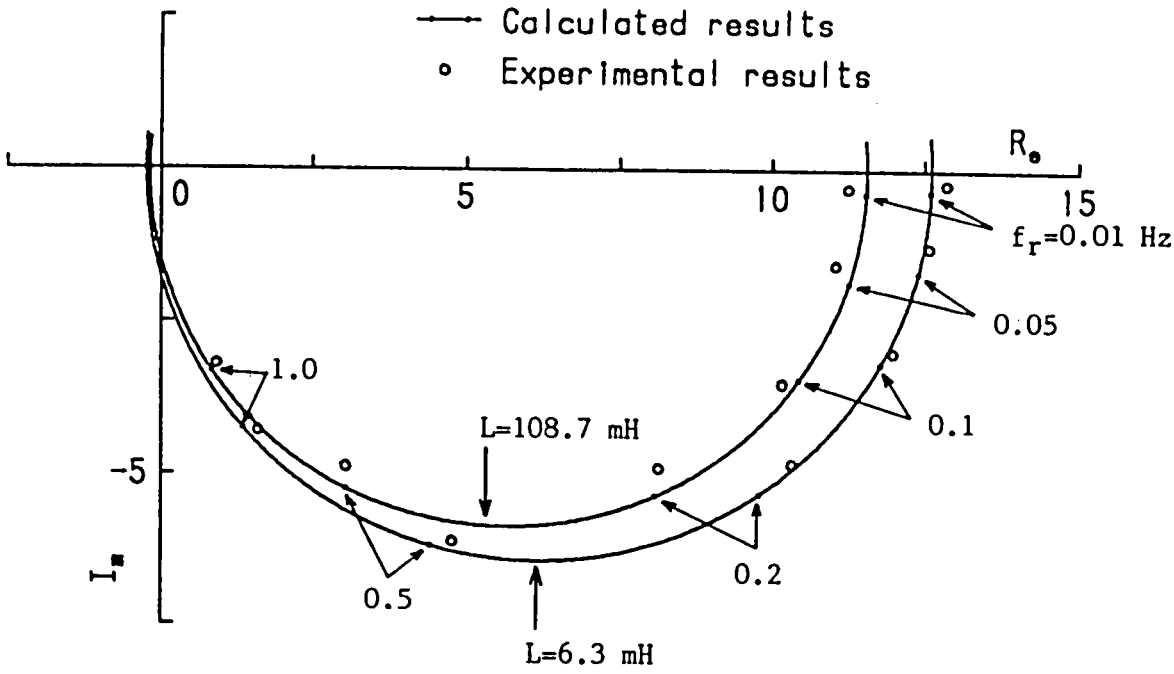

Fig.2.24. Frequency responses for G=20.9 mS, K_b=0, α=80° and e_l≒2.6 V .

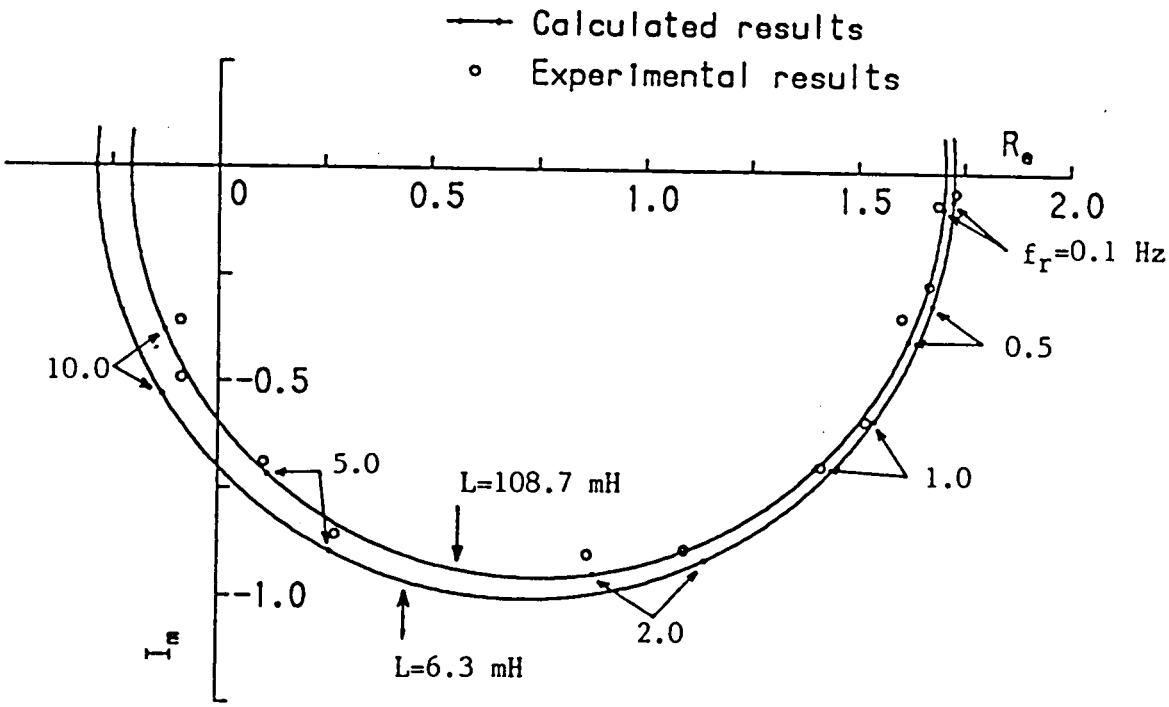

Fig.2.25. Frequency responses for G=20.9 mS, K_b=0.5, α=80° and e_l≒2.6 V .

From Figs.2.24 and 2.25, we can also see that the motor with the feedback responds faster to v_r than the one without the feedback. However, we must take care that the small vibration of the motor speed may increases when the motor responds very fast to v_r. When this vibration is too large to satisfy the relation given by Eq. (2.28), the motor performance in the actual control circuit shown in Fig.2.9 may become unstable. Hence the usable values of K_1 and K_b are limited.

2.5 Conclusion

The main results derived from the above investigations are as follows:

(1) The fundamental equations to analyse dynamic performances of the motor controlled by the single-phase half-wave thyristor rectifier circuit were introduced. In the equations, the fluctuation of the motor speed, the friction torque of the motor and the voltage drops on the brushes were considered, which are important factors for researching the motor performances. Next, the theoretical solution of the equations were obtained by using the four fundamental circuit modes which depend on the situation of the motor speed and the armature current which flows interruptedly.

(2) The transfer function of the motor controlled by the half-wave rectifier circuit was approximately derived from the analysis of change of the motor speed during one cycle of the ac supply frequency. By using the transfer function, the equivalent first order sampled data system, by which the dynamic characteristics of the motor can easily be calculated, were introduced. Also, in order to analyse the dynamic characteristics, the pulse transfer function and the frequency response in the rectifier control circuit were obtained.

(3) From the calculated results of the steady characteristics, which were obtained by the mode analyses, it was made clear that the average value of the motor speed decreases steeply with increases of the armature current and the inductance in the armature circuit. This is caused by the ohmic voltage drop and

occurrence of the large decrease of the armature terminal voltage.

(4) The influence of the inductance on the transfer function of the rectifier control circuit was investigated. The approximate time constant and the gain in the transfer function vary very much with change of the firing angle of the thyristor, when the inductance is small and the change of the armature current during one cycle is large.

(5) It was made clear that the approximate time constant T_m of the motor controlled by the half-wave rectifier circuit is several times larger than the analytical one T_d of the motor driven by the continuous direct current.

(6) It was shown from the calculated results of the frequency responses that the response speed of the motor can be accelerated by using the speed feedback control system.

(7) Appropriateness of the theoretical analysis was verified by ascertaining that the calculated results of the steady characteristics, the transient and the frequency responses agree well with the respective experimental ones.

CHAPTER 3

DYNAMIC CHARACTERISTICS OF DC MOTOR CONTROLLED BY THYRISTOR CHOPPER CIRCUIT

3.1 Introduction

A thyristor chopper circuit is available for obtaining a regulated voltage from a constant dc voltage source, and so the circuit is often used for the speed control system of a dc motor such as the one of an electric motor car. As described in the preceding chapter, the speed of the dc motor is efficiently controlled by regulating the armature terminal voltage of the motor. When the terminal voltage is regulated by a thyristor chopper circuit, the armature current flows intermittently and so the motor fluctuates a little.

Until now, a considerable amount of information describing the performance of a motor controlled by a chopper circuit has been published.[19]-[25] However, the analysis of the characteristics in the steady state has been mostly carried out under an assumption that the fluctuation of the motor speed is negligible. Research reports that have analysed the dynamic characteristics considering the fluctuation are rarely found.

In this chapter, first, a theoretical method to analyse the dynamic and steady performances of a separately excited dc motor controlled by a chopper circuit is introduced by using the theory of periodically interrupted electric circuit.[27] In the method, the fluctuation of the motor speed, the friction torque of the motor with a load and the voltage drops on the armature brushes are considered as in the preceding chapter. These factors have not been considered by the conventional theory, but they are important for researching the motor performances.[44]-[49] Also, as in the preceding chapter, transfer and pulse transfer functions of the

motor control system are introduced to present an good approximate method of the above precise one. And it is shown that the dynamic characteristics can be evaluated by an equivalent second order sampled data system.

Next, the steady and the dynamic characteristics are investigated in detail theoretically and experimentally.

In this connection, the author confirms the appropriateness of the theory by showing that the calculated results agree sufficiently well with the experimental results.

3.2 Fundamental Theory

3.2.1 Chopper circuit and fundamental equations

Figure 3.1 shows a circuit diagram of a thyristor chopper circuit for the speed control of a separately excited dc motor, where

e : output voltage of chopper circuit,

E : dc supply voltage,

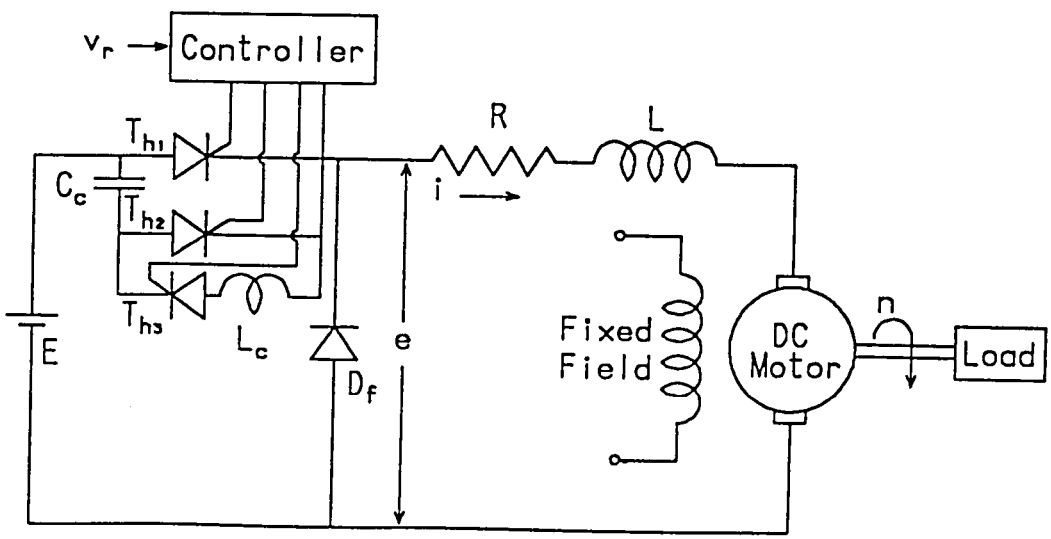

Fig.3.1. Chopper control circuit of separately excited dc motor.

i : armature current,

n : motor speed,

v_r : input voltage of controller,

L : total inductance of armature circuit,

R : total resistance of armature circuit,

C_c : condenser in commutation circuit,

L_c : inductor in commutation circuit,

D_f : freewheeling diode,

T_{h1} : main thyristor,

T_{h2} and T_{h3} : auxiliary thyristors in commutation circuit.

In the figure, the armature terminal voltage e is varied by changing the conduction interval of the main thyristor T_{h1}. The conduction interval of T_{h1} is regulated by v_r of the controller. When the motor speed is fed back to the controller, the motor is more precisely controlled. The thyristor T_{h1} is periodically turned on by gate signals generated by the controller, and then the armature current i is supplied to the dc motor from the dc voltage source E. Just after the auxiliary thyristor T_{h2} is turned on, T_{h1} is turned off by the aid of the reverse voltage charged in the condenser C_c, and then the current i transfers from T_{h1} to T_{h2}. After a short time i.e. the commutation interval, C_c is recharged with E and so T_{h2} is turned off. Subsequently, i circulates through the freewheeling diode D_f until i decreases to zero, or T_{h1} is turned on again. The polarity of the voltage of C_c is reversed in the resonance circuit consisted of C_c and L_c when T_{h1} and another auxiliary thyristor T_{h3} are turned on. The reversed voltage of C_c helps to turn T_{h1} off. In this connection, many other types of chopper circuit containing the various commutation circuits were proposed.[5],[6],[7] Also, in recent years, the chopper circuit without the commutation circuit were devised,[7],[50] in which a gate-turned-off thyristor or a power transistor is used in place of such main thyristor as T_{h1} in Fig.3.1.

The performance of the dc motor in Fig.3.1 can be analyse by the following

fundamental equations:

$$\left.\begin{aligned} e&=Ldi/dt+Ri+K_v n+E_b, \\ K_t i&=Jdn/dt+Fn+Q, \end{aligned}\right\} \tag{3.1}$$

where

e : output voltage of chopper circuit,

E_b : brush voltage drop,

F : viscous friction coefficient of motor with load,

J : moment of inertia of motor with load,

K_t : counter electromotive force coefficient of motor,

K_v : torque coefficient of motor,

Q : Coulomb friction torque of motor with load.

In this connection, in the conventional analysis, where the fluctuation of the motor speed is ignored, the following equations

$$\left.\begin{aligned} e&=Ldi/dt+Ri+K_v N, \\ K_t I_d&=FN+Q, \end{aligned}\right\} \tag{3.2}$$

where

I_d : average value of i,

N : constant motor speed,

have been used. By Eqs.(3.2), the steady characteristic of the dc motor can approximately be evaluated, but the dynamic one can't be done accurately.

We now assume that the turn-on and turn-off intervals of the thyristors and the commutation interval of the chopper can be neglected. Also, for simplifying analysis of circuit performances, we neglect an armature reaction of the motor and the nonlinearity of the circuit parameters. Then, Eqs.(3.1) are transformed to the following electrical equations,

$$\left.\begin{aligned} e&=E_1 H(t)-E_2 H(t') \\ &=Ldi/dt+Ri+v+E_b, \\ i&=Cdv/dt+Gv+I_q, \end{aligned}\right\} \tag{3.3}$$

where

$E_1=E-E_{th_1}$, $E_2=E+E_{df}$, $t'=t-t_{on}$,

E_{th} : voltage drop in T_{h1},

E_{df} : the same one in D_f,

$H(t)$: unit function,

$I_q=Q/K_t$: equivalent forced current of Q,

$v=K_v n$: counter electromotive force,

t_{on} : conduction interval of T_{h1},

$\alpha=t_{on}/\tau$: duty factor of chopper,

τ : chopper period,

$C=J/(K_t K_v)$: equivalent capacitance of J,

$G=F/(K_t K_v)$: equivalent conductance of F.

3.2.2 Circuit modes.

We can divide the circuit performances into four fundamental modes depending on the situations of i and v as follows:

mode 0 : i is zero and motor is at a standstill,

mode 1 : i is supplied, but motor can't rotate because lack of $K_t i$,

mode 2 : motor is driven by i,

mode 3 : i is blocked and motor is rotated by inertia.

The situations of i and v in each mode and the criteria for the mode transitions are shown in Fig.3.2, where

$I_s=Q_s/K_t$: equivalent constant current of Q_s,

Q_s : static friction torque which is needed to rotate a stalled motor,

$v=K_v n$: counter emf of motor,

$i_m=i_m(t)$: current i in mode m,

$v_m=v_m(t)$: voltage v in mode m,

t_m : duration of interval of mode m,

m=0, 1, 2, 3 : mode number.

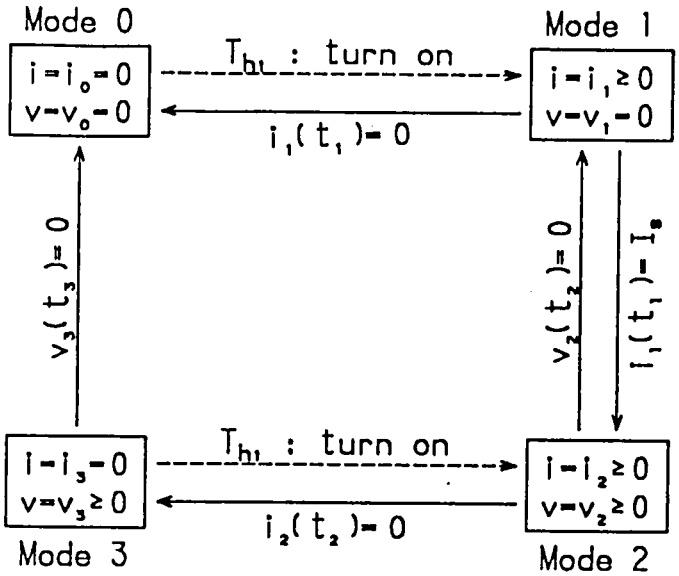

Fig.3.2. Circuit modes.

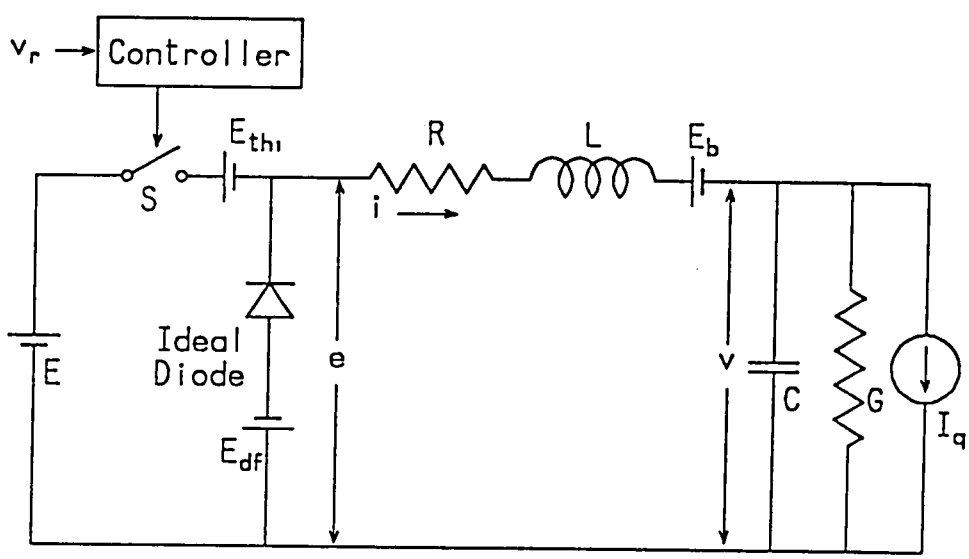

Fig.3.3. Electrical equivalent circuit.

The circuit performances in Fig.3.1 can be analysed by using Eqs. (3.3) and Fig.3.2.

3.2.3 Electrical equivalent circuit and mode analysis

(1) Electrical equivalent circuit

From Eqs. (3.3), we can derive the electrical equivalent circuit as shown in Fig.3.3. In the figure, the switch S, which corresponds to the main thyristor T_{h1} in Fig.3.1, operates periodically with the chopper period τ and the conduction interval t_{on}. The diode D_f in Fig.3.1 is replaced by an ideal diode and the equivalent voltage E_{df} to the internal voltage drop of D_f.

(2) Mode analyses

Let us derive the fundamental relations among e, i and v in each mode from Figs.3.2 and 3.3.

(i) Mode 0

We can readily arrive at the following equations

$$e=0, \quad i=0, \quad v=0. \tag{3.4}$$

(ii) Mode 1

Replacing e, i and v in mode 1 by e_1, i_1 and v_1, respectively, Eqs. (3.3) are transformed into

$$\left.\begin{aligned} e_1 &= L di_1/dt + Ri_1 + E_b, \\ v_1 &= 0. \end{aligned}\right\} \tag{3.5}$$

The above equations can be solved easily by the Hayashi theory of periodically interrupted electric circuit,[27] and the solutions are expressed by the following matrix form

$$\begin{bmatrix} i_1 \\ v_1 \end{bmatrix} = [\Phi_1(t)] + [X_1(t)] \begin{bmatrix} i_1^{+0} \\ v_1^{+0} \end{bmatrix} \tag{3.6}$$

where

$$[\Phi_1(t)] = \begin{bmatrix} (E_1-E_b)(1-\varepsilon^{-tR/L})H(t)/R - E_2(1-\varepsilon^{-t'R/L})H(t')/R \\ 0 \end{bmatrix},$$

$$[X_1(t)] = \varepsilon^{-tR/L}[U]H(t),$$

$$[U]=\begin{bmatrix}1&0\\0&1\end{bmatrix},$$

i_1^{+0} and v_1^{+0} : initial values of i and v.

(iii) Mode 2

The circuit performance in this mode is analysed by Eqs. (3.3). By using the Laplace transform and putting $e=e_2$, $i=i_2$ and $v=v_2$, Eqs. (3.3) are easily solved and the solutions are obtained as follows:

$$\begin{bmatrix}i_2\\v_2\end{bmatrix}=[\Phi_2(t)]+[X_2(t)]\begin{bmatrix}i_2^{+0}\\v_2^{+0}\end{bmatrix} \tag{3.7}$$

where

$$[\Phi_2(t)]=\mathfrak{L}^{-1}\frac{1}{LCD(s)}\begin{bmatrix}sC+G&-1\\1&sL+R\end{bmatrix}\begin{bmatrix}e_2(s)-E_b(s)\\-I_q(s)\end{bmatrix}$$

$$=\begin{bmatrix}(E_1-E_b)\{Gg_1(t)/(RG+1)+g_2(t)/L\}+I_qg_2(t)/(RG+1)\\(E_1-E_b)g_1(t)/(RG+1)-I_q\{Rg_1(t)/(RG+1)+g_2(t)/C\}\end{bmatrix}$$

$$-\begin{bmatrix}E_2\{Gg_1(t')/(RG+1)+g_2(t')/L\}\\E_2g_2(t')/(RG+1)\end{bmatrix},$$

$$[X_2(t)]=\mathfrak{L}^{-1}\frac{1}{D(s)}\begin{bmatrix}s+G/C&-1/L\\1/C&s+R/L\end{bmatrix}=\begin{bmatrix}g_3(t)-\sigma g_2(t)&-g_2(t)/L\\g_2(t)/C&g_3(t)+\sigma g_2(t)\end{bmatrix}$$

in which

$D(s)=s^2+(R/l+G/C)s+(RG+1)/(LC)$,

$g_1(t)=H(t)-\lambda g_2(t)-g_3(t)$, $g_2(t)=\varepsilon^{-\lambda t}\sinh\mu tH(t)/\mu$, $g_3(t)=\varepsilon^{-\lambda t}\cosh\mu tH(t)$,

$\lambda=0.5(R/L+G/C)$, $\sigma=0.5(R/L-G/C)$, $\mu=\{\sigma^2-1/(LC)\}^{1/2}$,

$e_2(s)$, $E_b(s)$ and $I_q(s)$: s-functions of e_2, E_b and I_q,

s : Laplace operator,

$\mathfrak{L}^{-1}$: inverse Laplace transform,

i_2^{+0} and v_2^{+0} : initial values of i_2 and v_2.

(iv) Mode 3

The circuit equations are given by

$$\left.\begin{aligned} e_3 &= v_3, \\ i_3 &= 0 = C\,dv_3/dt + Gv_3 + I_q, \end{aligned}\right\} \tag{3.8}$$

and the solutions are given by

$$\begin{bmatrix} i_3 \\ v_3 \end{bmatrix} = [\Phi_3(t)] + [X_3(t)] \begin{bmatrix} i_3^{+o} \\ v_3^{+o} \end{bmatrix} \tag{3.9}$$

where

$$[\Phi_3(t)] = \begin{bmatrix} 0 \\ -I_q(1-\varepsilon^{-tG/C})/GH(t) \end{bmatrix},$$

$$[X_3(t)] = \varepsilon^{-tG/C}[U]\,H(t),$$

e_3, i_3 and v_3 : e, i and v in mode 3,

$i_3^{+o}=0$ and v_3^{+o} : initial values of i_3 and v_3.

3.2.4 Analysis of circuit performances for one cycle and steady ones

The dynamic and steady characteristics of the electromechanical system in Fig.3.1 can be obtained by analysing the circuit performances during one cycle of the chopper frequency. We can readily think of the following four cases concerning to the circuit performances during one cycle

case 1 : motor doesn't rotate,

case 2 : motor, which stops, begins to rotate,

case 3 : motor rotates continuously,

case 4 : motor, which is rotating, stops.

These circuit performances can be analysed by using the criteria in Fig.3.2 and the results of mode analysis for the equivalent circuit shown in Fig.3.3. Here, we analyse the circuit performances, in the case 3 where the motor rotates continuously, which are concerned closely with the motor speed control.

We first analyse the circuit performances where i flows interruptedly. In the k-th cycle from the first cycle when the duty factor α of the chopper is settled, modes 2 and 3 appear successively, as shown in Fig.3.4. In the figure,

i_j : current in j-th cycle,

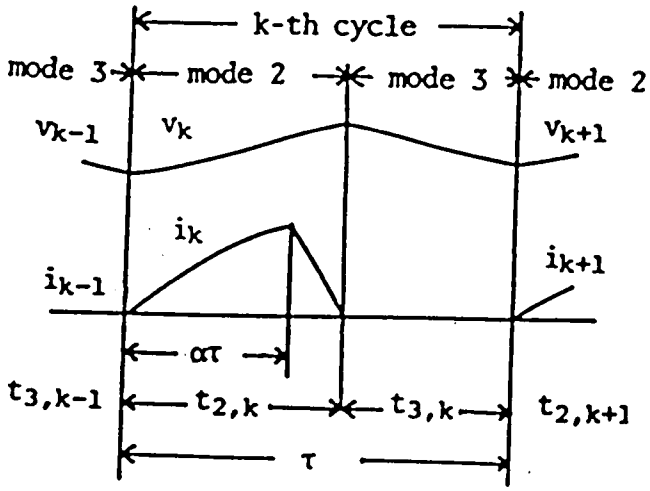

Fig.3.4. Illustrative waveforms of i and v in k-th cycle.

v_j : voltage in j-th cycle,

$t_{2,j}$: duration of mode 2 in j-th cycle,

$t_{3,j}$: duration of mode 3 in j-th cycle,

$j=k-1$, k or $k+1$.

By using Eqs. (3.7) and (3.9), the current $i=i_k$ and the voltage. $v=v_k$ in the k-th cycle are expressed as follows:

for $0 \leqq t \leqq t_{2,k} \leqq \tau$,

$$\begin{bmatrix} i_k \\ v_k \end{bmatrix} = \begin{bmatrix} i_{2,k} \\ v_{2,k} \end{bmatrix} = [\Phi_2(t)] + [X_2(t)] \begin{bmatrix} i_{2,k}^{+o} \\ v_{2,k}^{+o} \end{bmatrix}, \tag{3.10}$$

for $0 \leqq t \leqq t_{3,k} \leqq \tau$,

$$\begin{bmatrix} i_k \\ v_k \end{bmatrix} = \begin{bmatrix} i_{3,k} \\ v_{3,k} \end{bmatrix} = [\Phi_3(t)] + [X_3(t)] \begin{bmatrix} i_{3,k}^{+o} \\ v_{3,k}^{+o} \end{bmatrix}, \tag{3.11}$$

where

$t_{2,k}$ and $t_{3,k}$: durations of modes 2 and 3, respectively.

Also, $i_{2,k}$, $i_{3,k}$, $v_{2,k}$ and $v_{3,k}$ must satisfy the following conditions

$$\left.\begin{aligned}
&\begin{bmatrix} i_{2,k}^{\pm o} \\ v_{2,k}^{\pm o} \end{bmatrix} = \begin{bmatrix} i_{3,k-1} \\ v_{3,k-1} \end{bmatrix}_{t=t_{3,k-1}}, \qquad \begin{bmatrix} i_{3,k}^{\pm o} \\ v_{3,k}^{\pm o} \end{bmatrix} = \begin{bmatrix} i_{2,k} \\ v_{2,k} \end{bmatrix}_{t=t_{2,k}}, \\
&i_{2,k}^{\pm o} = i_{3,k}^{\pm o} = 0, \\
&t_{2,k} + t_{3,k} = \tau .
\end{aligned}\right\} \tag{3.12}$$

In the steady state when k becomes infinite, the following equations for the initial values are obtained,

$$\begin{bmatrix} i_2^{\pm o} \\ v_2^{\pm o} \end{bmatrix} = \{ [U] - [X_2(t_2)]\,[X_3(t_3)] \}^{-1} \{ [\Phi_3(t_3)] + [X_3(t_3)]\,[\Phi_2(t_2)] \}, \tag{3.13}$$

$$\begin{bmatrix} i_3^{\pm o} \\ v_3^{\pm o} \end{bmatrix} = [\Phi_2(t_2)] + [X_2(t_2)] \begin{bmatrix} i_2^{\pm o} \\ v_2^{\pm o} \end{bmatrix}, \tag{3.14}$$

where

$i_m^{\pm o}=0$: initial value of i in steady state,

$v_m^{\pm o}$: initial value of v in steady state,

$t_2+t_3=\tau$,

t_m : duration of interval of mode m in steady state,

m=2, 3 : mode number.

From Eqs. (3.13) and (3.14), the values of t_2, t_3, $v_2^{\pm o}$ and $v_3^{\pm o}$ are determined. Therefore, we can calculate the instantaneous values of i and v by substituting those values into Eqs. (3.10) and (3.11). Also, the average values E_d, I_d and V_d per τ of e, i and v can be calculated easily by using Eqs. (3.3) and (3.8). The results bring the following relations

$$\left.\begin{aligned}
E_d &= \alpha(E-E_{th_1}) - (\beta-\alpha)E_{df} - (1-\beta)I_q - (v_2^{\pm o}-v_3^{\pm o})C/(\tau G), \\
&= RI_d + V_d + \beta E_b, \\
I_d &= GV_d + I_q,
\end{aligned}\right\} \tag{3.15}$$

where

$$E_d = \frac{1}{\tau}\int_0^{\tau} e\,dt = \frac{1}{\tau}\int_0^{t_2} E_1\,dt + \frac{1}{\tau}\int_0^{t_3} v_3\,dt,$$

$$I_d = \frac{1}{\tau}\int_0^{\tau} i\,dt = \frac{1}{\tau}\int_0^{t_2} i_2\,dt,$$

$$V_d=\frac{1}{\tau}\int_0^{\tau} v dt=\frac{1}{\tau}\int_0^{t_2} v_2 dt+\frac{1}{\tau}\int_0^{t_3} v_3 dt,$$

$\alpha=t_{on}/\tau$, $\beta=t_2/\tau$.

Next, when i flows continuously and only mode 2 appears, $i=i_k$ and $v=v_k$ in the k-th cycle are expressed by

$$\begin{bmatrix} i_k \\ v_k \end{bmatrix}=\begin{bmatrix} i_{2,k} \\ v_{2,k} \end{bmatrix}=[\Phi_2(t)]+[X_2(t)]\begin{bmatrix} i_{2,k}^{+o} \\ v_{2,k}^{+o} \end{bmatrix}, \tag{3.16}$$

in which the initial values $i_{2,k}^{+o}$ and $v_{2,k}^{+o}$ are given by

$$\left.\begin{aligned} \begin{bmatrix} i_{2,k}^{+o} \\ v_{2,k}^{+o} \end{bmatrix}&=\begin{bmatrix} i_{2,k-1}^{+o} \\ v_{2,k-1}^{+o} \end{bmatrix}_{t_2=\tau}, \\ &=\{[U]-[X_2(\tau)]\}^{-1}\{[U]-[X_2(\tau)]^{k-1}\}[\Phi_2(\tau)] \\ &\quad+[X_2(\tau)]\begin{bmatrix} i_{2,1}^{+o} \\ v_{2,1}^{+o} \end{bmatrix}. \end{aligned}\right\} \tag{3.17}$$

In the steady state, the initial values are obtained by

$$\begin{bmatrix} i_2^{+o} \\ v_2^{+o} \end{bmatrix}=\{[U]-[X_2(\tau)]\}^{-1}[\Phi_2(\tau)], \tag{3.18}$$

and the instantaneous values of i and v are calculated by using Eqs.(3.16) and (3.18). Also, by putting $\beta=1$ and $v_3^{+o}=v_2^{+o}$ into Eqs.(3.15), the average values E_d, I_d and V_d are obtained as follows:

$$\left.\begin{aligned} E_d&=\alpha(E-E_{th_1})-(1-\alpha)E_{df}, \\ &=RI_d+V_d+E_b, \\ I_d&=GV_d+I_q. \end{aligned}\right\} \tag{3.19}$$

3.3 Analytical Method of Dynamic Performances

The detailed circuit performances of the electromechanical system in Fig.3.1 can be analysed by using the criteria shown in Fig.3.2 and the results of mode analyses given by Eqs.(3.4), (3.6), (3.7) and (3.9). In this section, we show the analytical method of the dynamic characteristics in the case where the motor

rotates continuously and the circuit situation is represented by modes 2 and 3 in every cycle of the chopper frequency.

3.3.1 Transfer function.

When the dc motor is driven by a dc source, the transfer function $G_d(s)$ of the system is usually expressed as follows: [39], [40]

$$G_d(s)=\frac{\Delta v(s)}{\Delta e(s)}=\frac{1}{RG+1}\ \frac{RG+1}{LCD(s)}, \tag{3.20}$$

where

$D(s)=s^2+(R/L+G/C)s+(RG+1)/(LC)$,

$\Delta e(s)$: s-function of increment of dc source voltage E,

$\Delta v(s)$: s-function of increment of v caused by $\Delta e(s)$.

Here, let us introduce the theoretical transfer function $G(s)$ in the case where the dc motor is driven by the chopper circuit and α is changed by $\alpha+\Delta\alpha$. When i flows continuously and only mode 2 occurs, the characteristic equation $D(s)=0$ is the same in Eq. (3.20). However, when i flows interruptedly, $D(s)$ is not decided exactly, because the circuit performances are divided into modes 2 and 3. Hence, we introduce the approximate characteristic equation and then the transfer function.

Let us assume that the circuit situation for α is in the steady state, and so the values of $i^{+o}=i_2^{\pm o}$, $v^{+o}=v_2^{\pm o}$, t_2 and t_3 are determined by Eqs. (3.13). We also assume that the variation $\Delta\alpha$ is very small and so the durations t_2 and t_3 for $\alpha+\Delta\alpha$ are nearly equal to those for α. Then, we can solve the following gradual equations for $\alpha+\Delta\alpha$

$$\begin{bmatrix} i_{2,k}^{\pm o} \\ v_{2,k}^{\pm o} \end{bmatrix}=\begin{bmatrix} i_{3,k-1} \\ v_{3,k-1} \end{bmatrix}_{t=t_3}, \qquad \begin{bmatrix} i_{3,k}^{\pm o} \\ v_{3,k}^{\pm o} \end{bmatrix}=\begin{bmatrix} i_{2,k} \\ v_{2,k} \end{bmatrix}_{t=t_2}. \tag{3.21}$$

By using Eqs. (3.10) and (3.11), the following result is derived, [27]

$$\left.\begin{aligned}\begin{bmatrix} i_{2,k}^{\pm o} \\ v_{2,k}^{\pm o} \end{bmatrix} &= \{ [U] - [X_3(t_3)]\,[X_2(t_2)] \}^{-1} \{ [U] - [X_3(t_3)]^{k-1}\,[X_2(t_2)]^{k-1} \} \\ &\times \{ [\Phi_3(t_3)] + [X_3(t_3)]\,[\Phi_2(t_2)]_{\alpha=\alpha+\Delta\alpha} \} \\ &+ [X_3(t_3)]^{k-1}\,[X_2(t_2)]^{k-1} \begin{bmatrix} i_{2,1}^{\pm o} \\ v_{2,1}^{\pm o} \end{bmatrix}.\end{aligned}\right\} \quad (3.22)$$

In the above equation, the transient term can be given as follows:

$$\left.\begin{aligned}&[X_3(t_3)]^{k-1}\,[X_2(t_2)]^{k-1} = [X_3(\overline{k-1}\,t_3)]\,[X_2(\overline{k-1}\,t_2)] \\ &= \frac{\varepsilon^{-(k-1)t_3 G/C}}{s_1 - s_2} \{ \varepsilon^{-(k-1)t_2 s_1} \begin{bmatrix} s_1+G/C & -1/L \\ 1/C & s_1+R/L \end{bmatrix} - \varepsilon^{-(k-1)t_2 s_2} \begin{bmatrix} s_2+G/C & -1/L \\ 1/C & s_2+R/L \end{bmatrix} \},\end{aligned}\right\} \quad (3.23)$$

where

s_1 and s_2 : solutions of $D(s)=0$.

By using the parameters

$$\left.\begin{aligned}&s_1' = \beta s_1 - (1-\beta)G/C, \qquad s_2' = \beta s_2 - (1-\beta)G/C, \\ &C' = C/\beta, \qquad G' = G/\beta, \qquad L' = L/\beta, \\ &R' = R + (1-\beta)LG/(\beta C), \qquad \beta = t_2/\tau,\end{aligned}\right\} \quad (3.24)$$

Eqs. (3.23) are transformed into

$$\left.\begin{aligned}&[X_3(t_3)]^{k-1}\,[X_2(t_2)]^{k-1} = \frac{1}{s_1 - s_2} \{ \varepsilon^{-(k-1)\tau s_1'} \begin{bmatrix} s_1'+G'/C' & -1/L' \\ 1/C' & s_1'+R'/L' \end{bmatrix} \\ &- \varepsilon^{-(k-1)\tau s_2'} \begin{bmatrix} s_2'+G'/C' & -1/L' \\ 1/C' & s_2'+R'/L' \end{bmatrix} \},\end{aligned}\right\} \quad (3.25)$$

Thus, the above transient term can be expressed by the following inverse Laplace transformation

$$[X_3(t_3)]^{k-1}\,[X_2(t_2)]^{k-1} = \mathfrak{L}^{-1} \{ \frac{1}{D'(s)} \begin{bmatrix} s+G'/C' & -1/L' \\ 1/C' & s+R'/L' \end{bmatrix} \}_{t=(k-1)\tau}, \quad (3.26)$$

in which

$$\left.\begin{aligned}D'(s) &= (s-s_1')(s-s_2') \\ &= s^2 + (R'/L' + G'/C')s + (R'G'+1)/(L'C').\end{aligned}\right\} \quad (3.27)$$

In the equation, $D'(s)$ is the same form with $D(s)$ in Eq. (3.20), and $D'(s)=0$ is now an approximate characteristic equation in the case where i flows interruptedly.

In this connection, in the case where i flows continuously, by putting $t_3=0$ and $t_2=\tau$ i.e. $\beta=1$, in Eqs.(3.24) and (3.27), we can get $D^*(s)=D(s)$.

Next, the gain K_m of the motor for $\Delta\alpha$ can be obtained by using Eqs.(3.13) and it is expressed as

$$K_m=\Delta v^{+o}/\Delta\alpha\cong\partial v_2^{+o}/\partial\alpha+(\partial v_2^{+o}/\partial t_2)(dt_2/d\alpha)+(\partial v_2^{+o}/\partial t_3)(dt_3/d\alpha), \tag{3.28}$$

where

$\Delta v^{+o}=\Delta v_2^{+o}$: change of initial value of v due to $\Delta\alpha$.

Now, the transfer function $G(s)$ between Δv^{+o} and $\Delta\alpha$ is written by

$$G(s)=\frac{\Delta v^{+o}(s)}{\Delta\alpha(s)}=K_m\frac{R^*G^*+1}{L^*C^*D^*(s)}, \tag{3.29}$$

where

$\Delta v^{+o}(s)$: s-function of Δv^{+o} ,

$\Delta\alpha(s)$: s-function of $\Delta\alpha$.

This is transformed to the following expression

$$G(s)=\frac{K_m\omega_n^2}{s^2+2\zeta\omega_n s+\omega_n^2}, \tag{3.30}$$

where

$\zeta=(R^*/L^*+G^*/C^*)/(2\omega_n)$: attenuation constant,

$\omega_n=\{(R^*G^*+1)/(L^*C^*)\}^{1/2}$: natural angular frequency.

The transfer function $G(s)$ is very useful to analyse the dynamic characteristics of the motor. The dynamic characteristics in Fig.3.1 is now derived from the equivalent sampled data system as shown in Fig.3.5, where

Δv : change of v due to v_r ,

Δv^{+o} : change of initial value of v,

Δv_r : change of input voltage v_r ,

$\Delta\alpha=K_c\Delta v_r$,

$H(s)=(1-\varepsilon^{-\tau s})/s$: zeroth order holding circuit,

K_c : gain in controller,

S_s : sampling switch with chopper period τ.

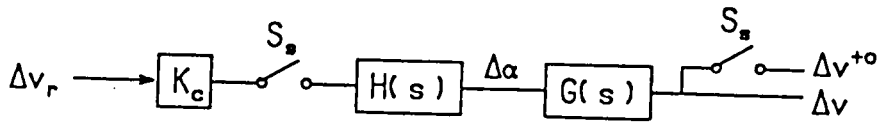

Fig.3.5. Equivalent sampled data system without speed feedback.

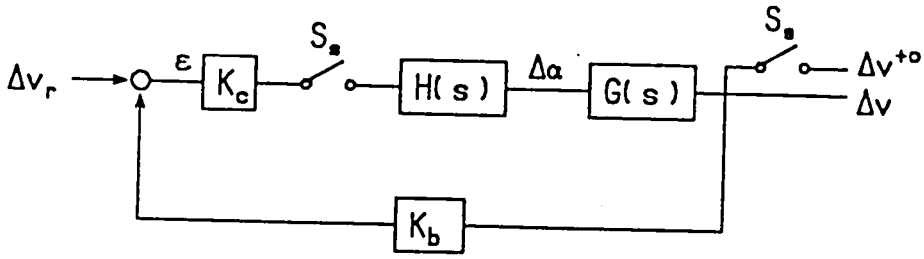

Fig.3.6. Equivalent sampled data system with speed feedback.

The switch S_s and the holding circuit $H(s)$ are used, because α is periodically given to the chopper circuit and is kept constant during τ. This sampled data system is easily applied in the case where the motor is driven with the speed feedback. In Fig.3.6, there is shown the equivalent system with the speed feedback, where

$\Delta\alpha=K_c\varepsilon$,

$\varepsilon=\Delta v_r-K_b\Delta v$: offset,

K_b : gain in feedback circuit.

3.3.2 Pulse transfer function

To analyse the dynamic characteristics of the systems as shown in Figs.3.5 and 3.6 which show the equivalent sampled data systems for the dc motor speed control system controlled by the thyristor chopper circuit, it is convenient to use a pulse transfer function. We first introduce the pulse transfer function of the control system with the speed feedback as shown in Fig.3.6. The total pulse transfer function $G_t(z)$ of the system is given by

$$G_t(z)=\frac{\Delta v^{+o}(z)}{\Delta v_r(z)}=\frac{K_c HG(z)}{1+K_b K_c HG(z)}=\frac{K_c K_m(N_1 z+N_2)}{M_1 z^2+M_2 z+M_3}, \tag{3.31}$$

where

$HG(z)$: z-function of $H(s)G(s)$,

$\Delta v^{+o}(z)$: z-function of Δv^{+o},

$\Delta v_r(z)$: z-function of Δv_r,

$z=\exp(s\tau)$,

$M_1=s_1'-s_2'$, $M_2=-M_1(\varepsilon^{\tau s_1'}+\varepsilon^{\tau s_2'})+K_b K_c K_m N_1$, $M_3=M_1\varepsilon^{\tau(s_1'+s_2')}+K_b K_c K_m N_2$,

$N_1=s_1'(1-\varepsilon^{\tau s_2'})-s_2'(1-\varepsilon^{\tau s_1'})$, $N_2=s_2'\varepsilon^{\tau s_2'}-s_1'\varepsilon^{\tau s_1'}+(s_1'-s_2')\varepsilon^{\tau(s_1'+s_2')}$,

$s_1'=-\zeta\omega_n+\omega_n(\zeta^2-1)^{1/2}$, $s_2'=-\zeta\omega_n-\omega_n(\zeta^2-1)^{1/2}$.

Now, in the speed control system shown in Fig.3.6, the stable control can be carried out in the case where the solutions z_1 and z_2 of the equation $M_1z^2+M_2z+M_3=0$ satisfy the following conditions

$$|z_1|<1, \qquad |z_2|<1, \tag{3.32}$$

where

$z_1=\{-M_2+(M_2^2-4M_1M_3)^{1/2}\}/(2M_1)$,

$z_2=\{-M_2-(M_2^2-4M_1M_3)^{1/2}\}/(2M_1)$.

When the above conditions are satisfied and the input voltage $\Delta v_r=\Delta V_r$ is constant, Δv^{+o} in the steady state is readily derived from Eqs. (3.31) as follows:

$$\Delta v^{+o}=\lim_{z\to 1}(1-z^{-1})G_t(z)\Delta v_r(z)=K_c K_m \Delta V_r/(1+K_b K_c K_m), \tag{3.33}$$

where

$\Delta v_r(z)=\Delta V_r/(1-z^{-1})$,

and also the offset ε is evaluated by

$$\varepsilon=\Delta V_r/(1+K_b K_c K_m). \tag{3.34}$$

Furthermore, we can now obtain the frequency response of the system by substituting $z=\exp(j\omega_r\tau)$ into Eq. (3.31) as follows:

$$G_t(z)=\Re_e+j\Im_m, \tag{3.35}$$

where

$\Re_e=\dfrac{K_c K_m l_1}{M_1(p^2+r^2)(q^2+r^2)}$: real part of $G_t(z)$,

$\Im_m=\dfrac{K_c K_m l_2}{M_1(p^2+r^2)(q^2+r^2)}$: imaginary part of $G_t(z)$,

f_r : frequency of input voltage v_r,

$\omega_r=2\pi f_r$, $z=\exp(j\omega_r\tau)$, $j=\sqrt[2]{-1}$,

$l_1=(N_1\cos\omega_r\tau+N_2)(pq-r^2)+N_1 r^2(p+q)$, $l_2=N_1 r(pq-r^2)-r(N_1\cos\omega_r\tau+N_2)(p+q)$,

$p=\cos\omega_r\tau-z_1$, $q=\cos\omega_r\tau-z_2$, $r=\sin\omega_r\tau$.

Next, in the control system without the feedback as shown in Fig.3.5, the pulse transfer function and the frequency response are easily obtained by putting $K_b=0$ into Eqs.(3.31) and (3.35), respectively.

3.4 Numerical Calculations and Experimental Results

In order to ascertain appropriateness of the above theoretical method, we compare the results numerically calculated by it with the experimental results. When the motor is controlled by the chopper circuit, to the armature circuit some inductance is usually added to reduce the ripple of the armature current, because the ripple often gives a bad influence on the commutation characteristic of the motor.[42],[43] Therefore, we also investigate the influence of the inductance on the dynamic characteristics of the motor.

3.4.1 Experimental circuit

Figure 3.7 shows the schematic diagram of the experimental circuit, where

g_1, g_2 and g_3 : gate signals for thyristors T_{h1}, T_{h2} and T_{h3},

I : ammeter to measure average value I_d of current i,

V : volt meter to measure average value V_d of counter emf v,

v_r : input voltage of controller,

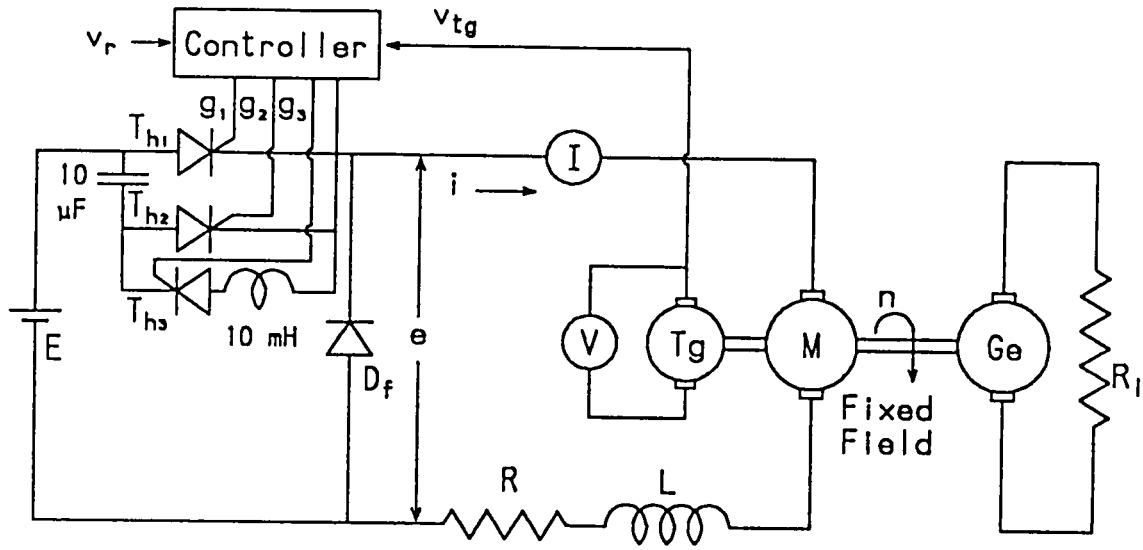

Fig.3.7. Schematic diagram of experimental circuit.

Table 3.1 Specification of dc motor

Type (Maker)	JKMM-6EM (Yasukawa Electric Co.)
Rated power	190 W
Rated voltage	40 V
Rated current	6 A
Rated speed	3000 rpm
Field excitation	Parmanent magnet

Table 3.2 Circuit parameters

Mechanical parameters	Electrical parameters
Kt = 0.096 N·m/A	E = 40 V
Kv = 0.096 V·s/rad	Eb = 1.02 V
F = 0.180 to 4.62 mN·m·s/rad	Edf = 0.757 V
J = 0.000282 Kg·m	Eth = 0.792 V
Q = 0.0837 to 0.0433 N·m	C = 30.6 mF
Ktg = 1.44	G = 0.0195 to 0.502 S
	Iq = 0.872 to 0.451 A
	L = 1.4, 42.6, 108 mH
	R = 5.96 Ω
	τ = 1/60 s

$v_{tg}=v/K_{tg}$: output voltage of T_g,

K_{tg} : voltage coefficient of T_g,

G_e : generator to regulate load of M,

M : supplied dc motor,

R_l : load resistor for G_e,

T_g : tachometer generator.

We can control the speed of M in Fig.3.7 by regulating v_r. Also, our experiment is carried out by a small-sized motor. The specification of the motor and the circuit parameters are shown in Tables 3.1 and 3.2, respectively. The waveforms of e, i and v are measured by using a synchroscope or a photo-recorder.

Next, Fig.3.8 shows the operation block diagram of the controller to generate the gate signals g_1, g_2 and g_3, where

e_b : bias voltage for comparator,

e_c : output of comparator, which determines α,

$e_l=K_1\varepsilon$: output of limited amplifier and $0\leqq e_l\leqq e_{lm}$,

e_{lm} : maximum voltage of e_l,

e_{re} : output of rectangular wave oscillator with chopper frequency $f=1/\tau$,

e_{sk} : skew-wave output of integration circuit,

$\varepsilon=v_r-K_bv$: offset,

K_b and K_{tg} : gains in feedback circuit,

K_1 : gain of limited amplifier,

τ : chopper period.

In the figure, g_1 and g_3 and τ are given by e_{re}. Also, g_2 and α are done by e_c, which is obtained by comparing e_b, e_l and e_{sk}. The illustrative waveforms of the signals is shown in Fig.3.9.

By Figs.3.8 and 3.9, we can get α expressed as following relations

$$\left.\begin{aligned}\alpha&=K_2(e_l+e_b)=K_2\{K_1(v_r-K_bv)+e_b)\\&=K_1(v_r-K_bv)+0.13,\end{aligned}\right\}\qquad(3.36)$$

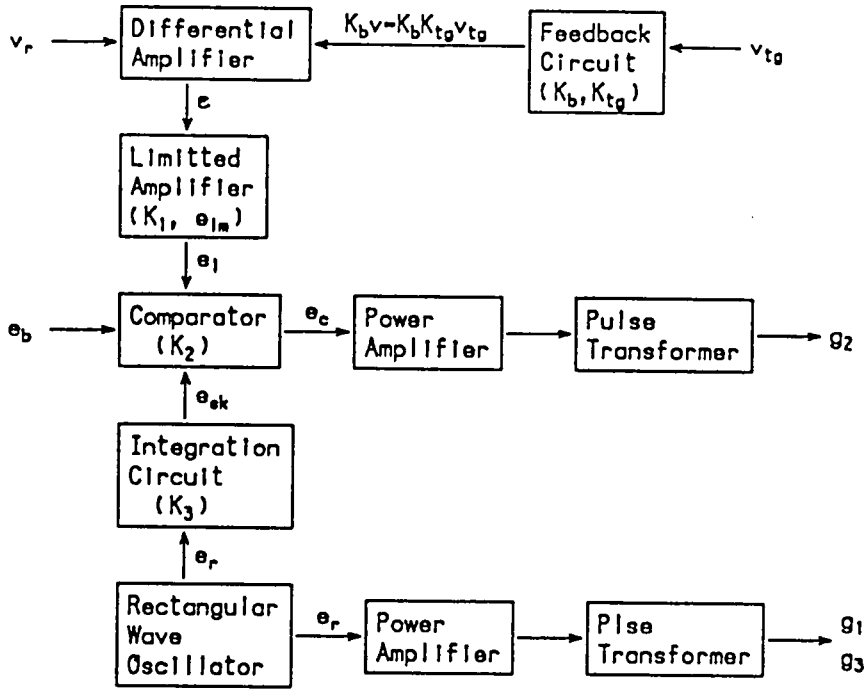

Fig.3.8. Block diagram of controller.

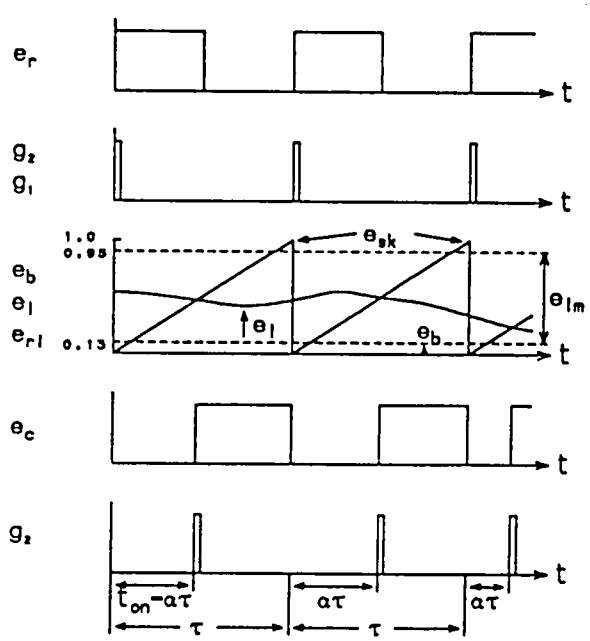

Fig.3.9. Signal waveforms in controller.

where

$0.13 \leqq \alpha \leqq 0.95$, $e_b = 0.13\ V$, $e_{lm} = 0.82\ V$,

$K_2 = 1$: gain in comparator.

The above condition $0.13 \leqq \alpha \leqq 0.95$ for α is set to acquire the stable operation of the chopper. Using Eqs.(3.36) and Fig.3.8, the gain K_c shown in Figs.3.5 and 3.6 can be obtained as follows:

$$K_c = K_1 K_2 = K_1 . \tag{3.37}$$

3.4.2 Steady characteristics[44], [48], [49]

Here, we investigate the fundamental characteristics of the motor in the steady state. For this purpose, the motor is driven without the feedback, namely $K_b = 0$ is set in the controller shown in Fig.3.7.

(1) Instantaneous waveforms

In Figs.3.10, 3.11 and 3.12, the calculated steady state waveforms of i and v, which are obtained by using Eqs.(3.7), (3.9), (3.13), (3.14) and (3.18), are presented

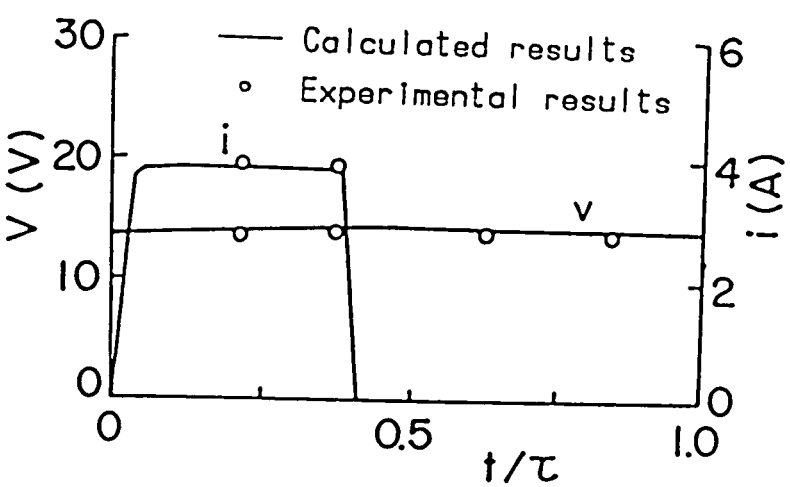

Fig.3.10. Steady state waveforms of i and v for $L = 1.4\ mH$ and $\alpha = 0.4$.

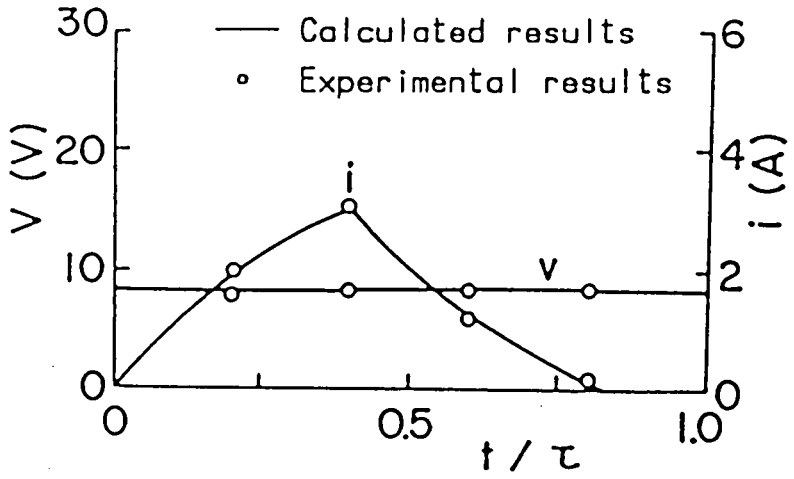

Fig.3.11. Steady state waveforms of i and v for L=42.6 mH and α=0.4.

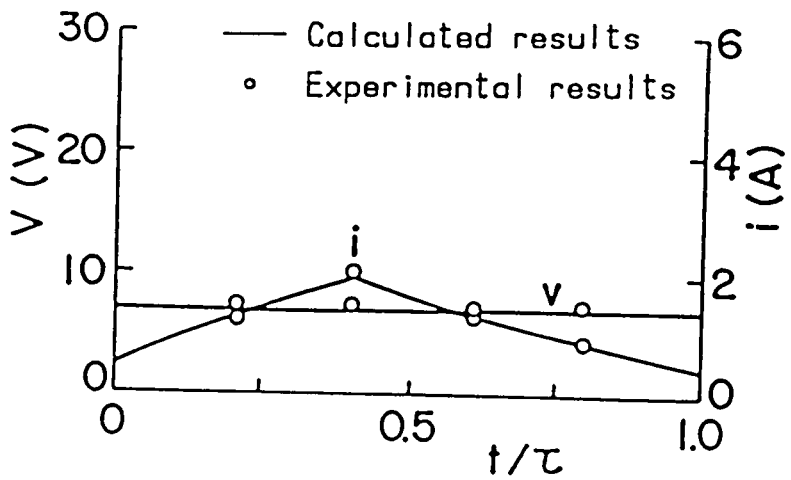

Fig.3.12. Steady state waveforms of i and v for L=108 mH and α=0.4.

for L=1.4, 42.6 and 108 mH, respectively, where α=0.4, G=0.0489 S and I_q=0.84 A. In Figs.3.10 and 3.11, the current i flows interruptedly, but in Fig.3.12 it flows continuously and is fairly smoothed by the aid of the large inductance L. From the figures, it is seen that the fluctuation of v is very small and the relations of $v \fallingdotseq V_d$ are satisfied. This is caused by the large value of J, i.e. C. In those figures, some experimental results measured with a synchroscope are marked, which agree well with the calculated results.

(2) Speed-torque characteristics

In Figs.3.13, 3.14 and 3.15, there are plotted the calculated relations between I_d and V_d for several values of L and α, which correspond to the speed-torque characteristics of the motor, where the relations for α=1.0 are obtained by driving directly the motor with E=40 V.

From Fig.3.13, we can see that V_d for $\alpha<1$ decreases more steeply with the increase of I_d than the one for α=1.0. This is owing to the large variation of the terminal voltage E_d in Eqs.(3.15), which occurs in the case where L is small and i flows interruptedly.

In Fig.3.15, the relations are shown by straight lines parallel with one another, which are expressed by $V_d=E_d-RI_d-E_b$. In this case, L is large and i flows continuously, and so E_d is uniquely determined by α, as shown in Eqs.(3.19).

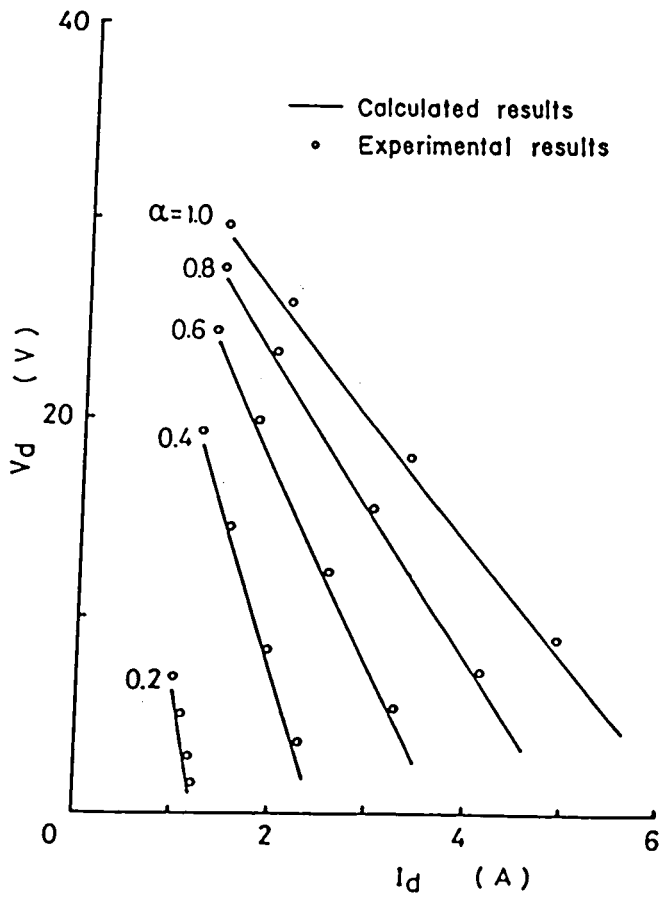

Fig.3.13. Relation between I_d and V_d for L=1.4 mH.

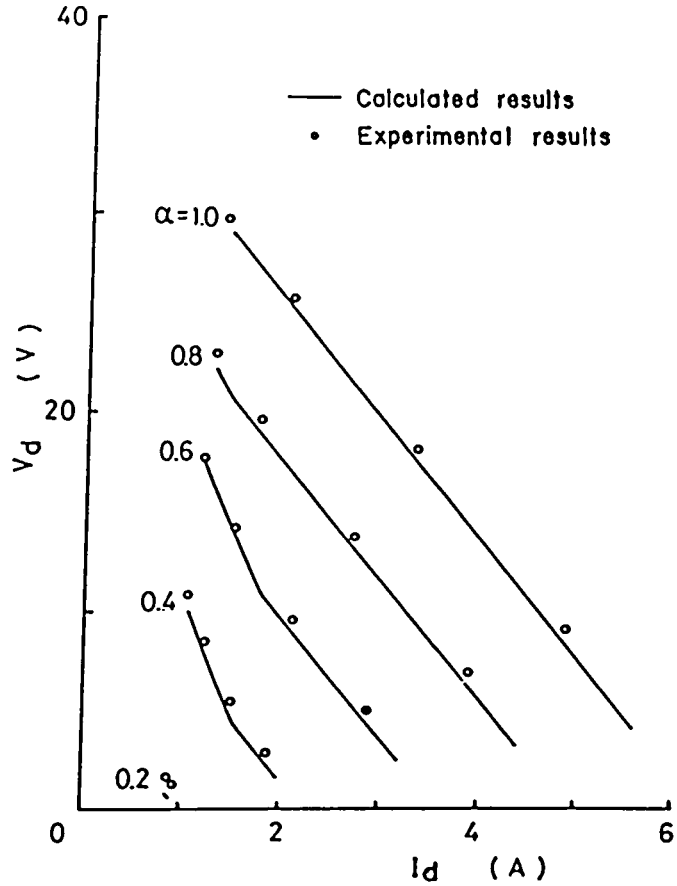

Fig.3.14. Relation between I_d and V_d for L=42.6 *mH*.

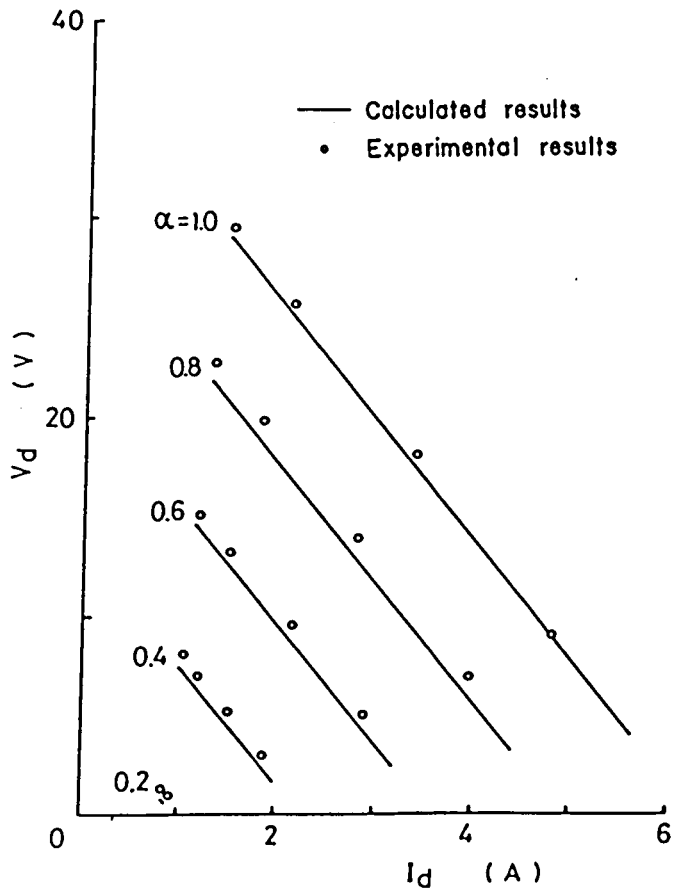

Fig.3.15. Relation between I_d and V_d for L=108 *mH*.

From the relations for α=0.4 and 0.6 in Fig.3.14, we can see that V_d changes in different manners depending on the situation whether i flows interruptedly or continuously.

In Figs.3.13 to 3.15, some experimental results are marked, which agree well with the calculated ones.

3.4.3 Transient characteristics[47], [49]

We investigate the transient characteristics of the motor driven under the conditions of G=0.0489 S and I_q=0.84 A.

In Figs.3.16 (a) and (b), we show the calculated and experimental transient waveforms of e, i and v for L=108 mH, α=0.56, and v_∞^{+o}=12 V, where K_b=0 and the motor is driven without the feedback. The actual input voltage v_r is regulated to get α=0.56 and $v \fallingdotseq V_d$=12 V in the steady state. We can see that i reaches the steady state quickly after v_r is impressed, but v increases slowly.

Next in Figs.3.17 (a) and (b), there are plotted the calculated and experimental waveforms e, i and v for v_r=12 V and K_c=0.18, where K_b=1 and the motor is driven with the feedback in Fig.3.7. The waveforms in Fig.3.17(a) are calculated by substituting the relation $\alpha=K_c(v_r-v)+0.13$ into Eqs.(3.16) and (3.17). Some offset $\varepsilon=v_r-K_b v$ remains in the steady state, which was given by Eq.(3.34). In the figure, the limited operations for α given by α=0.13 or 0.95 occur in early time after v_r is supplied.

Comparing the transient waveforms in Figs.3.17 with the those in Figs.3.16, we can see that the motor responds to v_r more quickly in the case with the feedback control system than in the case without the one.

Next, in Figs.3.18 (a) and (b), we show the waveforms for K_c=1.8. In this case, we can see that ε becomes very small, but the circuit performance is unstable.

In Figs.3.19 (a) and (b), the waveforms for L=1.4 mH are plotted. In this case, i flows pulsatively and the considerable ripple is observed in the waveform of v. These are undesirable phenomena for the precise control of the motor speed.

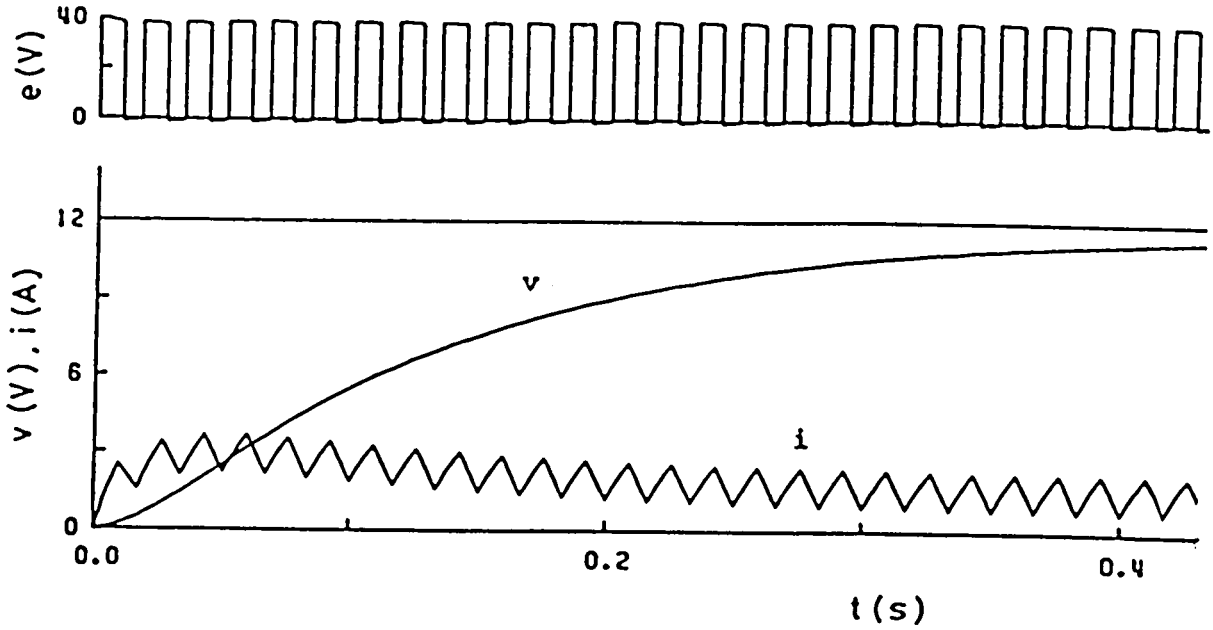

(a) Calculated waveforms.

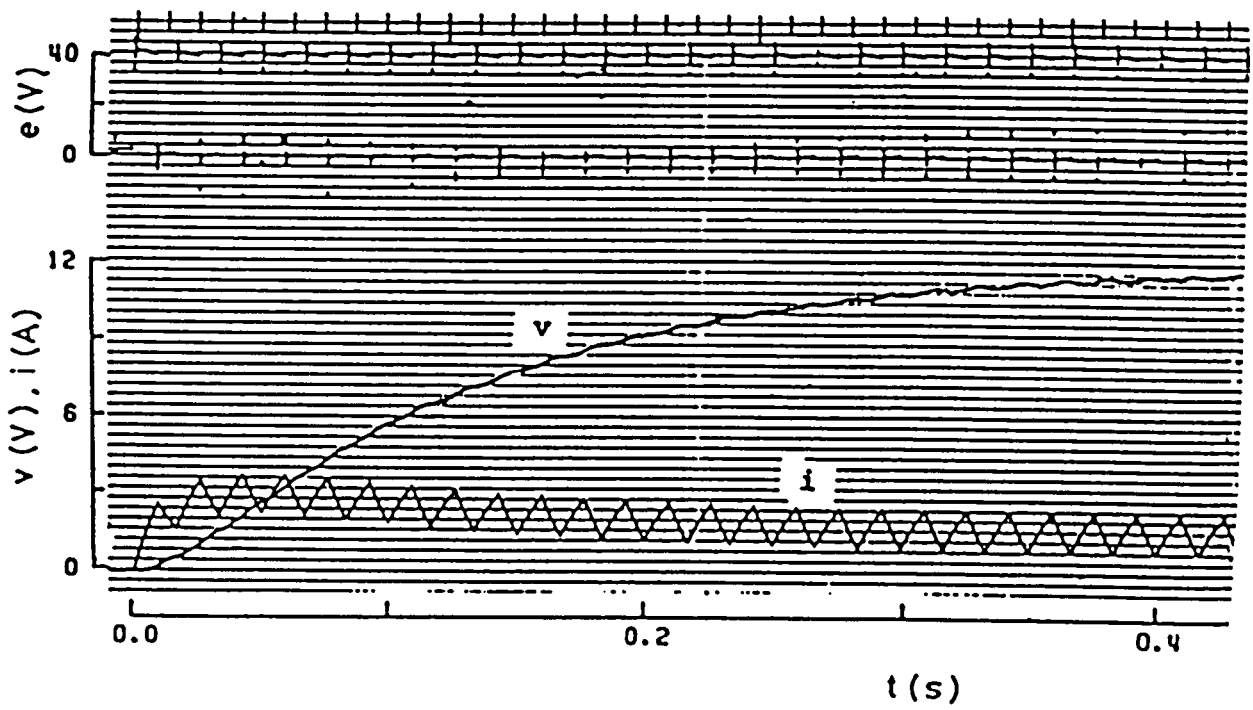

(b) Experimental waveforms.

Fig.3.16. Transient waveforms of e, i and v for L=108 mH, K_b=0 and α=0.56.

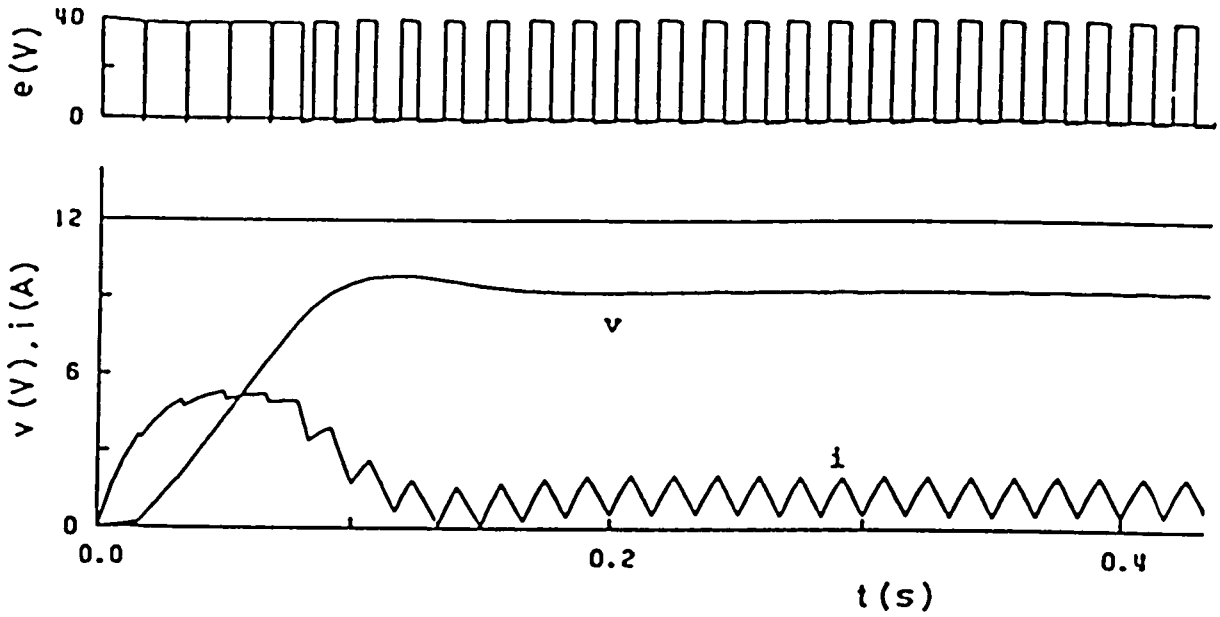

(a) Calculated waveforms.

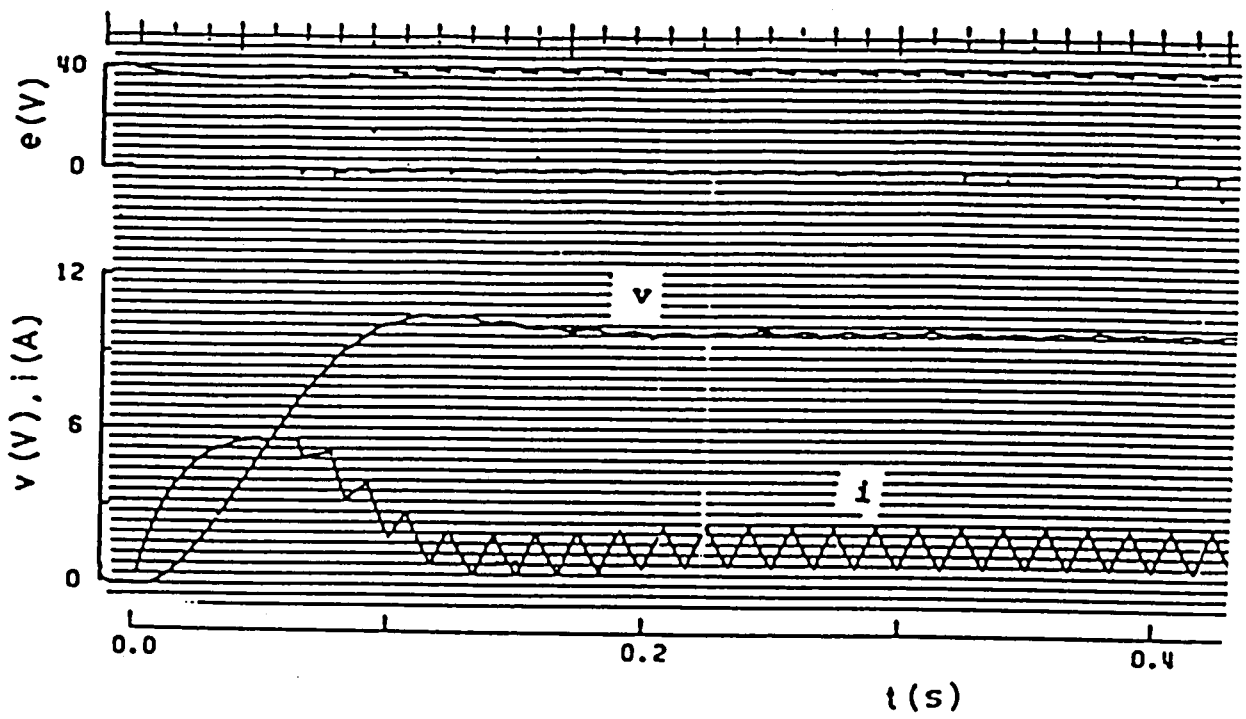

(b) Experimental waveforms.

Fig.3.17. Transient waveforms of e, i and v for L=108 mH, K_b=1, K_c=0.18, v_r=12 V and $\alpha=0.18(v_r-v^{+0})+0.13$.

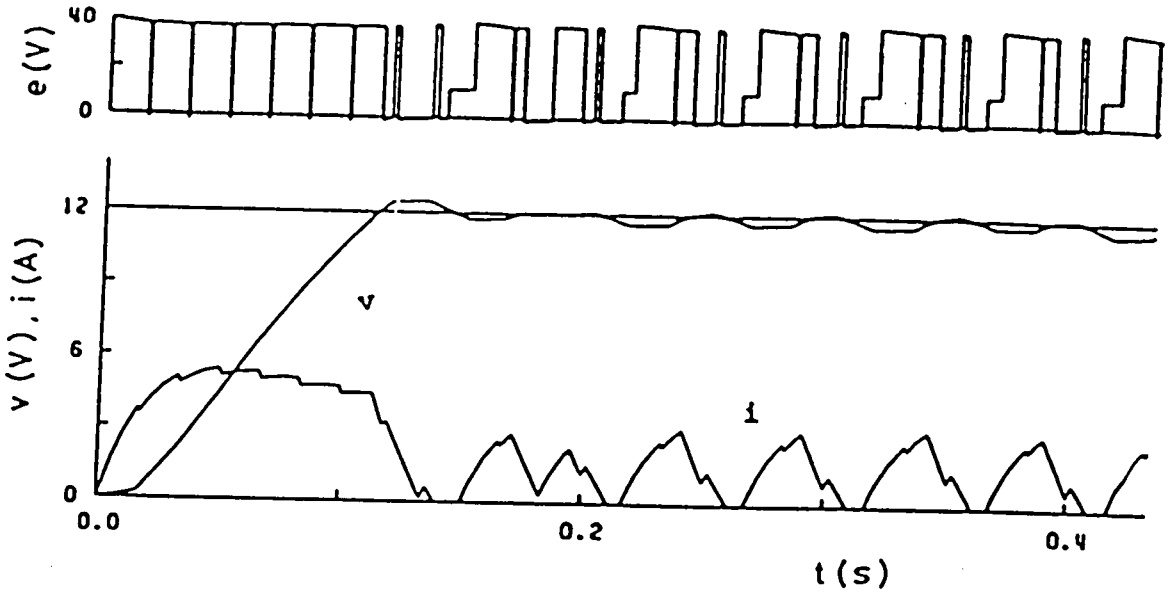

(a) Calculated waveforms.

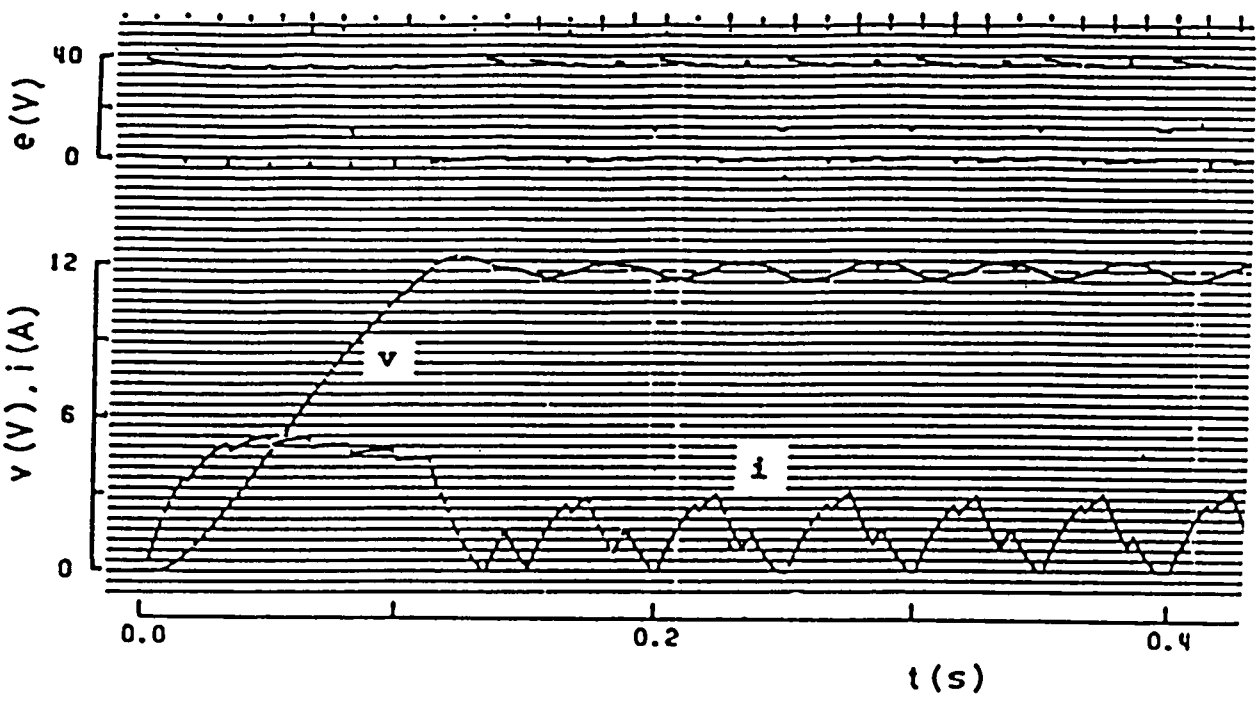

(b) Experimental waveforms.

Fig.3.18. Unstable waveforms of e, i and v for L=108 mH, K_b=1, K_c=1.8, v_r =12 V and $\alpha=1.8(v_r-v^{*0})+0.13$.

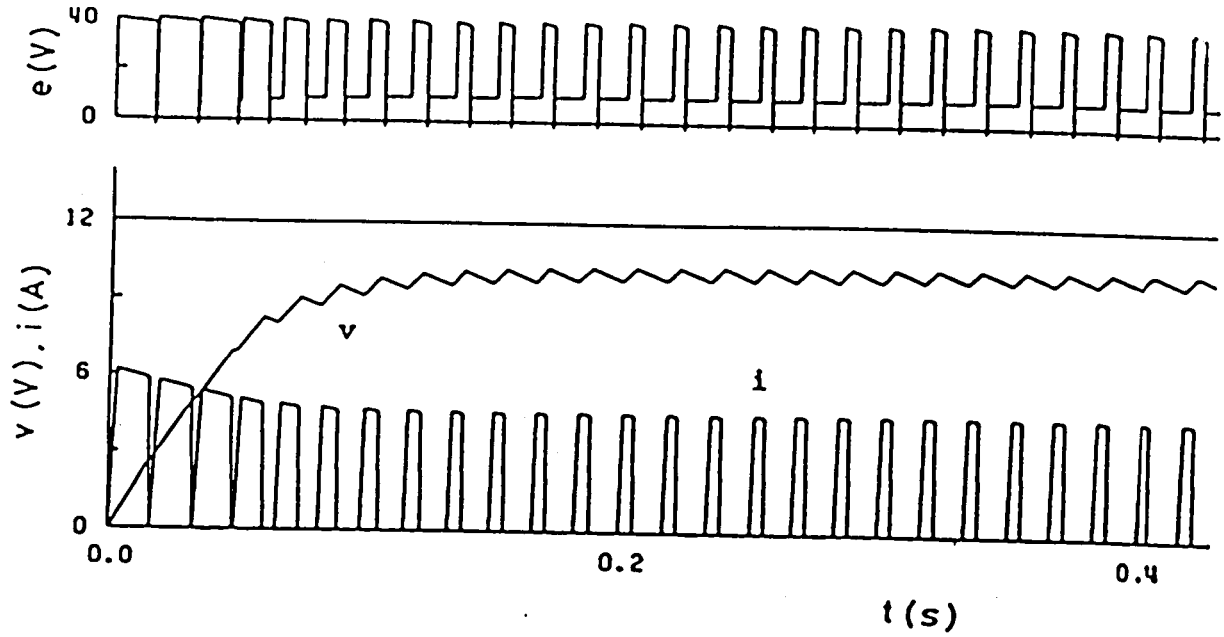

(a) Calculated waveforms.

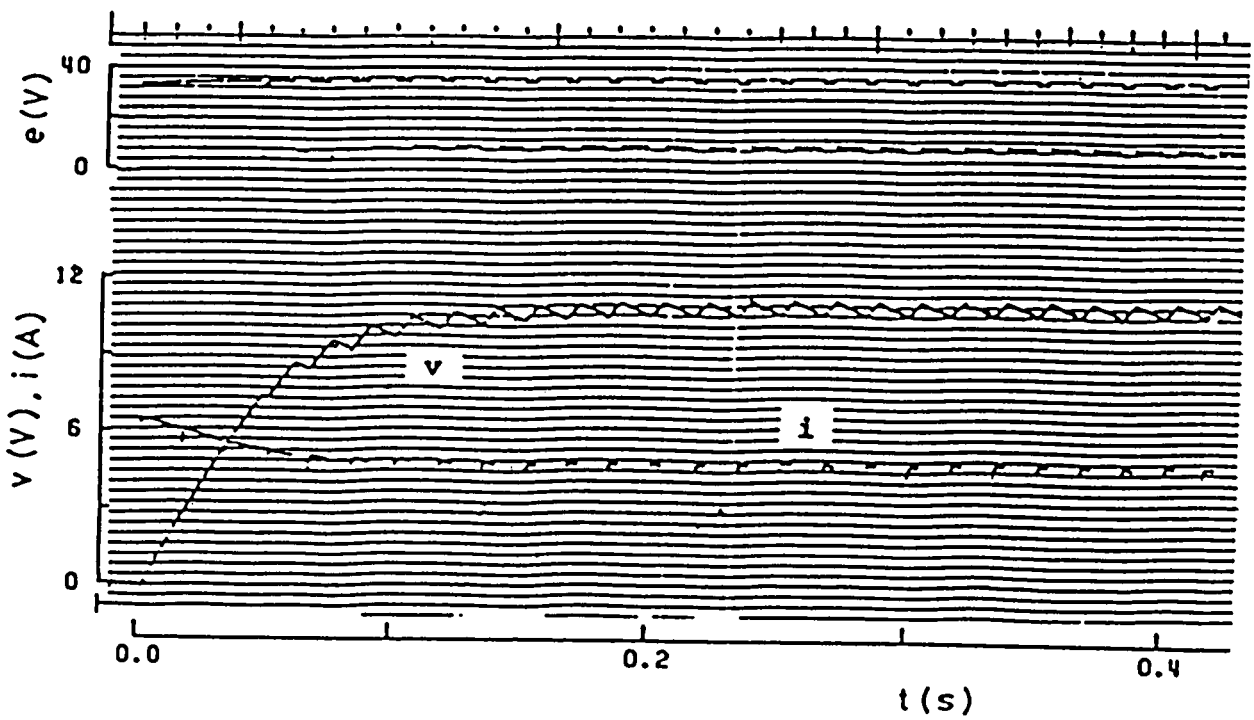

(b) Experimental waveforms.

Fig.3.19. Transient waveforms of e, i and v for L=1.4 mH, K_b=1, K_c=0.18, v_r=12 V and $\alpha=0.18(v_r-v^{t^o})+0.13$.

In this connection, as seen in Figs.3.16 to 3.19, the good agreement between the calculated results and the experimental ones are obtained.

3.4.4 Transfer function[45]-[49]

The relations of K_{cc}, K_m, V_d, ζ and ω_n v.s. α for G=0.0489 S, I_q=0.84 A, L=1.4, 42.6 and 108 mH, which concern to the transfer function $G(s)$ shown in Figs.3.5 and 3.6, are given in Figs.3.20, 3.21 and 3.22, respectively. In these figures, K_{cc} is the critical value of K_c to control the motor without instability, which is caluculated for K_b=1 under the conditions given by Eqs.(3.32). As seen in Fig.3.22, K_{cc}, K_m, ζ and ω_n for L=108 mH are independent on α, where i flows continuously. On the other hand, Figs.3.20 and 3.21 show that those values fairly change with α, where i flows intermittently. Also, from the relations of $V_d \fallingdotseq v^{+0}$ v.s. α, we can see that the motor can't keep rotating and so V_d=0 because of $I_d < I_q$, when α<0.13, α<0.16, or α<0.18 in Figs.3.20, 3.21 or 3.22, respectively.

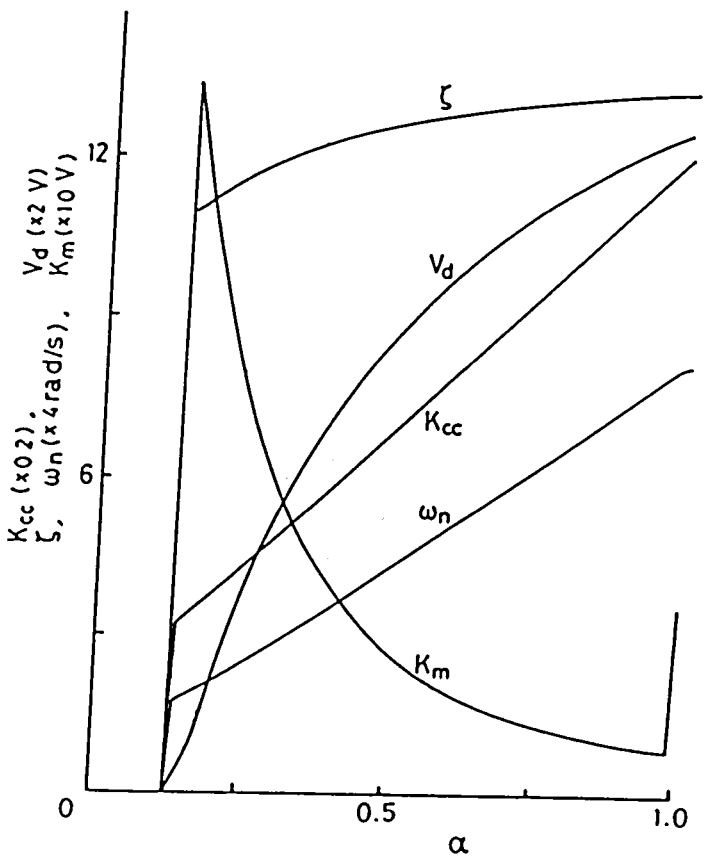

Fig.3.20. Relations of K_m, ζ, ω_n and K_{cc} vs. α for L=1.4 mH.

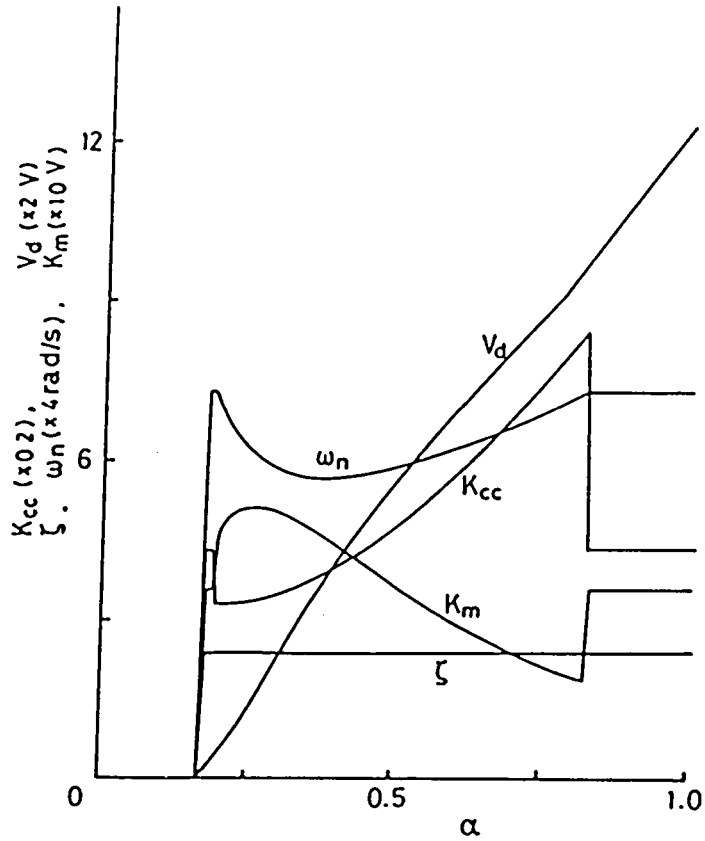

Fig.3.21. Relations of K_m, ζ, ω_n and K_{cc} vs. α for L=42.6 mH.

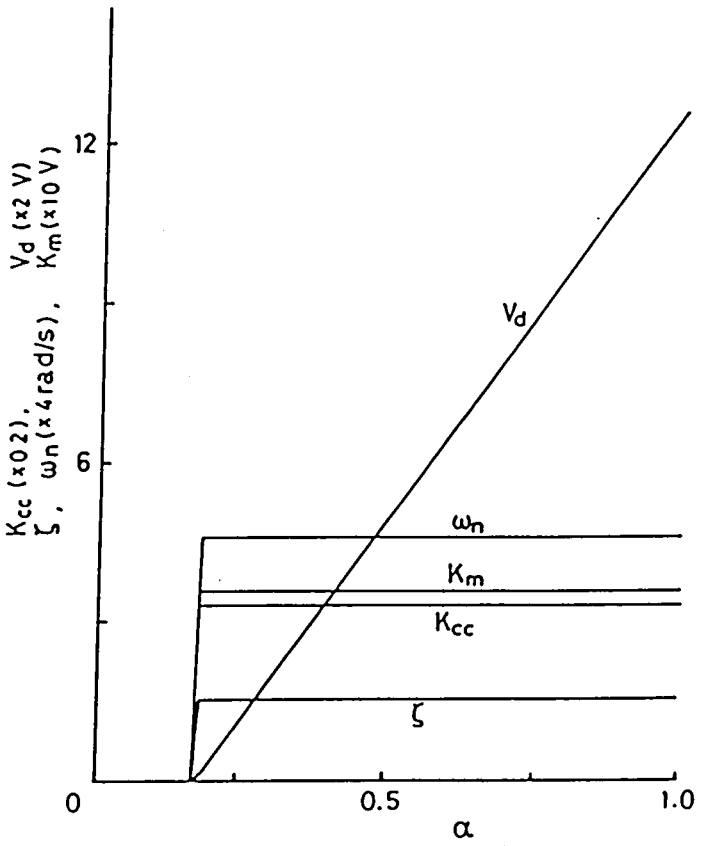

Fig.3.22. Relations of K_m, ζ, ω_n and K_{cc} vs. α for L=108 mH.

3.4.5 Frequency responses[49]

We investigate the frequency responses of the motor driven under the conditions of G=0.0489 S, I_q=0.84 A and K_c=0.18.

The calculated frequency responses of the motor for L=1.4 and 108 mH are shown in Figs.3.23(a) and 3.24(a), respectively, where K_b=0 and the motor is controlled without the feedback. The numerical calculation by Eq.(3.35) is carried out by using respective values of K_m, ζ and ω_n for the duty factor α to prepare V_d=12 V in Figs.3.20 and 3.22. In Figs.3.23 and 3.24, some experimental results are shown, which agree fairly well with the calculated results. The experimental results are obtained by using a transfer function analyser, where the input voltage v_r in Fig.3.7 is regulated to get V_d=12 V and the variation $\Delta\alpha$=0.05sin$(2\pi f_r t)$.

Next, the calculated frequency response for L=1.4 and 108 mH are shown in Figs.3.23(b) and 3.24(b), where the motor is driven with the feedback control system, and K_b=1 and v_r=12+sin$(2\pi f_r t)$ V. The values of K_m, ζ and ω_n are now evaluated for v_r=12 V. In the figures, the experimental results deviate a little from the calculated results. This is mainly caused by the measurememt error due to the existence of the ripple component of v, which can be observed from the waveforms of v shown in Figs.3.17(b) and 3.19(b).

From the frequency responses in Figs.3.23 and 3.24, we can see that the motor controlled by the circuit with the feedback system responds to v_r about ten times quicker than the one without the feedback system.

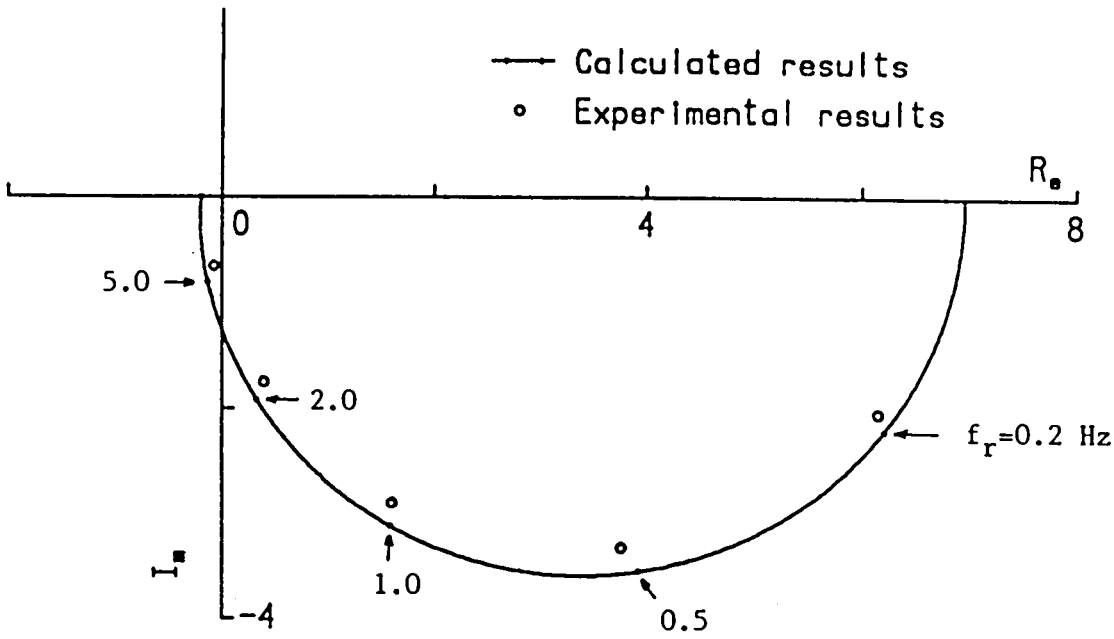

(a) K_b=0, K_c=0.18, K_a=38.7, ζ=10.5 *and* ω_n=76.6 .

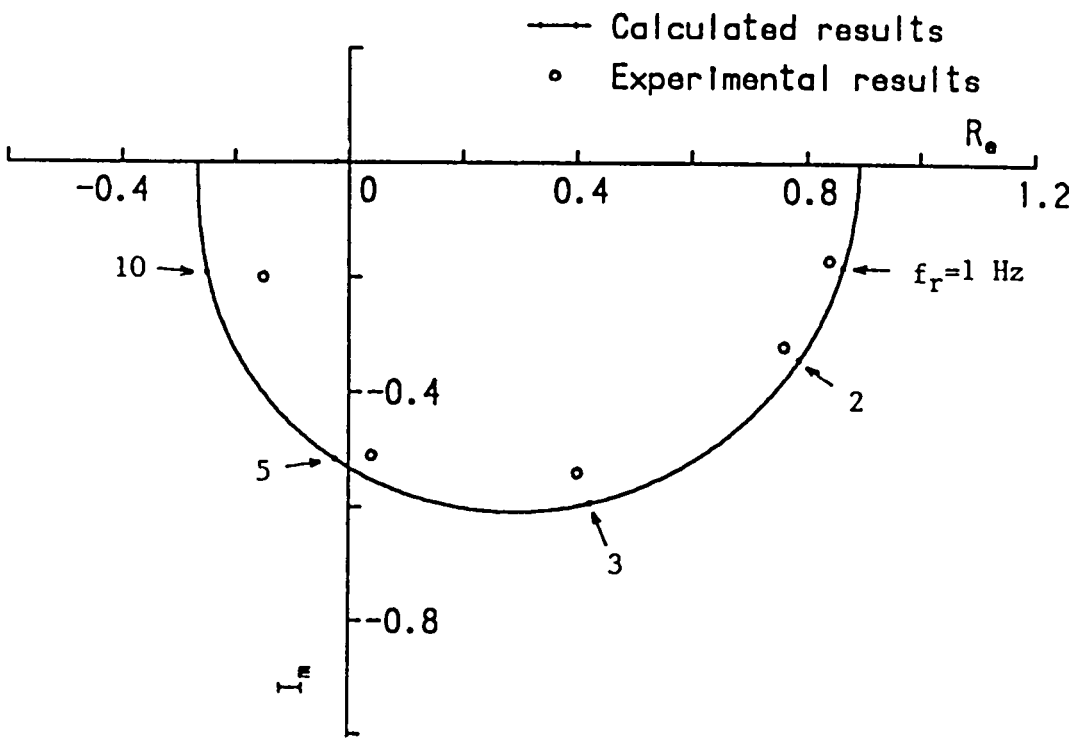

(b) K_b=1, K_c=0.18, K_a=45.9, ζ=10.2 *and* ω_n=68.1 .

Fig.3.23. Frequency responses for L=1.4 *mH*.

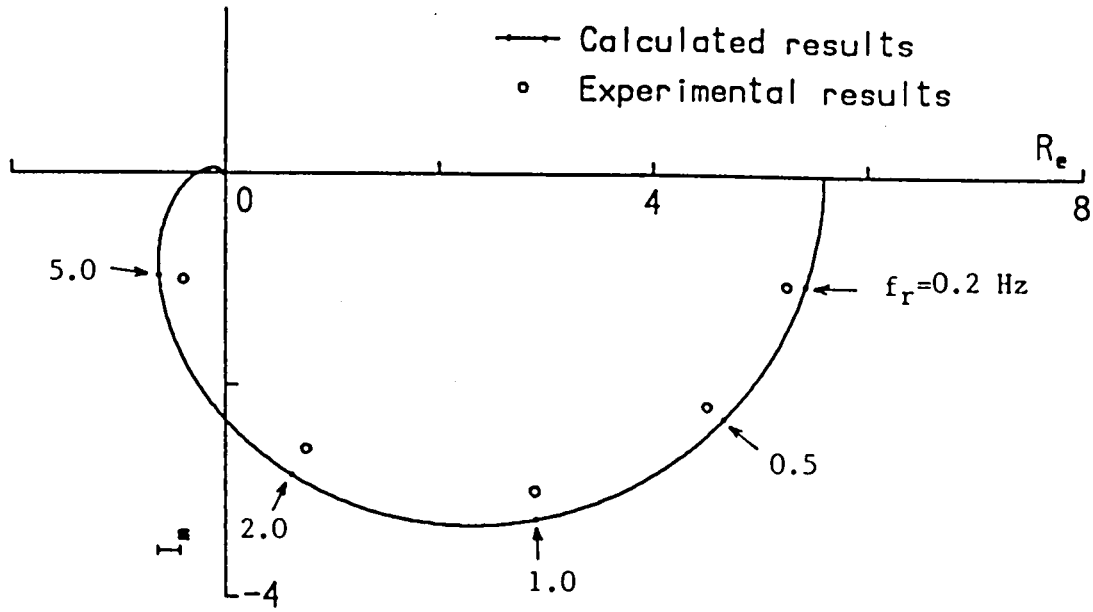

(a) K_b=0, K_c=0.18, K_m=31.1, ζ=1.44 and ω_n=19.9 .

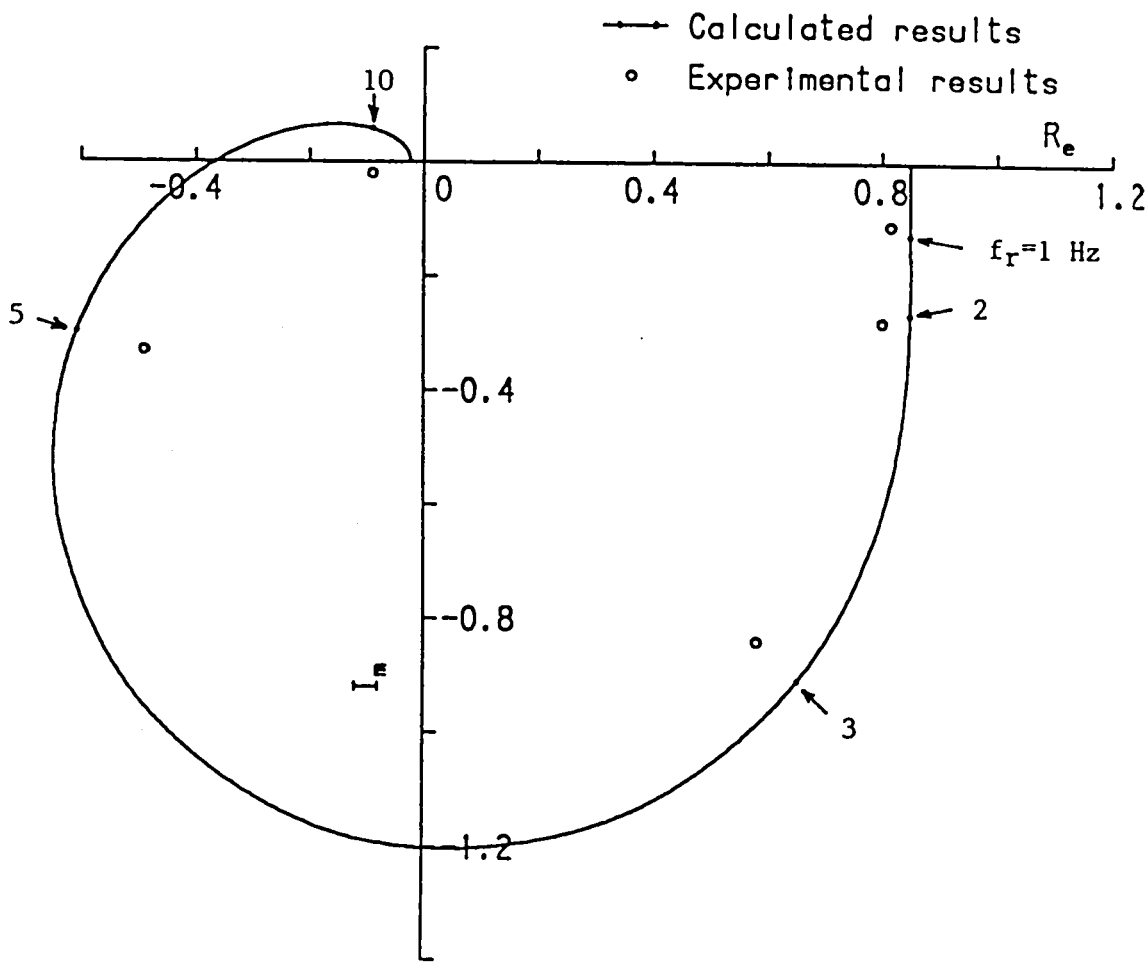

(b) K_b=1, K_c=0.18, K_m=31.1, ζ=1.44 and ω_n=19.9 .

Fig.3.24. Frequency responses for L=108 *mH*.

3.5 Conclusion

The main results derived from the above investigations are as follows:

(1) The fundamental equations to analyse dynamic performances of the motor controlled by the thyristor chopper circuit were introduced. In the equations, the fluctuation of the motor speed, the friction torque of the motor and the voltage drops on the brushes were considered, which are important factors for researching the motor performances. Next, the precise theoretical solutions were acquired by using the four fundamental circuit modes which depend on the situation of the armature current and the motor speed.

(2) The transfer function of the motor controlled by the chopper circuit was analytically derived from the analysis of the transient motor performances. By using the transfer function, the equivalent sampled data system, by which the dynamic characteristics of the motor can easily be calculated, were introduced. Also, in order to evaluate the dynamic characteristics, the pulse transfer function and the frequency response in the chopper control circuit were obtained.

(3) From the calculated results of the steady characteristics, which were obtained by the mode analysis, it was made clear that the average value of the motor speed decreases more steeply with the increase of the average armature current in the case where the inductance of the armature circuit is small and the armature current flows interruptedly, than the one in the case where the inductance is large and the current flows continuously. This is caused by large decrease of the armature terminal voltage in the former case.

(4) When the armature current flows continuously, the natural angular frequency, the attenuation constant and the gain in the transfer function are constant. On the other hand, when the current flows interruptedly, the above parameters considerably vary with the duty factor of the chopper circuit.

(5) Through the studies on the transient and the frequency responses of the motor, it was clarified that the speed response of the motor driven with the interrupted armature current is later than the one driven with the continuous

current. Also, it was shown that the speed response of the motor can be accelerated by using the speed feedback control system.

(6) Appropriateness of the theoretical analysis was proved by ascertaining that the calculated results of the steady characteristics and the transient and the frequency responses agree well with the experimental ones.

78 項欠

PART II

TWO-DIMENSIONAL ANALYSES OF TRANSIENT BEHAVIORS OF MAGNETIC FLUXES IN COMMUTATING ZONE AND SO ON OF SMALL-SIZED DC MOTOR

CHAPTER 1

GENERAL INTRODUCTION

1.1 Research Trend and Problem

As already described in Part I, the dc motors have a better speed-torque characteristic than the ac motor, and so it is widely applied as the precise variable speed machines, such as mill motor, traction motor, industrial servomotor, etc. And the torque and the speed of the dc motor are accurately, widely and quickly controlled by using the thyristor rectifier or chopper circuits. Here, in order to make the best use of the superior characteristic of the dc motor, it is essential to maintain always a good commutation characteristics not only in the steady state where the armature current is constant but also in the transient state where it abruptly changes.[1],[2],[3]

As is well known, to keep the good commutation, the ohmic and the reactive voltage drops in the commutated armature coils and the contact voltage drops between the brushes and the commutator segments must be immediately compensated by the speed electromotive forces(emf's) induced in the coils, that is called the commutating voltages. Here, the ohmic, the reactive and the contact voltage drops concern directly the armature current. On the other hand, the commutating voltage concerns the so-called commutating magnetic flux in the commutating zone containing the interpole airgap, which is mainly governed by the interpole exciting magnetomotive force(mmf), the armature reaction mmf, the magnetic reluctances of the interpole airgap and core, the armature and the yoke, and the eddy currents induced in the yoke and the interpole liners.

Therefore, even when the good commutation is maintained in the steady state, it is often deteriorated when an abrupt change of the armature current is occurred by

the fluctuations of the motor speed or load and so a regular distribution of the magnetic flux is disturbed. Especially, a serious commutation spark can occur when a large transitional delay of the response of the commutating flux to a change of the armature current is brought by the transient eddy currents induced in the yoke, the interpole liner and core, etc.. Because, due to the above delay of the commutating flux, the commutating voltage can't immediately compensate the voltage drops in the commutated coils.

Now, in large-sized and special small-sized dc motors, the laminated cores are used not only in the armature, the main poles and the interpoles but also in the yoke, in order to decrease the eddy current which delays the transient response of the commutating flux. On the other hand, in usual small-sized dc motors, the yoke is made of a solid core by economical and industrial reasons. Therefore, it is very important to analyse the transient response of the commutating flux of the usual small-sized dc motors, in whose yoke the eddy current is induced.

However, the study on the transient response of the commutating flux has not been done sufficiently because of difficulty of the analysis due to a complicated configuration of the dc motor, nonlinear magnetization characteristics of the structual cores, complicated influences of the transitional eddy current, etc.. Namely, in the early studies, the commutating flux in the steady state was analogically solved by using the analytical methods such as the images method, the mapping one, the separation of variables, etc. in a two-dimensional cross-section perpendicular to the motor axis, on the assumptions that the structual cores have a infinite permeability and so the magnetic circuit of the dc motor can be simplified very much.[4],[5] In this connection, even now, the Carter coefficient[4], which is introduced by Carter in 1901 year, is used to estimate the influence of the armature slots on the commutating flux. Also, the graphical mapping methods introduced by Stevenson et al.[6] in 1927 year and others[1],[5],[7] were used to obtain the approximate flux distribution of the interpole flux, by which, though the troublesome handworks are needed, the complicated shapes of the interpole, the

main pole and the yoke can be fairly considered.

In the recent studies, the two-dimensional steady flux distributions in not only the interpole airgap but also the interpole core, the armature, the yoke and the main pole were analysed approximately by using a large-sized digital computer and the finite difference[8],[9] and the finite element methods,[10] in which the complicated cross-section of the dc motor and the nonlinear permeability of the iron cores are considered. The fairly precise steady flux distributions obtained by Erdelyi, et al.[9] in 1970 may be used to investigate the commutation characteristics in the steady state.

Next, with respect to the transient response and distribution of the commutating flux, which relate closely to the commutation characteristics in the transient state where the armature current abruptly changes, many studies were carried out, too. However, those studies are mostly done on the assumption that the magnetic circuit containing the interpole can be simulated by a simplified single magnetic circuit model with some constant permeabilities. The calculated results of the commutating flux and the eddy current, which Rüdenberg,[11] Švajcr,[12] Sakabe,[13] and others[5],[14] obtained by the model and the two-dimensional analytical method of separation of variables, are at present used for rough estimation of the commutating flux, the eddy current and the commutation characteristics in the transient state.

However, the actual dc motor has the iron cores with nonlinear permeabilities, which is caused by the magnetic saturation and the hysteresis, and the complicated configuration. And it is thought that these factors have large influences on the transient flux responses and distributions in the dc motor and its transient commutation characteristics. Therefore, it is needed to analyse the transient response and distribution of the commutating flux in consideration of the nonlinear permeabilities and the complicated configuration.

Next, as seen from the above-mentioned, it is little impossible to calculate the transient responses and distributions of the magnetic fluxes in the motor by

the conventional analytical methods in consideration of the nonlinear permeability and the complicated configuration. Furthermore, though the fluxes distribute three-dimensionally in the motor, it is too difficult to get the precise three-dimensional solutions, because abnormal much handwork and computation time are needed. Accordingly, two-dimensional numerical solutions, to which the finite difference, the finite element methods, etc., are applied, should be used.

However, the finite difference method, in which the physical law about the magnetic fluxes can be approximated at any grid of the rectangular meshes, is difficult to apply to the complicatedly shaped magnetic circuit of the dc motor. The finite element method, in which arbitrary triangular meshes are usually used and the variational principle is used to approximate the physical law at each node of the meshes, has flexibility to be able to apply to the complicatedly shaped magnetic circuit. However, Hannalla,[15] Dermerdash[16] pointed out that the finite element method has weak points for treating the rectangular conductor such as the an armature coil carrying uniform current, and for doing rapidly varying currents or voltages such as the surge in a transmission line, eddy current induced in a iron core of the dc motor, etc.. Accordingly, the nodal method was presented by Hannalla, et al.,[15] in which the acute-angled triangular meshes are used and the physical law is approximated by the principle in the finite difference method. This method is a superior one, but it has a weak point that the usable triangle must be acute-angled. Therefore, it is needed to increase the flexibility of the nodal method.

Furthermore, the nonlinearity of the permeability of the iron cores of the dc motor depends not only on the saturated magnetization curve but also the hysteresis one. However, in the conventional two-dimensional analyses, influences of the hysteresis on behaviors of the magnetic fluxes in the motor was not investigated at all.

1.2 Purpose and Synopsis of Part II

In the recent dc motors which are used as the precise variable speed machines, it is the most important to maintain the good commutation independent of the abrupt change of the armature current. Then it is needed to analyse experimentally and theoretically in detail the transient behaviors of the commutating flux and so on, which relate closely to the commutating voltage. Also, for the theoretical analyses, it is necessary to improve satisfactorily the usual two-dimensional numerical calculation, so that the influences of the magnetic fluxes in the interpole airgap and core, the yoke, the armature, etc., the eddy currents induced in the yoke and the interpole liners, and the magnetic saturation and the hysteresis on the commutating flux can be investigated accurately.

In Chapter 2, first, there are introduced the two-dimensional fundamental equations with respect to the vector potential from the Maxwell equations in the elctromagnetic field, where the one is used to obtain easily both the magnetic flux and the eddy current distributions in the dc motor. And in order to solve numerically the above fundamental equations, the nodal equation at each node of the triangular meshes, by which the region to be analysed is subdivided, is got by a new nodal method, which is more improved than the conventional nodal method by using any shape of the triangle. Next, the time derivative of the vector potential in the nodal equation, which is needed to calculate the eddy current, is approximated by the Crank-Nikolson finite difference method.[17],[18],[19] Also, the author shows a numerical method for deriving the nonlinear reciprocal permeabilities from the magnetization and the hysteresis curves of the iron cores, in which the Frölich formula is used. Furthermore, from every nodal equation with the above approximated time derivative and the boundary conditions, the final fundamental nonlinear simultaneous nodal equations are derived. Lastly, the calculation processes to solve numerically the nodal equations are shown.

In Chapter 3, first, the author introduces a new equivalent magnetic circuit model, by which the transient responses of the magnetic fluxes in the usual

small-sized dc motor containing the solid iron yoke can be researched, that can't be done by the conventional model.[5],[11]-[14] Next, he gets experimental results to study on the transient responses of the fluxes in the interpole airgap, the interpole core and the yoke to the abrupt change of the armature current. Also, by using the numerical solution shown in Chapter 2, he evaluates the transient flux responses, and ascertains the validity of his solution by showing that the calculated results agree well with the experimental ones. It is made clear that the magnetic flux and the eddy current concentrate in the inner skin region of the yoke for an initial duration after the change of the armature current. Furthermore, it is shown that the magnetic hysteresis has a large influence on the transient behavior of the flux near the surface of the yoke, and that the conductivity of the yoke has a large one on the same behaviors in not only the yoke but also the interpole core and airgap.

In Chapter 4, there is first introduced the theoretical commutation equations to clarify close relations between the commutating flux and the commutation characteristics. Then, by using a small-sized dc motor, the author experimentally confirms that the initial delay of the transient response of the commutating flux density to the abrupt change of the armature current deteriorates the transient commutation characteristics. Next, through the experimental and the calculated results of the transient responses of the flux density in the interpole airgap and the fluxes in the interpole core and the yoke, it is shown that the above flux density and the fluxes delay to the change of the armature current by the eddy currents induced in the yoke and the interpole liners. Also, the calculated distributions of the magnetic flux and eddy current density present that the much magnetic flux and the large eddy current density concentrate in the inner skin region of the yoke and they delay the flux response in not only the yoke but also the interpole airgaps and cores. Furthermore, it is shown that the magnetic saturation and the magnetic hysteresis in the inner skin region of the yoke have considerable influences on the transient responses and distributions of the

magnetic fluxes. Finally, the effect of lamination of the region near the inner surface of the yoke on improvement of the transient responses of the fluxes is quantitatively investigated by the numerical analyses.

CHAPTER 2

TWO-DIMENSIONAL NUMERICAL SOLUTION OF TRANSIENT MAGNETIC FLUX DISTRIBUTION IN ELECTRIC MACHINES

2.1 Introduction

As described in Chapter 1, it is little impossible to calculate the transient responses and distributions of the magnetic fluxes in the motor by the conventional analytical methods in consideration of the nonlinear permeability and the complicated configuration. Furthermore, though the fluxes distribute three-dimensionally in the motor, it is too difficult to get the precise three-dimensional solutions, because abnormal much handwork and computation time are needed. Accordingly, two-dimensional numerical solutions, to which the finite difference, the finite element methods, etc. are applied, should be used.

However, the finite difference method,[8],[9] in which the physical law about the magnetic fluxes can be approximated at any grid of the rectangular meshes, is difficult to apply to the complicatedly shaped magnetic circuit of the dc motor. The finite element method,[10] in which arbitrary triangular meshes are usually used and the variational principle is used to approximate the physical law at each node of the meshes, has flexibility to be able to apply to the complicatedly shaped magnetic circuit. However, Hannalla et al.[15] pointed out that the finite element method has weak points for treating the rectangular conductor. So, they presented a new nodal method, in which the acute-angled triangular meshes are used and the physical law is approximated by the principle in the finite difference method. This method is a superior one, but it has a weak point that all usable triangles must be acute-angled ones. Therefore, it is needed to remove the weak point of the nodal method.

Furthermore, the nonlinearity of the permeability of the iron cores of the dc motor depends not only on the saturated magnetization curve but also the hysteresis one. However, in the conventional two-dimensional analyses, influence of the hysteresis on behaviors of the magnetic fluxes in the motor was not investigated at all.

In this chapter, first, there are derived two-dimensional fundamental equations with respect to the vector potential from the Maxwell equations in electromagnetic field, where the vector potential is used to obtain easily both the magnetic flux and the eddy current distributions in the dc motor. And in order to solve numerically the above fundamental equations, the nodal equation at each node of the triangular meshes, by which the region to be analysed is subdivided, is introduced by a new nodal method which is more improved than the former nodal method by using any shape of triangle.[20]-[25]

Next, the time derivative of the vector potential in the nodal equation, which is needed to calculate to the eddy current, is approximated by using the Crank-Nikolson finite difference method.[17],[18],[19] Also, the author shows the numerical method for deriving the nonlinear reciprocal permeabilities from the magnetization and the hysteresis curves of the iron cores, in which the Frölich formula is used.

Furthermore, from every nodal equation with the above approximated time derivative and the boundary conditions, the final fundamental nonlinear simultaneous nodal equations are derived. Lastly, the calculation processes to solve numerically the nodal equations are shown.

2.2 Fundamental Equations

The magnetic flux distribution in electric machines can be obtained by solving the following Maxwell equations of electromagnetic field

$$\mathrm{rot}\boldsymbol{H}=\boldsymbol{J}, \tag{2.1}$$

$$\mathrm{rot}E=-\frac{\partial B}{\partial t}, \tag{2.2}$$

$$\mathrm{div}B=0, \tag{2.3}$$

and the additional relations

$$B=\mu H, \tag{2.4}$$

$$J=J_s+\sigma E, \tag{2.5}$$

where

B : magnetic flux density,

E : electric field intensity,

H : magnetic field intensity,

J : total current density,

J_s : current density supplied to conductors of exciting winding,

σE : eddy current density induced in iron cores,

μ : permeability which may vary with magnitude of B and H,

σ : conductivity,

t : time.

In the equations, the displacement current and the free-space charge are ignored. Also, we assume that the density of the eddy current induced in the conductors is negligible compared with J_s and the conductivity in each core is uniform.

By using the magnetic vector potential A which is given by

$$\mathrm{rot}A=B \tag{2.6}$$

so that Eq. (2.3) may be satisfied, where

$$\mathrm{div}A=0, \tag{2.7}$$

we can derive

$$E=-\frac{\partial A}{\partial t} \tag{2.8}$$

from Eqs. (2.2). Then, by Eqs. (2.2) to (2.8), Eq. (2.1) is transformed into the following equation with respect to A and J_s

$$\mathrm{rot}(\nu \mathrm{rot} A)=J_s-\sigma\frac{\partial A}{\partial t}, \tag{2.9}$$

where $\nu=1/\mu$ is the reciprocal permeability.

If A can be obtained by solving Eqs. (2.7) and (2.9), B, H and J are evaluated by

$$B=\mathrm{rot}A, \tag{2.10}$$

$$H=\nu \mathrm{rot}A, \tag{2.11}$$

$$J=J_s-\sigma\frac{\partial A}{\partial t}. \tag{2.12}$$

Then, the magnetic flux Φ passing through an arbitrary cross-sectional area S with the contour C is calculated by

$$\Phi=\int_S B\cdot dS=\oint_C A\cdot dl. \tag{2.13}$$

For simplifying the analysis, let us investigate the two-dimensional flux distribution in an x-y cross-section, which is perpendicular to the rotor axis, of the magnetic circuit in the electric machine. We assume that B and H don't vary in the z direction perpendicular to the cross-section, and that A and J_s have only their respective z components. Then, by using the following relations

$$A=kA(x,y,t)=kA, \tag{2.14}$$

$$J_s=kJ_s(x,y,t)=kJ_s, \tag{2.15}$$

where

k : fundamental unit vector in z direction,

Eq. (2.9) is reduced to the following two-dimensional equation

$$\mathrm{rot}(\nu \mathrm{rot}kA)=k\left(J_s-\sigma\frac{\partial A}{\partial t}\right), \tag{2.16}$$

where the condition

$$\mathrm{div}A=\mathrm{div}kA=0 \tag{2.17}$$

must be always satisfied.

Substituting Eqs. (2.14) and (2.15) into Eqs. (2.10) to (2.13), the following

equations are obtained:

$$B_x=\frac{\partial A}{\partial y}, \quad B_y=-\frac{\partial A}{\partial x}, \tag{2.18}$$

$$H_x=\nu\frac{\partial A}{\partial y}, \quad H_y=-\nu\frac{\partial A}{\partial x}, \tag{2.19}$$

$$J=J_s-\sigma\frac{\partial A}{\partial t}, \tag{2.20}$$

$$\Phi=\oint_C kA\cdot dl=\Delta A\, l_z, \tag{2.21}$$

where

B_x and B_y : x and y components of B,

H_x and H_y : x and y components of H,

J : z component of J,

ΔA : difference between vector potentials at some two points on contour C in x-y cross-section of magnetic circuit,

l_z : length of magnetic circuit in z direction.

Next, an equi-vector-potential line shows the corresponding magnetic flux line, because the following relation

$$\frac{dy}{dx}=\frac{B_y}{B_x} \tag{2.22}$$

is derived from the condition of the derivative

$$dA=(\frac{\partial A}{\partial x})dx+(\frac{\partial A}{\partial y})dy=0 \tag{2.23}$$

on the line and Eqs. (2.18).

2.3 Numerical Solution of Fundamental Equations

2.3.1 Application of nodal method to basic equations

In order to obtain an approximate numerical solution of Eq. (2.16) under some given boundary conditions, we use a nodal method as already mentioned.

Now, the domain where Eq. (2.16) should be solved is subdivided into a large number of triangular elements, in which J_s, ν *and* σ can be assumed to be constant. Then, Eq. (2.16) is transformed to simultaneous discrete nodal equations with an unknown vector potential at each vertex of every triangular element.

In this section, we study on the case where the vector potential is assumed to be expressed by a first order function of position in each element.

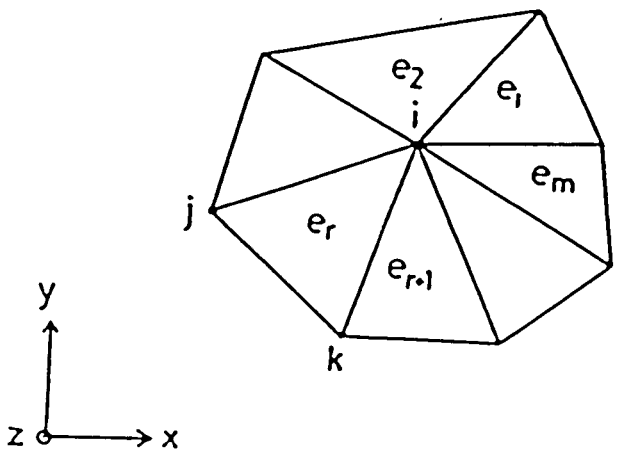

Fig.2.1 Node i and adjoining elements holding i in common.

At any point (x,y) in a triangular element e_r with nodes i, j and k as shown in Fig.2.1, the vector potential $A=A_r(x,y,t)=A_r$ is assumed to be given by the following linear approximation

$$A_r=a_r+b_rx+c_ry, \quad r=1,2,\ldots,m, \tag{2.24}$$

in which

$$\begin{bmatrix} a_r \\ b_r \\ c_r \end{bmatrix}=\frac{1}{D_r}\begin{bmatrix} a_{ri} & a_{rj} & a_{rk} \\ b_{ri} & b_{rj} & b_{rk} \\ c_{ri} & c_{rj} & c_{rk} \end{bmatrix}\begin{bmatrix} A_{ri} \\ A_{rj} \\ A_{rk} \end{bmatrix},$$

$a_{ri}=x_{rj}y_{rk}-x_{rk}y_{rj}$, $b_{ri}=y_{rj}-y_{rk}$, $c_{ri}=x_{rk}-x_{rj}$,

$a_{rj}=x_{rk}y_{ri}-x_{ri}y_{rk}$, $b_{rj}=y_{rk}-y_{ri}$, $c_{rj}=x_{ri}-x_{rk}$,

$a_{rk}=x_{ri}y_{rj}-x_{rj}y_{ri}$, $b_{rk}=y_{ri}-y_{rj}$, $c_{rk}=x_{rj}-x_{ri}$,

$D_r=a_{ri}+a_{rj}+a_{rk}$,

A_{rq}, x_{rq} and y_{rq} : A, x and y at node q in e_r, where, $q=i,j,k$,

and we can find the following relations about Fig.2.1,

$A_{ri}=A_i$, $x_{ri}=x_i$, $y_{ri}=y_i$ for $r=1,2,\ldots,m$,

$A_{rj}=A_{r-1,k}=A_j$, $x_{rj}=x_{r-1,k}=x_j$, $y_{rj}=y_{r-1,k}=y_j$,

$A_{rk}=A_{r+1,j}=A_k$, $x_{rk}=x_{r+1,j}=x_k$, $y_{rk}=y_{r+1,j}=y_k$,

where

A_q, x_q and y_q : A, x and y at common node q.

From Eqs.(2.18), (2.19) and (2.24), the x and y components B_x, B_y, H_x and H_y of B and H in element e_r are derived as follows:

$$B_x=\frac{1}{D_r}\sum_{q=i}^{k}c_{rq}A_{rq},\quad B_y=-\frac{1}{D_r}\sum_{q=i}^{k}b_{rq}A_{rq}, \tag{2.25}$$

$$H_x=\frac{\nu_r}{D_r}\sum_{q=i}^{k}c_{rq}A_{rq},\quad H_y=-\frac{\nu_r}{D_r}\sum_{q=i}^{k}b_{rq}A_{rq}, \tag{2.26}$$

which are constant, where $\nu=\nu_r$ is determined by the relation between $B_r=(B_x^2+B_y^2)^{1/2}$ and $H_r=(H_x^2+H_y^2)^{1/2}$ in e_r (see Article 2.3.3).

When the expressions similar to Eqs.(2.24) to (2.26) are applied to every element, the continuity of the normal component B_n of B on the boundary line of two adjoining elements is maintained. For example, B_n on both sides of the boundary line $\overline{ik}$ of elements e_r and e_{r+1} in Fig.2.1 is given by the following same expression

$$B_n=(A_i-A_k)/\{(x_i-x_k)^2+(y_i-y_k)^2\}^{1/2} \tag{2.27}$$

where A_i, A_k, x_i, x_k, y_i and y_k are A, x and y at nodes i and k.

On the other hand, the continuity of the tangential component H_t of H on the boundary line can't be expressed by the equation similar to Eq.(2.27). So, to keep

the physical law, in our nodal method the above boundary condition for H is replaced by the following Ampēre circuital law

$$\oint_C H \cdot dl = \int_S (J_s - \sigma \frac{\partial A}{\partial t}) dxdy \tag{2.28}$$

around each node, where the integral path C is a specific one, for example, as shown by the broken line in Fig.2.2, and S is the domain enclosed by C. In this connection, i', j' and k' in the same figure are the middle points of three sides $\overline{jk}$, $\overline{ki}$ and $\overline{ij}$, respectively, p is the outer center of element e_r, and the node i is had in common by elements e_1, e_2,..., e_m.

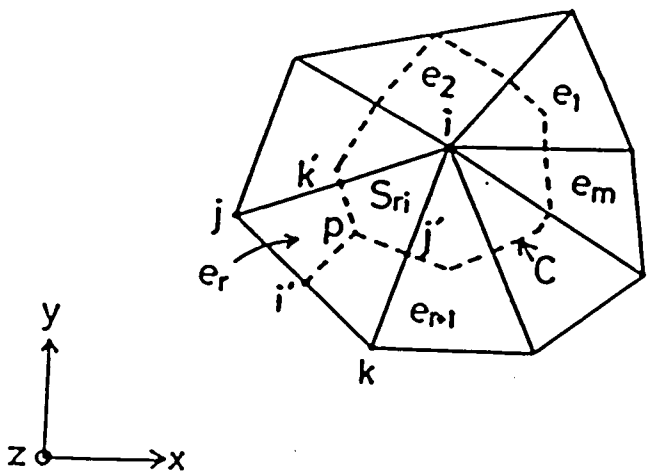

Fig.2.2 Integral path C around node i.

From Eqs. (2.24), (2.26) and (2.28) in element e_r, we can derive the following discrete nodal equations

$$\int_{k'pj'} H dl = \frac{\nu_r}{2D_r} \sum_{q=i}^{k} (b_{ri} b_{rq} + c_{ri} c_{rq}) A_{rq}, \tag{2.29}$$

$$\int_{ik'pj'i} J_s dxdy = J_{sr} S_{ri}, \tag{2.30}$$

$$\int_{ik'pj'i} (\sigma \frac{\partial A}{\partial t}) dxdy = \sigma_r S_{ri} \frac{\partial A_{ri}}{\partial t} = \sigma_r S_{ri} \frac{\partial A_i}{\partial t}, \tag{2.31}$$

for node i, where

$$\left.\begin{aligned} S_{ri}&=\frac{1}{16S_r}\{|b_{ri}b_{rk}+c_{ri}c_{rk}|(b_{rj}^2+c_{rj}^2)+|b_{ri}b_{rj}+c_{ri}c_{rj}|(b_{rk}^2+c_{rk}^2)\}, \\ S_r/4&\leqq S_{ri}\leqq S_r/2. \end{aligned}\right\} \tag{2.32}$$

In these equations, J_{sr}, ν_r and σ_r are the values of J_s, ν and σ in element e_r, respectively, and $S_r=D_r/2$ is its area. Here, we must notice that the contributions of $\partial A_j/\partial t$ and $\partial A_k/\partial t$ to the integration result of Eq. (2.31) were neglected, because those contributions may disturb the resultant eddy current density at node i to approximate the exact one $\sigma\partial A_i/\partial t$.[16],[21],[22] Also, when the element is an obtuse-angled triangle, of which the outer center lies outside itself, as the element e_2 in Fig.2.2, we must put $S_{ri}=S_r/4$ or $S_{ri}=S_r/2$ into Eqs. (2.30) and (2.31) according to whether the vertical angle of the element at node i is smaller or greater than $\pi/2$.

In this connection, in the conventional nodal method, every element must be an acute-angled triangle. Hence, it is difficult for the conventional one to be applied to a complex field region as in electric machines. Also, the finite element method, in which $S_{ri}=S_r/3$ is substituted into Eq. (2.30) instead of Eq. (2.32), has a weak point for treating the rectangular conductor carrying a uniformly distributed current such as the one in the armature slot of a dc motor.[15]

Next, by using the integration results in Eqs. (2.29), (2.30) and (2.31) and completing the Ampēre circuital law (2.28) around node i shown in Fig.2.2, the following nodal equation is obtained

$$h_i=f_i-g_i\frac{\partial A_i}{\partial t}, \tag{2.33}$$

where

$$h_i=\oint_C H dl=\sum_{r=1}^{m}\frac{\nu_r}{2D_r}\sum_{q=i}^{k}(b_{ri}b_{rq}+c_{ri}c_{rq})A_{rq}=h_{ii}A_i+\sum_{r=1}^{m}h_{ij}A_{rj}, \tag{2.34}$$

$$f_i=\int_S J_s dxdy=\sum_{r=1}^{m}J_{sr}S_{ri}, \tag{2.35}$$

$$g_i=\int_S \sigma dxdy=\sum_{r=1}^{m}\sigma_r S_{ri}\,, \tag{2.36}$$

in which

$$h_{ii}=\sum_{r=1}^{m}\frac{\nu_r}{2D_r}(b_{ri}^2+c_{ri}^2)\,,$$

$$h_{ij}=\sum_{r=1}^{m}\{\frac{\nu_r}{2D_r}(b_{ri}b_{rj}+c_{ri}c_{rj})+\frac{\nu_{r-1}}{2D_{r-1}}(b_{r-1,i}b_{r-1,k}+c_{r-1,i}c_{r-1,k})\}\,.$$

In Eq. (2.34), A_{rq} is the vector potential at node q in e_r, and $A_{ri}=A_i$ is defined in common for $r=1,2,\ldots,m$.

When b_{rq}, c_{rq}, D_r, etc. approach infinitely zero, Eq. (2.33) may sufficiently approximate the two-dimensional fundamental equation (2.10) at node i. In this connection, as previously stated, if the terms $\partial A_j/\partial t$ and $\partial A_k/\partial t$ were considered in the integration result in Eq. (2.31), those terms should disturb the resultant eddy current $g_i\partial A_i/\partial t$ in Eq. (2.33) to approximate $\sigma\partial A_i/\partial t$ accurately.

2.3.2 Numerical method for time derivative[17], [18], [19]

In Eq. (2.33), for node i of $g_i>0$, there is contained the time derivative $g_i\partial A_i/\partial t$. Therefore, in order to numerically solve the equation, we apply the Crank-Nikolson finite difference method to $g_i\partial A_i/\partial t$, by which a sufficiently accurate approximation of $g_i\partial A_i/\partial t$ can be obtained.

When the value of g_iA_i at time t is obtained, the value at $t+\Delta t$ is calculated by the following equation

$$(g_iA_i)_{t+\Delta t}=(g_iA_i)_t+\Delta t\{\varepsilon_i(g_i\frac{\partial A_i}{\partial t})_{t+\Delta t}+(1-\varepsilon_i)(g_i\frac{\partial A_i}{\partial t})_t\}\,, \tag{2.37}$$

where ε_i is a weight factor of the time derivative and $0\leqq\varepsilon_i\leqq1$. From Eqs. (2.33) and (2.37), we can get the following nodal equation

$$(g_iA_i+\varepsilon_i\Delta th_i)_{t+\Delta t}=\{g_iA_i-(1-\varepsilon_i)\Delta th_i\}_t+\Delta t\{\varepsilon_i(f_i)_{t+\Delta t}+(1-\varepsilon_i)(f_i)_t\}\,. \tag{2.38}$$

Next, for node i of $g_i=0$ and $h_i=f_i$, the nodal equation at $t+\Delta t$ can readily obtained by putting $g_i=0$ and $\varepsilon_i=1$ in Eq. (2.38).

2.3.3 Numerical determination of nonlinear reciprocal permeability

When the element e_r belongs to the region consisting of the air or the winding conductors, the reciprocal permeability $\nu=\nu_r$ in Eqs.(2.26), (2.29) and (2.34) is assumed to be equal to the one of the vacuum, namely

$$\nu_r=\nu_0=10^7/(4\pi) \quad m/H. \tag{2.39}$$

However, when e_r belongs to the iron core region, ν_r is determined by the nonlinear and multivalued relation between B and H, which are the magnitudes of B and H, respectively. And the relation is usually given by the B-H curves such as the initial magnetization curve and the hysteresis one. Here, let us introduce the numerical method for obtaining ν_r corresponding to $B=B_r$ in e_r, where B_r is determined by Eq.(2.25) as follows

$$B_r=(B_x^2+B_y^2)^{1/2}=\frac{1}{D_r}\{(\sum_{q=i}^{k}b_{rq}A_{rq})^2+(\sum_{q=i}^{k}c_{rq}A_{rq})^2\}^{1/2}. \tag{2.40}$$

(1) Derivation of ν_r from magnetization curve[18],[19],[23]

When $B=B_r$ increases from an initial unmagnetized value, the B-H curve is expressed by the initial magnetization curve $OP_1P_2P_3P_4$ as shown in Fig.2.3. Then, $H=H_r$ corresponding to B_r is found by the curve, and sequentially the exact value $\nu_r=H_r/B_r$ can be obtained. However, this process is too complicated to be used for practical calculation.

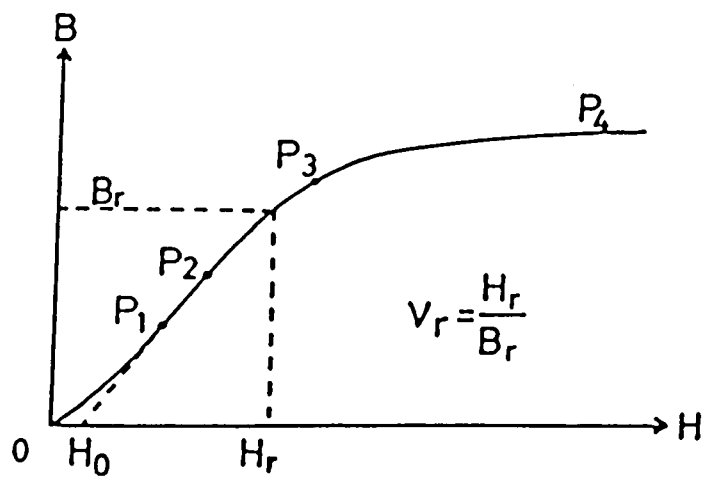

Fig.2.3 Frölich formula for obtaining reciprocal permeability ν_r by initial magnetization curve.

In our numerical method, the following Frölich formula

$$B=\frac{H-H_0}{\eta+\xi(H-H_0)} \tag{2.41}$$

is adopted to obtain the approximate value of ν_r, where η, ξ and H_0 are the coefficients determined by the B-H curve. By applying Eq. (2.41) to the segment $P_1P_2P_3$ of the curve in Fig.2.3, ν_r is expressed by

$$\nu_r=\frac{H_r}{B_r}=\frac{\eta}{1-\xi B_r}+\frac{H_0}{B_r}, \quad B_1\leqq B_r\leqq B_3, \tag{2.42}$$

where

$$\eta=\frac{(B_1-B_2)(B_2-B_3)(B_3-B_1)(H_1-H_2)(H_2-H_3)(H_3-H_1)}{B_1B_2(H_1-H_2)+B_2B_3(H_2-H_3)+B_3B_1(H_3-H_1)}, \tag{2.43}$$

$$\xi=\frac{B_1(H_3-H_2)+B_2(H_1-H_3)+B_3(H_2-H_1)}{B_1B_2(H_1-H_2)+B_2B_3(H_2-H_3)+B_3B_1(H_3-H_1)}, \tag{2.44}$$

$$H_0=\frac{B_1B_2H_3(H_1-H_2)+B_2B_3H_1(H_2-H_3)+B_3B_1H_2(H_3-H_1)}{B_1B_2(H_1-H_2)+B_2B_3(H_2-H_3)+B_3B_1(H_3-H_1)}, \tag{2.45}$$

in which

B_i and H_i : B and H at P_i, i=1, 2, 3.

By the above process, we can get ν_r for any value of B_r on the B-H curve. In this connection, when B_r given by Eq. (2.40) is estimated over the saturation value of B, for example $B_r>B_4$, ν_r is calculated by $\nu_r=H_4/B_4$, where $B=B_4$ and $H=H_4$ at point P_4.

(2) Derivation of ν_r from hysteresis curve[24]

When B decreases from the point P_1 on the initial magnetization curve, the B-H curve is expressed by the hysteresis segment $P_1P_2P_3P_4$ as shown in Fig.2.4. Now, ν_r for $B=B_r$ on the one $P_1P_2P_3$ is obtained by substituting the values of B and H at three points P_1, P_2 and P_3 into Eqs. (2.42) to (2.45) as follows:

$$\nu_r=\frac{\eta}{1-\xi B_r}+\frac{H_0}{B_r}, \tag{2.46}$$

where

$$\eta=\frac{(B_2-B_1)(H_1-H_3)H_3}{B_1B_2H_1} \quad : \text{equal to slope } dB/dH \text{ at } P_3, \tag{2.47}$$

$$\xi=\frac{B_1H_3+B_2(H_1-H_3)}{B_1B_2H_1}, \tag{2.48}$$

$$H_0=H_3<0, \tag{2.49}$$

in which

B_i and H_i : B and H at P_i, i=1, 2, 3.

In this connection, $B=B_2$ at P_2 and $H=H_3$ at P_3 are called the residual magnetism and the coercive force, respectively.

When $B=-B_r$ becomes negative on the hysteresis segment P_3P_4, η and H_0 keep the values given by Eqs. (2.47) and (2.49), and so only the value of ξ in Eq. (2.46) is replaced by

$$\xi=\frac{H_4-H_3-\eta B_4}{B_4(H_4-H_3)}, \tag{2.50}$$

where

$B_4=-B_1$ and $H_4=-H_1$: B and H at P_4.

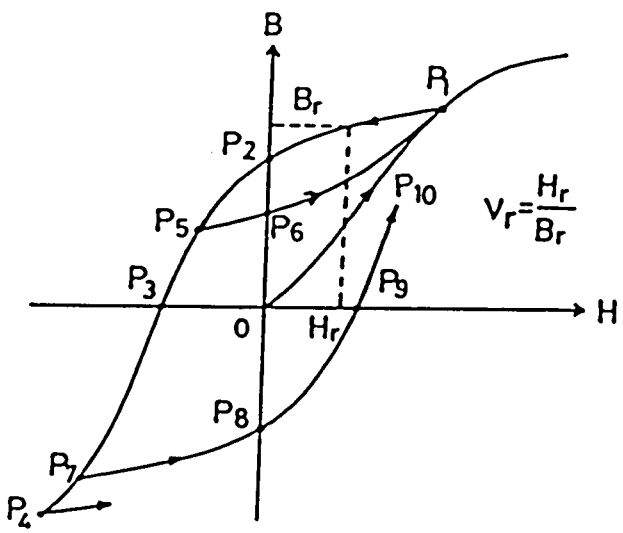

Fig.2.4 Application of Frölich formula to hysteresis curve for obtaining reciprocal permeability ν_r

Next, let us consider ν_r in the case where B stops to decrease at some point on the hysteresis segment and inversely increases from the point. When $B=B_r$ increases from point P_5 on the segment $P_1P_2P_3$ in Fig.2.4, $B=B_6$ at point P_6 is first evaluated under the assumption that the line segment $\overline{P_5P_6}$ is parallel to the one $\overline{P_1P_2}$, so that η, ξ, H_0 and ν_r may be obtained by using the values of B and H at three points P_5, P_6 and P_1 as well as in Eqs. (2.42) to (2.45).

When $B=B_r$ increases from point P_7 on the segment P_3P_4, the segment $P_7P_8P_9P_{10}$ is evaluated by Eq. (2.41) under the assumption that the segment $\overline{P_7P_8}$ is parallel to $\overline{P_1P_2}$ and dB/dH at P_9 is equal to the one at P_3. Then, ν_r for $B=B_r$ is obtained by the similar computation process to the one given by Eqs. (2.46) to (2.50).

2.3.4 Basic nodal equations considering boundary conditions

Here, let us introduce the nodal equation for node i which exists on the boundary line, as shown in Figs.2.5 (a) and (b). On a boundary line where the normal component B_n of B is zero, the relation $A=A_i=A_k$, which doesn't depend on x and y, is obtained by substituting $B_n=0$ into Eq. (2.27). Then, the nodal equation (2.38) for i is rewritten as follows:

$$\Delta t\,(h_i)_{t+\Delta t}=\Delta t\,(f_i)_{t+\Delta t}, \tag{2.51}$$

where

$h_i=A_i$, $g_i=0$, $\varepsilon_i=1$,

$f_i=A_c$: vector potential given on boundary line.

(a) $B_n=0$ (b) $H_t=0$

Fig.2.5 Typical boundary conditions.

On another boundary where the tangential component H_t of H is zero, the nodal equation for node i is derived from integrating Eq. (2.28) in a circuital integral region given by the broken line in Fig.2.5(b), where C_{out} and C_{in} are the outside and the inside paths of our integral region, respectively. In this case, the line integration along C_{out} vanishes because of $H_t=0$, and the one along C_{in} is easily carried out by Eqs. (2.29) and (2.34). As a result, we can get the discrete nodal equation similar to Eq. (2.38), where $f_i=0$ and $g_i=0$ because of $J_s=0$ and $\sigma=0$ near the boundary line.

Finally, from Eqs. (2.38) and (2.51), the basic nonlinear simultaneous nodal equations for all nodes are readily derived as follows:

$$([G]+\Delta t[\varepsilon][H])[A]_{t+\Delta t}=\{[G]-\Delta t([U]-[\varepsilon])[H]\}[A]_t$$
$$+\Delta t\{[\varepsilon][F]_{t+\Delta t}+([U]-[\varepsilon])[F]_t\}, \qquad (2.52)$$

in matrix form, where

$$[A]=\begin{bmatrix} A_1 \\ A_2 \\ \vdots \\ A_i \\ \vdots \\ A_n \end{bmatrix}, \quad [F]=\begin{bmatrix} f_1 \\ f_2 \\ \vdots \\ f_i \\ \vdots \\ f_n \end{bmatrix}, \quad [G]=\begin{bmatrix} g_1 & 0 & \cdots & 0 \\ 0 & g_2 & \cdots & 0 \\ \vdots & \vdots & & \vdots \\ 0 & \cdots & g_i & 0 \\ \vdots & & & \vdots \\ 0 & \cdots & 0 & g_n \end{bmatrix},$$

$$[H]=\begin{bmatrix} h_{11} & h_{12} & \cdots & h_{1n} \\ h_{21} & h_{22} & \cdots & \vdots \\ \vdots & & & \vdots \\ h_{i1} & \cdots & h_{ii} & h_{in} \\ \vdots & & & \vdots \\ h_{n1} & \cdots & \cdots & h_{nn} \end{bmatrix}, \quad [\varepsilon]=\begin{bmatrix} \varepsilon_1 & 0 & \cdots & 0 \\ 0 & \varepsilon_2 & \cdots & 0 \\ \vdots & \vdots & & \vdots \\ 0 & \cdots & \varepsilon_i & 0 \\ \vdots & & & \vdots \\ 0 & \cdots & 0 & \varepsilon_n \end{bmatrix}.$$

In these equations,

n : total number of nodes,

$[A]$: row matrix constructed with unknown vector potentials at all nodes,

$[F]$: row matrix derived from f_i in Eq. (2.35) and $f_i=A_c$ in Eq. (2.51),

[G] : diagonal coefficient matrix derived from g_i in Eq. (2.36) and g_i=0 in Eq. (2.51),

[H] : nonlinear and sparse coefficient matrix, in which coefficients h_{ij} (i and j=1,2,...,n) are derived from coefficients for A_i and A_{rj} in Eq. (2.34), and h_{ii}=1 and h_{ij}=0 for $i \neq j$ in Eq. (2.51),

[ε] : diagonal matrix constructed with ε_i in Eq. (2.38) and ε_i=1 in Eq. (2.51),

[U] : unit matrix.

By numerically solving Eqs. (2.52), the transient values of [A] at all nodes are obtained. Also, by putting Δt=1, g_i=0 and ε_i=1 for i = 1 to n in Eqs. (2.52), the values of vector potential in the steady state, where the eddy current vanishes, can be obtained.

2.3.5 Numerical calculation process

In Fig.2.6, there is shown the flow chart of a calculation processes for numerically solving the nonlinear simultaneous equations (2.52) and obtaining the transient responses of the vector potentials [A] for the change of the exciting current. The calculation processes are as follows:

(1) We provide the input information about the shape, the dimensions, the structural materials, etc. of the machine, and the boundary conditions.

(2) The analysed domain is subdivided into a large number of triangular elements.

(3) We provide the initial values of the vector potentials [A] at all nodes of the elements.

(4) The supplied current density J_s at time $t+\Delta t$ is calculated by dividing the current in the conductor of the exciting winding by its cross-sectional area, where Δt is determined enough small to obtain the accurate transient responses of [A].

(5) By using the already determined $[A]_t$ and J_s, the calculation of the right side terms of Eqs. (2.52) is carried out.

(6) The approximate values of $[A]_{t+\Delta t}$ are estimated.

(7) By using approximate values of $[A]_{t+\Delta t}$, the nonlinear reciprocal permeabilities ν_r's in elements within iron core are calculated by the method shown in Article 2.3.3.

(8) By solving Eqs. (2.52), the approximate solutions of $[A]_{t+\Delta t}$ are determined.

(9) The processes (6) to (8) are iterated till the convergence of $[A]_{t+\Delta t}$ is ascertained. In this connection, the approximate values in a next iteration are evaluated by the successive relaxation method, by which repetition time can be fairly decreased. [17], [18], [19]

(10) The above processes (4) to (9) for the next successive time $t=t+\Delta t$ are repeated till $t=t_{max}$, where t_{max} is the calculation interval needed to investigate the transient responses of $[A]$.

Next, when the transitional change of $[A]$ by the one of the current density J_s proportional to the exciting current are calculated, the transitional distribution of the magnetic flux can be shown by the equi-vector-potential lines, namely the flux lines. The distribution of the flux density is derived from Eqs. (2.25). Also, by Eqs. (2.33) and (2.36), the eddy current density in the iron core can numerically be evaluated

$$-\frac{g_i}{S_i}\frac{\Delta A_i}{\Delta t}=-\frac{\sum_{r=1}^{m}\sigma_r S_{ri}}{S_i}\frac{\Delta A_i}{\Delta t}, \tag{2.53}$$

where

ΔA_i : increment of $A=A_i$ at node i during Δt,

$S_i=\sum_{r=1}^{m}S_{ri}$.

Furthermore, the transient response of the magnetic flux Φ in a cross-section of the magnetic circuit can easily be calculated by Eq. (2.21).

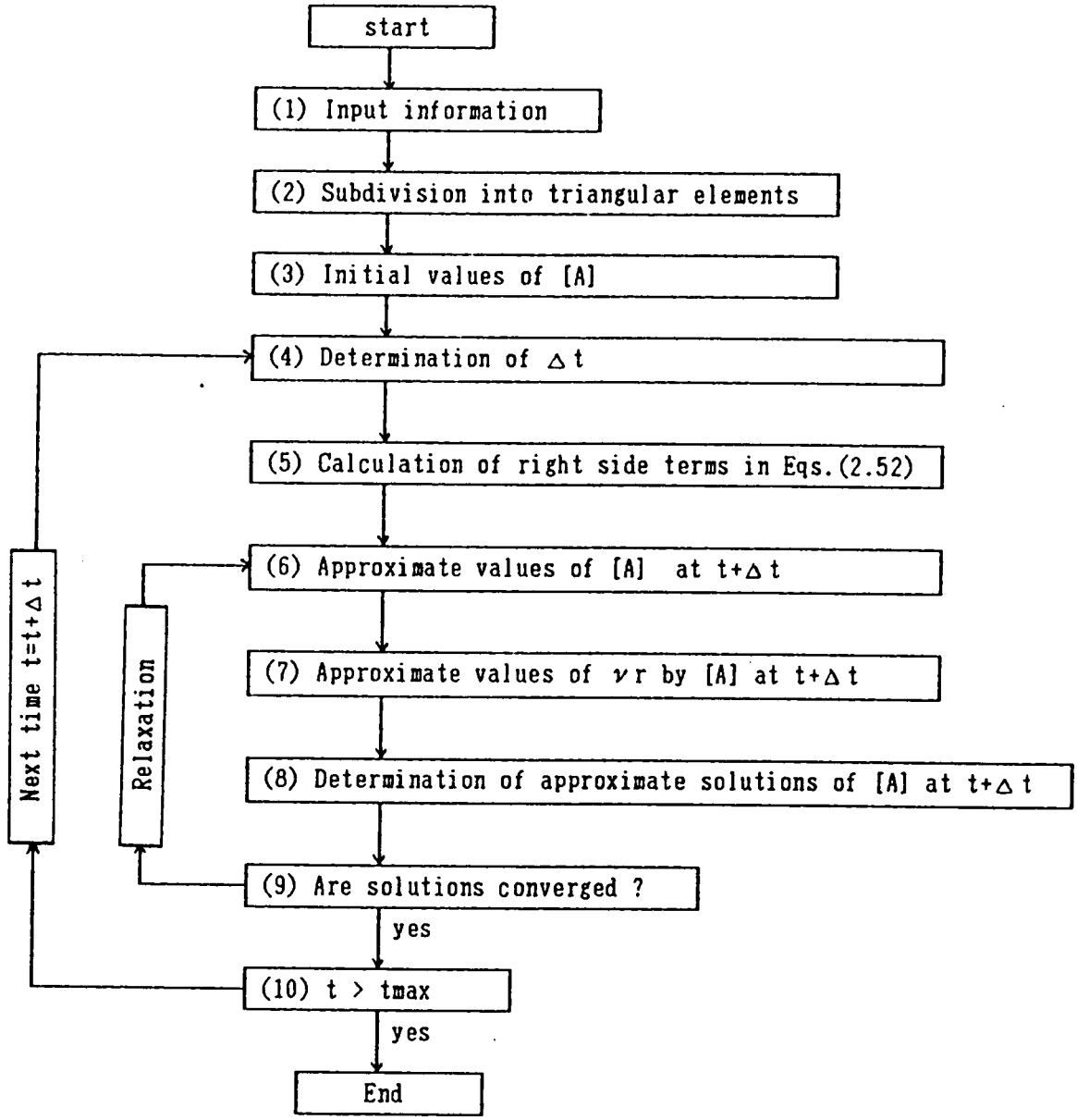

Fig.2.6 Flow chart of calculation processes for solving Eqs.(2.52).

2.4 Conclusion

The main results obtained by the investigation of the numerical solution in this chapter are as follows:

(1) By using the magnetic vector potential, the two-dimensional fundamental equations, by which the transient flux distribution in electric machines can be analysed, were derived from the Maxwell equations for the electromagnetic field. In the equation, the eddy current induced in iron cores and the nonlinear permeability were considered.

(2) The nodal method, which is known as the finite difference method using triangular elements, was applied to solve the two-dimensional equations, and the nodal equation at node of the element was introduced.

(3) The time derivative $g_i \partial A_i / \partial t$ contained in the nodal equation was approximated by the Crank-Nikolson finite difference method, and then the final discrete nodal equation was introduced.

(4) The numerical method for deriving the nonlinear reciprocal permeability ν_r from the magnetization and the hysteresis curves of iron cores was obtained by using the Frölich formula.

(5) The nodal equations considering the basic boundary conditions concerning to the magnetic flux density and the magnetic field intensity were obtained. Furthermore, the nonlinear simultaneous nodal equations for all nodes were introduced.

(6) The calculation processes to solve the nonlinear simultaneous equation were shown. In the processes, the successive relaxation method should be used for decreasing repetition time required to solve the equations.

CHAPTER 3

APPROXIMATE ANALYSIS OF TRANSIENT MAGNETIC FLUX IN DC MOTOR BY USING EQUIVALENT MAGNETIC CIRCUIT

3.1 Introduction

Many studies on the transient response of the interpole flux and so on were reported. However, those studies have been performed mostly on the assumptions that the magnetic flux doesn't leak out from the structual iron cores of the dc motor and the magnetic circuit containing the interpole can be simulated by a simplified single equivalent magnetic circuit model with some constant permeabilities. The calculated results of the commutating flux and the eddy current, which Rüdenberg,[11] Sakabe,[13] and others[12],[14] obtained by the above model and the two-dimensional analytical method of separation of variables, are at present used for rough estimation of the interpole flux, the eddy current and the commutation characteristics in the transient state.

However, the actual motor has iron cores with nonlinear permeabilities, which is caused by the magnetic saturation and the hysteresis. And it is thought that the nonlinear permeability has large influences on the transient behaviors of the commutating flux and so on in the motor and so its transient commutation characteristics. Also, it is wanted that the more suitable equivalent circuit than the above old one is found out for grasping more clearly the above transient behaviors.

In this chapter, first, the author introduces a new equivalent magnetic circuit model, by which the transient response of the magnetic flux in the usual small-sized dc motor containing the solid iron yoke can be researched, that can't be done by the conventional model. Next, he get experimental results to study on

the transient responses of the fluxes in the interpole airgap, the interpole core and the yoke to the abrupt change of the armature current.

Next, by using the numerical solution shown in Chapter 2, he evaluates the transient flux responses, and ascertains the validity of his solution by showing that the calculated results agree well with the experimental ones. Also, it is made clear that the magnetic flux and the eddy current concentrate in an inner skin region of the yoke for an initial duration after the change of the armature current.

Furthermore, it is shown that the magnetic hysteresis has a large influence on the transient behavior of the flux near the inner surface of the yoke, and that the conductivity of the yoke has a large one on the same behaviors in not only the yoke but also the interpole core and airgap.

3.2 Equivalent Magnetic Circuit Model of DC Motor

In Fig.3.1, the simplified paths of magnetic fluxes in a dc motor are shown by the broken lines, where

A_r : armature core,

I_p : interpole,

M_p : main pole,

Y_o : yoke,

I_a : current flowing in armature and interpole circuits,

Φ_a, Φ_g, Φ_i and Φ_y : magnetic fluxes in armature core, interpole airgap, interpole core and yoke.

In this connection, the current in the armature coil to be mechanically commutated by the brushes is $I_a/2$ as showing in the figure.

When it is assumed that the influence of the main pole and the armature slots on the interpole flux can be neglected, the magnetic circuit equation in Fig.3.1 can be simplified as follows:

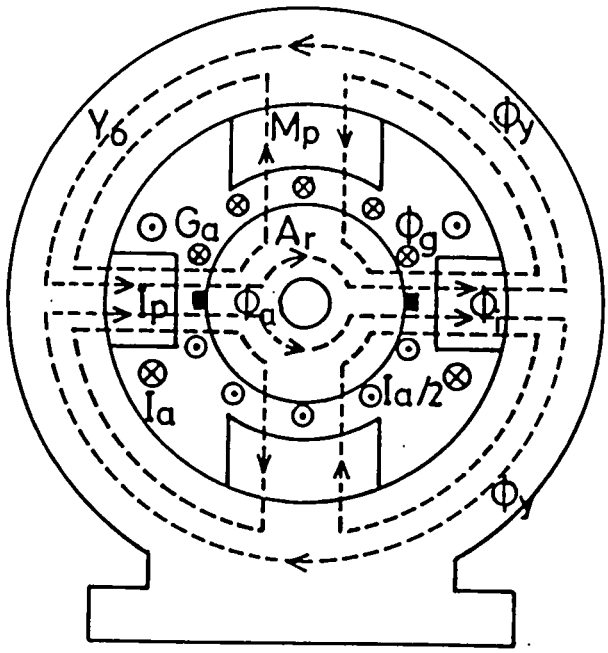

Fig.3.1 Simplified paths of magnetic flux in dc motor.

$$AT_i - AT_a = \mathcal{R}_a\Phi_a + \mathcal{R}_g\Phi_g + \mathcal{R}_i\Phi_i + \mathcal{R}_y\Phi_y, \tag{3.1}$$

where

AT_i : magnetomotive force(mmf) due to interpole exciting current I_a,

AT_a : counter mmf due to armature coil current $I_a/2$,

$\mathcal{R}_a$, $\mathcal{R}_g$, $\mathcal{R}_i$ and $\mathcal{R}_y$: magnetic reluctances of armature, interpole airgaps, interpole cores and yoke,

When the relations among Φ_a, Φ_g, Φ_i and Φ_y are found, we can obtain the transient response of Φ_g to any change of $AT_i - AT_a$, namely to that of I_a. Here, the flux Φ_g in the interpole airgap may correspond to the commutating flux, and so it relates closely to the commutation characteristics of the dc motor.

Next, when the leakage flux can be ignored, the following relations

$$\Phi_a = \Phi_g = \Phi_i = 2\Phi_y \tag{3.2}$$

are obtained. Then, Eq.(3.1) is rewritten by

$$AT_i - AT_a = (\mathcal{R}_a + \mathcal{R}_g + \mathcal{R}_i + \mathcal{R}_y/2)\Phi_g. \tag{3.3}$$

The conventional equivalent magnetic circuit model shown in Fig.3.2 has been derived from Eqs.(3.2) and (3.3) for a dc motor, of which the armature and the yoke are made of laminated cores and the interpole done of a solid core. In Fig.3.2,

A_r : laminated core corresponding to armature core,

G_a : airgap corresponding to interpole airgap,

I_p : solid core corresponding to interpole core,

Y_o : laminated core corresponding to yoke,

W : exciting winding to supply mmf AT_i-AT_a .

About this model, where the transitional eddy current may be induced in the interpole, the numerical analysis of the transient response of the interpole airgap flux Φ_g to the abrupt change of the armature current I_a has been already and considerably achieved.[11]-[14],[18],[19]

However, the usual small-sized dc motor has the yoke of a solid core and the interpole of a laminated core, and the eddy current is induced not in the interpole but in the yoke. Therefore, for example, an another model such as shown in Fig.3.3

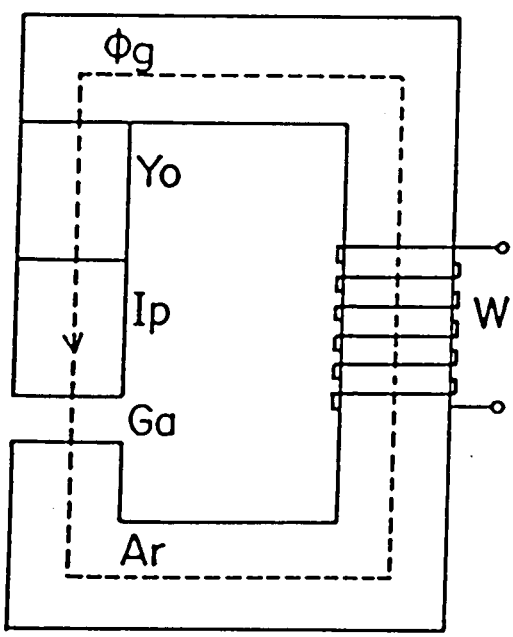

Fig.3.2 Conventional single magnetic circuit model.

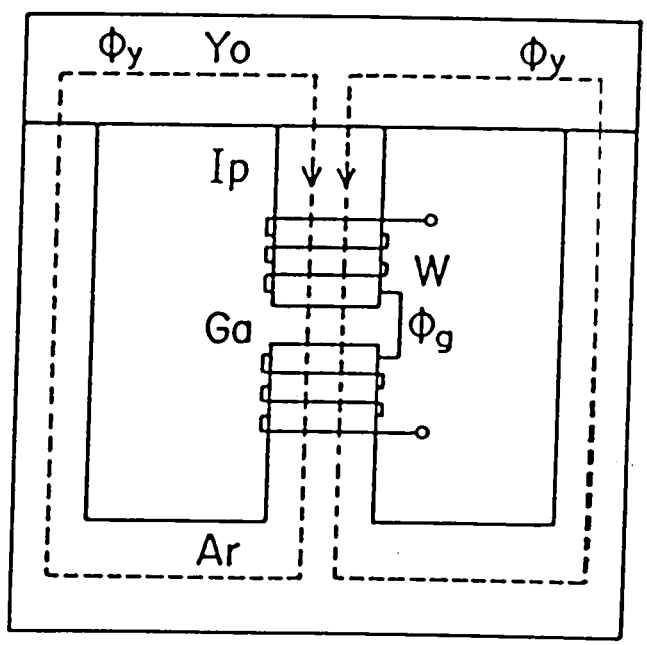

Fig.3.3 Magnetic circuit model considering yoke of solid iron.

must be used, because the eddy current in the yoke disturbs the relations (3.2). In Fig.3.3,

A_r : laminated core corresponding to armature core,

G_a : airgap corresponding to interpole airgap,

I_p : laminated core corresponding to interpole core,

Y_o : solid core corresponding to yoke,

W : exciting winding to supply mmf AT_i-AT_a .

In Fig.3.4, there is shown the magnetic circuit model to be used for the author's experimental investigation of the transient responses of the magnetic fluxes and to examine the validity of our numerical calculation described in Chapter 2. Figure 3.5 shows the settlement of search coils and GaAs Hall cell to record the transient responses of magnetic fluxes. In Figs.3.4 and 3.5

W_{i1} and W_{i2} : exciting windings to supply AT_i ,

W_{a1} and W_{a2} : exciting windings to supply AT_a ,

H_a : GaAs Hall cell to record transient response of Φ_4 ,

S_{c1} , S_{c2} and S_{c3} : search coils to record transient responses of Φ_1, Φ_2 and Φ_3 , respectively,

Φ_1, Φ_2, Φ_3 and Φ_4 : magnetic fluxes to be measured.

Here, the fluxes Φ_1, Φ_2 and Φ_4 correspond to the fluxes Φ_i, Φ_y and Φ_g in Fig.3.1, respectively, and Φ_3 corresponds to the flux through the inner part of 20 % of the yoke. In our experimental magnetic circuit model, A_r and I_p are made of laminated silicon steel plates, and Y_o of a solid wrought iron, and the windings W_{i1}, W_{i2}, W_{a1} and W_{a2} are bound by 2000 turns, respectively.

The B-H magnetization curves of the used cores are shown in Fig.3.6. In this figure, the representative hysteresis curves are shown, too.

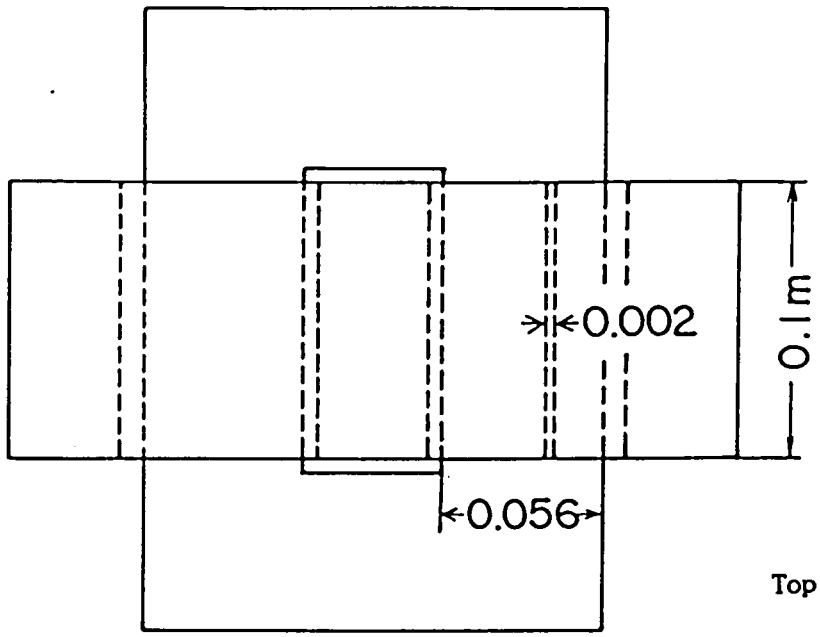

Top view.

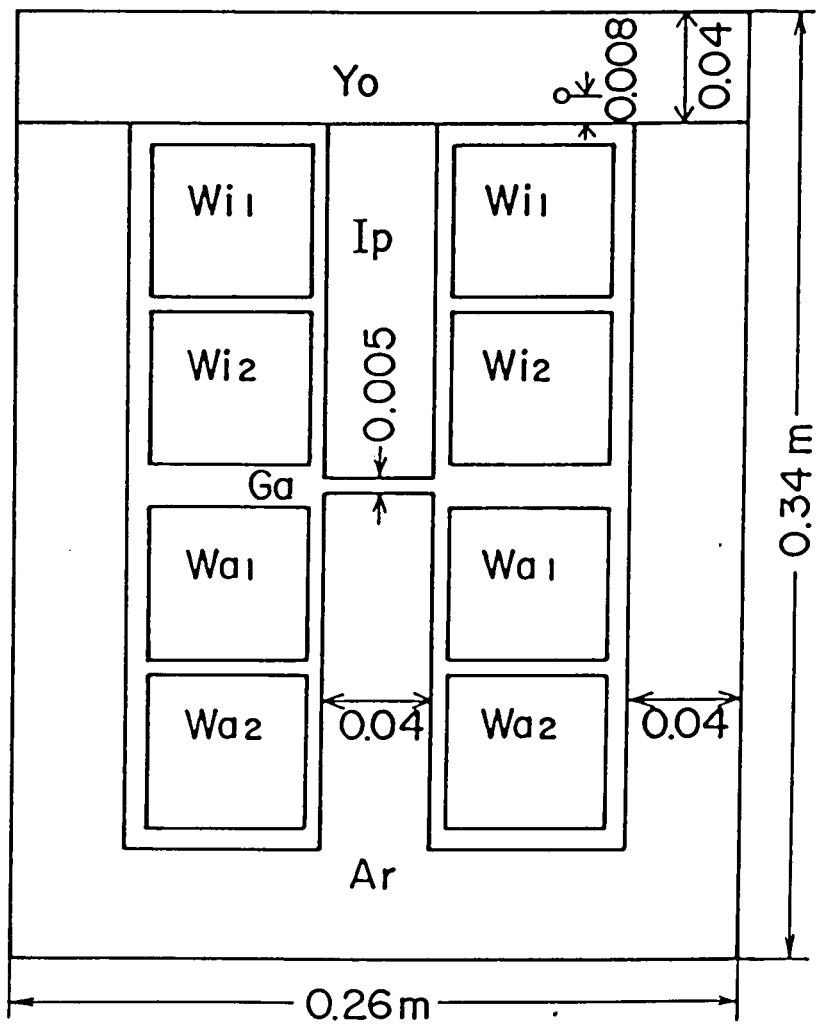

Front view.

Fig.3.4 Magnetic circuit model in experiment.

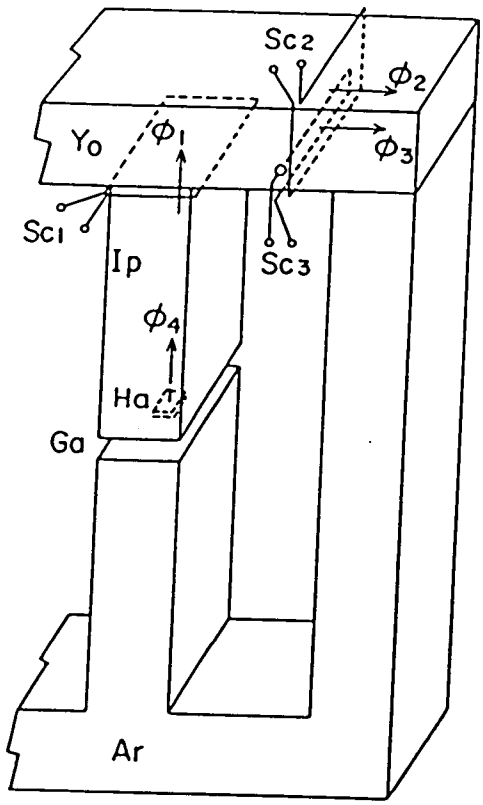

Fig.3.5 Settlement of search coils S_{c1}, S_{c2} and S_{c3} and Hall cell H_a in model.

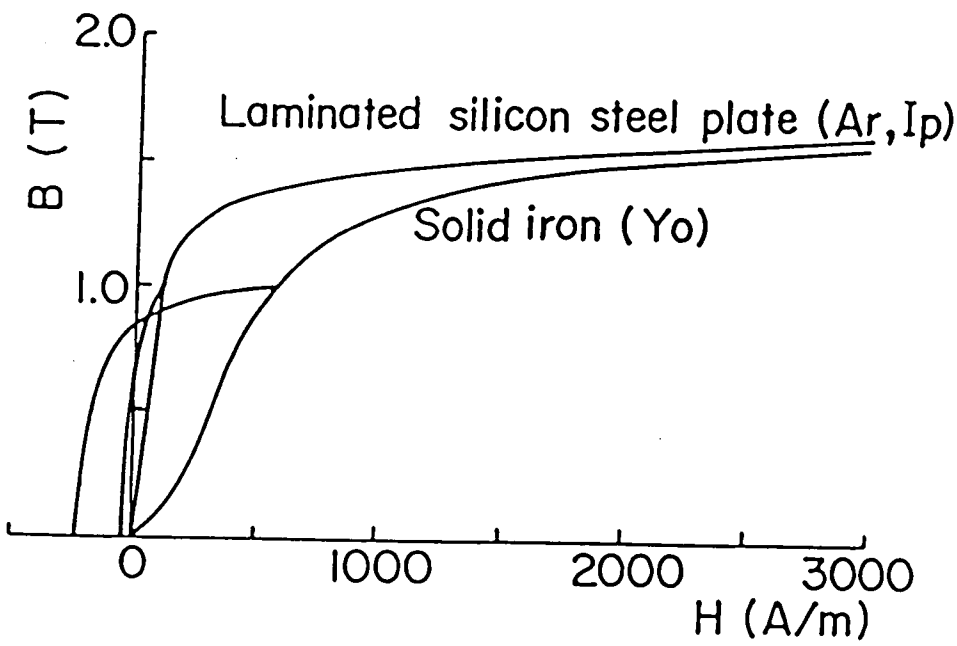

Fig.3.6 Magnetization curves.

3.3. Theoretical and Experimental Analyses

3.3.1 Experimental circuit

Figure 3.7 shows a schematic diagram of the experimental circuit, where

E : direct current source voltage,

I : supply current of W_{i1}, W_{i2} and W_{a1},

$5I$: terminal voltage of shunt resistance 5 Ω,

R : variable resistance,

S : switch.

In the circuit, an exciting current I is suddenly supplied to W_{i1}, W_{i2} and W_{a1} from E by closing S. The magnitude and the time constant of I are varied by changing E and R. Then, the transient response of fluxes Φ_1, Φ_2 and Φ_3 in S_{c1}, S_{c2} and S_{c3} are measured as follows:

$$\Phi_r=\frac{1}{N_r}\int_0^t v_r dt, \quad r=1,2,3, \tag{3.4}$$

where

v_r : induced voltage in search coil S_{cr},

$N_r=3$: number of turns of S_{cr}.

Also, the flux Φ_4 in G_a is evaluated by

$$\Phi_4=S_g B_g, \tag{3.5}$$

where

B_g : magnetic flux density measured by H_a,

$S_g=0.04\times0.1\ m^2$: cross-sectional area of airgap G_a.

The experiment must be started after the sufficient decrease of the residual magnetism in the magnetic circuit model. The measured data are processed by the personal micro-computer.

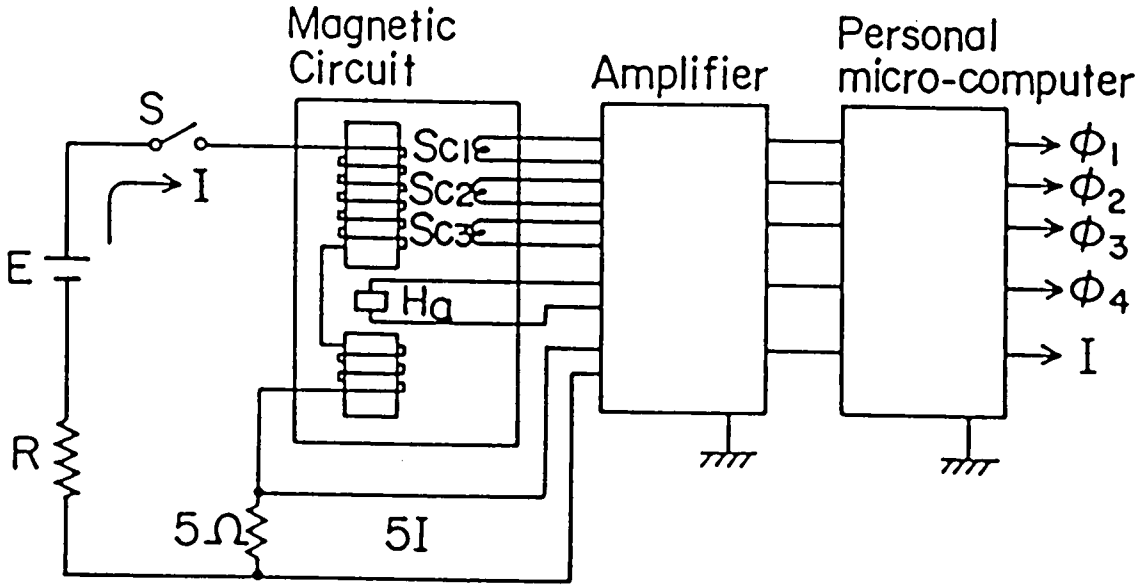

Fig.3.7 Schematic diagram of experimental circuit.

3.3.2 Assumptions for numerical calculation and boundary conditions

The transient response and distribution of the magnetic flux, the eddy current etc. in the magnetic circuit model as shown in Fig.3.4 are calculated under the following assumptions:

(1) The two-dimensional analysis is carried out in the rectangular region $OP_1P_2P_3$ as shown in Fig.3.8, where $\overline{OP_3}$ is the center line of the cross-section of our magnetic circuit, and the magnetic flux distributes symmetrically with respect to the line. In the figure, the leakage fluxes from the boundary lines $\overline{OP_1}$, $\overline{P_1P_2}$ and $\overline{P_2P_3}$ are assumed to be negligible. The rectangular region is subdivided into the many triangular elements as shown in Fig.3.9.

(2) In I_p and A_r made of laminated cores, the induced eddy current can be neglected, and so the conductivity is assumed to be zero. The conductivity $\sigma=\sigma_y$ of a solid core Y_o is assumed to be uniform, and $\sigma_y=1$ MS/m is measured.

(3) It is assumed that the current density J_s in the exciting windings W_{i1}, W_{i2} and W_{a1} is uniform and $J_s=2000\times I/(0.058\times 0.054)$ A/m^2.

(4) The reciprocal permeability $\nu=\nu_r$ in element e_r made of iron cores is calculated by the B-H curves in Fig.3.6 and Eqs. (2.40) to (2.50), as described in Article 2.3.3. Also, $\nu=\nu_r$ of the airgap and the winding conductors is assumed to be equal to that of the vacuum and is given by Eq. (2.39).

(5) Initial values of the vector potentials at all nodes are zero under the assumption that the residual magnetism is sufficiently decreased.

Next, let us consider the boundary conditions on boundary lines $\overline{OP_1}$, $\overline{P_1P_2}$ and $\overline{P_2P_3}$ in Fig.3.9. From the assumption (1), the normal component B_n on the lines vanishes. Also, we can put $B_n=0$ on the line $\overline{OP_3}$. Then, on those lines, we have $A=A_c$

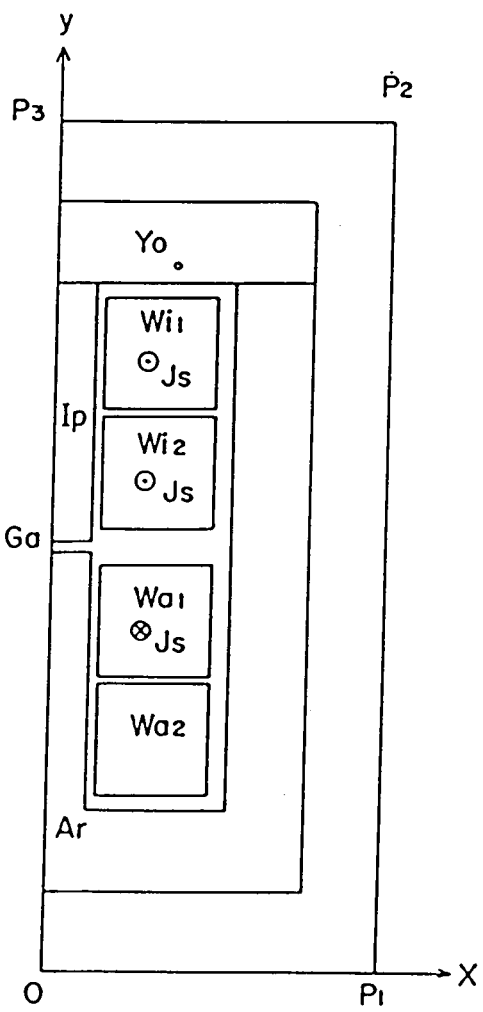

Fig.3.8 Cross-sectional view to investigate flux distribution.

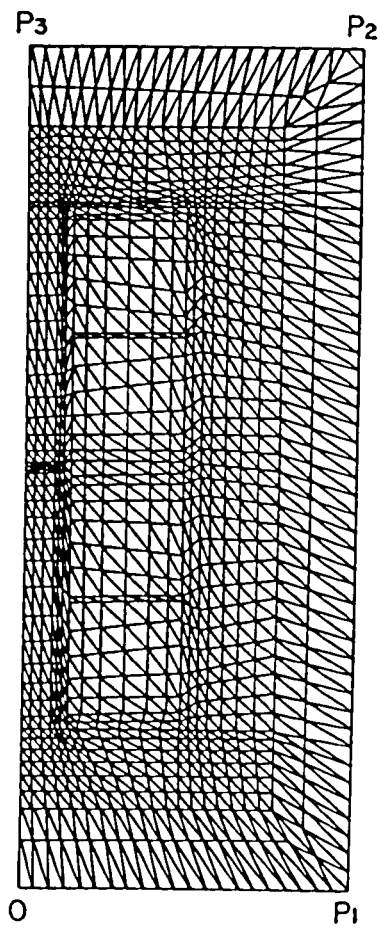

Fig.3.9 Meshes of triangles for nodal method.

which is independent of x and y. Furthermore, the additional constraint to A_c is given as follows:

$$\sigma_y \frac{\partial A_c}{\partial t}=0, \tag{3.6}$$

on the line $\overline{OP_3}$, on which the eddy current must be vanished. Accordingly, A_c becomes independent of not only x and y but also t, and so we put $A_c=0$ for simplifying the analysis.

Now, the transient value of the vector potential A_i at each node in Fig.3.9 is obtained by numerically solving the nodal equations (2.52) in Chapter 2 under the above assumptions and the boundary and initial conditions. As a result, the transient response and distribution of the magnetic flux, the eddy current etc. can be evaluated.

3.3.3 Experimental and calculated results[24], [25], [26]

The experimental results of the current I and the fluxes Φ_1 to Φ_4 are shown in Fig.3.10(a), when the switch S in Fig.3.7 is suddenly closed, where $T_m=0.051$ s is a measured time constant of I. In Fig.3.10(a), a ripple is seen in the waveform of Φ_4, which is caused by the Hall cell H_a. In Fig.10(b), the calculated results by Eqs. (2.52) and (2.21) are shown, where $I=0.5\{1-\exp(-t/T_m)\}$ A and $\sigma_y=1$ MS/m. Though the actual magnetic flux distributes in the three-dimensional space, the calculated results by our two-dimensional analysis agree fairly well with the experimental ones.

In Figs.3.10 (a) and (b), the relations $\Phi_4 \fallingdotseq \Phi_1/2$ and $\Phi_2 \fallingdotseq \Phi_1/2$ are satisfied, and these show that the flux leaks out considerably from the side surfaces of I_p but doesn't do so much from the side surfaces of Y_o. We can also see that the relation $\Phi_3 \fallingdotseq \Phi_2/2$ is satisfied in Y_o immediately after the supply of I and also this relation is be kept in the steady state where the induced eddy current vanishes. These phenomena are thought to be caused by the early eddy current induced in Y_o and the magnetic hysteresis, which are discussed more fully in the

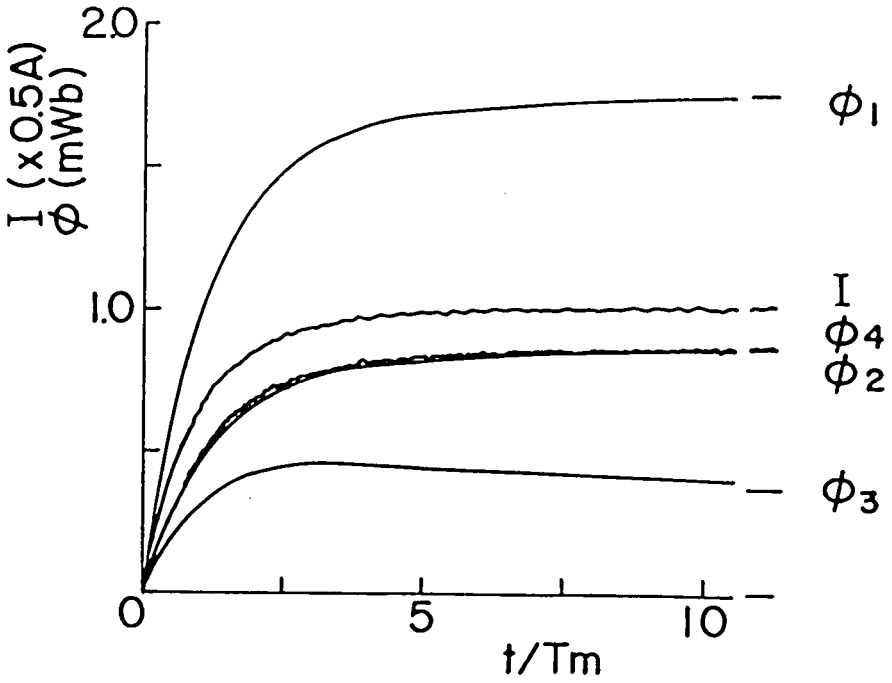

(a) Experimental results.

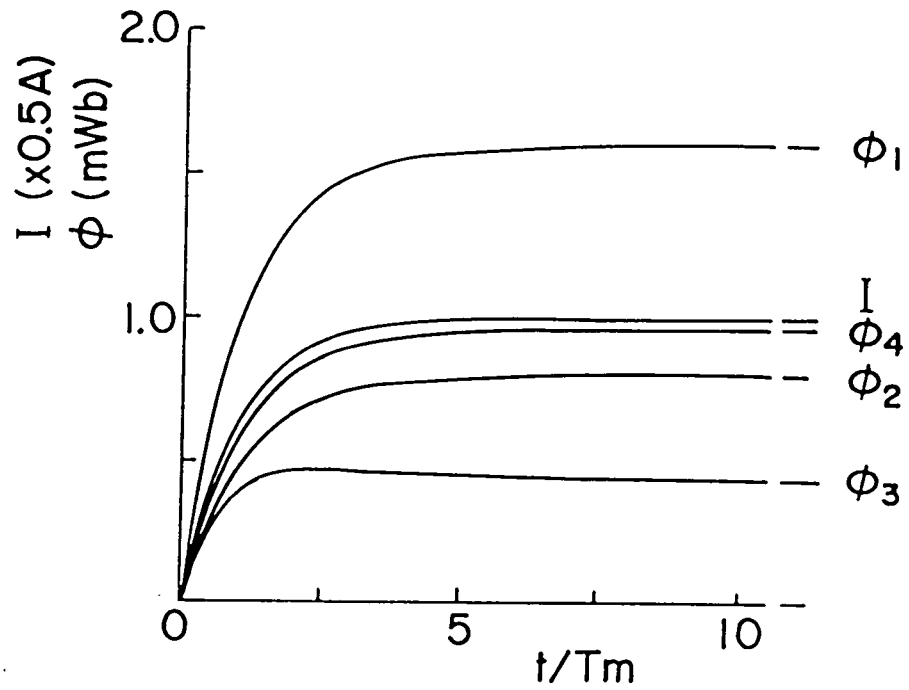

(b) Calculated results.

Fig.3.10 Transient responses of magnetic fluxes for T_s=0.051 s and σ_y=1 MS/m.

following Articles 3.3.4 and 3.3.5.

In Figs.3.11 (a) to (f), the calculated flux distributions at $t=T_m$, $2T_m$, $4T_m$, $6T_m$ and $10T_m$ and in the steady state($t\rightarrow\infty$) are shown, where ΔA_{eq} is a contour interval of A between neighbouring equi-vector-potential lines, which are flux lines. Figures 3.12 (a) to (f) show the magnetic flux density distributions corresponding to Figs.3.11 (a) to (f), respectively. We can see that the magnetic saturation is brought about in an inner skin region of Y_o. Also, the induced eddy current density distributions, which correspond to Figs.3.11 (a) to (e) are shown in Figs.3.13 (a) to (e), where the eddy current densities are calculated by Eq.(2.53) in Chapter 2. We can see that the eddy current density concentrates in an inner skin region till $t\fallingdotseq 2T_m$ and thereafter gradually decreases.

It is made clear from Figs.3.11 to 3.13 that the magnetic flux through Y_o made of a solid core inclines to be concentrated in the inner skin region of Y_o by the induced eddy current and the magnetic hysteresis. Consequently, the relations in Eqs.(3.2) are now not satisfied. Therefore, the conventional numerical calculation, in which the linear theory and the single magnetic circuit model in Fig.3.2 are used, is not useful for analysing the transient magnetic flux in the dc motor of which the yoke is made of a solid core.

Next, in Figs.3.14 (a) and (b), there are shown the experimental and calculated results of the transient response of the fluxes Φ_1 to Φ_4 for T_m=0.116 s and σ_y=1 MS/m. There is seen a fairly good agreement between both results as well as in Figs.3.10 (a) and (b). The fluxes Φ_1 to Φ_4 respond a little faster to I than those in Figs.3.10. We can also see that the ratio Φ_3/Φ_2 is somewhat lower than that in Figs.3.10, because the eddy current and the flux concentration in the inner skin region of Y_o become small.

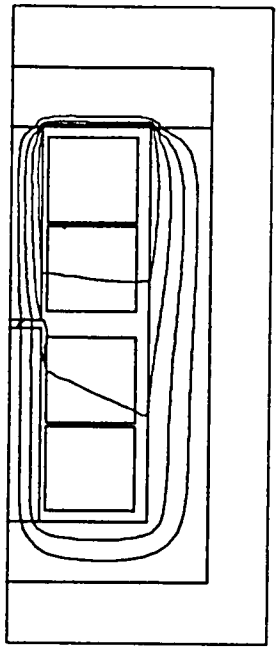

(a) $t=T_s$ and I=0.316 A.

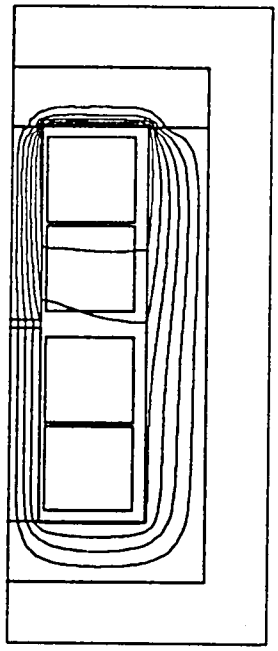

(b) $t=2T_s$ and I=0.432 A.

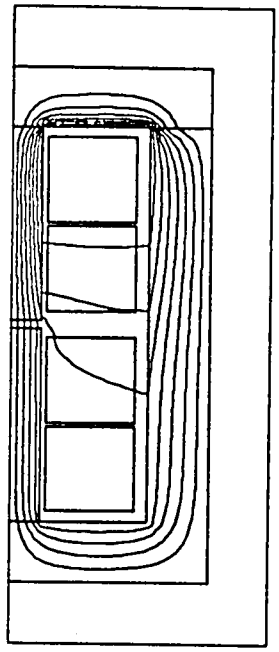

(c) $t=4T_s$ and I=0.491 A.

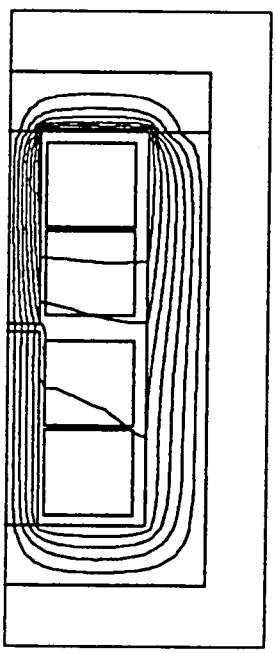

(d) $t=6T_s$ and I=0.499 A.

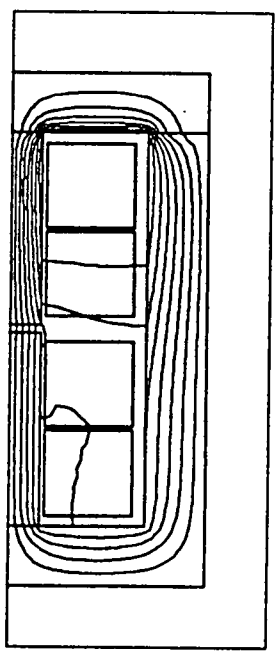

(e) $t=10T_s$ and I=0.5 A.

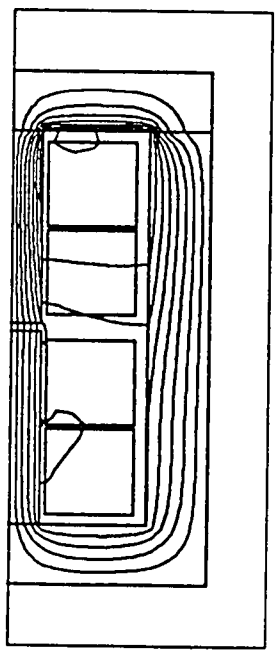

(f) $t\rightarrow\infty$ and I=0.5 A.

Fig.3.11 Magnetic flux distributions for T_s=0.051 s and σ_y=1 MS/m and ΔA_{eq}=1 mWb/m.

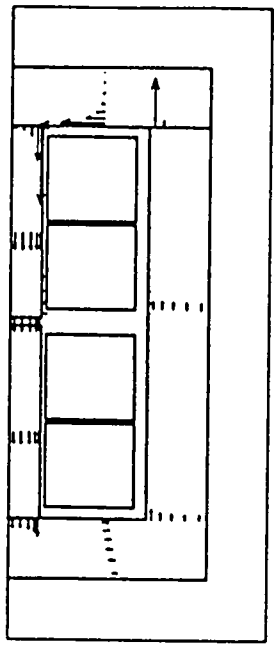

(a) $t=T_s$ and I=0.316 A.

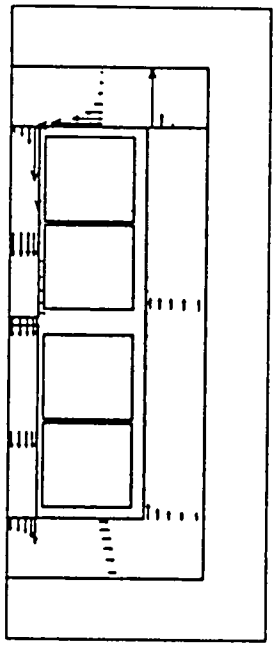

(b) $t=2T_s$ and I=0.432 A.

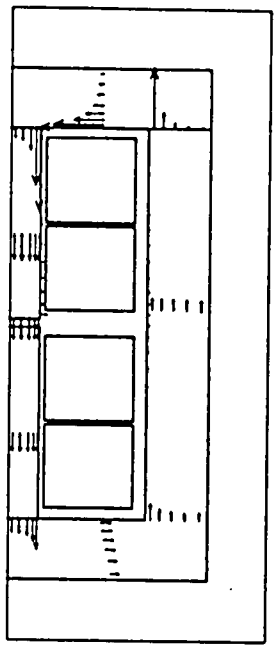

(c) $t=4T_s$ and I=0.491 A.

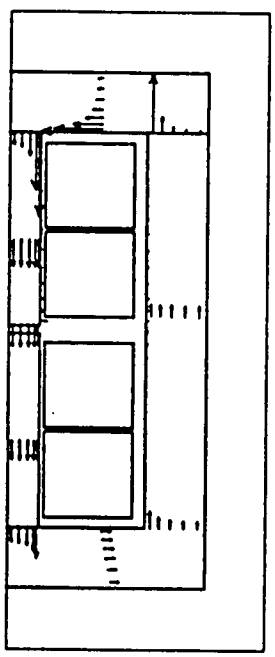

(d) $t=6T_s$ and I=0.499 A.

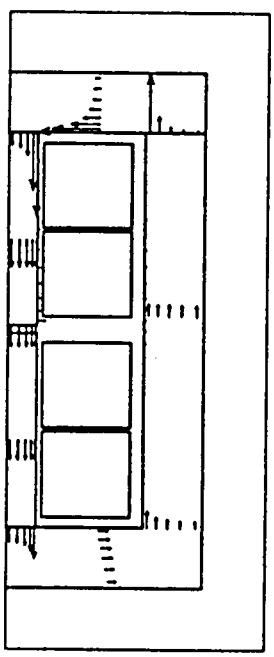

(e) $t=10T_s$ and I=0.5 A.

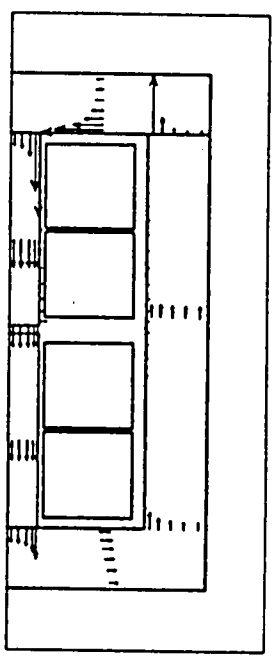

(f) $t\rightarrow\infty$ and I=0.5 A.

Fig.3.12 Magnetic flux density distributions for T_s=0.051 s and σ_y=1 MS/m.

⟶ 1.0 T

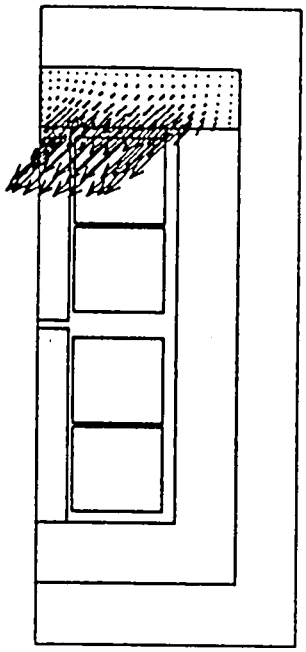

(a) $t=T_s$ and $I=0.316$ A.

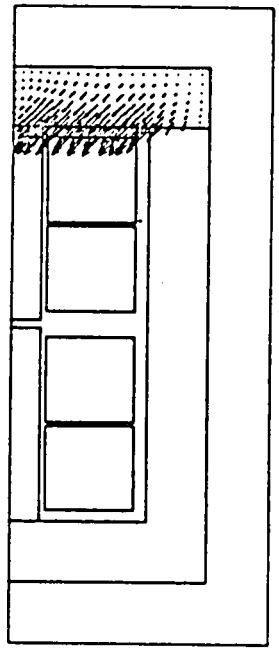

(b) $t=2T_s$ and $I=0.432$ A.

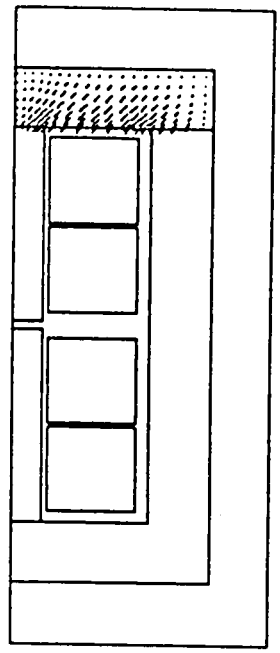

(c) $t=4T_s$ and $I=0.491$ A.

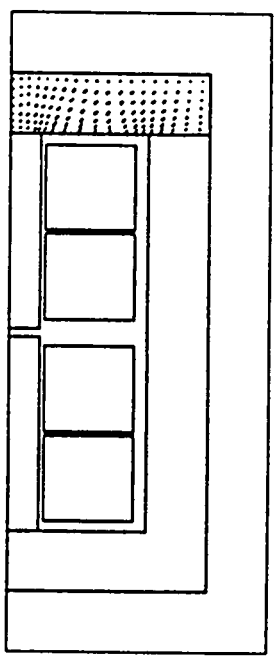

(d) $t=6T_s$ and $I=0.499$ A.

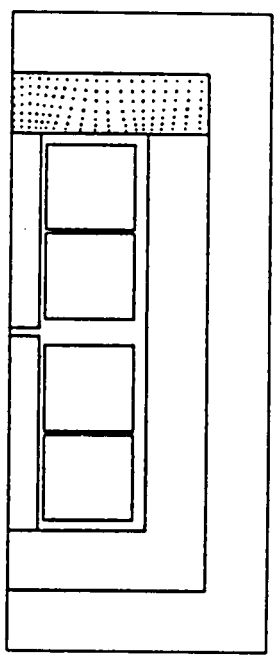

(e) $t=10T_s$ and $I=0.5$ A.

Fig.3.13 Eddy current density distributions for $T_s=0.051$ s and $\sigma_y=1$ MS/m.

⟶ 100 KA/m²

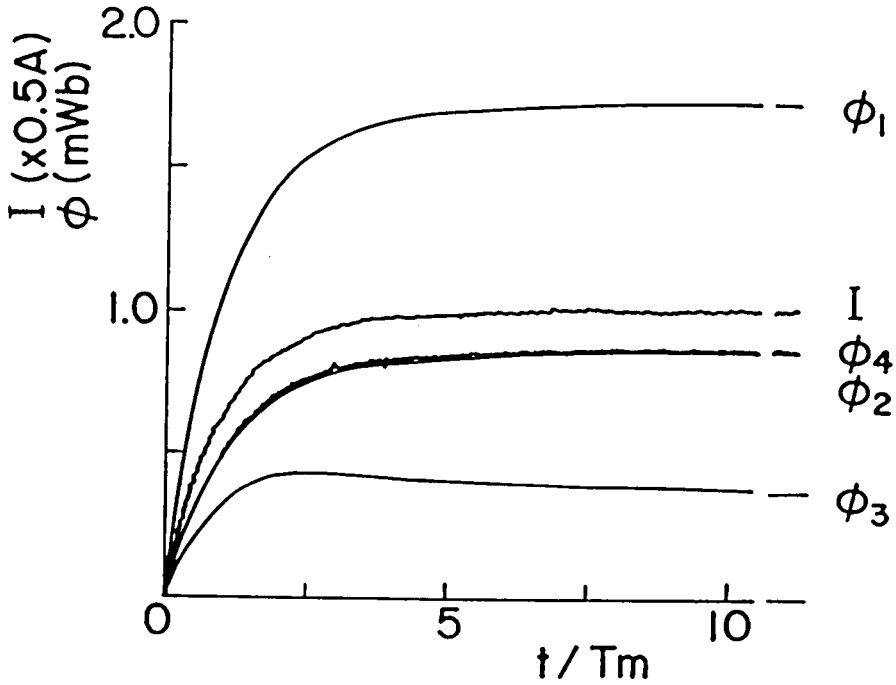

(a) Experimental results.

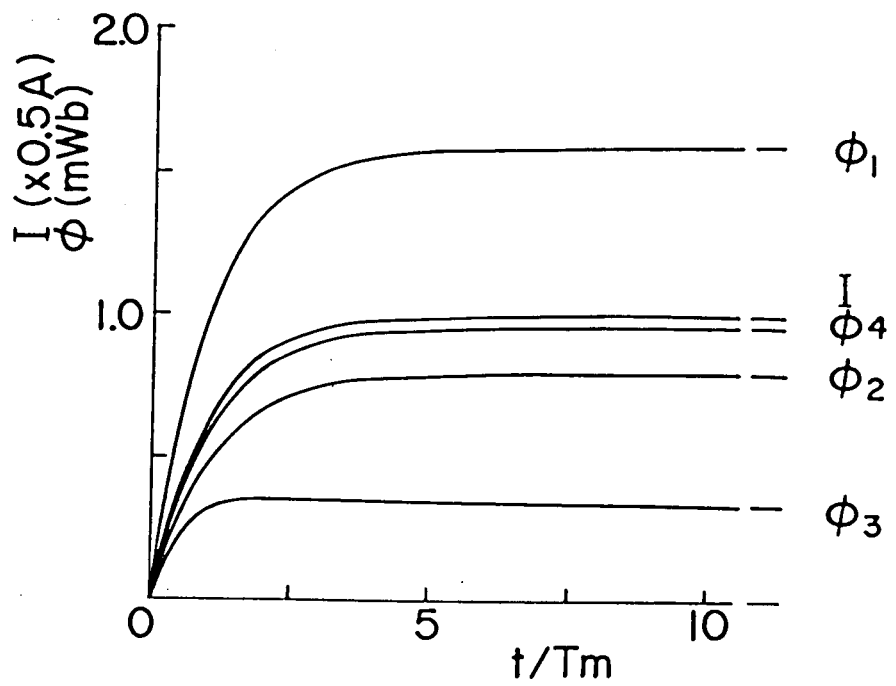

(b) Calculated results.

Fig.3.14 Transient responses of magnetic fluxes for T_a=0.116 s and σ_y=1 *MS/m*.

3.3.4 Influence of conductivity of yoke on transient responses of magnetic fluxes[24]

The calculated results of the transient responses of the magnetic fluxes for T_m=0.051 s and σ=0, 1 and 5 MS/m are plotted in Fig.3.15. We can see that the conductivity σ_y has a great influence on the flux Φ_3 through the inner skin region of Y_o.

In the case of σ_y=0, the fluxes Φ_1 to Φ_4 respond to I without delay time and also Φ_3 approaches $\Phi_2/5$ when the time t tends to infinity, because the eddy current is not induced and so the magnetic flux is apt to be uniformly distributed in Y_o as shown in Figs.3.16 (a) to (f).

In the other case of σ_y=5 MS/m, the fluxes respond most slowly to I. As shown in Figs.3.17 (a) to (f), the strong concentration of the flux occurs near the inner surface of Y_o. Also, the eddy current density distributions are shown in Figs.3.18 (a) to (e). It can be seen that the eddy current becomes about five times larger than the one for σ_y=1 MS/m in Fig.3.13 (a) to (e).

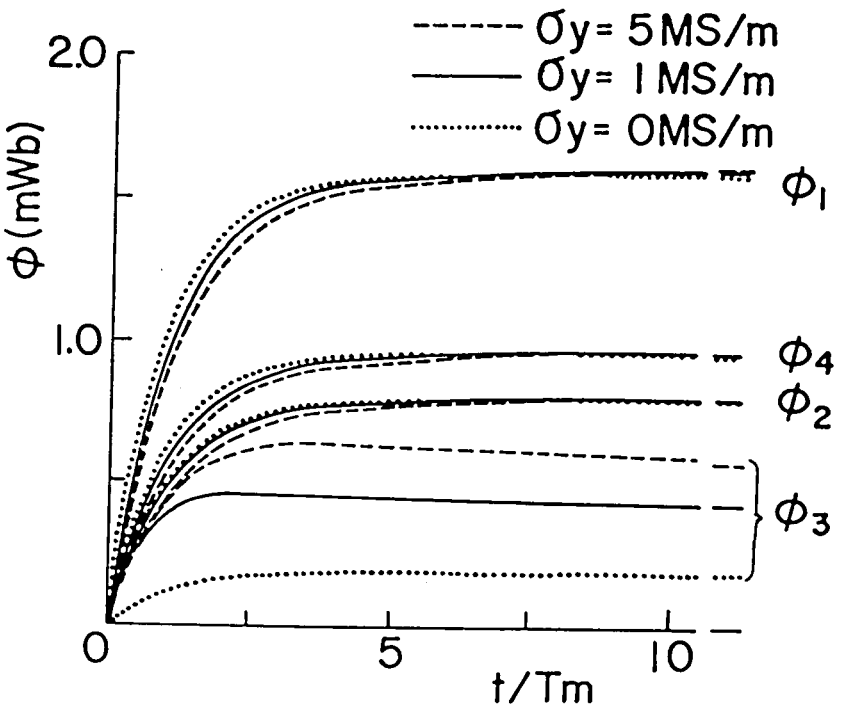

Fig.3.15 Influence of σ_y on transient responses of magnetic fluxes.

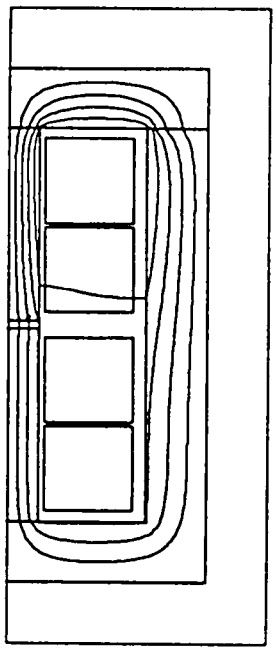

(a) $t=T_s$ and I=0.316 A.

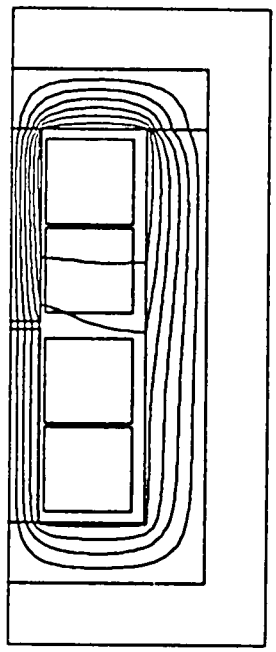

(b) $t=2T_s$ and I=0.432 A.

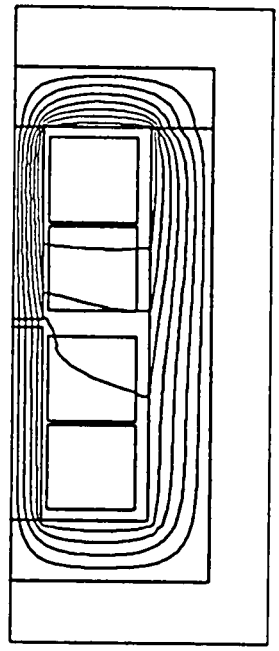

(c) $t=4T_s$ and I=0.491 A.

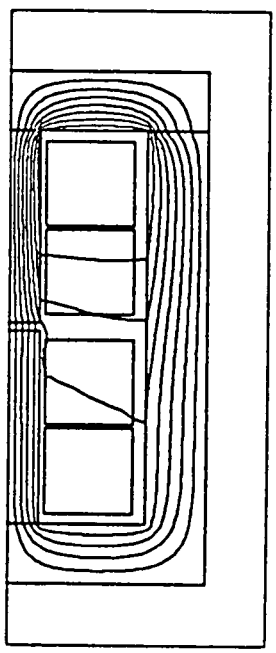

(d) $t=6T_s$ and I=0.499 A.

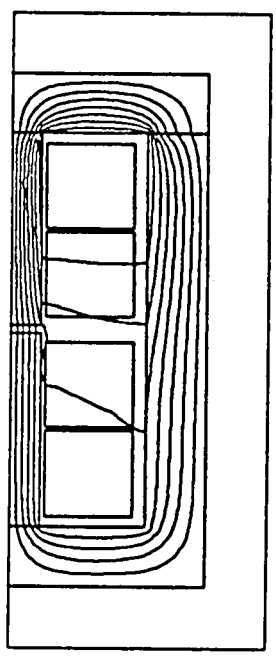

(e) $t=10T_s$ and I=0.5 A.

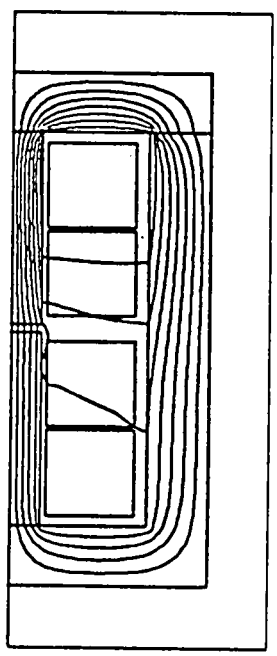

(f) $t\rightarrow\infty$ and I=0.5 A.

Fig.3.16 Magnetic flux distributions for T_s=0.051 s and σ_y=0 MS/m and ΔA_{eq}=1 mWb/m .

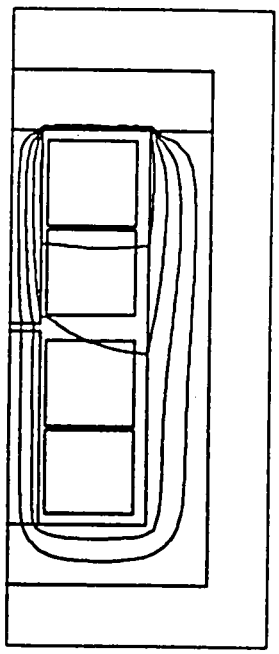

(a) $t=T_s$ and I=0.316 A.

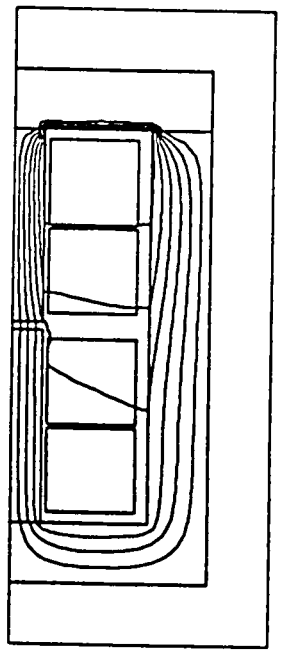

(b) $t=2T_s$ and I=0.432 A.

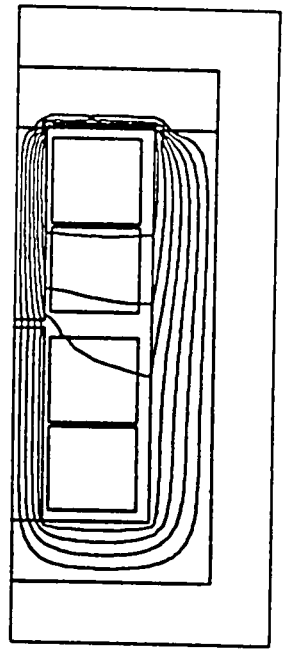

(c) $t=4T_s$ and I=0.491 A.

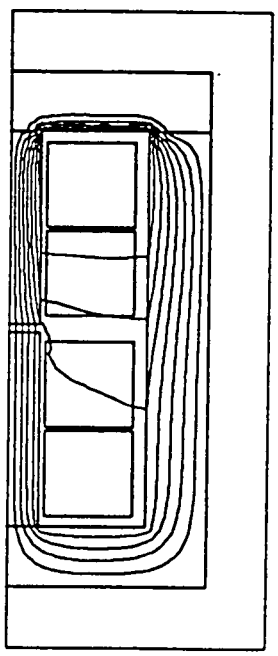

(d) $t=6T_s$ and I=0.499 A.

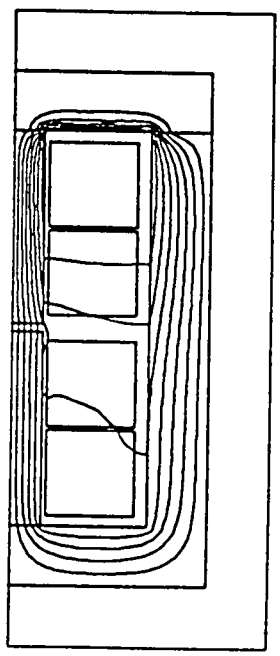

(e) $t=10T_s$ and I=0.5 A.

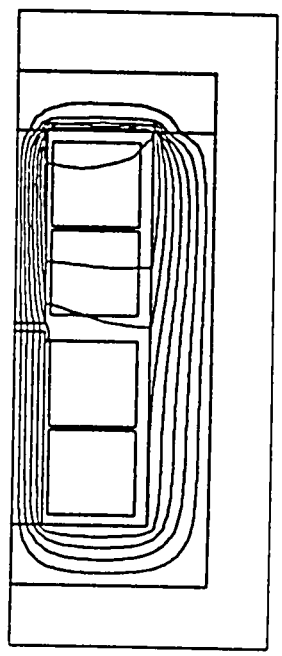

(f) $t\rightarrow\infty$ and I=0.5 A.

Fig.3.17 Magnetic flux distributions for T_s=0.051 s and σ_y=5 MS/m and ΔA_{eq}=1 mWb/m.

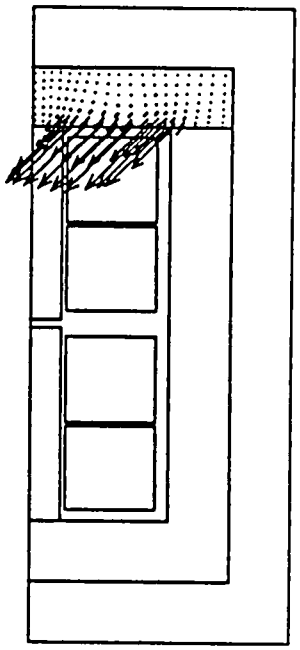

(a) $t=T_s$ and I=0.316 A.

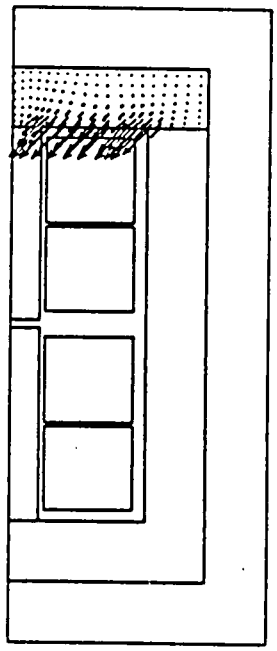

(b) $t=2T_s$ and I=0.432 A.

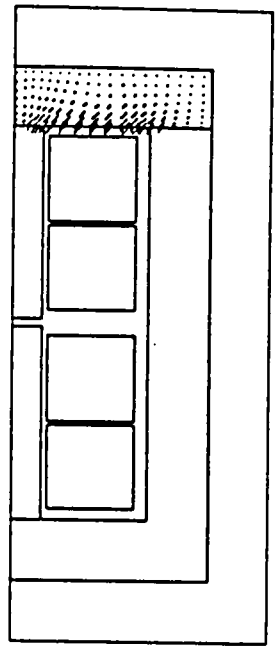

(c) $t=4T_s$ and I=0.491 A.

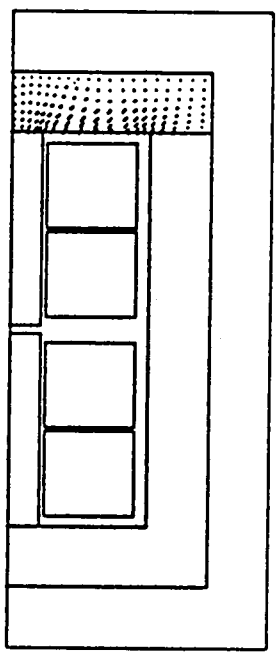

(d) $t=6T_s$ and I=0.499 A.

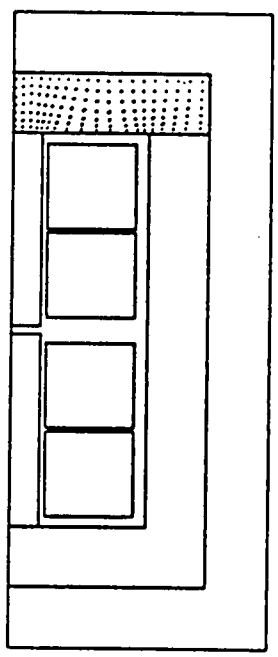

(e) $t=10T_s$ and I=0.5 A.

Fig.3.18 Eddy current density distributions for T_s=0.051 s and σ_y=5 MS/m.

⟶ 500 KA/m²

3.3.5 Influence of magnetic hysteresis on transient responses of magnetic fluxes[24], [27]

Let us make clear that the magnetic hysteresis has a large influence on the flux distribution in the solid iron yoke of the dc motor. In Fig.3.19, the transient responses of the magnetic fluxes for T_m=0.051 s and σ_y=1 MS/m are shown for two cases, namely the one where the magnetic hysteresis is taken into consideration, and the other one where it is not considered and only the magnetic saturation curve in Fig.3.6 is used for computation. We can see that the magnetic hysteresis has a large influence on only Φ_3 and not on Φ_1, Φ_2 and Φ_4. Till $t \fallingdotseq 2T_m$ when the fluxes Φ_3's in both cases pass their maximum values, Φ_3's are nearly equal to each other. In the case considering hysteresis, for $t>2T_m$, Φ_3 decreases only a little, and it agrees well with the experimental result as already shown in Figs.3.10(a) and (b). On the other hand, in the case neglecting hysteresis, Φ_3 decreases with the lapse of time and becomes $\Phi_2/5$ in the steady state, because the flux distribution in Y_o becomes gradually uniform as shown in Figs.3.20 (a) to (f).

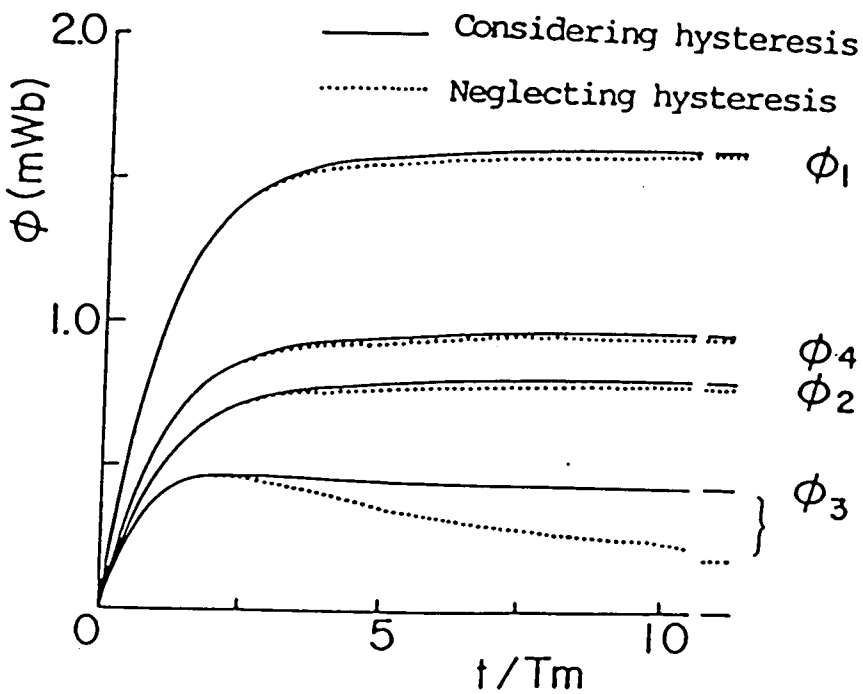

Fig.3.19 Influence of magnetic hysteresis on transient responses of magnetic fluxes.

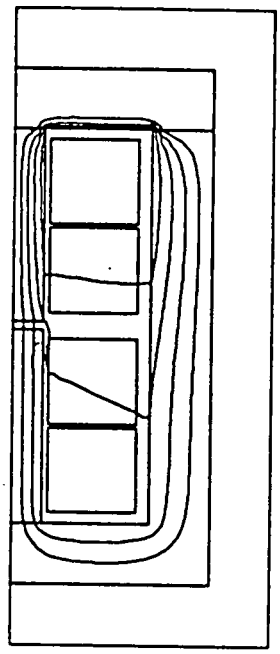

(a) $t=T_s$ and I=0.316 A.

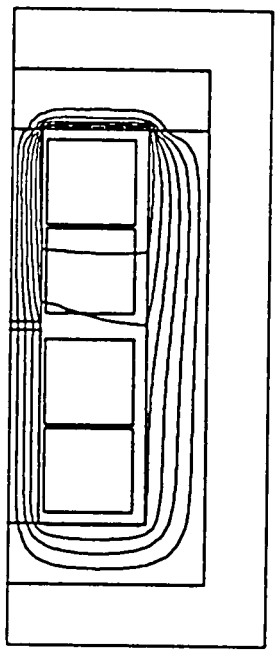

(b) $t=2T_s$ and I=0.432 A.

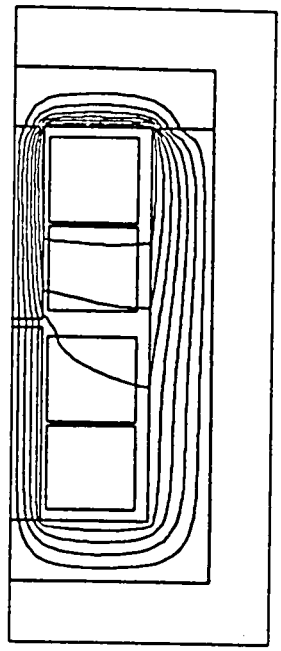

(c) $t=4T_s$ and I=0.491 A.

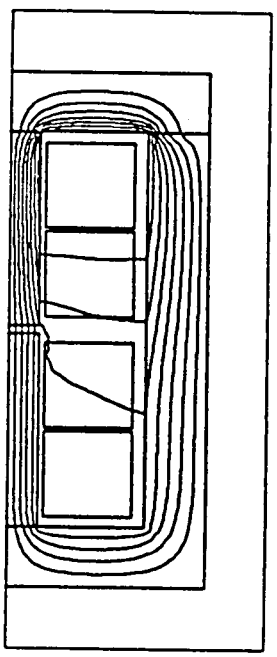

(d) $t=6T_s$ and I=0.499 A.

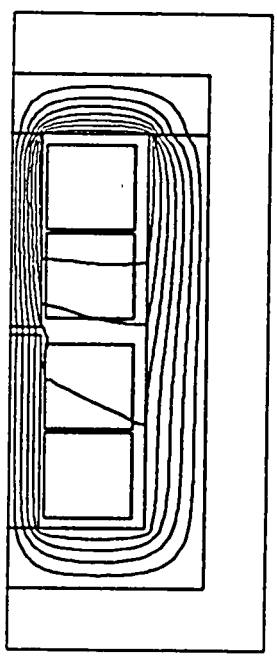

(e) $t=10T_s$ and I=0.5 A.

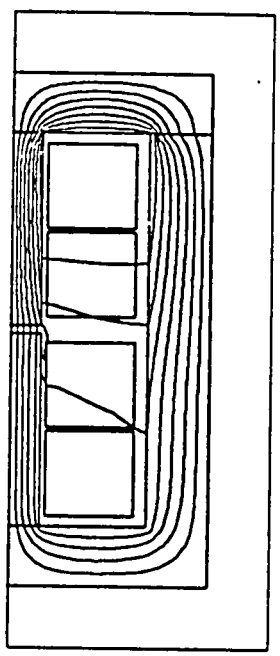

(f) $t\rightarrow\infty$ and I=0.5 A.

Fig.3.20 Magnetic flux distributions in case neglecting hysteresis for T_s=0.051 s and σ_y=1 MS/m and ΔA_{eq}=1 mWb/m .

Also, comparing Figs.3.20 with Figs.3.11, we can see that the magnetic hysteresis has little influence on the flux distrbutions in I_p and A_r of the laminated cores. Therefore, we can say that the analysis of transient responses of the magnetic fluxes can be achieved by solving the equations (2.52) under the assumption that the magnetic hysteresis can be ignored in I_p and A_r of the laminated cores.

Next, in order to decrease the calculation time needed to solve Eqs.(2.52), let us study on the cases where the magnetic hysteresis is considered only in some partial region near the inner surface of Y_o.

In Fig.3.21, the transient responses of the fluxes Φ_1 to Φ_4 are shown for T_m=0.051 s and σ_y=1 MS/m in the cases, where the hysteresis is considered only in the partial region of η=10, 15, 20 , 25 or 30 % of the cross-sectional area near the inner surface of Y_o. In the figure, there is also plotted the flux responses already shown in Fig.3.10(b), where the hysteresis is considered in I_p and A_r, too, and η=100 %. Figure 3.21 shows that the responses of Φ_1, Φ_2 and Φ_4 in all cases agree well with one another and the ones of Φ_3 for $\eta \geqq 20$ % agree well with one another, too.

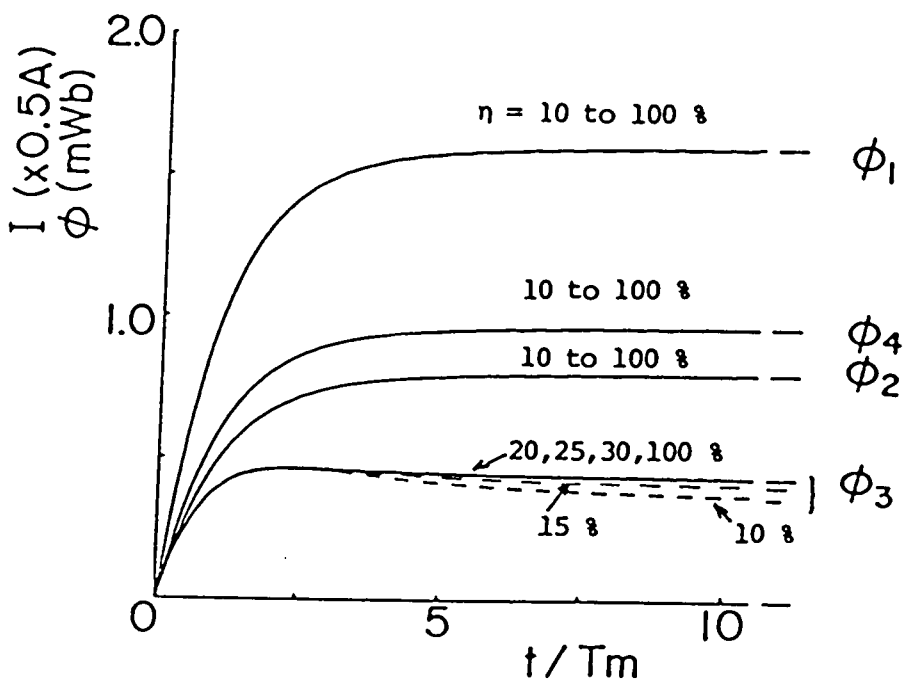

Fig.3.21 Influence of η on transient responses of magnetic fluxes.

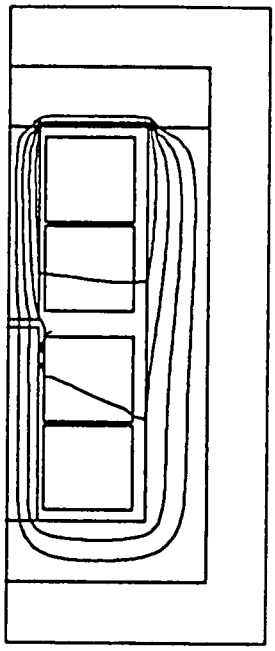

(a) $t=T_s$ and $I=0.316$ A.

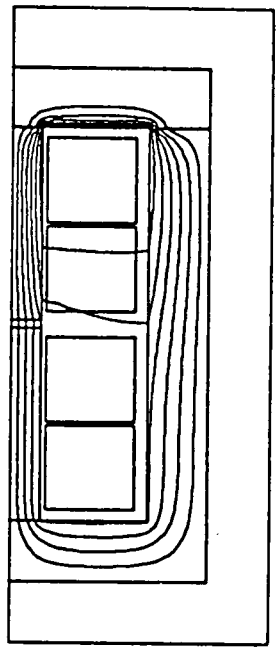

(b) $t=2T_s$ and $I=0.432$ A.

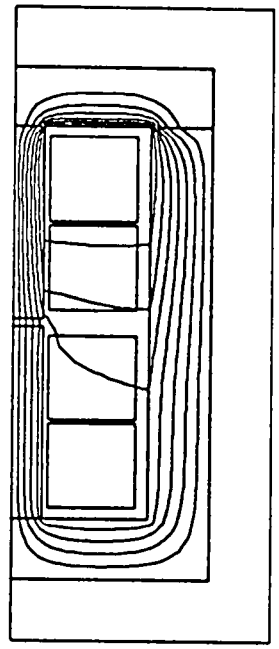

(c) $t=4T_s$ and $I=0.491$ A.

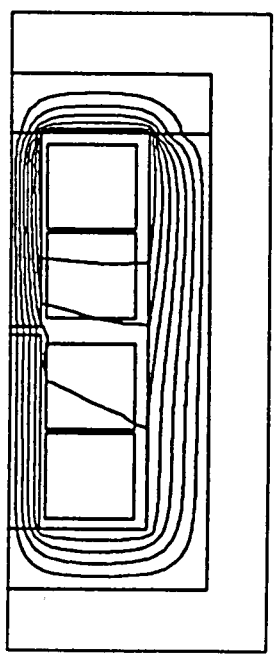

(d) $t=6T_s$ and $I=0.499$ A.

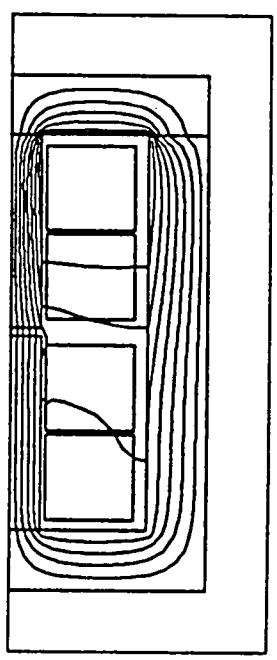

(e) $t=10T_s$ and $I=0.5$ A.

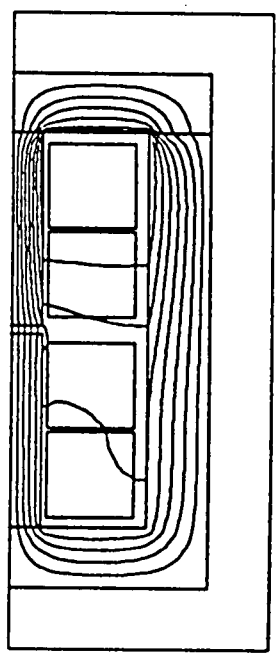

(f) $t\rightarrow\infty$ and $I=0.5$ A.

Fig.3.22 Magnetic flux distributions for $T_s=0.051$ s and $\sigma_y=1$ MS/m, $\eta=20$ % and $\Delta A_{eq}=1$ mWb/m.

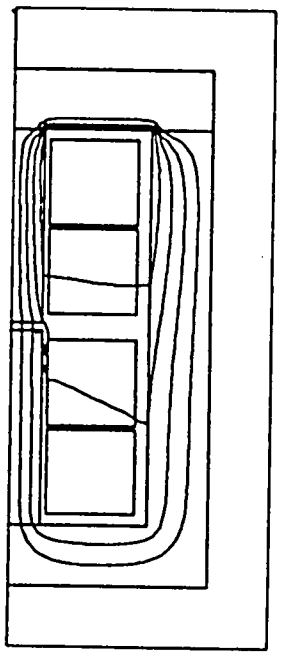

(a) $t=T_s$ and $I=0.316$ A.

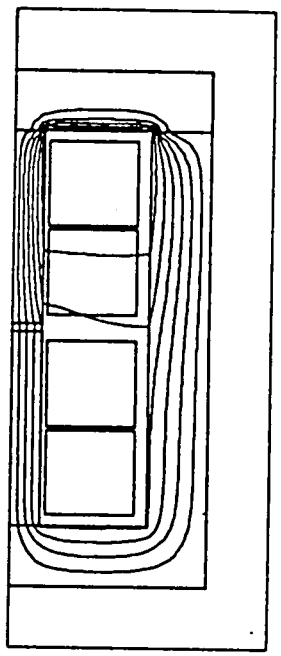

(b) $t=2T_s$ and $I=0.432$ A.

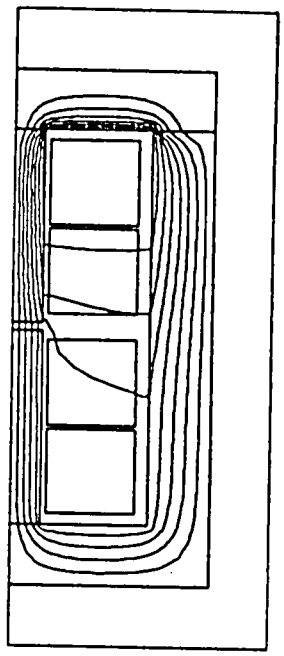

(c) $t=4T_s$ and $I=0.491$ A.

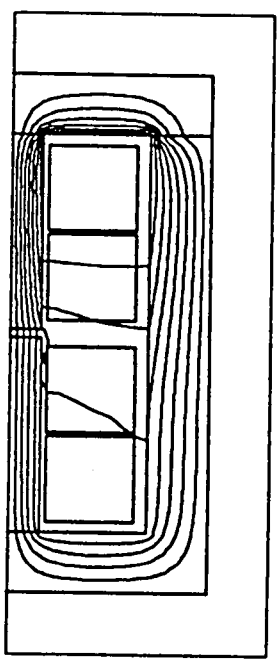

(d) $t=6T_s$ and $I=0.499$ A.

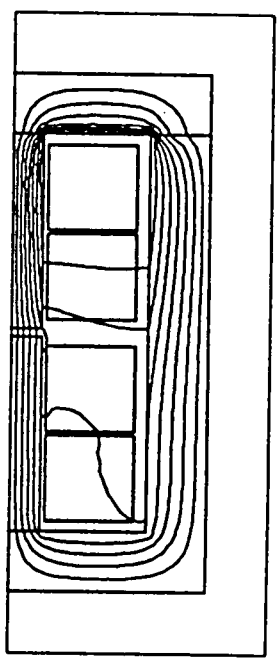

(e) $t=10T_s$ and $I=0.5$ A.

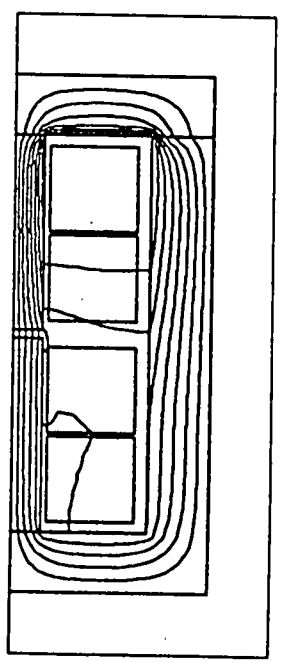

(f) $t\rightarrow\infty$ and $I=0.5$ A.

Fig.3.23 Magnetic flux distributions for $T_s=0.051$ s and $\sigma_y=1$ MS/m, $\eta=25$ % and $\Delta A_{eq}=1$ mWb/m .

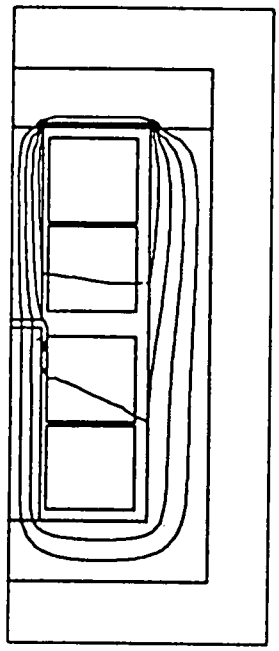

(a) $t=T_s$ and I=0.316 A.

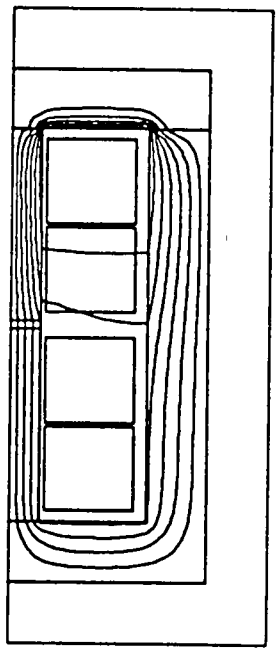

(b) $t=2T_s$ and I=0.432 A.

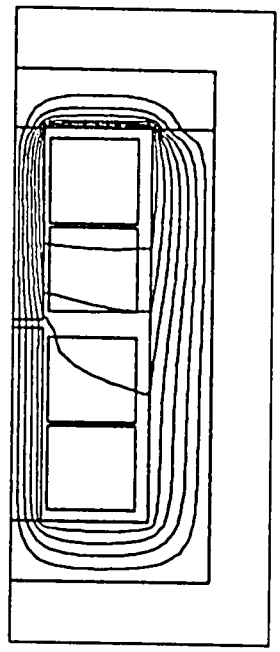

(c) $t=4T_s$ and I=0.491 A.

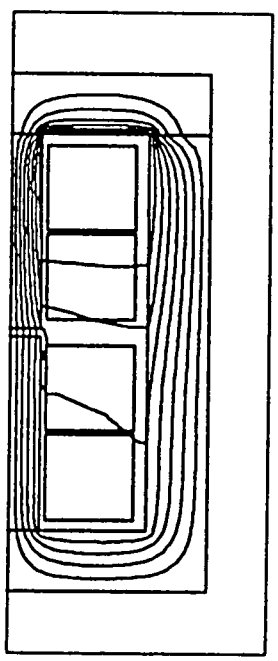

(d) $t=6T_s$ and I=0.499 A.

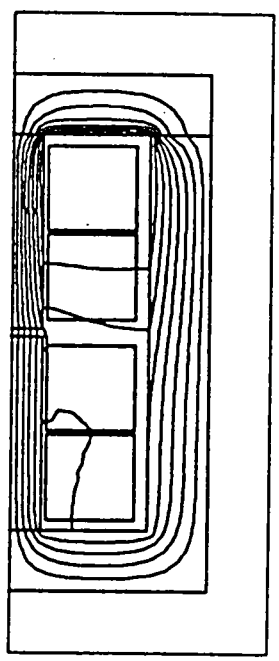

(e) $t=10T_s$ and I=0.5 A.

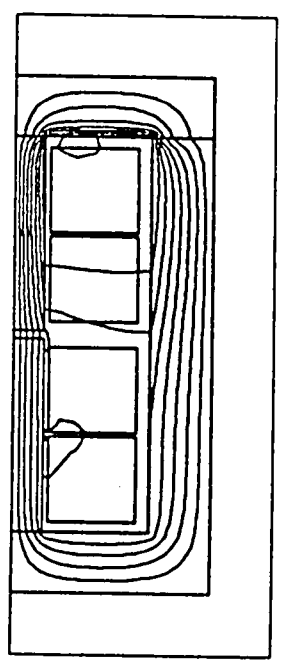

(f) $t\rightarrow\infty$ and I=0.5 A.

Fig.3.24 Magnetic flux distributions for T_s=0.051 s and σ_y=1 MS/m, η=30 % and ΔA_{eq}=1 mWb/m .

Next, let us investigate the flux distributions in the magnetic circuit for $\eta \geqq 20$ %. In Figs.3.22 to 3.24, the flux distributions are shown for η=20, 25 and 30 %, respectively. By comparing their distributions with the ones for η=100 % in Fig.3.11, it can be seen that they are in good agreement with one another at $t=T_m$ and $2T_m$. However, at $t \geqq 6T_m$ there arises in Y_0 the visible difference of the flux distributions for η=20 and 25 % from the ones for η=100 %. On the other hand, the flux distributions for η=30 % agree well with the ones for η=100 %.

Furthermore, we were able to ascertain that the magnetic flux density and the eddy current density distributions for η=30 % agree well with those for η=100 % in Figs.3.12 and 3.13, too.

Consequently, the sufficiently accurate analysis of the magnetic flux can be achieved by considering the magnetic hysteresis in the limited inner region of about 30 % of Y_0. This makes it possible to decrease in large degree calculation time required for solving Eqs.(2.52).

3.4 Conclusion

The main results obtained by the above numerical calculation and experiment are as follows:

(1) The author introduced a new equivalent magnetic circuit model, by which the transient responses of the magnetic fluxes in the usual small-sized dc motor containing the solid iron yoke can be analysed, that can't be done by the conventional model.

(2) From the experimental results by the new magnetic circuit model, it was made clear that the responses of the magnetic fluxes in the interpole airgap, the interpole core and the yoke are delayed for the change of the armature current. Also, it was ascertained that the considerable magnetic flux leaks out from the sides of an interpole core and the magnetic flux in the yoke concentrates in the inner skin region. It can't be obtained by the conventional magnetic circuit model.

(3) The validity of author's two-dimensional nodal method for numerical calculation described in Chapter 2 was ascertained by showing that the calculated results of the transient responses of the magnetic fluxes agree well with the experimental ones.

(4) From the calculated distributions of the magnetic flux, the magnetic flux density and the eddy current density, the author made clear that the magnetic flux and the eddy current concentrate in an inner skin region of the yoke for an initial duration after the supply of the exciting armature current, and also that the concentrated magnetic flux, which brings about the magnetic saturation near the inner surface of the yoke, is kept its magnitude for a long time by the magnetic hysteresis.

(5) It was made clear that the conductivity of the yoke has a great influence on the transient response of the magnetic flux, the flux distribution and the eddy current density in the yoke.

(6) It was shown that the magnetic hysteresis has a large influence on the flux distribution near the inner surface of the yoke, but has little influence on the ones in the interpole and the armature.

(7) We made it possible to decrease in large degree calculation time needed to solve the equations (2.52) for analysing the transient flux responses by considering the magnetic hysteresis in the limited inner region of about 30 % of the yoke.

CHAPTER 4

TRANSIENT BEHAVIORS OF MAGNETIC FLUXES IN DC MOTOR

4.1 Introduction

The approximate analyses by using the magnetic circuit model are very useful for a rough evaluation of the transient commutation characteristic of the dc motor. However, in order to get more practical and accurate evaluation, it is necessary to analyse accurately the transient response and distribution of the magnetic flux in consideration of the actual complex configuration of the motor, such as arrangement of the armature coils, shapes of armature slots, interpoles, main poles, etc.. In this connection, the two-dimensional investigation of the flux distribution in the motor, which is driven by a constant armature current, was already carried out by Erdely, Fuch, et al..[8],[9] They used the finite difference method for numerical calculation of the flux distribution in the complex cross-section of the motor. However, up to now, the transient flux distribution was little investigated, although it is necessary to clarify the transient commutation and the speed-torque characteristics of the dc motor.

In this chapter, there is first introduced the theoretical commutation equations to clarify close relations between the commutating flux in a commutating zone in the interpole airgap and the commutation characteristics. Then, by using a small-sized dc motor, the author experimentally confirms that the initial delay of the transient response of the commutating flux density to the abrupt change of the armature current deteriorates the transient commutation characteristics.

Next, through the experimental and the calculated results of the transient responses of the flux density in the interpole airgap and the fluxes in the interpole core and the yoke, it is shown that the above flux density and the fluxes

delay to the change of the armature current by the eddy currents induced in the yoke and the interpole liners. Also, the calculated distributions of the magnetic flux and the eddy current density present that the much magnetic flux and the large eddy current density concentrate in the inner skin region of the yoke and they delay the flux response in not only the yoke but also the interpole airgaps and cores. Furthermore, it is shown that the magnetic saturation and the magnetic hysteresis in the inner skin region of the yoke have considerable influences on the transient responses and distributions of the magnetic fluxes.

Finally, the effect of lamination of the region near the inner surface of the yoke on improvement of the transient responses of the fluxes is quantitatively investigated by the numerical analysis.

4.2 DC Motor for Experiment

For the experimental and theoretical analyses of the commutation characteristic and the magnetic flux distribution of a dc motor in the case where the armature current changes abruptly, the author made the small-sized dc motor specified as shown in Table 4.1

Next, the cross-sectional view perpendicular to an axial direction of this motor is shown in Fig.4.1, where

A_r and Y_o : armature and yoke cores,

I_{p1}, I_{p2}, I_{p3} and I_{p4} : interpole cores

M_{p1}, M_{p2}, M_{p3} and M_{p4} : main pole cores,

I_a : armature current equal to interpole exciting current,

$I_a/2$: armature coil current,

I_f : main pole exciting current,

B_{mg1}, B_{mg2}, B_{ig1}, B_{ig2} and B_{as} : magnetic flux densities in main pole airgap, interpole airgap and armature slot, respectively,

H_{a1}, H_{a2}, H_{a3}, H_{a4} and H_{a5} : GaAs Hall cells to measure above flux densities,

Table 4.1 Specification of supplied dc motor

Rating			
Power	: 3kw	Speed	: 1800rpm
Terminal voltage	: 220V	Number of poles	: 4
Armature current	: 16A	Field excitation	: external excitation

Armature			
Type of winding	: wave	Number of parallel circuits	: 2
Number of coils	: 75	Number of slots	: 25
Number of turns of coil	: Nc=5	Number of conductors/slot	: 30
Outside diameter of core	: Da=170mm	Inside diameter of core	: 60mm
Axial length of core	: la=90mm	Cross-sectional area of conductor	: 28.3mm^2
Material of core : silicon steel plate of thikness 0.5mm			

Brush and Commutator			
Number of brushes	: 4	Number of commutator segments	: 75
Width of brush	: 12mm	Width of segment	: 4mm
Axial length of brush	: 25mm	Width of insulating mica	: 0.4mm
Outside diameter of commutator	: 110mm		

Main Pole			
Number of turns of coil/pole	: 1000	Height of core	: 66mm
Width of core	: 50mm	Height of liner	: 1mm
Axial length of core	: lm=90mm	Ratio of pole arc	: 67%
Airgap under center of pole	: 3mm	Cross-sectional area of conductor	: 3.14mm^2
Material of core : cast iron plate of thickness 1mm			

Interpole			
Number of turns of coil/pole	: 70	Number of turns of auxiliary coil/pole	: 10
Width of core	: 18mm	Axial length of core	: li=80mm
Height of core	: 62.5mm	Hight of liner	: 2.5mm
Airgap under center of interpole	: 3.5mm	Cross-sectional area of conductor	: 28.3mm^2
Material of core : silicon steel plate of thickness 0.5mm			

Yoke			
Outside diameter	: 347mm	Inside diameter	: 312mm
Axial length	: ly=225mm	Thickness	: ty=17.5mm
Material of yoke	: solid cast iron		

Search coils	GaAs Hall cells
Sc1, Sc2 : yoke	Ha1, Ha2 : airgap under center of main pole
Sc3, Sc4 : interpole core	Ha3, Ha4 : airgap under center of interpole
Number of turns of Sc1 to Sc4 :4	Ha5 : armature slot
C1, C2, C3 : armature coil	Hall voltage : 1.55 V/T

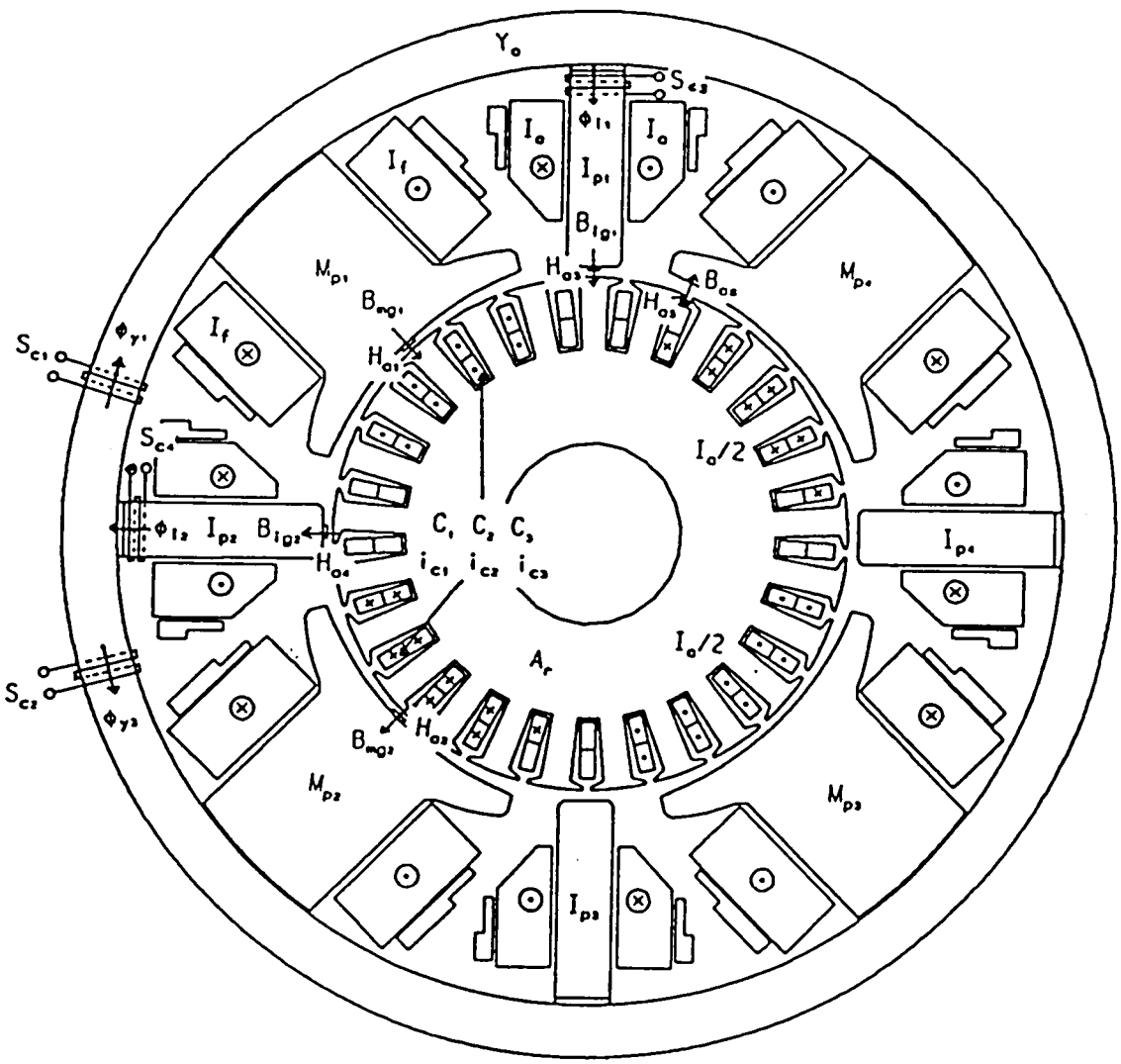

Fig.4.1 Cross-sectional view of supplied dc motor.

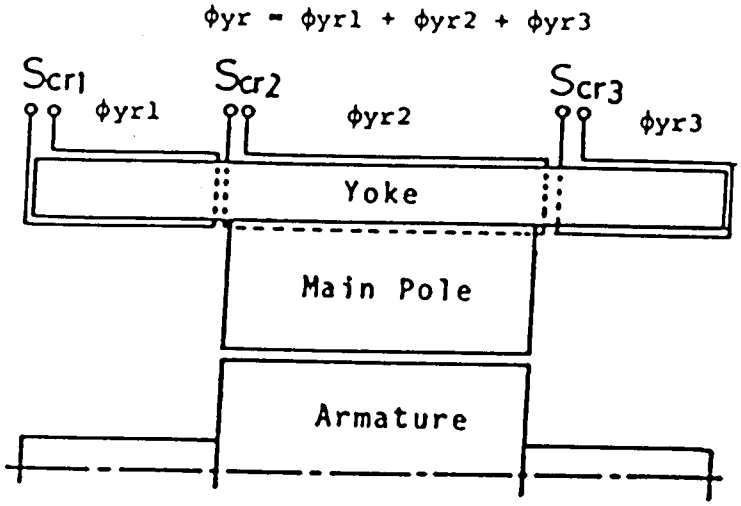

Fig.4.2 Subdivision of search coil S_{cr} (r=1 and 2) due to axial expansion of yoke flux.

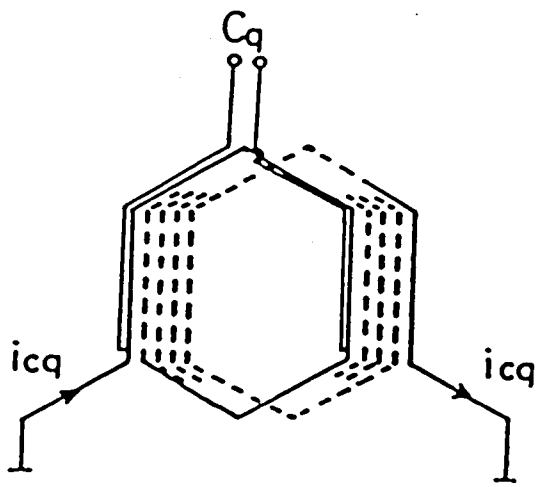

Fig.4.3 Settlement of search coil C_q (q=1, 2 and 3) on armature coil.

i_{c1}, i_{c2} and i_{c3} : currents in three coils of which sides are placed in top of one slot and bottom of another slot,

C_1, C_2 and C_3 : search coils to measure i_{c1}, i_{c2} and i_{c3}, respectively,

Φ_{y1}, Φ_{y2}, Φ_{i1} and Φ_{i2} : magnetic fluxes through yoke and interpole cores neighbouring yoke,

S_{c1}, S_{c2}, S_{c3} and S_{c4} : search coils to measure Φ_{y1}, Φ_{y2}, Φ_{i1} and Φ_{i2}, respectively.

Here, the fluxes Φ_{y1} to Φ_{i2} are obtained by integrating the electromotive force(emf) induced in the respective search coils S_{c1} to S_{c4}. In this connection, we must think of the axial expansion of Φ_{y1} and Φ_{y2}, because the axial length l_y of Y_o is 2.5 times as long as the ones l_a and l_m of A_r and M_{p1} to M_{p4}. Then, Φ_{y1} and Φ_{y2} in Fig.4.1 are measured by using S_{cr} (r=1 and 2) which are divided into S_{cr1}, S_{cr2} and S_{cr3} as shown in Fig.4.2, where

$\Phi_{yr}=\Phi_{yr1}+\Phi_{yr2}+\Phi_{yr3}$, r=1,2 : flux through S_{cr} in Fig.4.1,

Φ_{yr1}, Φ_{yr2} and Φ_{yr3} : fluxes through divided coils S_{cr1}, S_{cr2} and S_{cr3}.

Moreover, the armature coil currents i_{c1}, i_{c2} and i_{c3} are obtained by measuring the respective ohmic voltage drops by C_1, C_2 and C_3 which are set on the armature coil as shown in Fig.4.3.

4.3 Commutation Characteristics

Commutation characteristics are the most important ones for the dc motor as well as the speed-torque one. So, we first describe the commutation mechanism in the dc motor. Especially, we touch upon the relation between the magnetic flux or its density in an interpole airgap and the commutation characteristics. Next, we try to do an experiment on the transient commutation characteristic by using the dc motor specified as shown in Table 4.1 and Figs.4.1 to 4.3.

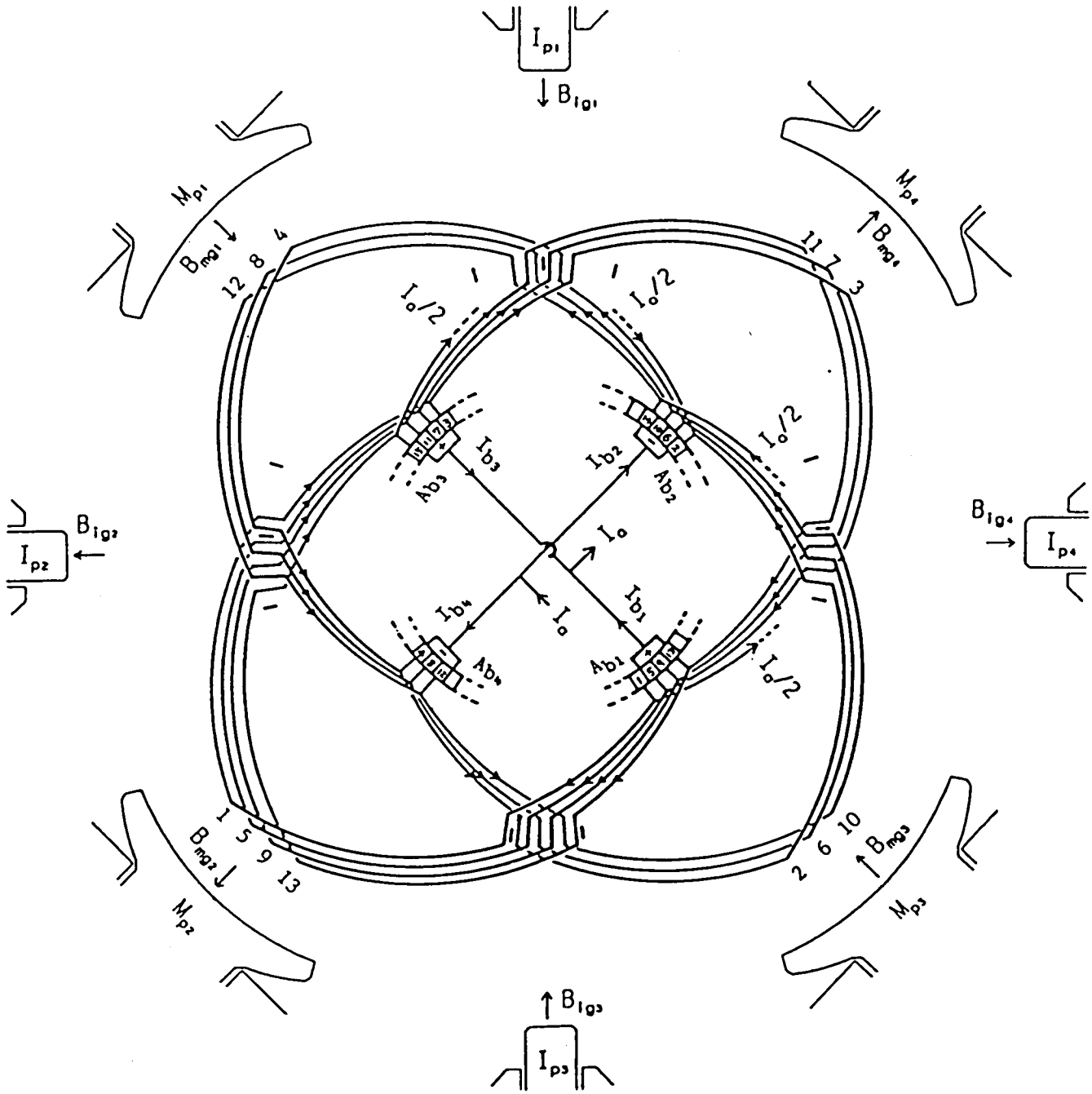

Fig.4.4 Armature coils short-circuited by brushes and commutator segment.

4.3.1 Commutation mechanism

When an armature slot passes the interpole airgap, which is called the commutating zone, the armature coils in the slot may be short-circuited by the brushes and the commutator segments. Then, the directions of the coil currents are reversed during a short-circuited period which is called the commutating period. This mechanism is well known as the commutation one.[1],[7],[28]

In our dc motor introduced in the preceding section 4.2, the 13 coils out of 75 are short-circuited at the same time as shown in Fig.4.4, where

A_{b1}, A_{b2}, A_{b3} and A_{b4} : brushes,

I_{b1}, I_{b2}, I_{b3} and I_{b4} : direct currents in above brushes,

B_{igk} , k=1,2,3,4 : airgap flux density of I_{pk} ,

$B_{\blacksquare gk}$, k=1,2,3,4 : airgap flux density of M_{pk} .

In the figure, the numbers of 1 to 13 are assigned to the short-circuited coils, and the ones of 1 to 15 to the commutator segments, which are connected with the coils. Also, the directions of currents are shown by the arrows.

Now, we can find an electric circuit equation for each short-circuited coil in Fig.4.4. For example, the equation for coil 1 is found by the circuit of A_{b1} -segment 1 -coil sides in airgaps of I_{p3} and I_{p2} -segment 3 -A_{b3} -A_{b1}. Ultimately, when the dc motor is driven in the steady state and I_a is constant, we can obtain the following equations for the 1-st to the 13-th short-circuited armature coil currents i_1 to i_{13} :

$$N_c l_a u \begin{bmatrix} B_{i3,1}+B_{i2,1} \\ B_{i4,2}+B_{i3,2} \\ B_{i1,3}+B_{i4,3} \\ B_{i2,4}+B_{i1,4} \\ \cdot \\ \cdot \\ B_{i3,13}+B_{i2,13} \end{bmatrix} = \begin{bmatrix} L_{1,1} & L_{1,2} & L_{1,3} & . & . & L_{1,13} \\ L_{2,1} & L_{2,2} & L_{2,3} & . & . & L_{2,13} \\ L_{3,1} & L_{3,2} & L_{3,3} & . & . & L_{3,13} \\ L_{4,1} & L_{4,2} & L_{4,3} & . & . & L_{4,13} \\ . & . & . & . & . & . \\ . & . & . & . & . & . \\ L_{13,1} & L_{13,2} & L_{13,3} & . & . & L_{13,13} \end{bmatrix} \frac{d}{dt} \begin{bmatrix} i_1 \\ i_2 \\ i_3 \\ i_4 \\ . \\ . \\ i_{13} \end{bmatrix}$$

$$+R_c\begin{bmatrix} i_1 \\ i_2 \\ i_3 \\ i_4 \\ \cdot \\ \cdot \\ i_{13} \end{bmatrix} +R_b\begin{bmatrix} I_{b3}-I_{b1} \\ I_{b2}-I_{b4} \\ I_{b1}-I_{b3} \\ I_{b4}-I_{b2} \\ \cdot \\ \cdot \\ I_{b3}-I_{b1} \end{bmatrix} +\begin{bmatrix} V_{s1}-V_{s3} \\ V_{s2}-V_{s4} \\ V_{s3}-V_{s5} \\ V_{s4}-V_{s6} \\ \cdot \\ \cdot \\ V_{s13}-V_{s15} \end{bmatrix} . \qquad (4.1)$$

In the equations,

$B_{ik,r}$: airgap flux density of I_{pk} , which links to coil r,

$N_c l_a u B_{ik,r}$: speed emf induced in one coil side of short-circuited coil r,

N_c=5 : number of turns of armature coil,

l_a=90 mm : axial length of armature core,

u : peripheral velocity of armature surface,

$L_{r,r}$: self-inductance of coil r,

$L_{r,p}$: mutual-inductance between coils r and p,

R_b : resistance of brush,

R_c : resistance of armature coil,

V_{sq} : contact voltage between segment q and brush,

k=1,2,3,4 : interpole number,

q=1,2,....,15 : commutator segment number,

r and p =1,2,....,13 : coil number.

Also, from Fig.4.4 we can derive the following additional equations for the brush currents I_{b1} to I_{b4}

$$\left.\begin{aligned} I_{b1} &= -I_a/2-i_1+i_3-i_5+i_7-i_9+i_{11}-i_{13}, \\ I_{b2} &= I_a/2-i_2+i_4-i_6+i_8-i_{10}-I_a/2-i_{12}, \\ I_{b3} &= I_a-I_{b1}, \\ I_{b4} &= I_a-I_{b2}. \end{aligned}\right\} \qquad (4.2)$$

Equations (4.1) and (4.2) are often called the commutation equations. Also, the left-side and the first term in the right side of Eqs.(4.1) are called the commutating and the reactance voltage matrices, respectively.

As is well known, when the commutating voltages are too small to overcome the

reactance voltages in Eqs.(4.1), the reversions of the current directions in the short-circuited coils are decelerated. This kind of the commutation is called the under-commutation. On the other hand, when the commutating voltages are too large and the reversions are over-accelerated, it is called the over-commutation. Especially, when the commutating voltages are suitable to overcome not only the reactance voltages but also the ohmic drops and the contact voltages in Eq.(4.1), the reversions may be done in a constant time rate. This commutation is called the straight-line one, and the r-th coil current i_r is given by the following equation

$$i_r=\frac{I_a}{2}\ \frac{15-2r}{13}\ (1-\frac{2t}{T_c}),\quad r=1,2,3,\ldots,13, \tag{4.3}$$

where

$-I_a/2\leq i_r\leq I_a/2$,

T_c : commutating period.

Also, it is well known that commutation spark may occur in the cases of the under- and over-commutation. To prevent the occurrence of the spark, it is very important to obtain the smooth reversions of the currents, such as the ones in the straight-line commutation.

For getting the smoothed reversions, it is needed to analyse the commutation characteristics by solving Eqs.(4.1) and (4.2). However, it is too difficult to solve the equations exactly, because the parameters $L_{r,p}$, $B_{ik,r}$, V_{sq}, etc. vary in both time and space, even when the motor is driven in the steady state. Nowadays, approximate analyses are carried out by giving some practical assumptions to the above variational parameters.[29]-[33] In this connection, for simplifying estimation of the commutating voltage, the speed emf $N_c l_a u B_{ik,r}$ in Eqs.(4.1) is often replaced by the following approximate expression

$$N_c l_a u B_{ik,r}\fallingdotseq N_c l_a u\overline{B_{ig}}=\frac{N_c\pi D_a}{W_c}\frac{N}{60}\overline{\Phi_{ig}}, \tag{4.4}$$

where

$\overline{B_{ig}}=\frac{1}{52}\sum_{k=1}^{4}\sum_{r=1}^{13}B_{ik,r}$: average magnetic flux density in interpole airgap,

$\overline{\Phi_{ig}}=l_a W_c \overline{B_{ig}}$: average magnetic flux through interpole airgap,

$N=60u/(\pi D_a)$: revolutions of dc motor per minute,

D_a : outside diameter of armature core,

W_c : width of commutating zone,

under the assumption that every coil in Fig.4.4 crosses equally $\overline{B_{ig}}$ or $\overline{\Phi_{ig}}$.

By the above discussions, we showed that the magnetic flux density $B_{ik,r}$ or the magnetic flux $\overline{\Phi_{ig}}$ in the interpole airgap has a great influence on the commutation characteristics of the dc motor which is driven in the steady state. Furthermore, with respect to the dc motor driven in the transient state such as in the case where the armature current I_a changes abruptly, the theoretical analysis of the transient commutation characteristics is an important subject for the future study, although the variations of $L_{r,p}$, $B_{ik,r}$, V_{sq}, etc. are much more complicated than the ones in the steady state. In order to bring light on the subject, it seems to be suggested that transient responses of the magnetic flux density distribution or the average magnetic flux in the interpole airgap to the sudden change of I_a must be sufficiently analysed.

4.3.2 Experimental circuit for study on transient commutation characteristics

Figure 4.5 shows the schematic circuit diagram for the experimental investigation of the transient commutation characteristics of the motor supplied in Section 4.2, where the motor is driven as the generator for simplifying the investigation. In the figure,

G_e : dc motor driven as generator,

M : dc motor for driving G_e,

E_f=100 V, R_f and I_f=1.3 A : supply voltage, resistance and field current of exciting field circuit of G_e,

E_m and R_{ms} : variable supply voltage and starter of armature circuit of M,

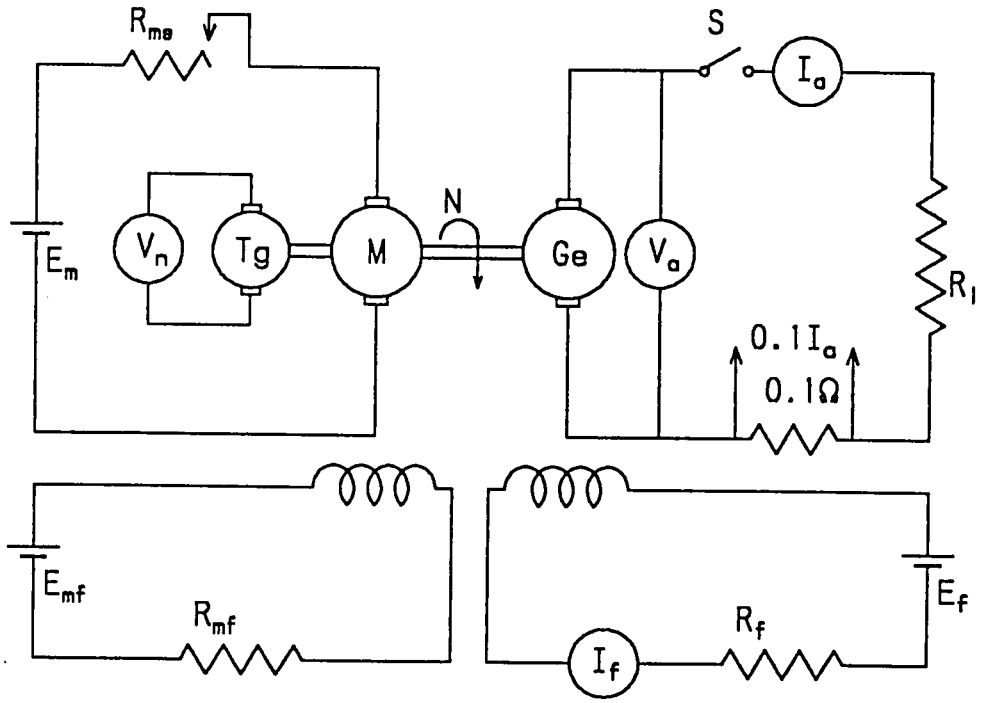

Fig.4.5 Scheme of experimental circuit for studying on transient commutation characteristics.

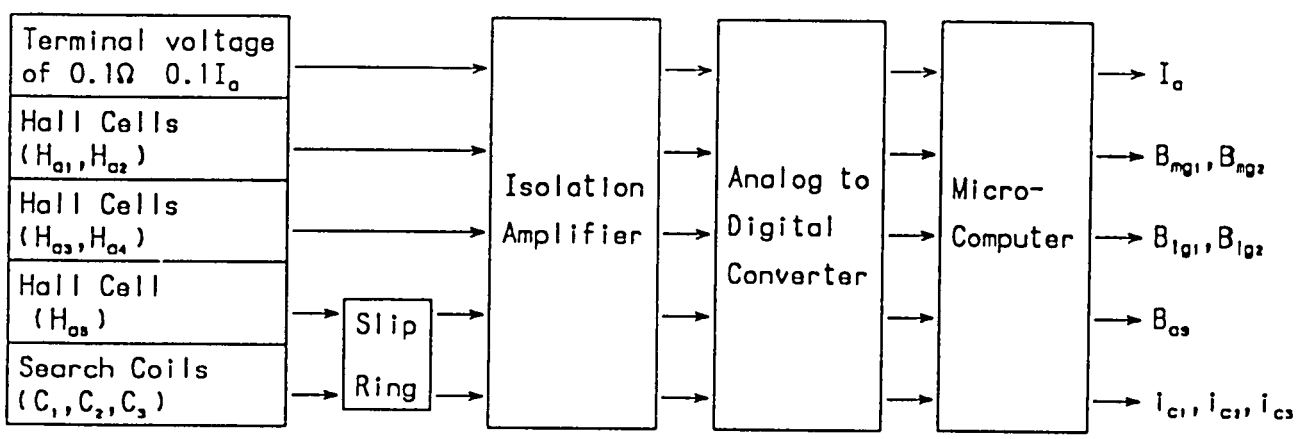

Fig.4.6 Measurement system for circuit in Fig.4.5.

E_{mf}=220 V and R_{mf} : supply voltage and resistance of field circuit of M,

$0.1I_a$: terminal voltage of shunt resistance 0.1Ω,

N : revolutions of G_e and M per minute,

R_l, V_a and I_a : load resistance, output voltage and armature current of G_e,

S : switch,

T_g : tachometer generator,

V_n : output voltage of T_g.

When the abrupt change of I_a is brought on by closing S in Fig.4.5, the transient commutation characteristics of G_e can be investigated by measuring the changes of the armature coil currents i_{c1}, i_{c2} and i_{c3} and the magnetic flux densities B_{mg1}, B_{mg2}, B_{ig1}, B_{ig2} and B_{as} in Fig.4.1. Here, the electromotive forces induced in search coils S_{c1}, S_{c2}, S_{c3} and S_{c4} are fluctuated by the influences of the armature slots and the commutating currents, and so the fluxes Φ_{y1}, Φ_{y2}, Φ_{i1} and Φ_{i2} can't be measured accurately. Figure 4.6 shows the measurement system, in which quantities measured by the search coils, GaAs Hall cells, etc. are processed by a personal micro-computer.

4.3.3 Experimental results and discussion[34]

Figures 4.7 (a) and (b) show the response waveforms of i_{c1}, i_{c2}, i_{c3}, B_{mg1}, B_{mg2}, B_{ig1}, B_{ig2} and B_{as} to the abrupt change of I_a, which is generated by closing S under the initial conditions of I_f=1.3 A, N=2100 rpm, V_a=162 V and I_a=0 in Fig.4.5, where R_l=8.96 Ω, which gives I_a=16 A, N=2000 rpm and V_a=145 V in the steady state for I_f=1.3 A, and T_m=1.15 ms that is the time constant of I_a.

We can see in Fig.4.7(a) that i_{c1}, i_{c2} and i_{c3} are under-commutated for the initial duration $0<t<5T_m$, and at about $t=5T_m$ those currents turn to good commutating states. The under-commutation for $0<t<5T_m$ may be brought forth by the initial lack of the commutating voltage, which is occurred by the delays of the responses of B_{ig1} and B_{ig2} to the rapid increase of I_a, as shown in Fig.4.7(b). It is thought that the delays are caused by the eddy current induced in the yoke Y_o.

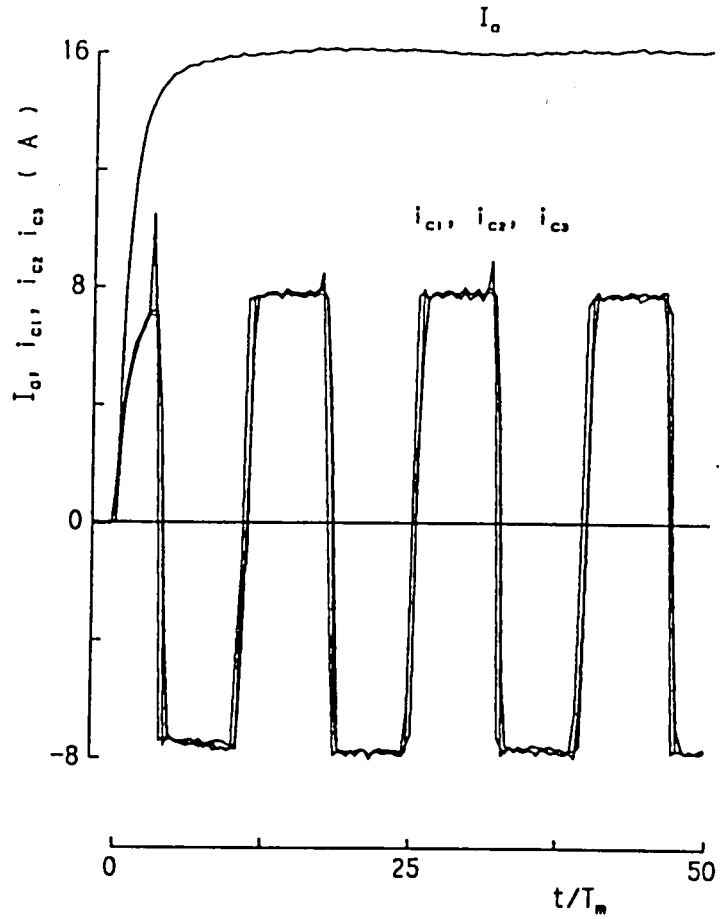

(a) Transient commutation waveforms of armature coil currents.

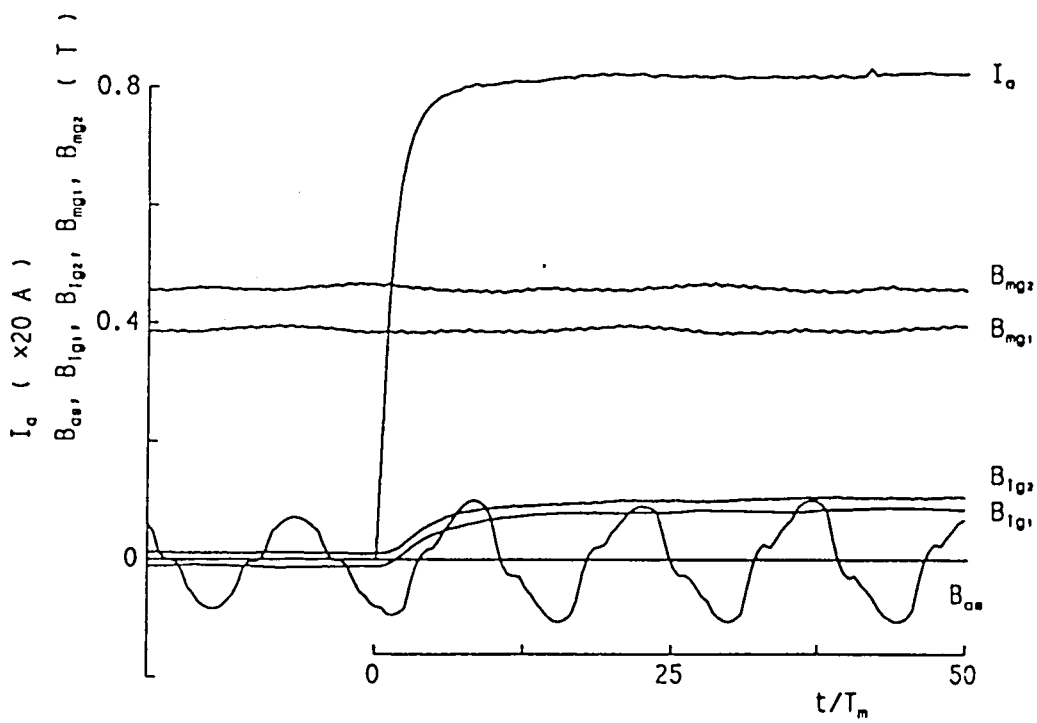

(b) Transient responses of magnetic flux densities.

Fig.4.7 Experimental results of transient commutation characteristics for T_s=1.15 *ms*, N=2000 *rpm* and I_f=1.3 *A*.

On the other hand, as is well known, B_{mg1} and B_{mg2} are not influenced by I_a as shown in Fig.4.7(b). Also, from B_{as} plotted in Fig.4.7(b), we can see that the flux density distribution in the peripheral airgap of the armature is fairly disturbed by I_a. This is well known as an armature reaction by I_a. In Fig.4.7(b), some visible differences between B_{mg1} and B_{mg2} and between B_{ig1} and B_{ig2} may depend on the errors of measurement by the GaAs Hall cells and the residual magnetism.

Furthermore, from Figs.4.7 (a) and (b), it is suggested that the transient commutation for the abrupt increase of I_a may be improved by intensifying B_{ig1} and B_{ig2} during the initial duration $0<t<5T_m$. For this purpose, we usually strengthen the interpole magnetomotive force(mmf) by using an auxiliary interpole exciting winding as given in Table 4.1.

Figures 4.8(a) and (b) show the experimental results, where the 10-turn auxiliary winding is added to the 70-turn usual interpole winding, and T_m=1.58 ms. In the experiment, the initial conditions are the same as the ones for Figs.4.7, but T_m=1.58 ms and R_l=9.46 Ω, N=2000 rpm, V_a=153 V, I_f=1.3 A and I_a=16 A in the steady state differ a little from the ones for Figs.4.7, that is caused by intensifying the interpole mmf. Now, we can see that B_{ig1} and B_{ig2} in Fig.4.8(b) are about 1.2 times stronger than those in Fig.4.7(b), and so that the commutation of i_{c1}, i_{c2} and i_{c3} for the initial duration $0<t<5T_m$ are much improved more than the ones in Fig.4.7(a). However, with the lapse of time, the over-commutation arises as observed in Fig.4.8(a).

From the experimental results shown in Figs.4.7 and 4.8, we can affirm that the transient responses of the flux densities, such as B_{ig1} and B_{ig2}, in the interpole airgaps to the abrupt change of I_a have a great influence on the transient commutation characteristics of the dc motor. Therefore, it is very important to analyse the transient response of the magnetic flux in the interpole airgap. Also, in the analysis, we must take account of the eddy current induced in the solid iron yoke and the interpole liner, because the eddy current delays not only the responses of the fluxes in the yoke and the interpole core but also the ones in the

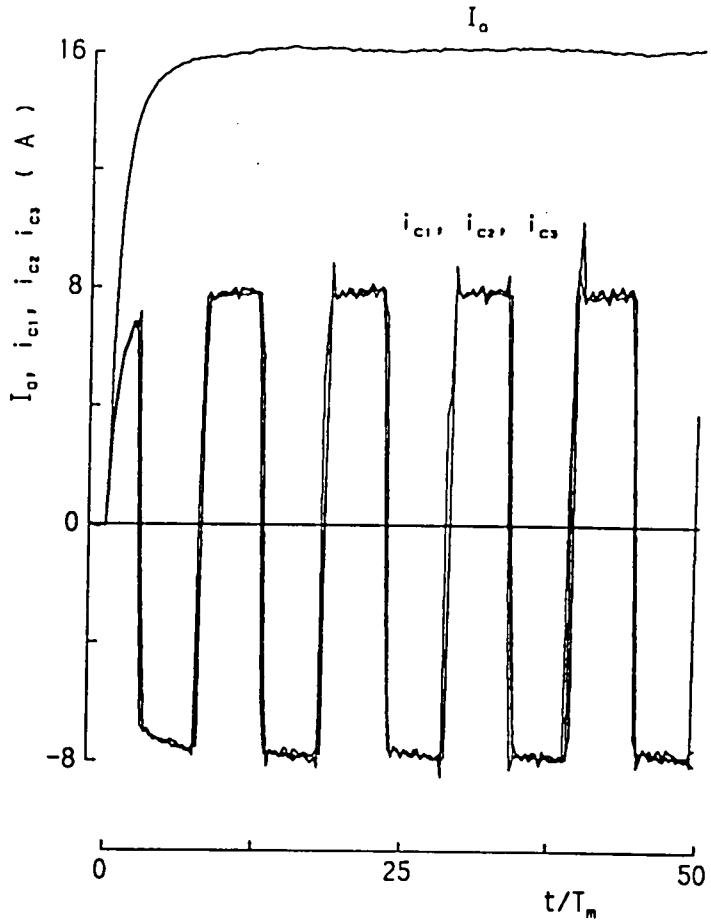

(a) Transient commutation waveforms of armature coil current.

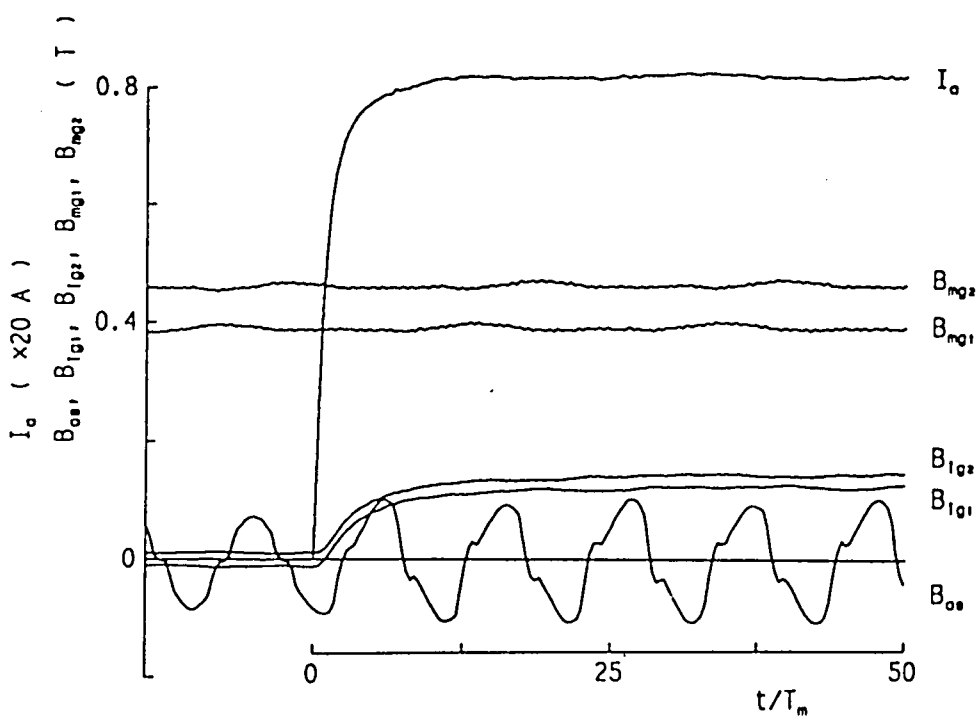

(b) Transient responses of magnetic flux densities.

Fig.4.8 Improvement of initial transient commutation by intensifying interpole exciting mmf for T_m=1.58 *ms*, N=2000 *rpm* and I_f=1.3 *A*.

interpole airgaps.

In some of the latest dc motors, the responsibility of the flux in the interpole airgap is improved by the automatic control of the interpole exciting mmf. Also, the partial inner surface region of the yoke is often laminated so as to reduce the initial large eddy current induced in its region.

4.4 Theoretical and Experimental Analyses of Transient Response and Distribution of Magnetic Flux

4.4.1 Experimental circuit

By using the search coils S_{c1} to S_{c4} and the Hall cells H_{a1} to H_{a4} in Fig.4.1, we experimentally study on the transient responses of the fluxes Φ_{y1}, Φ_{y2}, Φ_{i1} and Φ_{i2} and the flux densities B_{mg1}, B_{mg2}, B_{ig1} and B_{ig2} to the abrupt change of the armature current I_a in the dc motor specified in Table 4.1. Here, the experiment is performed under the condition that the dc motor stands still at the position shown in Fig.4.1, because it is too difficult to obtain the transient responses of the fluxes, when the dc motor is rotating and so the induced emf's in the search coils are fluctuated by the influences of the armature slots and the commutating armature coil currents.

Figure 4.9 shows a scheme of the experimental circuit, for studying on the transient responses of the magnetic fluxes and the magnetic flux densities, where

G_e : supplied dc motor specified in Table 4.1,

E_s, I_a and R_l : variable supply voltage, armature current and resistance in armature circuit of G_e,

E_f=100 V, R_f and I_f=1.3 A : supply voltage, resistance and field current in exciting field circuit of G_e,

$0.1I_a$: terminal voltage of shunt resistance 0.1 Ω,

S : switch.

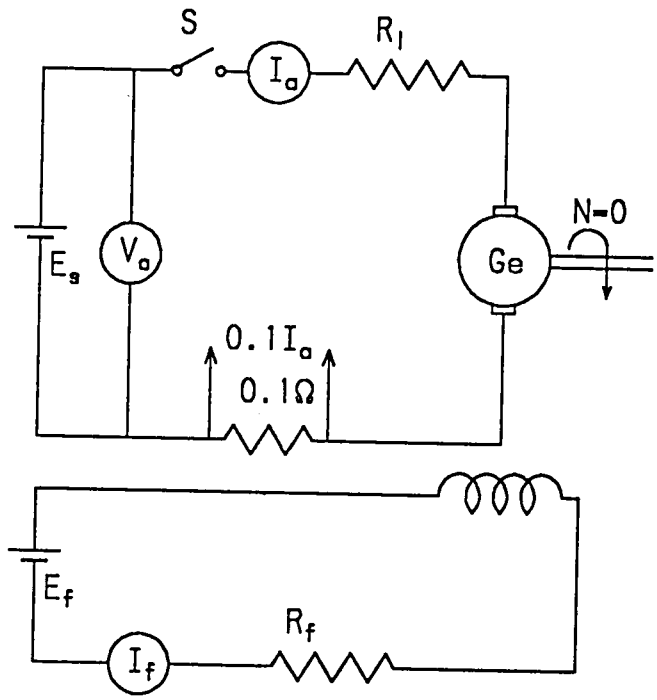

Fig.4.9 Schematic experimental circuit for transient responses of magnetic flux and flux densities.

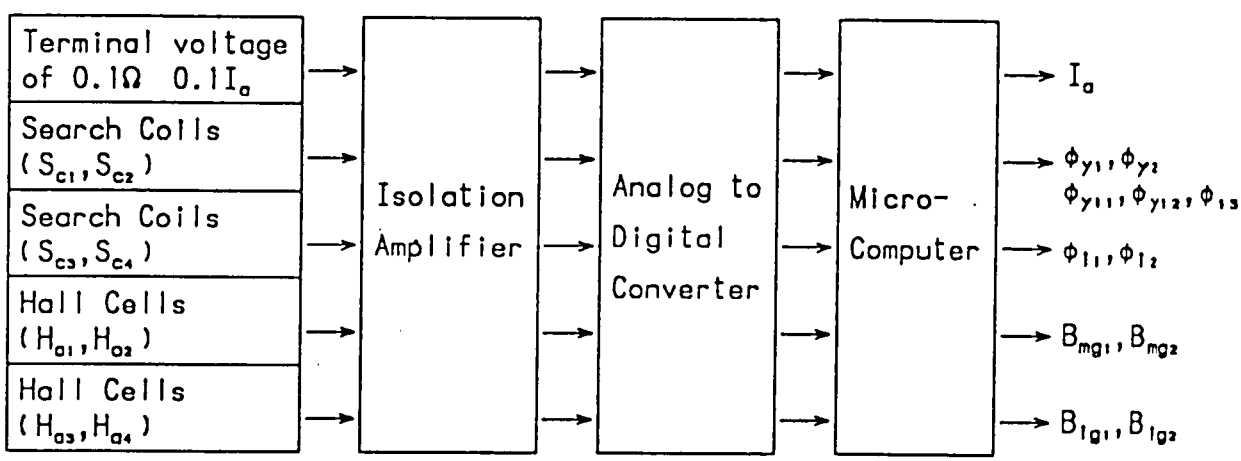

Fig.4.10 Measurement system for Fig.4.9.

In the experiment, I_a is suddenly supplied to the armature and the interpole exciting windings by closing S. In this addition, the measured data are processed by the personal micro-computer as shown in Fig.4.10.

4.4.2 Assumptions and boundary conditions for numerical solution

Theoretical analysis of the transient responses and distributions of the magnetic fluxes, the eddy current, etc. by the two-dimensional nodal method described in Chapter 2 are carried out under the following assumptions:

(1) It is assumed that the armature stands still at the position shown in Fig.4.1, because the numerical analysis is too difficult when the relative position between the armature and the stater is being varied by the rotation.

(2) In the armature, the main pole and the interpole cores, which are made of laminated steel plates, we assume that the induced eddy current can be ignored and their conductivities are zero. The conductivity $\sigma=\sigma_y$ of the solid iron yoke and the one $\sigma=\sigma_l$ of the interpole and the main pole liners are assumed to be constant, and $\sigma_y=\sigma_l=5$ MS/m are the measured values. In this connection, when it is assumed that the yoke is partially laminated in the numerical analysis, we put $\sigma=0$ in the laminated region.

(3) It is assumed that the supplied armature current I_a and field exciting current I_f flow uniformly in the respective winding conductors. Then, the current density J_s in each winding conductor is evaluated by

$$J_s=\frac{\text{current flowing in each winding conductor}}{\text{cross-sectional area of conductor}} \tag{4.5}$$

Furthermore, the currents i_1 to i_{13} in the armature coils short-circuited by the brushes as shown in Fig.4.4 are assumed to be in the straight-line commutation states, and they are obtained by putting $t=0$ into Eq. (4.3).

(4) It is assumed that the reciprocal permeabilities ν's of the iron cores are calculated by the Frölich formula described in Article 2.3.3, which is derived from the B-H curves shown in Fig.4.11. However, by referring to the conclusion (7) in

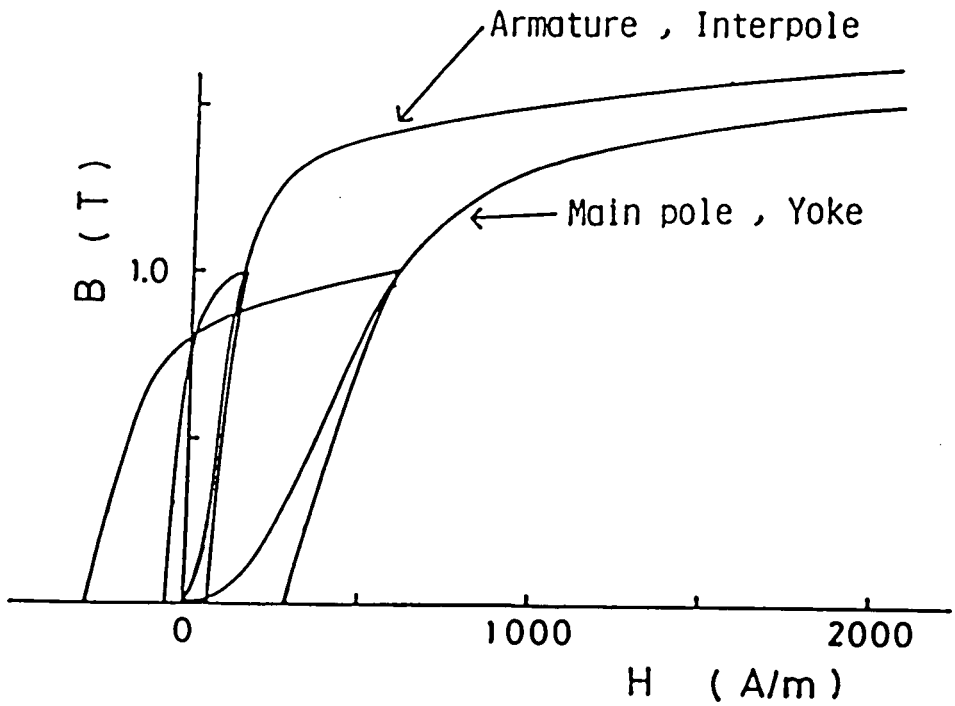

Fig.4.11 Magnetization curves.

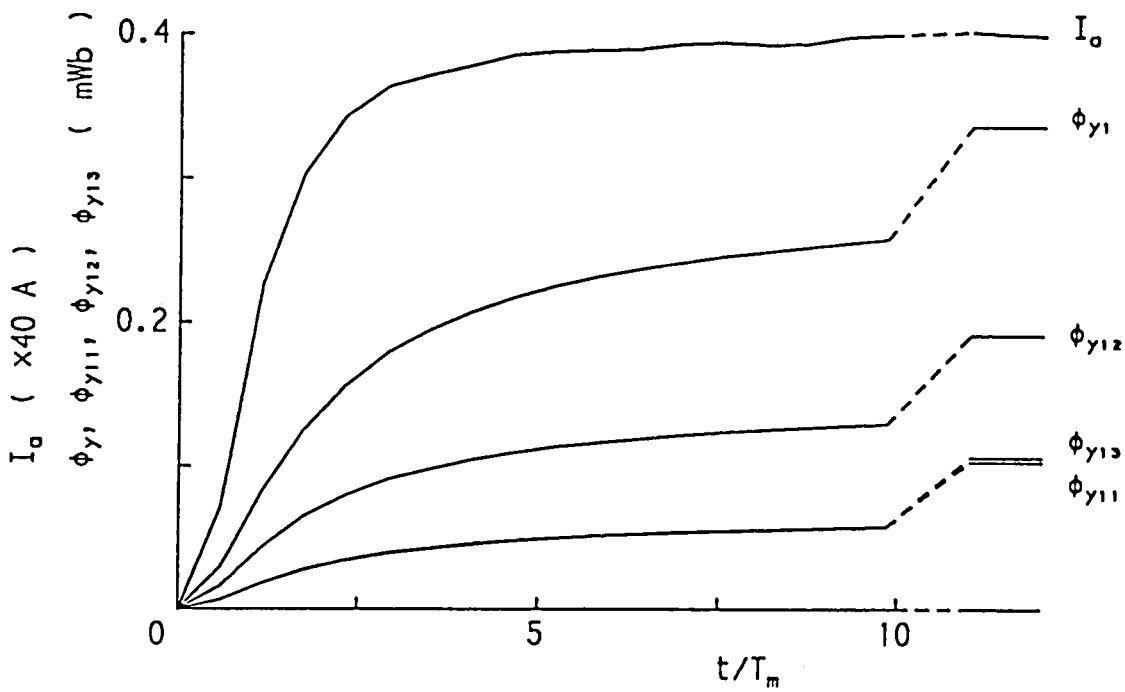

Fig.4.12 Experimental results of transient responses of magnetic fluxes in yoke for T_m=1.15 *ms*.

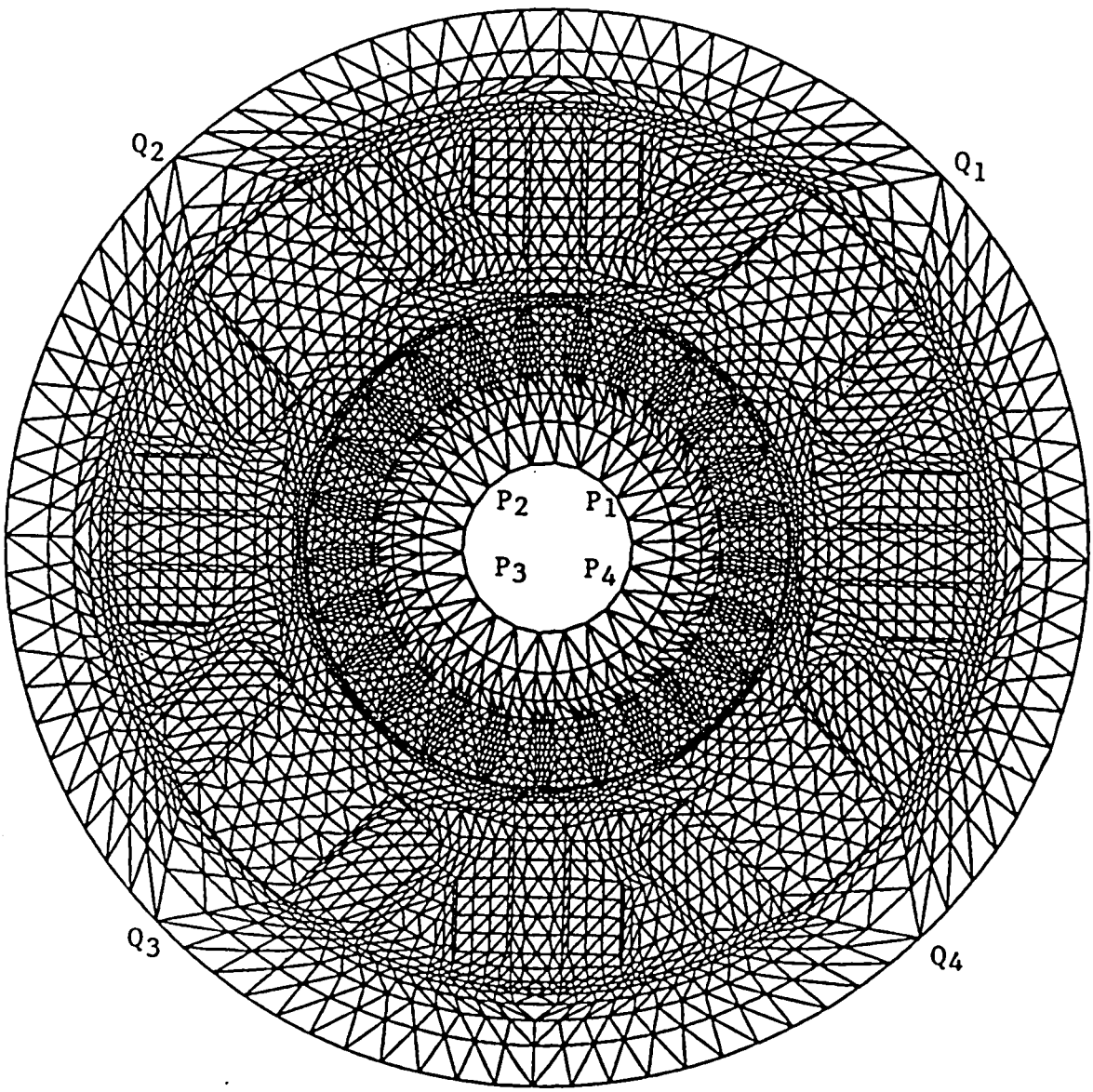

Fig.4.13 Arrangement of triangular mesh for nodal method.

Section 3.5, the magnetic hysteresis is considered only in the inner skin region of about 30 % of the yoke, so as to reduce the memory and the computation time of the digital computer for solving the nonlinear discrete equations (2.52).

(5) As shown in Table 4.1, the axial length l_y of the yoke is 2.5 times longer than the ones l_a and l_m of the armature and the main pole cores. Correspondingly, we must consider the flux expansion of the axial direction in the yoke. Figure 4.12 shows the transient responses of Φ_{y11}, Φ_{y12}, Φ_{y13} and Φ_{y1} to I_a of T_m=1.15 *ms*, which are obtained by using the search coils in Fig.4.2. In Fig.4.12, Φ_{y11} and Φ_{y13} show the flux expansion of the axial direction, and Φ_{y12} the flux through the part of the yoke, which has the same length as l_a and l_m. Here, the following relations

$$\left.\begin{aligned} &\Phi_{y11}+\Phi_{y13}\fallingdotseq\Phi_{y12}, \\ &\Phi_{y1}=\Phi_{y11}+\Phi_{y12}+\Phi_{y13}\fallingdotseq 2\Phi_{y12}, \end{aligned}\right\} \tag{4.6}$$

are obtained. By the relation of $\Phi_{y1}\fallingdotseq 2\Phi_{y12}$ in Eqs.(4.6), our two-dimensional analysis is performed under the assumption that the axial length $l_a=l_m=l_y$=90 *mm* and the above flux expansion can be taken into account by doubling the actual thickness t_y=17.5 *mm*.

(6) With respect to the interpole core of the axial length l_i=80 *mm*, it is made equal to $l_a=l_m$=90 *mm* by changing $\nu=\nu_i$ to ν_i' given by the following equation

$$\nu_i'=\frac{2}{2.5}\,\frac{9}{8}\nu_i. \tag{4.7}$$

Figure 4.13 shows the cross-sectional area of the dc motor with triangular meshes for numerical calculation, in which the thickness of the yoke is doubled by the assumption (5). In the figure, very small triangles are applied to the regions near the outer surface of the armature and the inner one of the yoke, the airgap around the armature, etc., in which the flux may distribute very variably.

Next, let us give the conditions on the boundary of the motor in Fig.4.13 as follows:

(1) The leakage flux from the inner surface of the armature core to the shaft is assumed to be negligible, and we put the vector potential A=0 on the boundary

$P_1P_2P_3P_4P_1$.

(2) Neglecting the leakage flux out of the outer surface of the yoke, we put A=0 on the boundary $Q_1Q_2Q_3Q_4Q_1$.

Now, under the above assumptions and the boundary conditions, the vector potential at each vertex of a triangle in Fig.4.13 can be obtained by solving the simultaneous nodal equations (2.52) for given I_f and I_a. Furthermore, using the results, the transient response of the flux, the flux distribution, the induced eddy current density, etc. can be evaluated by the numerical method described in Chapter 2.

4.4.3 Experimental and calculated results[22], [23], [35], [36]

Figure 4.14 shows the experimental transient responses of B_{mg1}, B_{mg2}, B_{ig1} and B_{ig2} to the abrupt change of I_a, where T_m=1.15 ms and I_f=1.3 A. We can see that B_{ig1} and B_{ig2} respond late to the change of I_a, but B_{mg1} and B_{mg2} are scarcely influenced by I_a. Though the results shown in Fig.4.14 are obtained under the condition that the supplied dc motor G_e stands still, they agree well with the ones in Fig.4.7(b) under the condition that G_e is rotating.

Figure 4.15 shows the experimental results of the transient responses of Φ_{y1}, Φ_{y2}, Φ_{i1} and Φ_{i2} to the change of I_a. In the figure, the steady fluxes by I_f are not plotted, because the above results are obtained by integrating the change of the induced emf's in search coils S_{c1} to S_{c4} in Fig.4.1. In Fig.4.15, we can find the visible delay of the transient responses of the fluxes in the yoke and the interpole cores to I_a. That is caused by the eddy current induced in the yoke and the interpole liners.

In Figs.4.14 and 4.15, though the fluxes Φ_{y1}, Φ_{y2}, Φ_{i1} and Φ_{i2} need long time to reach the respective final values owing to the large influence of the induced eddy currents, the flux densities B_{ig1} and B_{ig2}, which closely relate to the commutating voltage, reach the respective steady values at about t=10T_m.

Next, the numerical analysis is performed by the following processes, as

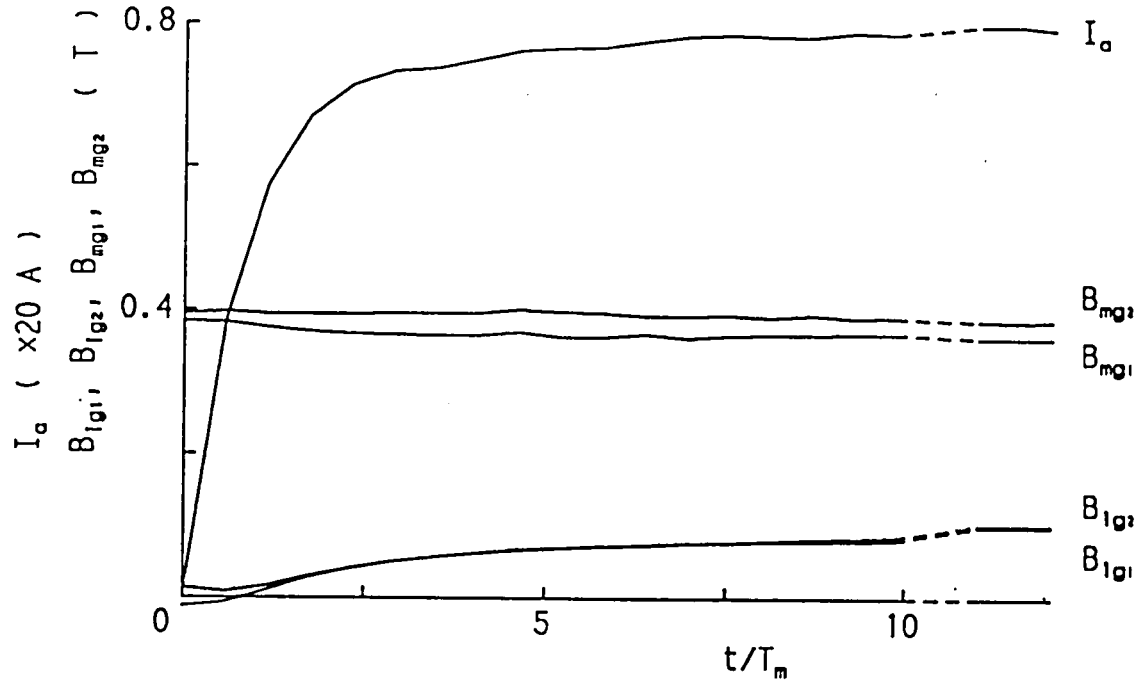

Fig.4.14 Experimental results of transient responses of magnetic flux densities for T_m=1.15 ms.

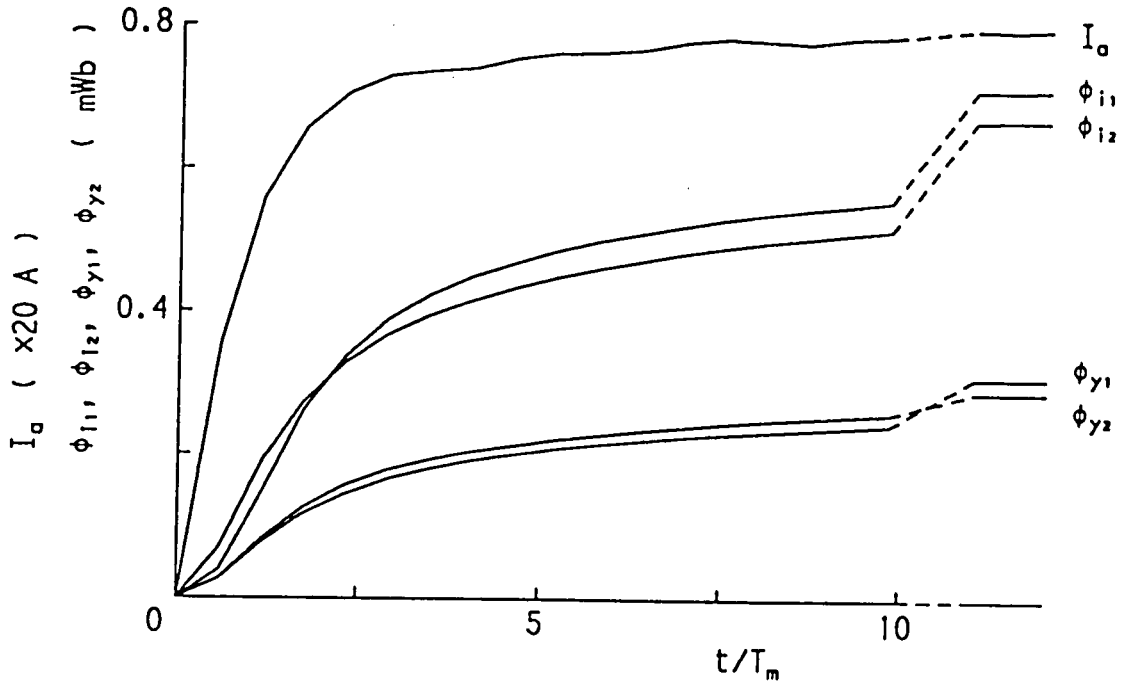

Fig.4.15 Experimental results of transient responses of magnetic fluxes for T_m=1.15 ms.

described shortly in Article 2.3.5. The initial values of the vector potentials A_i's at all nodes are calculated by Eqs.(2.52) under the conditions that I_f=1.3 A, I_a=0, $\sigma_y=\sigma_l=0$, and the residual magnetism is zero. Subsequently, the numerical solutions of A_i's at successive time are derived from Eqs.(2.52) under the conditions of I_f=1.3 A, $\sigma_y=\sigma_l$=5 MS/m, $I_a=16\{1-\exp(-t/T_m)\}$ A, T_m=1.15 ms and $0\leqq t\leqq 10T_m$. Also, the solutions in the steady state($t\to\infty$) are obtained under the conditions of I_f=1.3 A, $\sigma_y=\sigma_l=0$ and I_a=16 A.

Figure 4.16 shows the transient responses of the fluxes Φ_{y1}, Φ_{y2}, Φ_{i1} and Φ_{i2} and the flux densities B_{ig1} and B_{ig2} to the change of I_a, which are obtained by using the solution of A_i's and Eqs.(2.21) and (2.25). Though the actual fluxes in the dc motor distribute three-dimensionally, the results by our two-dimensional method agree well with the experimental results shown in Figs.4.14 and 4.15.

In order to study more fully on the transient responses of the fluxes, let us investigate the flux, the flux density and the induced eddy current density distributions in a cross-section of the supplied motor, too.

Figures 4.17 (a) to (e) show the calculated flux distributions at t=0,

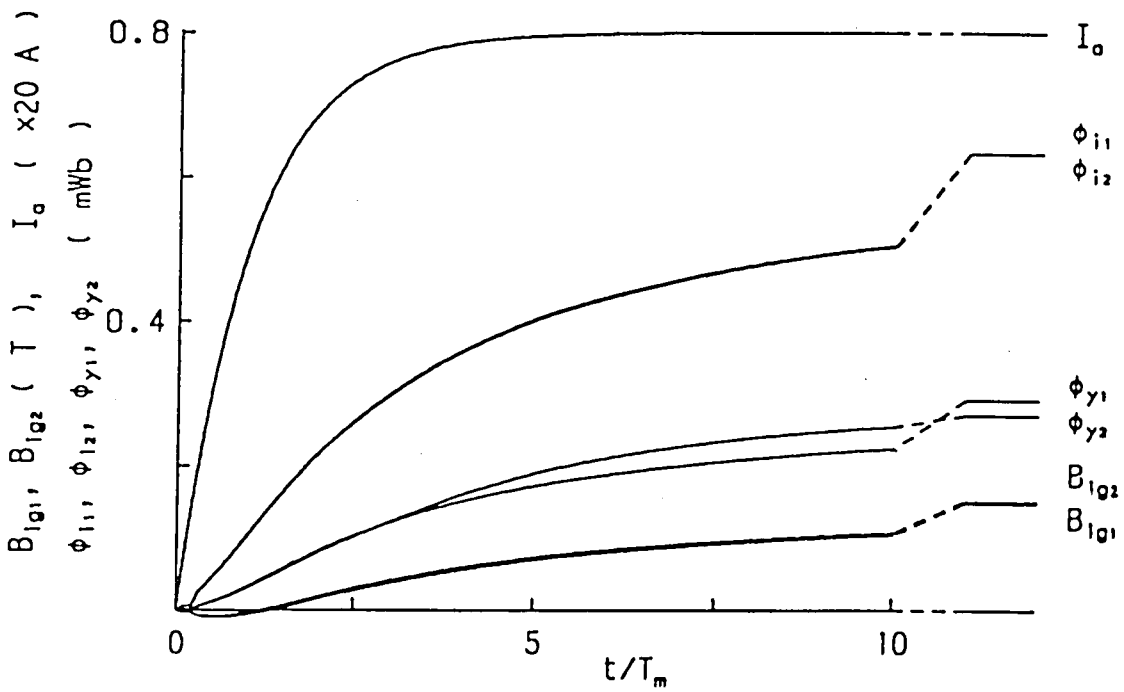

Fig.4.16 Calculated results of transient responses of magnetic fluxes and flux densities for T_m=1.15 ms.

$2T_m$, $5T_m$, $10T_m$ and ∞, where ΔA_{eq}=1.5 *mWb/m* is the contour interval between two neighbouring equi-vector-potential lines, which are called the flux lines. Here, the figure (a) is the initial flux distribution, and the one (e) is the distribution in the steady state where the eddy current vanishes. We can see that the flux distribution changes with time. Especially, the fluxes in the interpole and the inner skin region of the yoke vary violently. In this connection, the approximate study on the concentration of the flux in the inner skin region of the yoke, which is caused by the eddy current induced in the region, was already performed in Chapter 3.

In Figs.4.18 (a) to (e), the flux density distributions corresponding to Figs.4.17 (a) to (e), respectively, are presented. We can see occurrence of the magnetic saturation in some part of the inner skin region of the yoke, which is kept after a lapse of time by the magnetic hysteresis. The magnetic saturation decelerates the change of Φ_{y1} much more than the one of Φ_{y2} in Fig.4.16.

Figures 4.19 (a) to (c) show the eddy current density distributions in the yoke and the liners at $t=2T_m$, $5T_m$ and $10T_m$, which are approximately calculated by Eq.(2.53). We can recognize the large eddy current densities in the inner skin region of the yoke and the both outer ones of the interpole liners for the initial duration $0<t\leqq 2T_m$. Those large eddy current densities cause delays of not only the fluxes Φ_{y1}, Φ_{y2}, Φ_{i1} and Φ_{i2} but also the flux densities B_{ig1} and B_{ig2} as shown in Fig.4.16. We can also see that the small eddy current may be remained after $t=10T_m$ and so the fluxes in Fig.4.16 need long time to reach their steady values.

Next, in Figs.4.20 (a) to (e), we show the flux density distributions in the commutating zones in the interpole airgaps of I_{p1}, I_{p2}, I_{p3} and I_{p4}, which correspond to (a) to (e) in Figs.4.17 and 4.18, respectively. As already shown in Eqs.(4.1), these distributions relates closely to the transient commutation characteristics of the dc motor. And the delay of the flux densities to the change of I_a, especially the large delay for $0<t\leqq 5T_m$, cause the bad under-commutating states as shown in Fig.4.7(a).

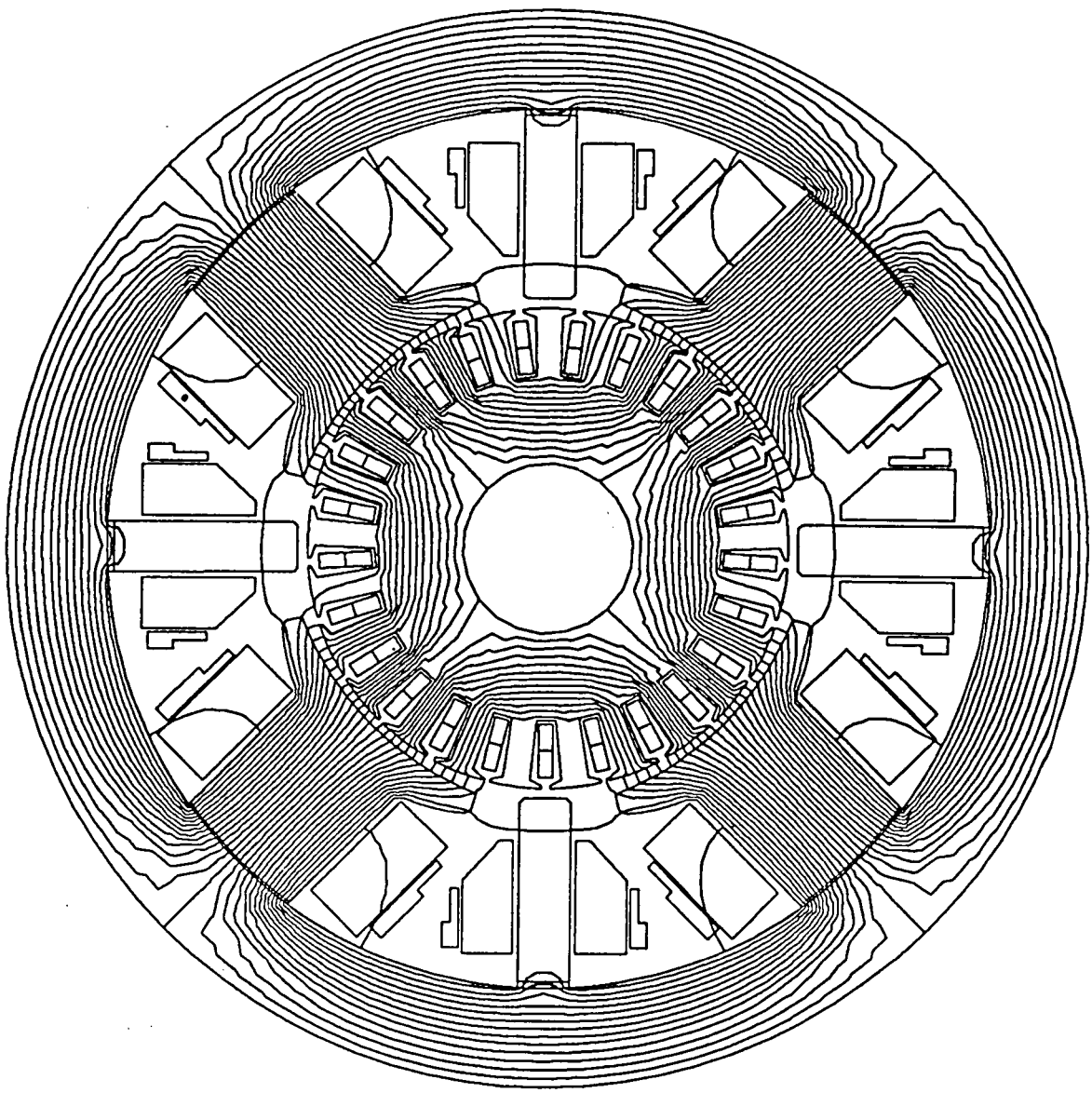

Fig.4.17 (a) t=0 and I_a=0.

Fig.4.17 Transitional magnetic flux distributions for T_a=1.15 ms and $\Delta\Lambda_{eq}$=1.5 mWb/m.

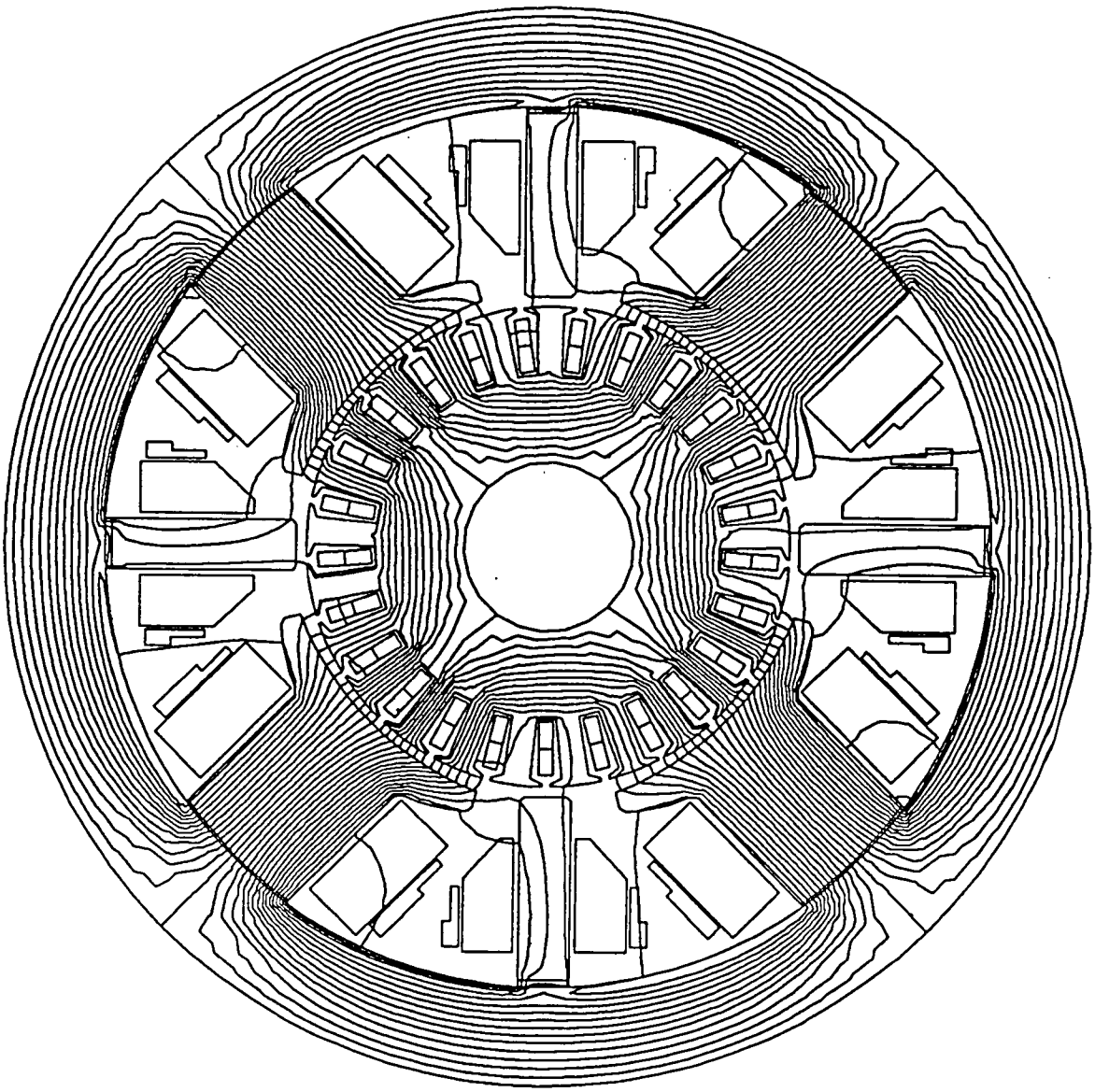

Fig.4.17 (b) $t=2T_s$ and $I_a=13.8\ A$.

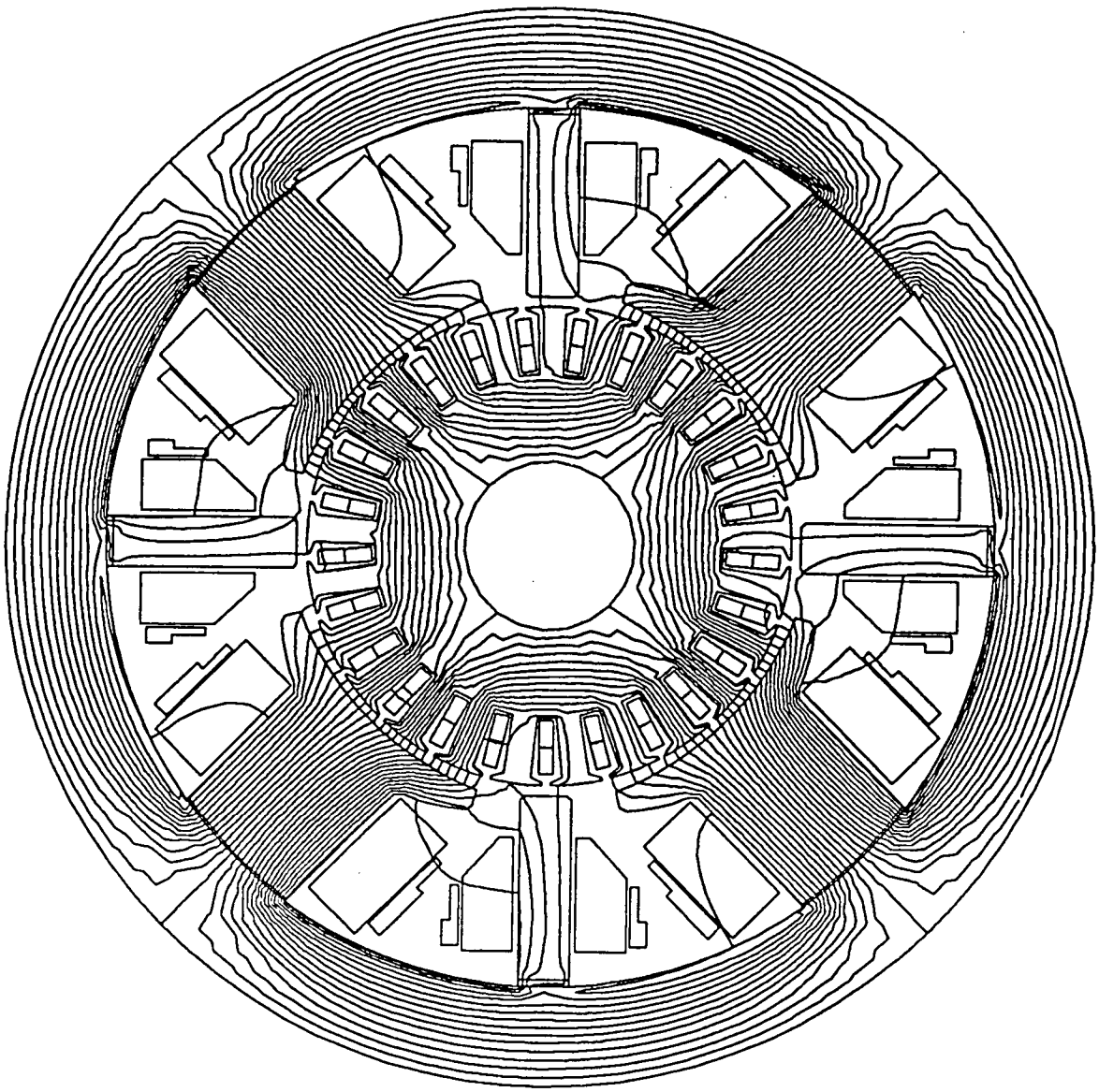

Fig.4.17 (c) $t=5T_s$ and $I_a=15.9\ A$.

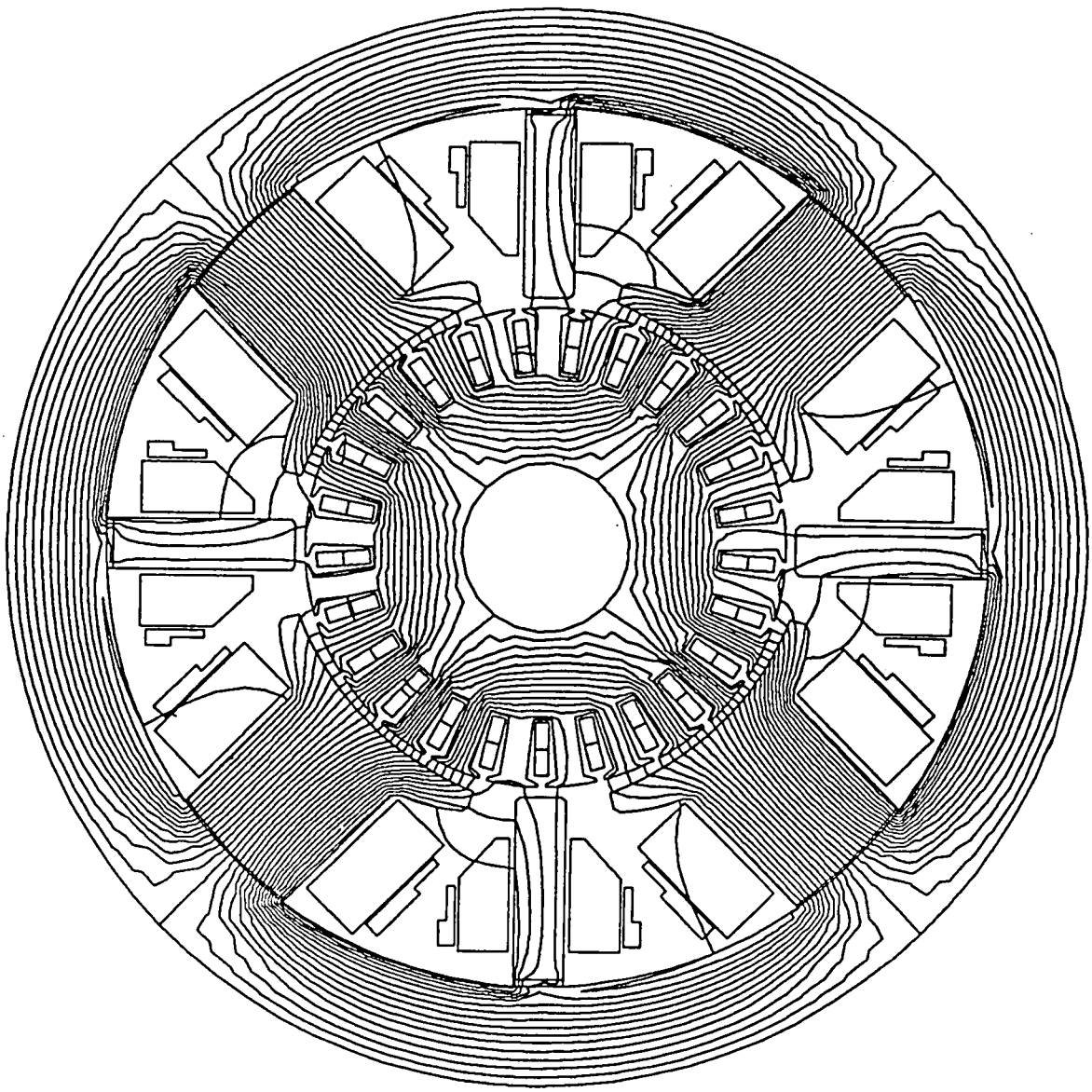

Fig.4.17 (d) t=10T_s and I_a=16.0 A.

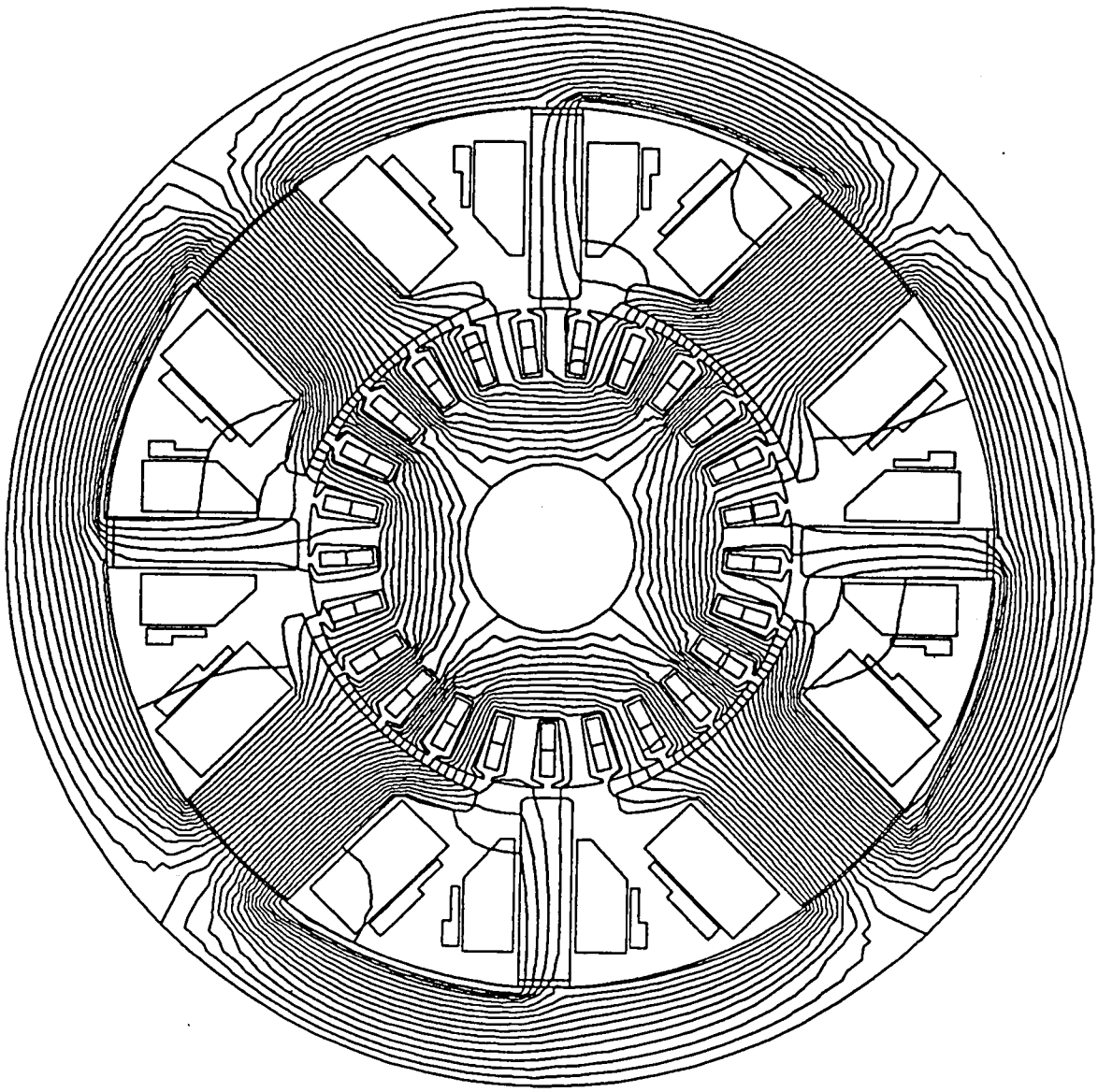

Fig.4.17 (e) $t \rightarrow \infty$ and I_a=16.0 A.

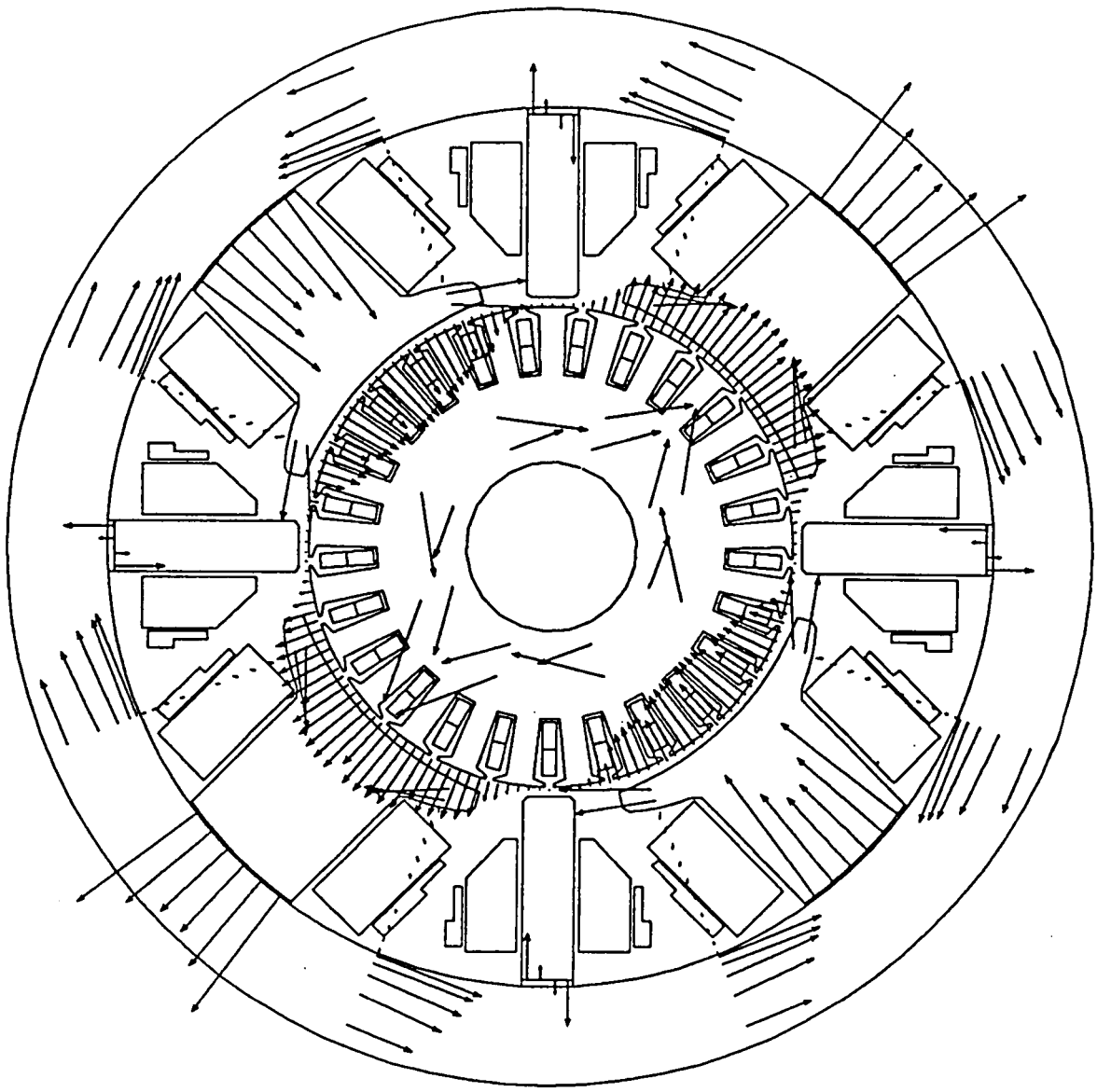

Fig.4.18 (a) t=0 and I_a=0.

Fig.4.18 Transitional magnetic flux density distributions for T_m=1.15 ms.

⟶ 2.0 T

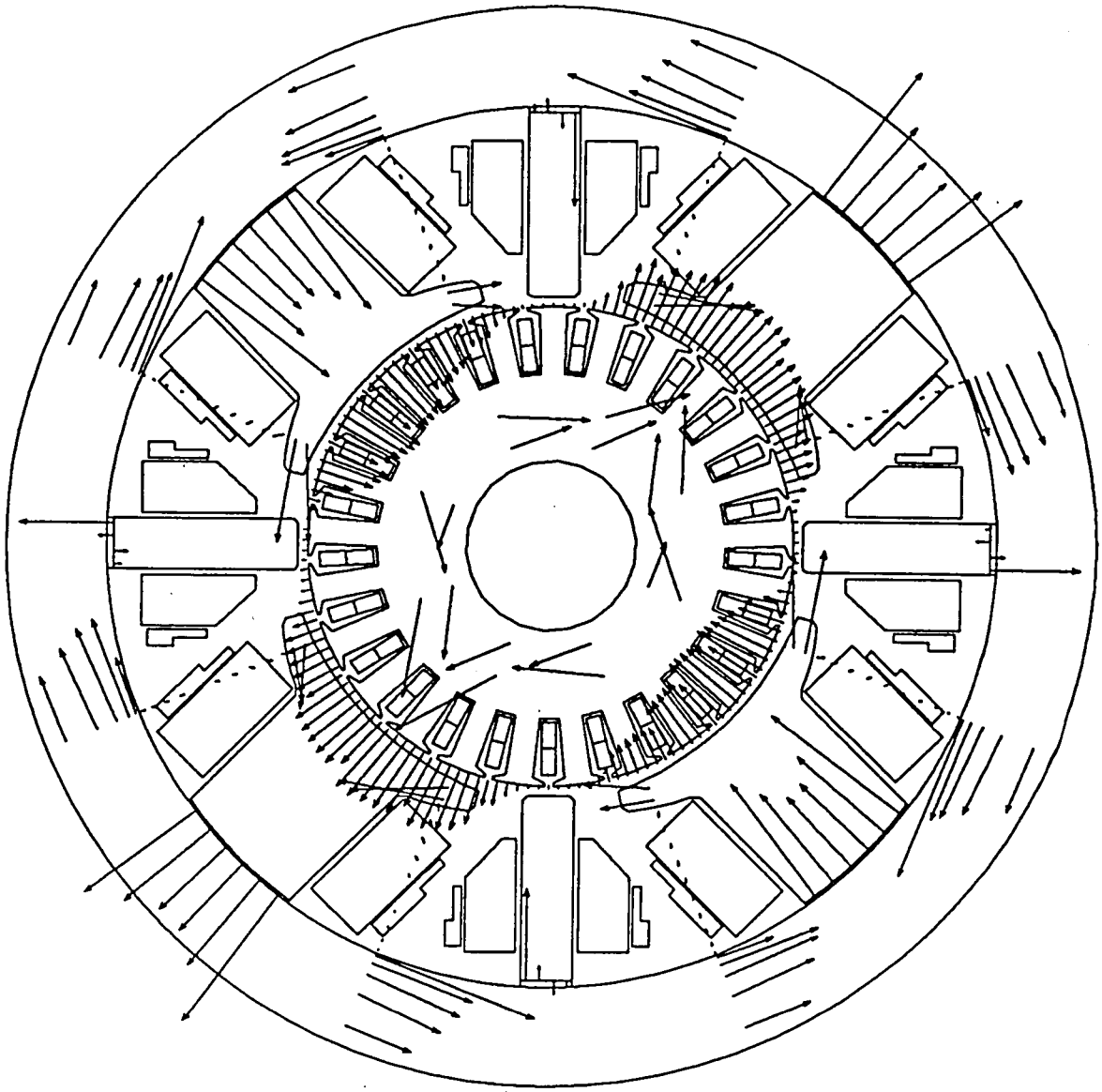

Fig.4.18 (b) $t=2T_s$ and $I_a=13.8\ A$.

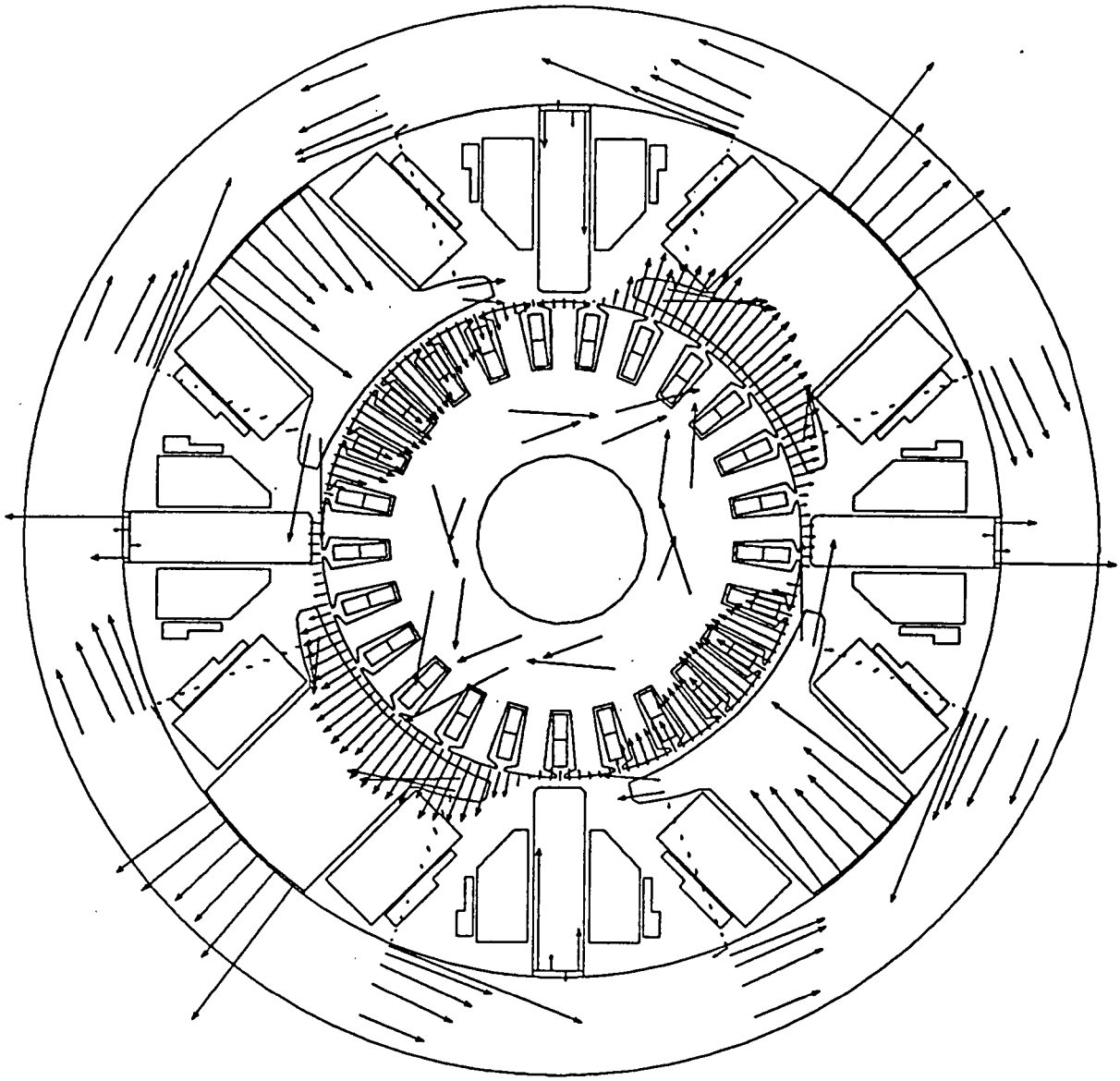

Fig.4.18 (c) $t=5T_s$ and $I_a=15.9\ A$.

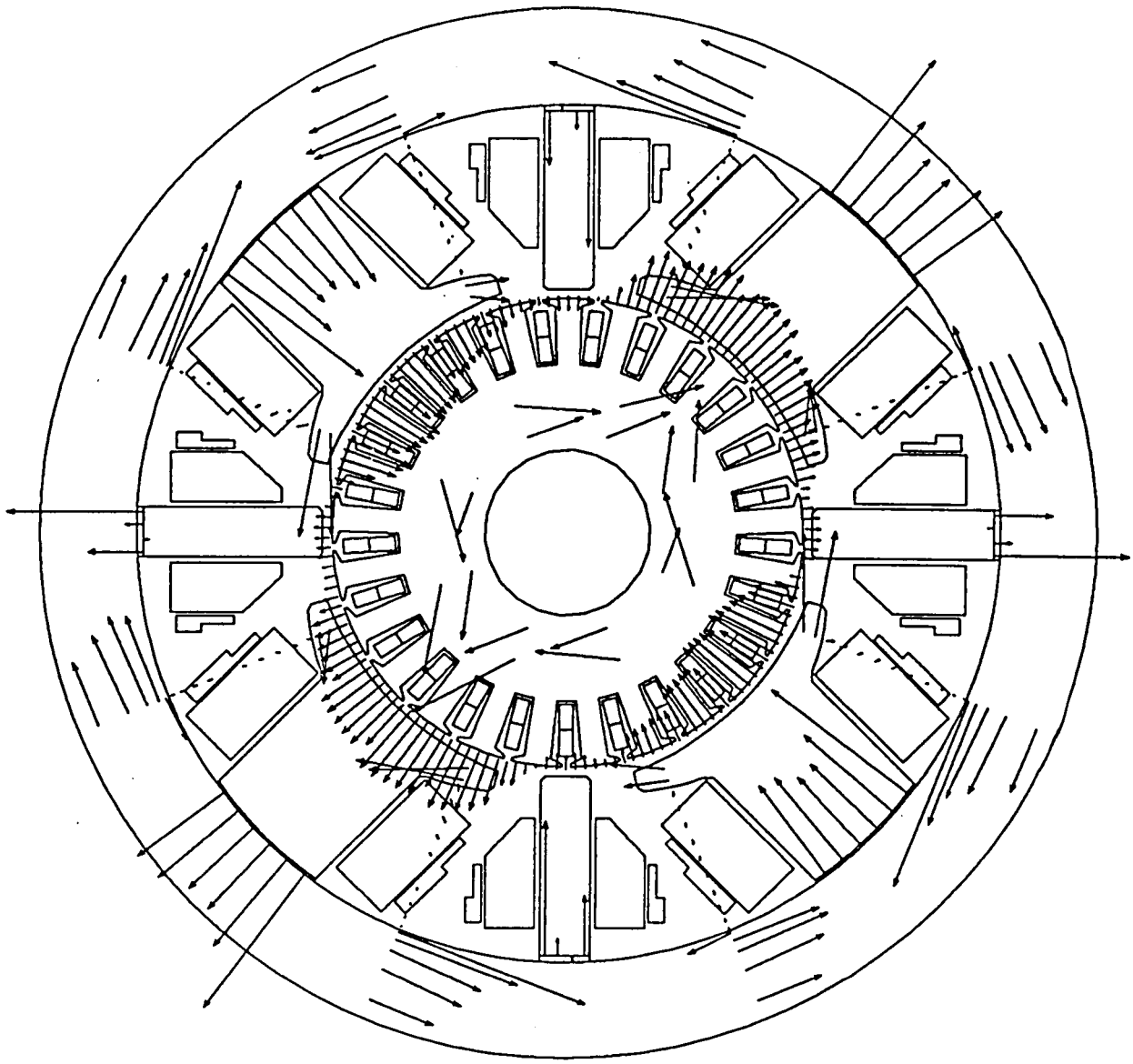

Fig.4.18 (d) t=10T_s and I_a=16.0 A.

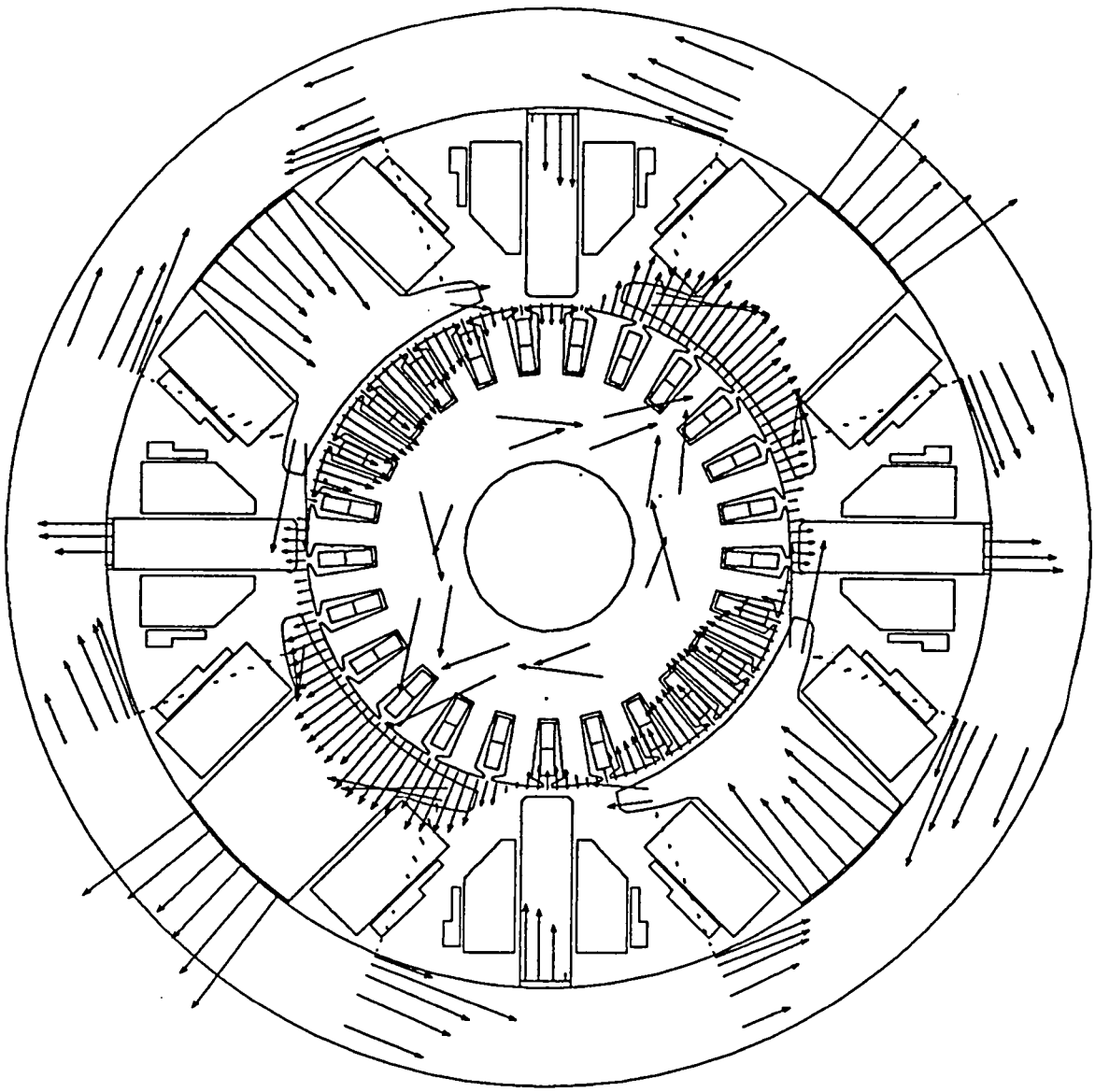

Fig.4.18 (e) $t \rightarrow \infty$ and I_a=16.0 A.

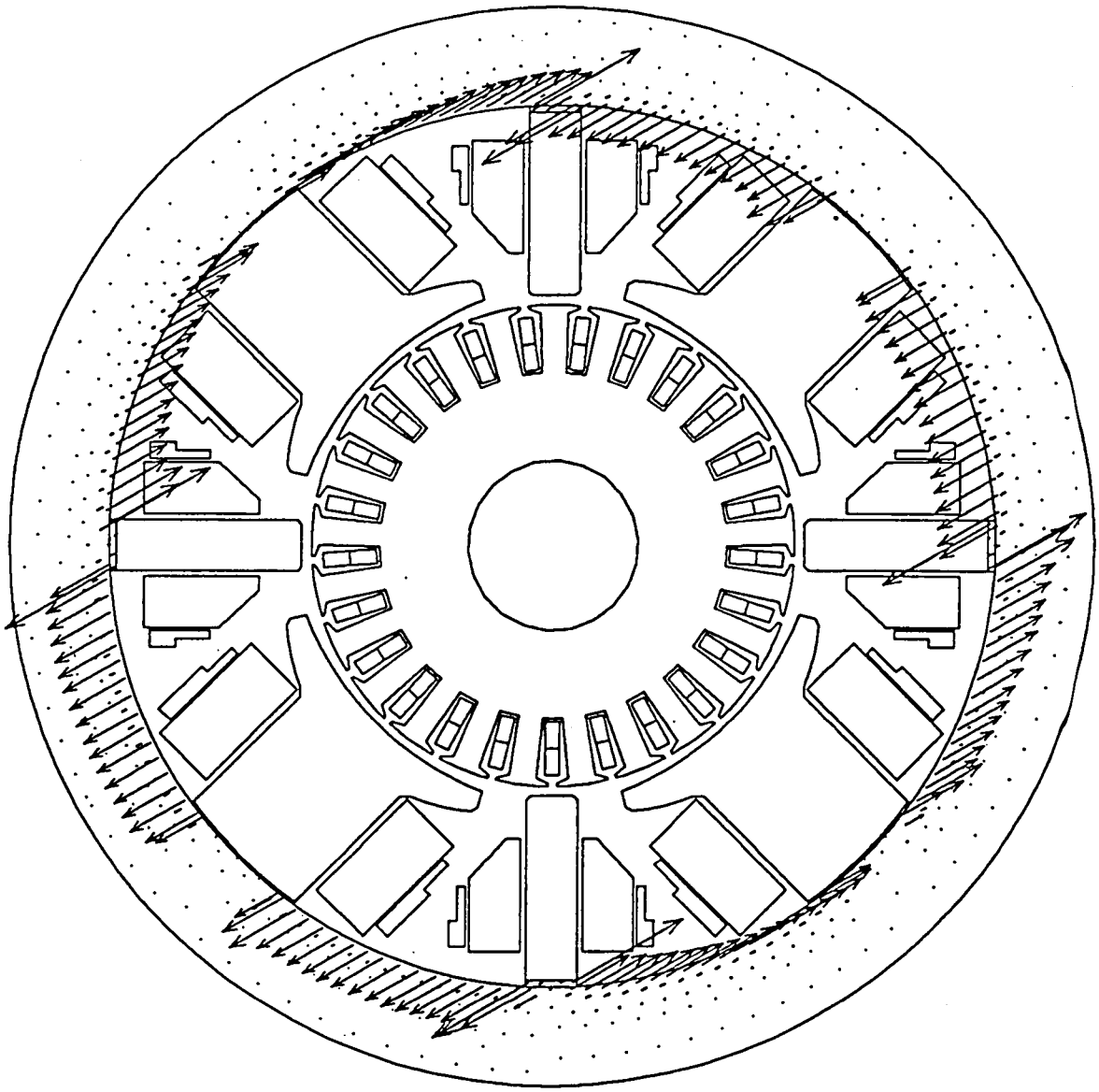

Fig.4.19 (a) $t=2T_m$ and $I_a=13.8\ A$.

Fig.4.19 Transitional eddy current density distributions for $T_m=1.15\ ms$.

$\longrightarrow$ 2.0 MA/m^2

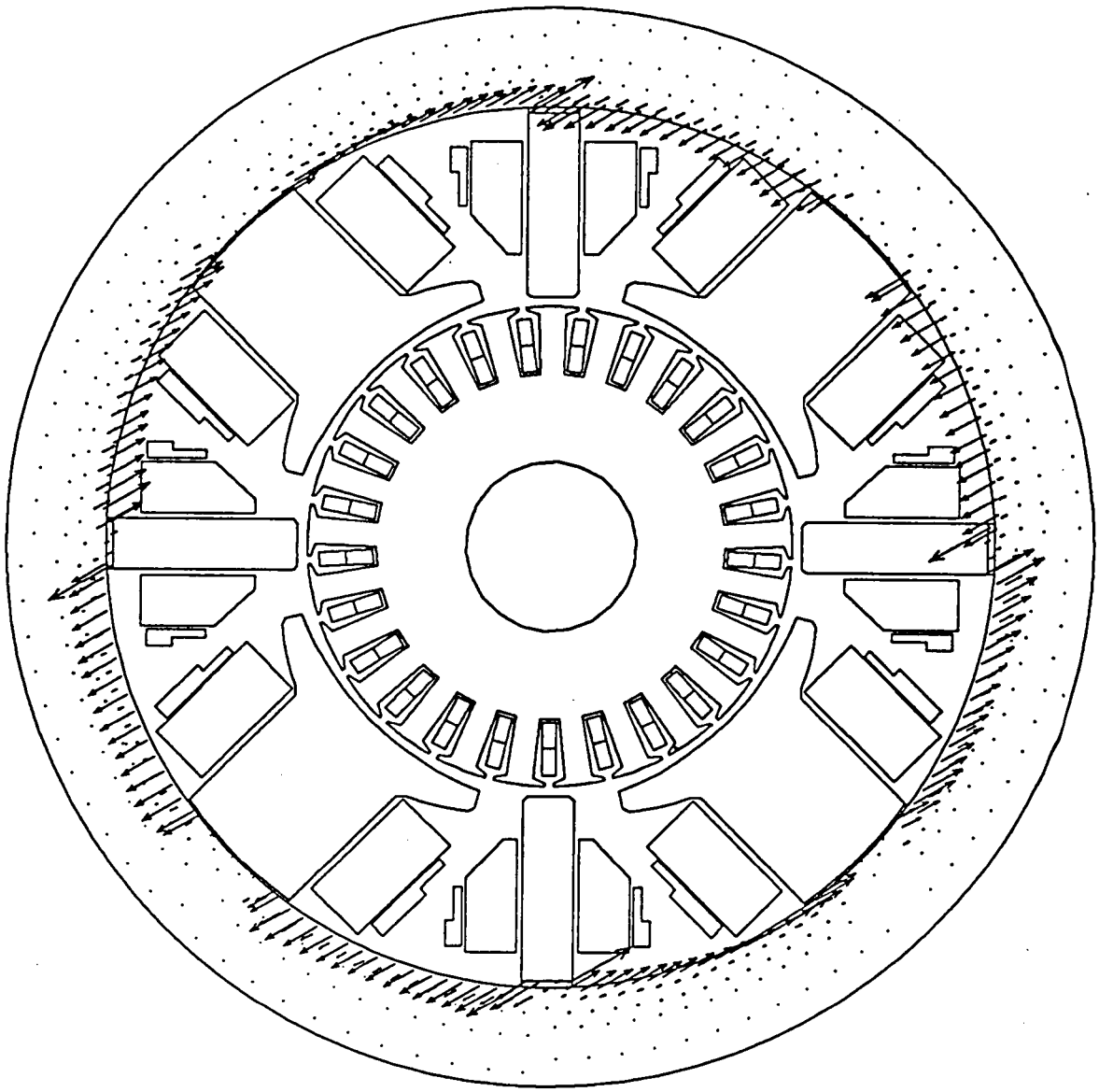

Fig.4.19 (b) $t=5T_s$ and $I_a=15.9\ A$.

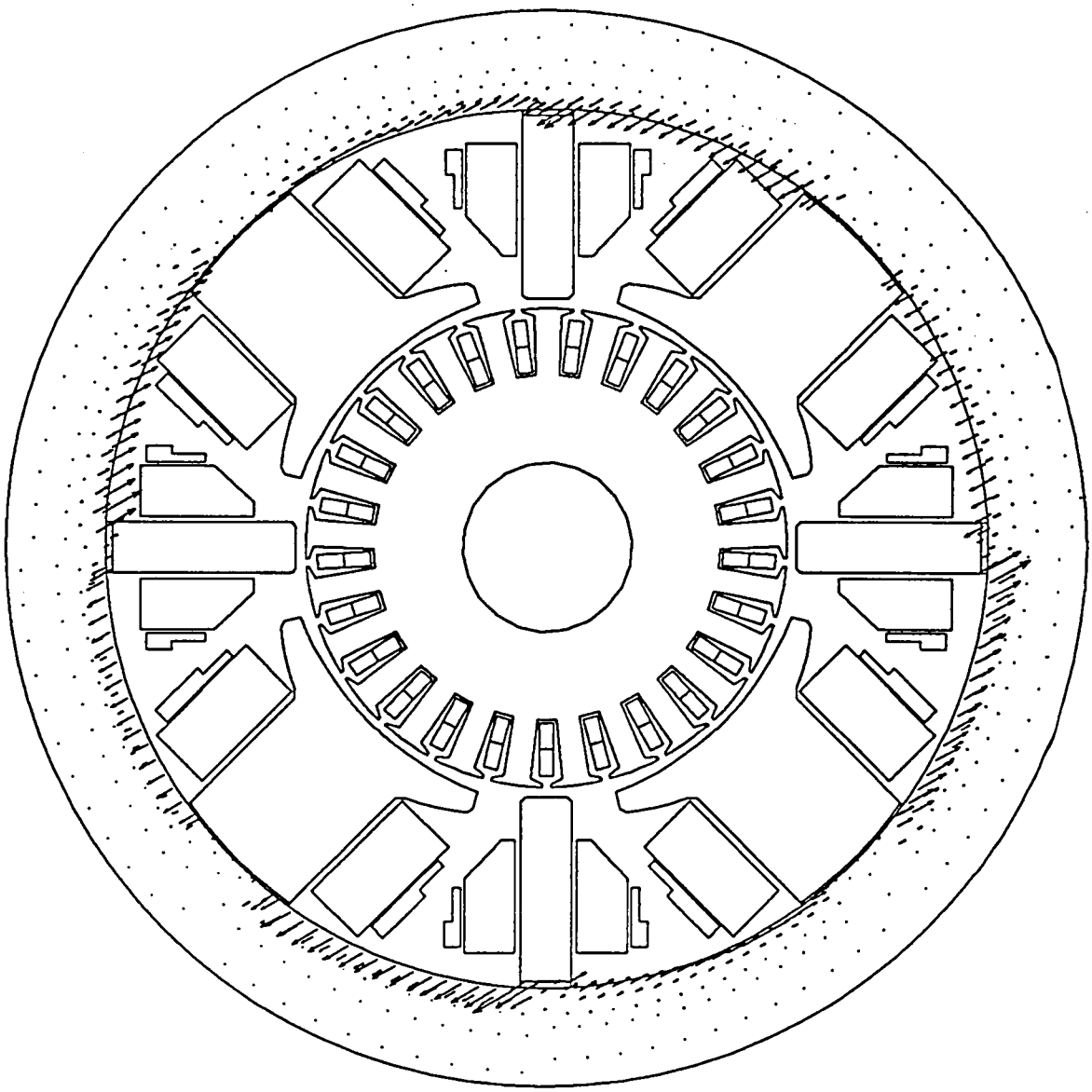

Fig.4.19 (c) t=10T_s and I_a=16.0 A.

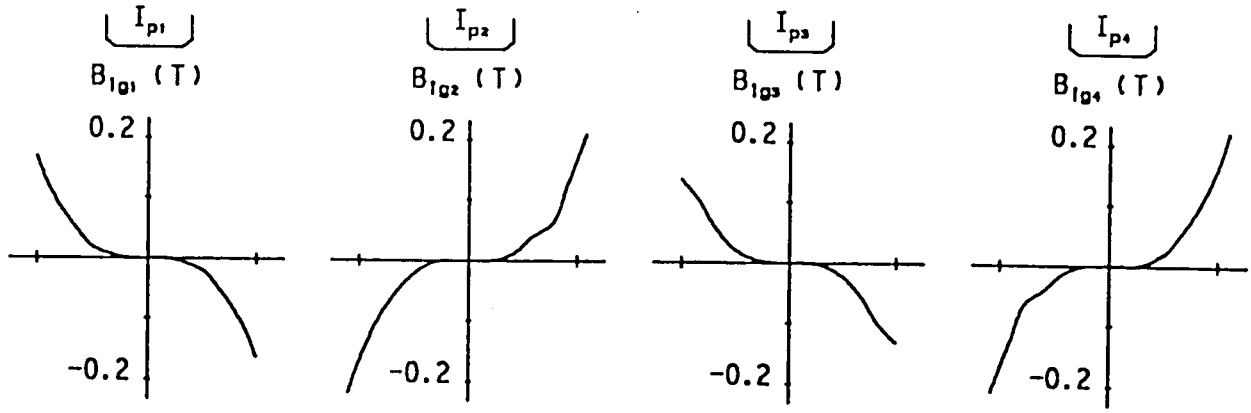

Fig.4.20 (a) t=0 and I_a=0.

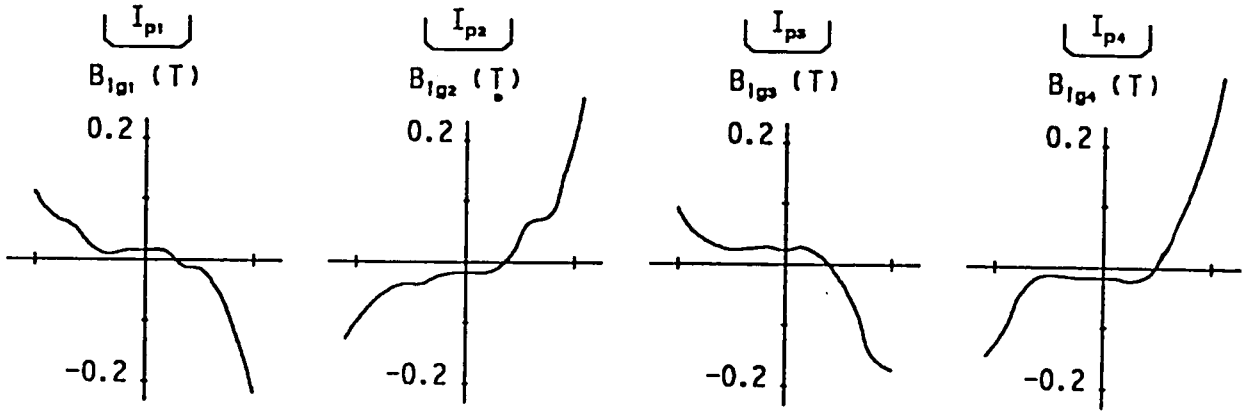

Fig.4.20 (b) $t=2T_s$ and I_a=13.8 A.

Fig.4.20 Transitional magnetic flux density distributions in commutating zones for T_s=1.15 ms.

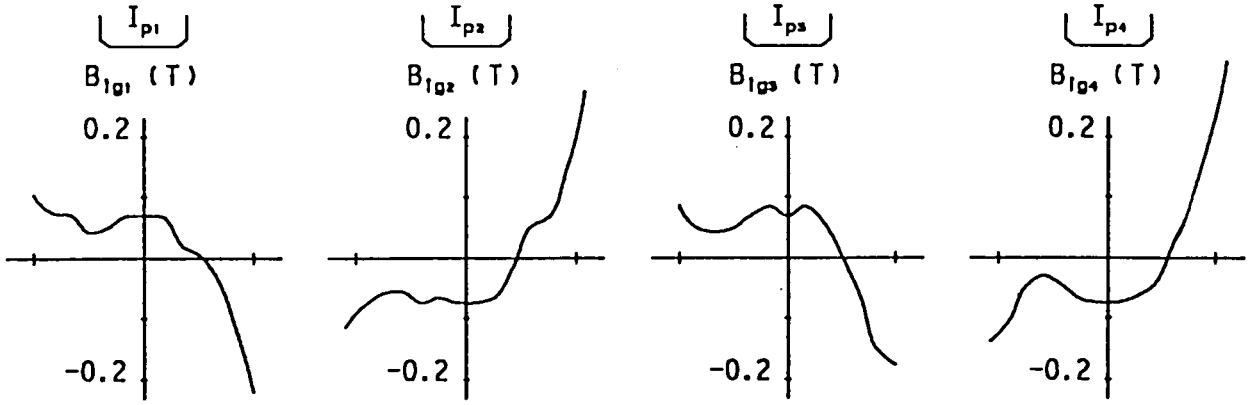

Fig.4.20 (c) t=5T_s and I_a=15.9 A.

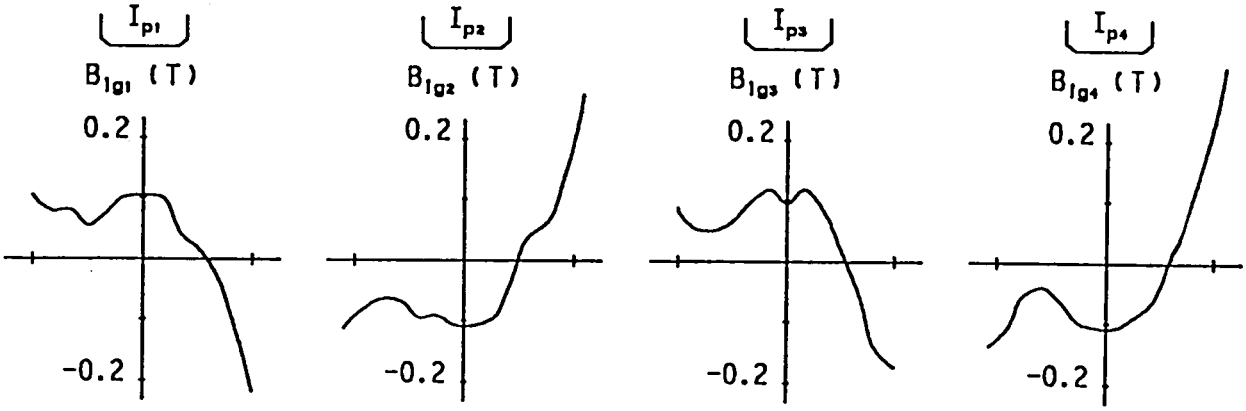

Fig.4.20 (d) t=10T_s and I_a=16.0 A.

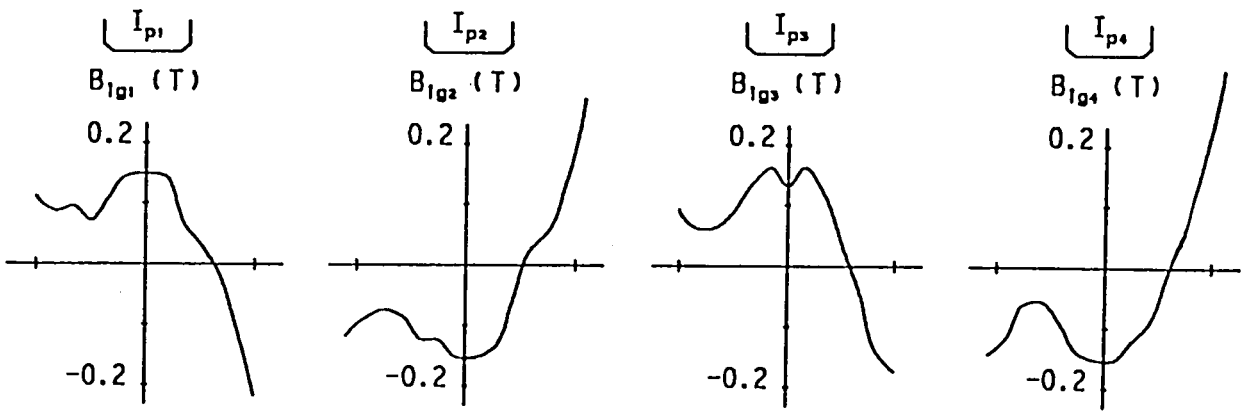

Fig.4.20 (e) $t\to\infty$ and I_a=16.0 A.

4.4.4 Improvement of transient response of magnetic flux by using partially laminated yoke

In Chapter 3 and in Article 4.4.3 we made clear experimentally and theoretically that the delay of the transient flux responses to an abrupt change of the armature current is mainly caused by the eddy current induced in the inner skin region of the yoke. Also, in Section 4.3, it has been shown that the delay has a bad influence on the commutation characteristics of an actual dc motor. Recently, in the small-sized dc motor for the special application, the laminated core is often used in the inner skin region of the yoke, as shown in Fig.4.21, so as to decrease the induced eddy current and improve the transient flux responses and so the commutation characteristics. In the figure, L_y is the thickness of the laminated core. However, the quantitative grasp of the lamination on the above decrease and the improvement has been yet done.

Therefore, we investigate quantitatively effects of the use of the laminated core in the yoke by numerical analyses. Here, it is assumed that thin iron plate of the thickness 1 *mm* is used for the laminated core, of which the conductivity is zero. However, in the analysis, its actual thickness L_y is doubled by the

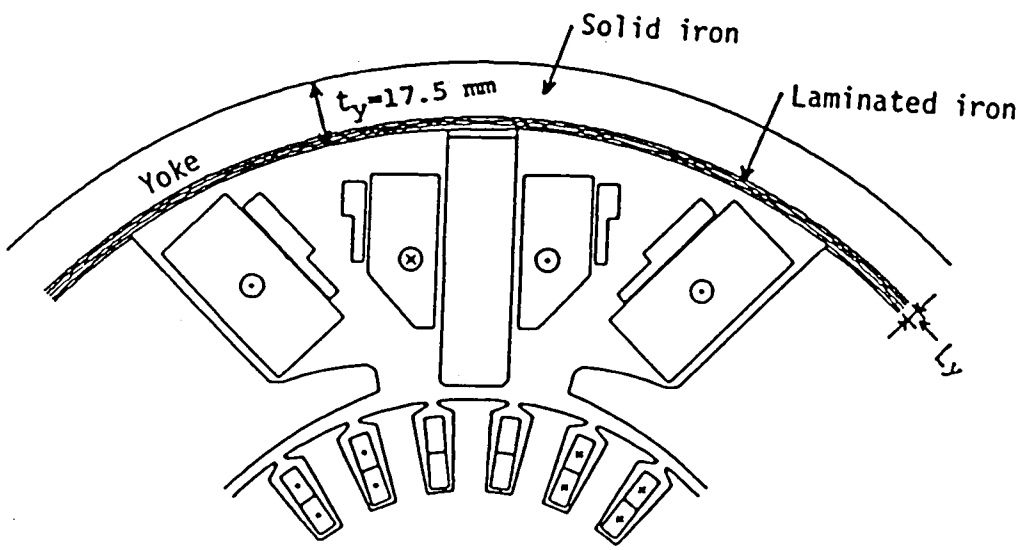

Fig.4.21 Laminated iron in inner skin region of yoke.

assumption (5) shown in Article 4.4.3, as follows

$$L_y' = 2L_y. \tag{4.8}$$

Also, for simplifying the analysis, it is assumed that the magnetization characteristic of the iron plate is the same as the one of the solid iron yoke shown in Fig.4.11 and the initial flux distribution is the same as shown in Fig.4.17(a).

Figure 4.22 shows the calculated responses of Φ_{y1}, Φ_{y2}, Φ_{i1}, Φ_{i2}, B_{ig1} and B_{ig2} to the change of I_a, where L_y'=2 *mm*, I_f=1.3 *A*, I_a=16 {1-exp(-t/T_m)} *A* and T_m=1.15 *ms*. In this case, the flux in the yoke, which is excited by I_a, incline to be concentrated mostly in the laminated region, because the penetration of the flux into the residual solid iron is obstructed by the induced eddy current. Then, the magnetic saturation and the hysteresis phenomena are arose without delaying to I_a in the laminated region in which the eddy current is not induced. As the result, a large difference between Φ_{y1} and Φ_{y2} is occurred. However, in comparison with the

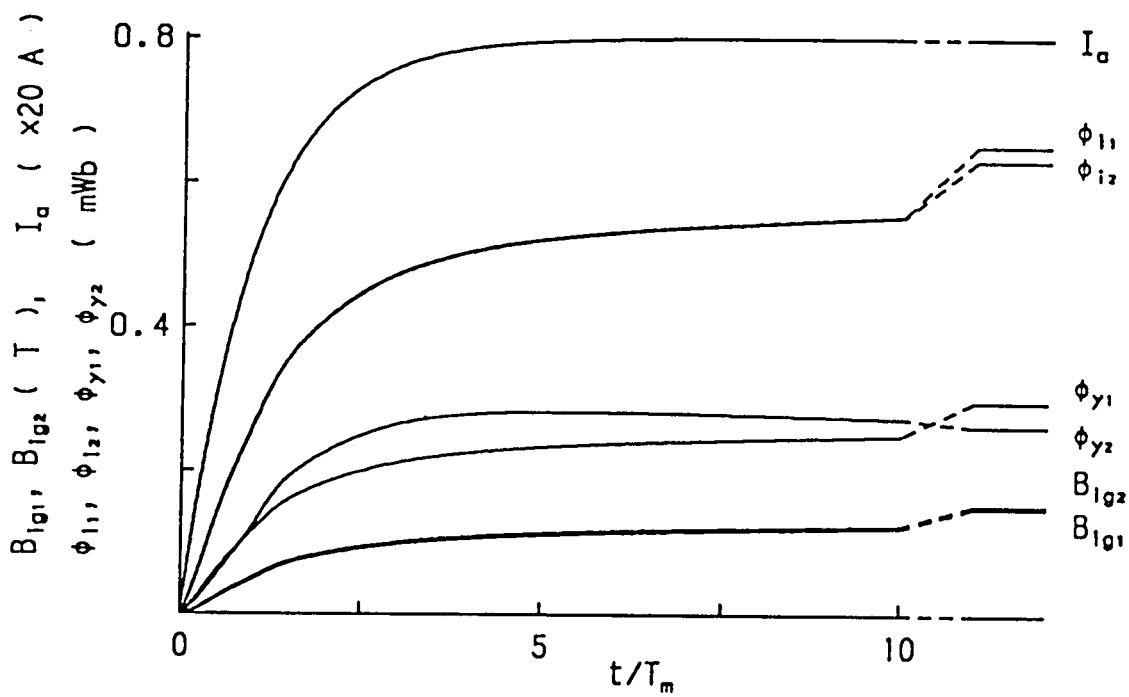

Fig.4.22 Calculated results of transient responses of magnetic fluxes and flux densities for T_m=1.15 *ms* and lamination L_y'=2 *mm*.

results in Fig.4.16 for L_y=0, we can see that the delays of the responses are fairly decreased by the use of the laminated plate of L_y'=2 *mm*.

In Figs.4.23 (a) and (b), we show the flux density distributions at $t=2T_s$ and $5T_s$ in the commutating zones for L_y'=2 *mm*. We can readily see that the flux density distributions are much improved in comparison with the ones in Figs.4.20 (b) and (c) for L_y=0.

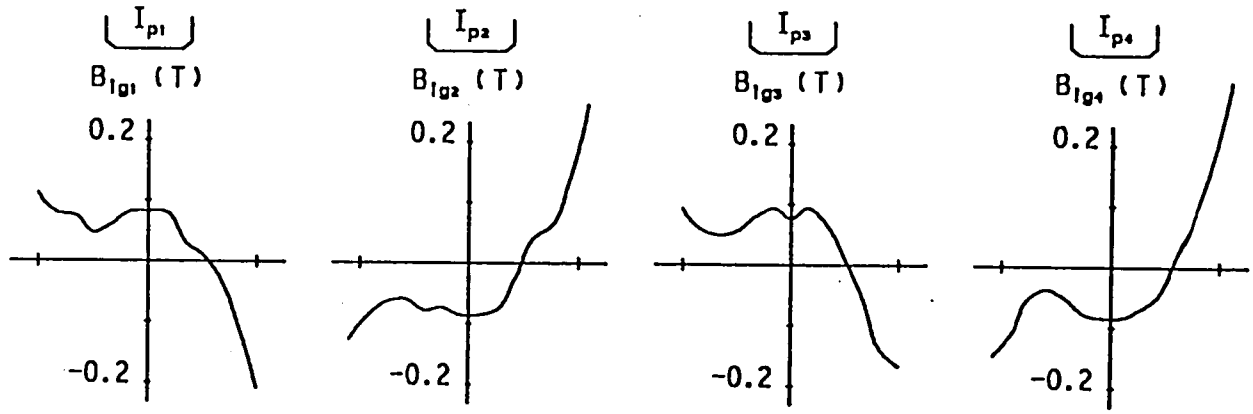

Fig.4.23 (a) $t=2T_s$ and I_a=13.8 *A*.

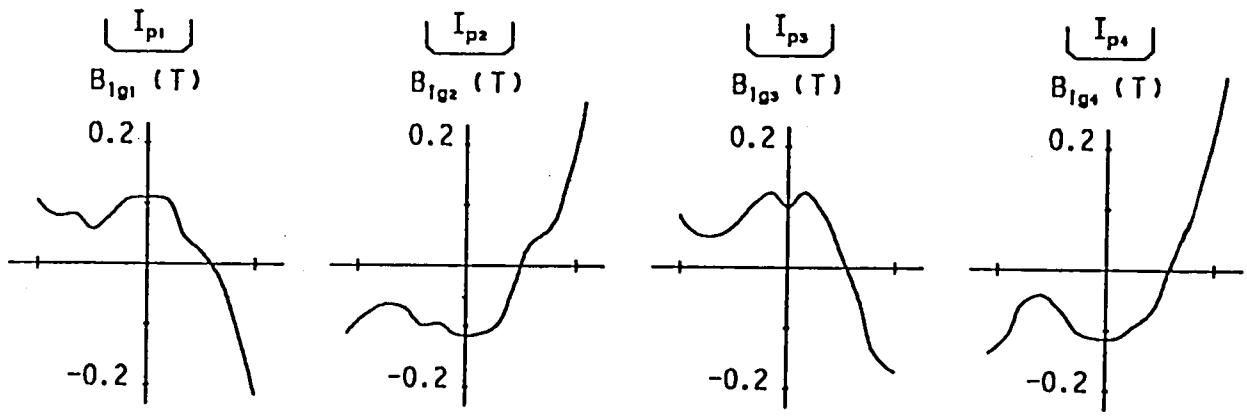

Fig.4.23 (b) $t=5T_s$ and I_a=15.9 *A*.

Fig.4.23 Transitional magnetic flux density distributions in commutating zones for T_s=1.15 *ms* and lamination L_y'=2 *mm*.

Figure 4.24 shows the calculated results of the transient flux responses for L_y'=4 *mm*, where the other parameters are the same as the ones in Figs.4.16 and 4.22. In the yoke, the flux by I_a mainly passes through the laminated region and so the eddy current induced in the other region is decreased very much. Therefore, the responses in Fig.4.24 are considerably fastened than the ones in Figs.4.16 and 4.22. And, the fastened responses of B_{ig1} and B_{ig2} may improve the initial commutation characteristics of the dc motor. However, from visible difference between Φ_{y1} and Φ_{y2} for the initial duration $0<t\leqq 2T_m$ in Fig.4.24, it is seen that the magnetic saturation and the hysteresis phenomenon occur in the laminated region of the yoke. Now, it is needless to say that the flux density distributions in the commutating zones, which are nearly equal to the ones for L_y'=6 *mm* as shown late in Figs.4.29, are much improved more than the ones for L_y=0 and L_y=$L_y'/2$=1 *mm*.

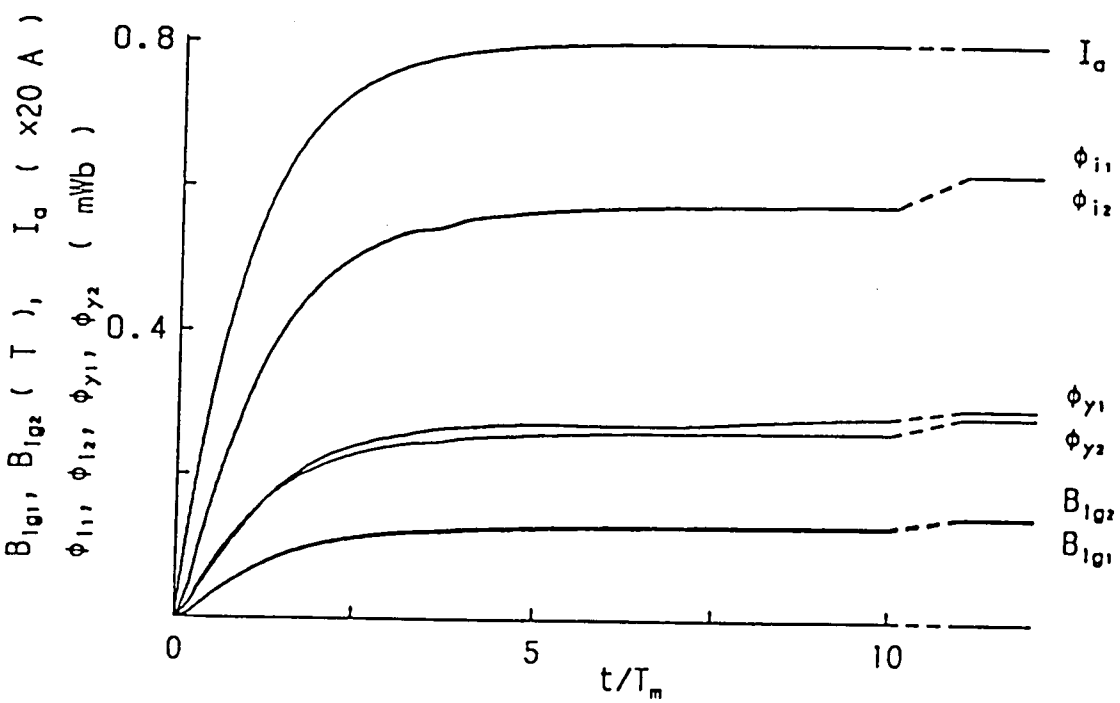

Fig.4.24 Calculated results of transient responses of magnetic fluxes and flux densities for T_m=1.15 *ms* and lamination L_y'=4 *mm*.

Figure 4.25 shows the same calculated results for L_y'=6 *mm*. We can see that responses of Φ_{y1}, Φ_{y2}, Φ_{i1}, Φ_{i2}, B_{ig1} and B_{ig2} to I_a is sufficiently improved, since the values at $t=6T_m$ exceed about 96 % of their final ones. From these results, it may be suggested that a good commutation of the dc motor specified in Table 4.1 can be obtained for $L_y=L_y'/2$=3 *mm*.

In Figs.4.26 (a) and (b), there are shown the flux distributions at $t=2T_m$ and $5T_m$, where ΔA_{eq}=1.5 *mWb/m*. We can see that the flux change in the yoke is mainly occurred in the laminated region. Also, we can see that the fluxes through the interpole cores and its airgaps are more increased than the ones in Figs.4.17 (b) and (c) for L_y=0. Figures 4.27 (a) and (b) give the flux density distributions at $t=2T_m$ and $5T_m$. In the laminated region of the yoke, the flux density is smaller than 1.1 *T*, and so the magnetic saturation is not occurred.

Also, the eddy current density distributions are shown in Figs.4.28 (a) and (b), from which it is seen that the eddy current densities induced in the yoke is much smaller than the ones in Figs.4.19 (b) and (c) for L_y=0.

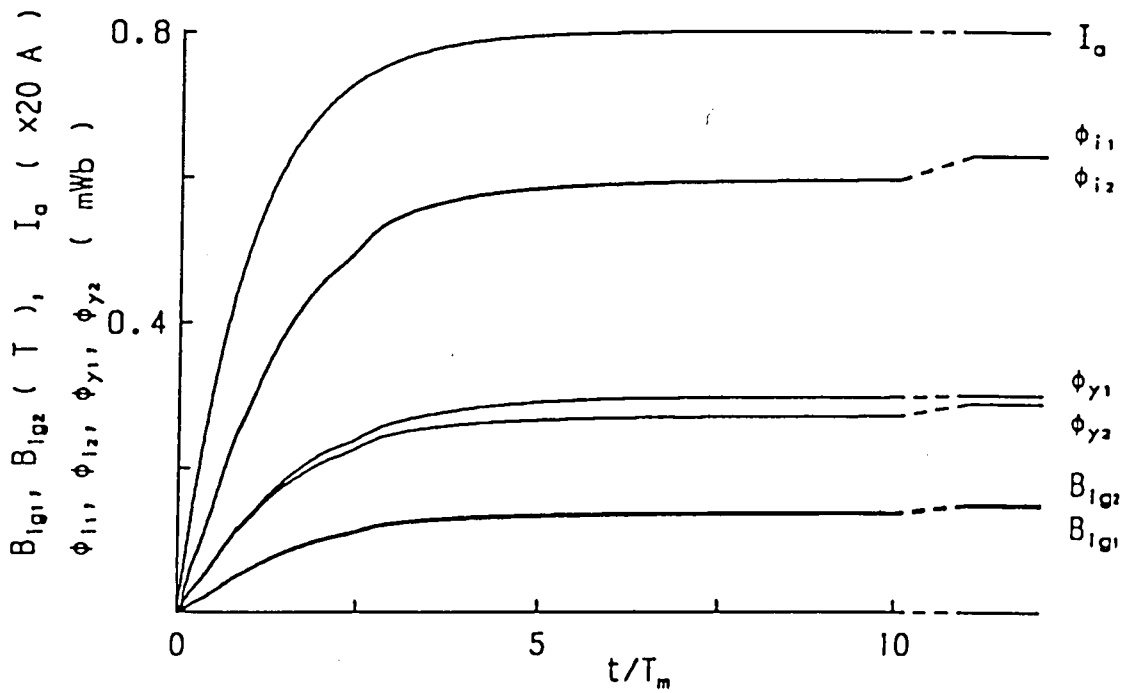

Fig.4.25 Calculated results of transient responses of magnetic fluxes and flux densities for T_m=1.15 *ms* and lamination L_y'=6 *mm*.

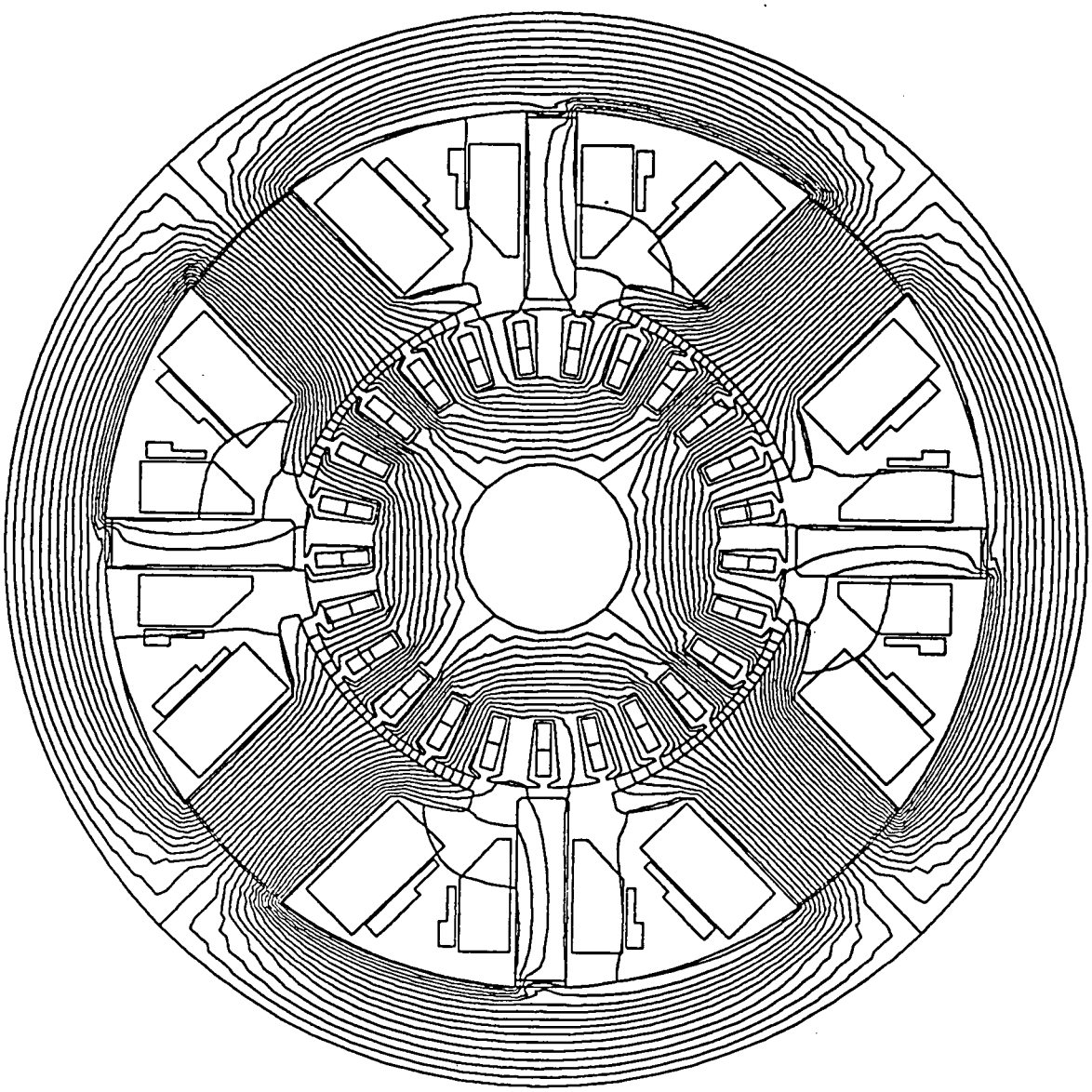

Fig.4.26 (a) $t=2T_s$ and $I_a=13.8\ A$.

Fig.4.26 Transitional magnetic flux distributions for $T_s=1.15\ ms$, lamination $L_y'=6\ mm$ and $\Delta A_{eq}=1.5\ mWb/m$.

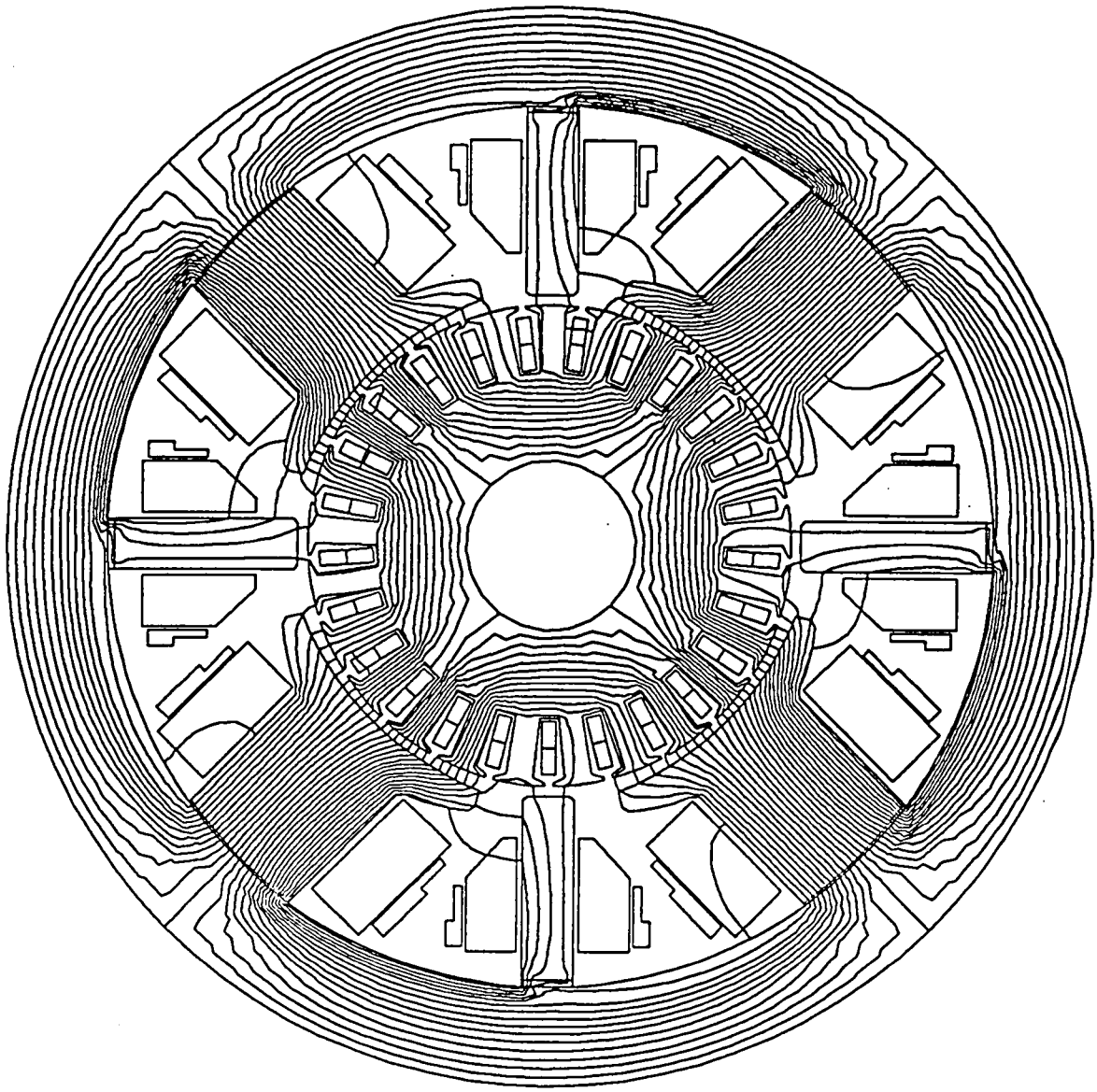

Fig.4.26 (b) $t=5T_s$ and $I_a=15.9\ A$.

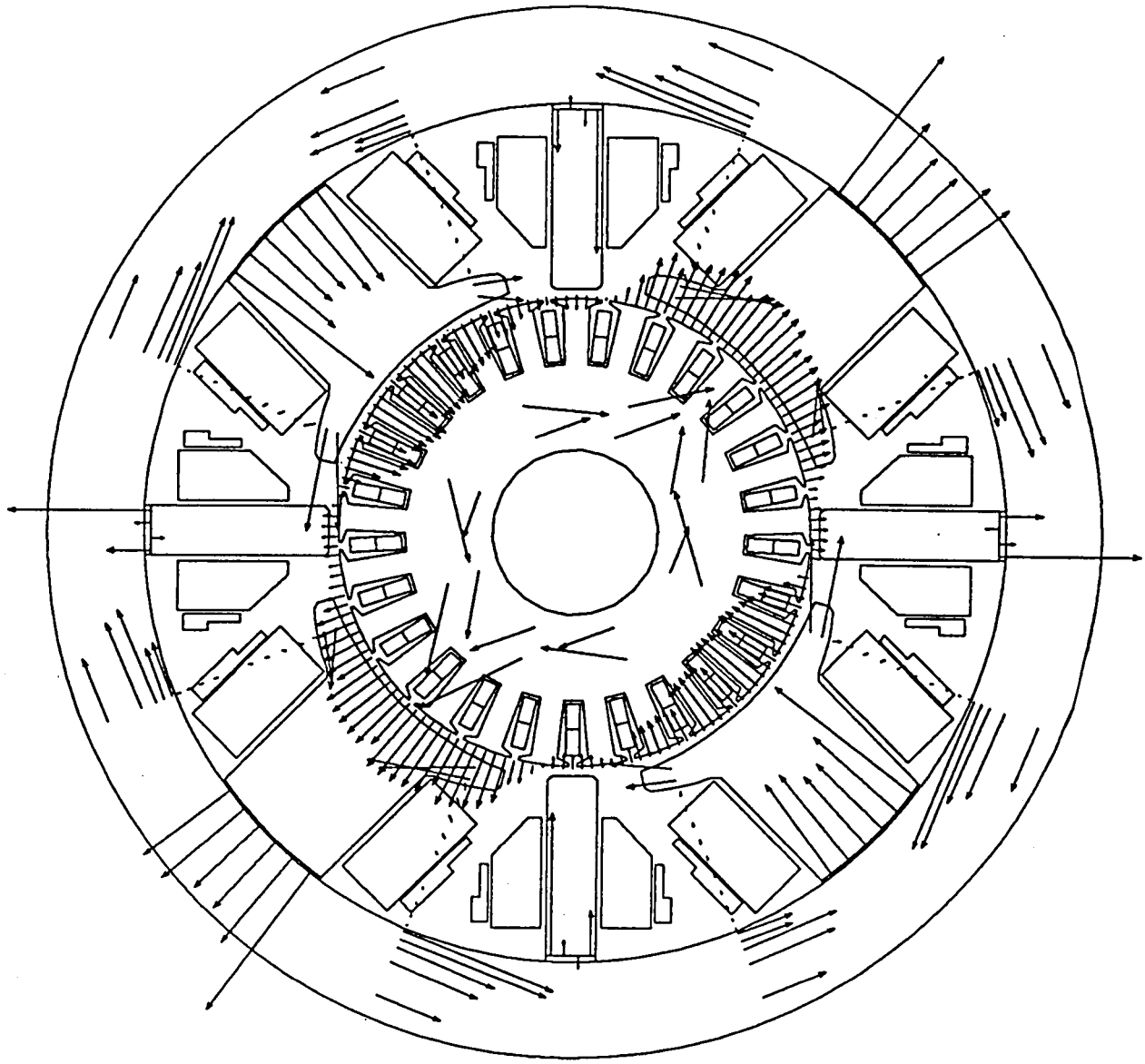

Fig.4.27 (a) $t=2T_s$ and $I_a=13.8\ A$.

Fig.4.27 Transitional magnetic flux density distributions for $T_s=1.15\ ms$ and lamination $L_y'=6\ mm$.

⟶ 2.0 T

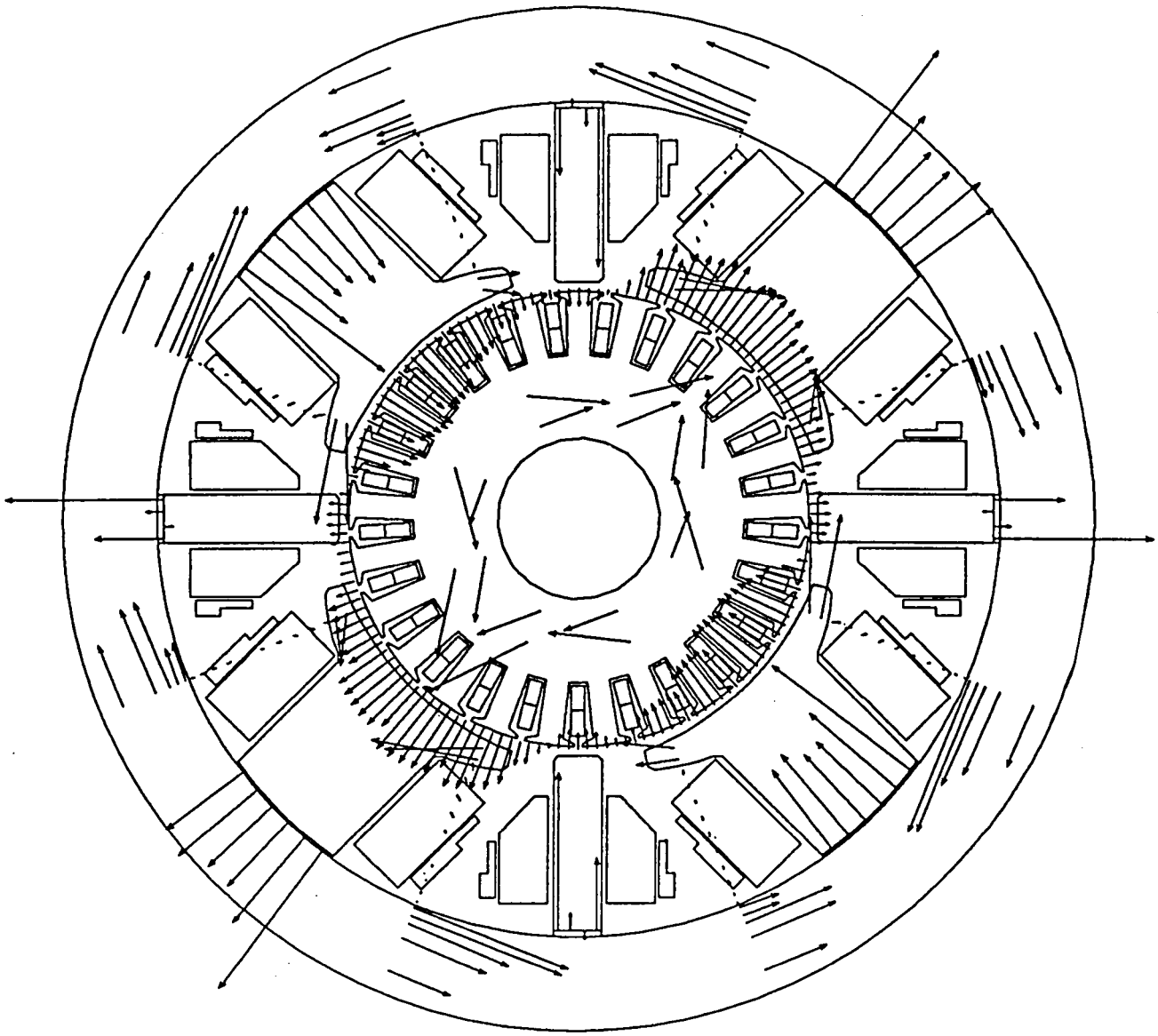

Fig.4.27 (b) t=5T_s and I_a=15.9 A.

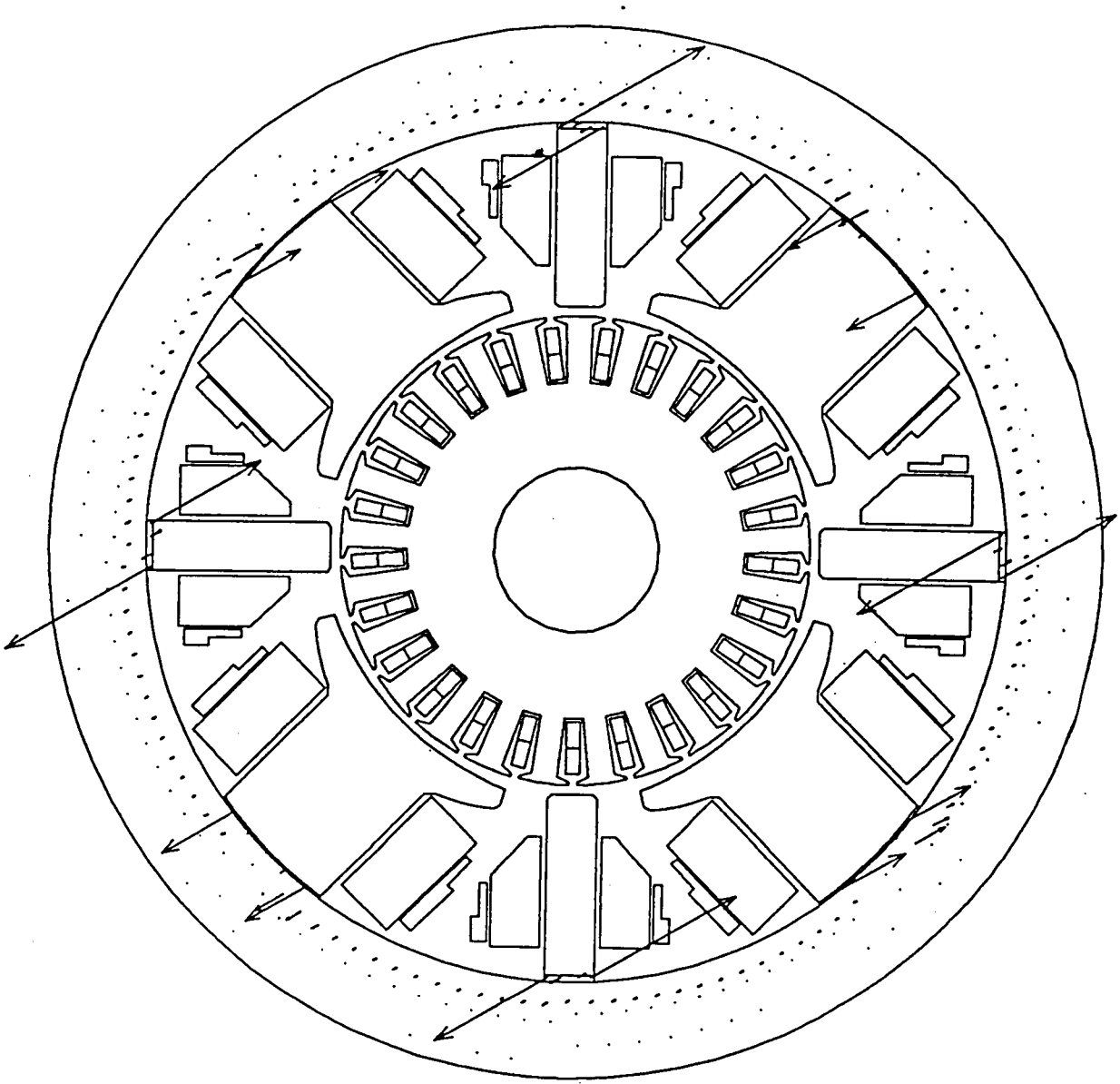

Fig.4.28 (a) $t=2T_s$ and $I_a=13.8\ A$.

Fig.4.28 Transitional eddy current density distributions for $T_s=1.15\ ms$ and lamination $L_y'=6\ mm$.

⟶ 2.0 MA/m²

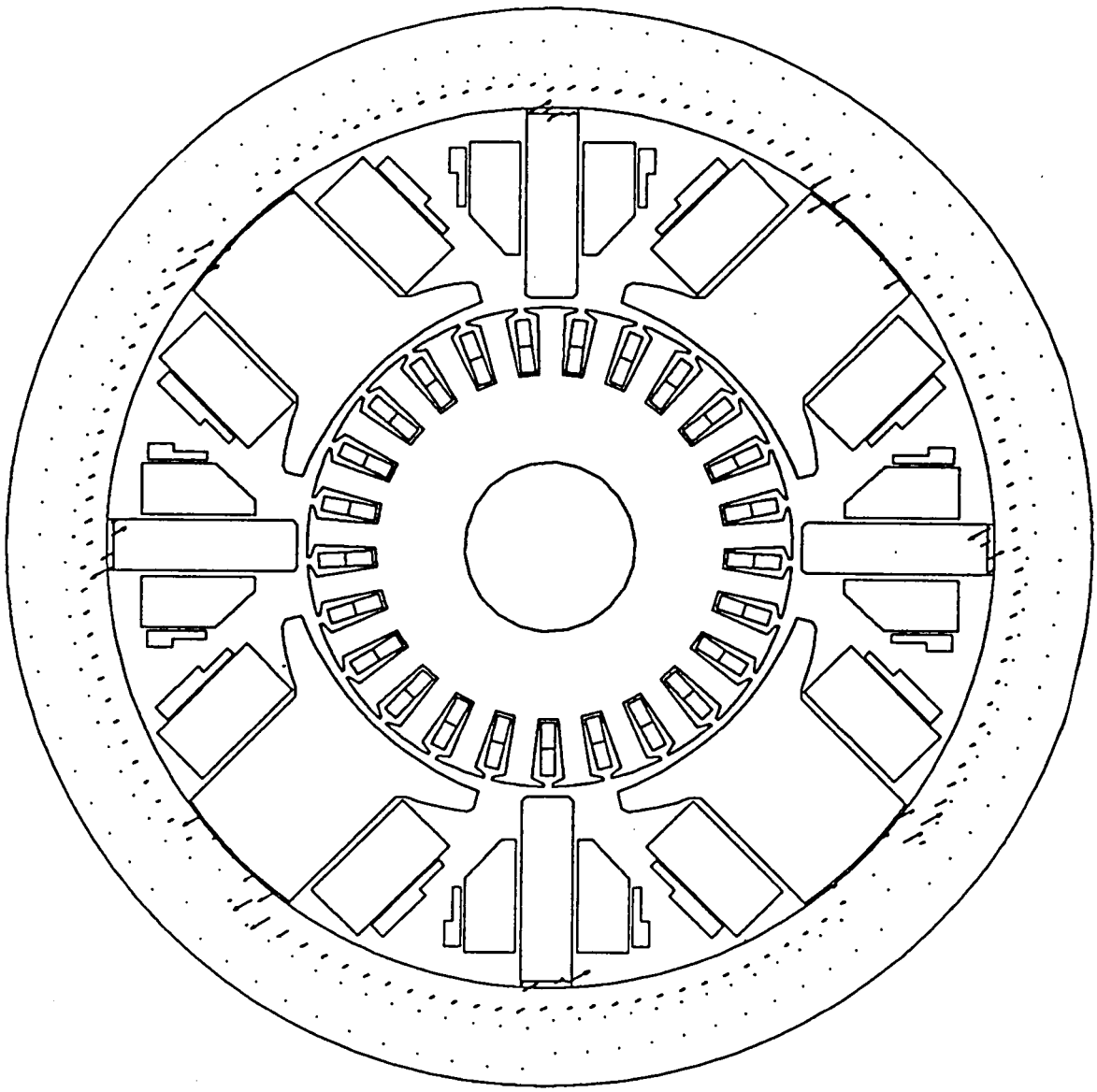

Fig.4.28 (b) t=5T_s and I_a=15.9 A.

In Figs.4.29 (a) and (b), there are shown the flux density distributions for L_y'=6 *mm* at $t=2T_s$ and $5T_s$ in the commutating zones. We can see that those distributions respond well to I_a and are improved enough to get the good commutation characteristics of the dc motor.

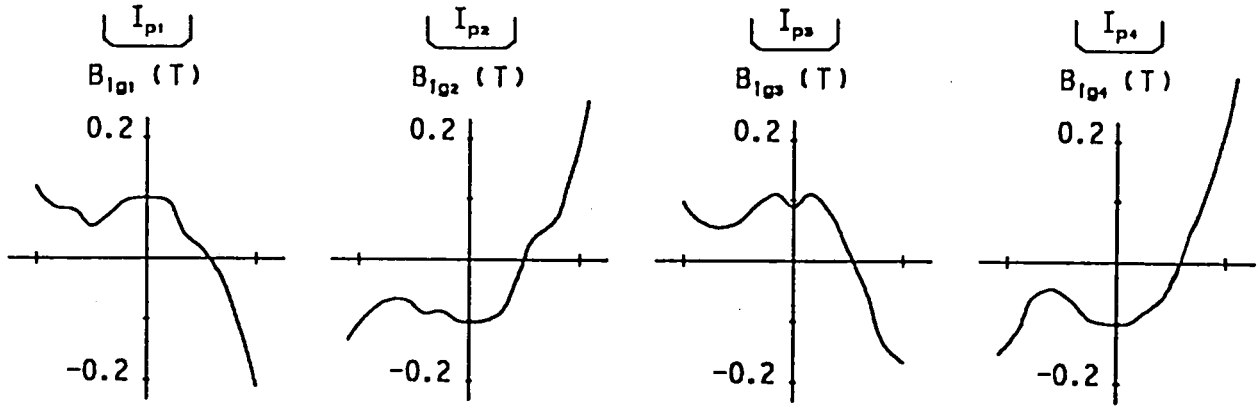

Fig.4.29 (a) $t=2T_s$ and I_a=13.8 *A*.

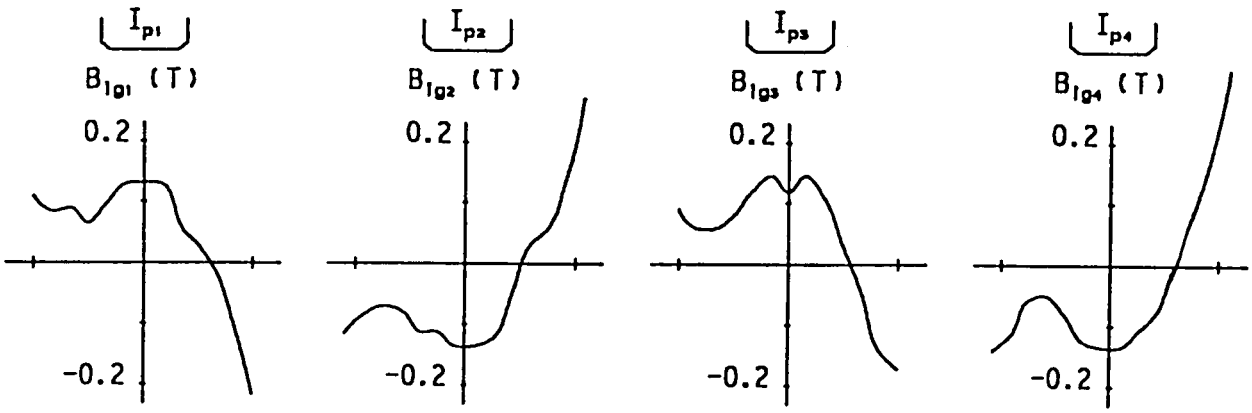

Fig.4.29 (b) $t=5T_s$ and I_a=15.9 *A*.

Fig.4.29 Transitional magnetic flux density distributions in commutating zones for T_s=1.15 *ms* and lamination L_y'=6 *mm*.

Figure 4.30 shows the transient responses of the fluxes and the flux densities for L_y'=8mm. Now, the results are almost equal to the ones for the next case where the yoke is fully laminated.

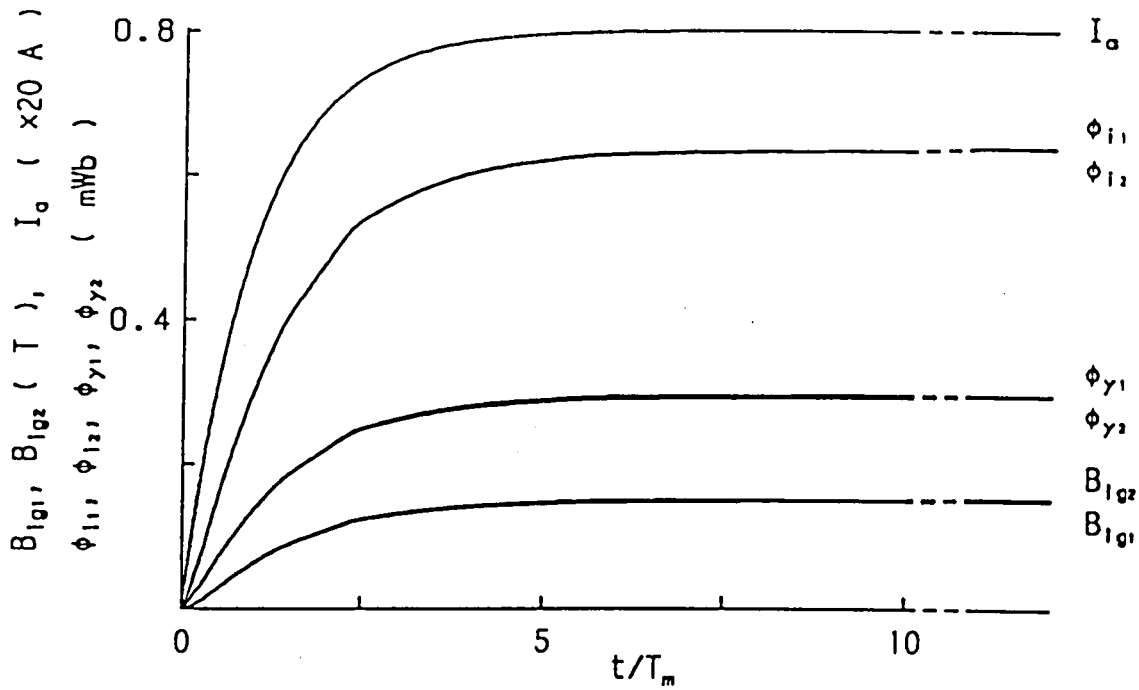

Fig.4.30 Calculated results of transient responses of magnetic fluxes and flux densities for T_m=1.15 ms and lamination L_y'=8 mm.

Next, we investigate the transient responses of the fluxes and the flux densities for the dc motor whose yoke is fully laminated and L_y'=35 mm. In this case, the eddy current is induced only in the liners, and so the fluxes and the flux densities can fast respond to I_a as shown in Fig.4.31. We can readily find the relation of $\Phi_{y1} \fallingdotseq \Phi_{y2}$. This means that the flux in the yoke, which is excited by I_a, may distribute uniformly in the whole yoke and so the magnetic saturation and the hysteresis can't occur. Also, we can see that the responses of the flux densities B_{ig1} and B_{ig2} are nearly equal to the ones in Fig.4.25 for L_y'=6 mm. In this addition, the flux density distribution at $t=2T_m$ and $5T_m$ became much the same as the ones in Figs.4.27 and 4.29.

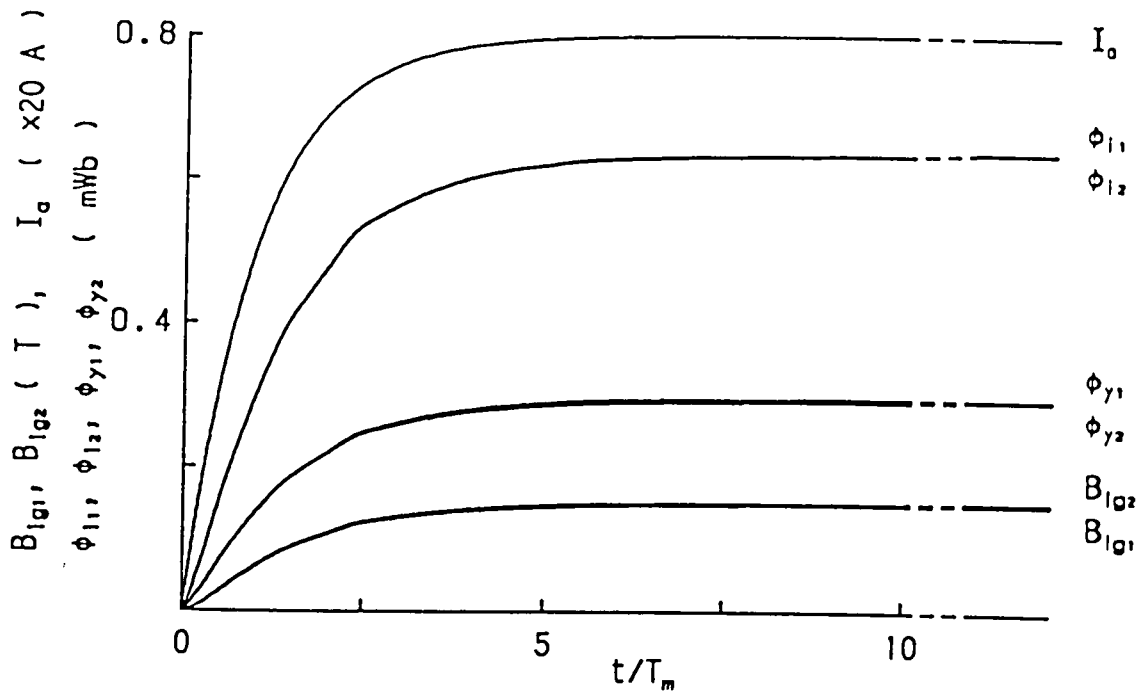

Fig.4.31 Calculated results of transient responses of magnetic fluxes and flux densities for T_a=1.15 *ms* and lamination L_y'=35 *mm*.

4.5 Conclusion

The main results, which were obtained by the above experiment and numerical calculation, are as follows:

(1) The specification of a small-sized dc motor to be used for an experiment was shown, in which the search coils and the GaAs Hall cells are set to measure transient commutation characteristics of the armature coil current and the transient responses of the magnetic flux and the flux density in important regions of the motor when the armature current changes abruptly.

(2) The theoretical commutation equations for the specified dc motor for experiment were introduced. Then, it was suggested that the transient responses of the magnetic flux density distribution and the average magnetic flux in the

interpole airgap are closely concerned to the transient commutation characteristics of the dc motor whose armature current I_a changes abruptly.

(3) From the experimental results of the transient commutation characteristics, it was affirmed that the under-commutation arises for the initial duration $0<t\leqq 5T_m$ after an abrupt change of I_a because of the initial delay of the transient response of the magnetic flux density in the interpole airgap.

(4) From the experimental results of the transient responses of the magnetic flux and the flux density when the dc motor stands still and I_a is suddenly supplied, it was seen that the responses of the magnetic fluxes in the yoke and the interpole cores are considerably delayed by the eddy currents induced in the yoke and the interpole liner, and so that the one of the magnetic flux density in the interpole airgap is delayed, too, for the initial duration $0<t\leqq 10T_m$.

(5) The numerical analysis of the transient distribution of the magnetic flux was carried out by the two-dimensional nodal method derived in Chapter 2, where the magnetic hysteresis was considered only in the inner skin region of about 30 % of the yoke by referring to the conclusion (7) in Section 3.5, and the actual thickness t_y =17.5 *mm* of the yoke was doubled in the numerical analysis.

(6) The validity of the above analysis was ascertained by showing that the calculated results of the transient responses of the magnetic fluxes in the yoke and the interpole, the flux densities in the interpole airgap, etc. agree well with the experimental results.

(7) From the calculated results of the transient distributions of the magnetic flux, the flux density and the eddy current density, it was made clear that the much magnetic flux and the large eddy current density concentrate in the inner skin region of the yoke and the outer skin one of an interpole liner for the initial duration. Also, in the skin region of the yoke, the concentrated magnetic flux, which brings about the magnetic saturation, is kept its magnitude after a lapse of time by the magnetic hysteresis.

(8) It was denoted that the initial large eddy current density delays not only

the transient responses of the magnetic fluxes in the yoke and the interpole but also the one of the magnetic flux density in the interpole airgap. Also, it was pointed out that the eddy current density slowly decreases and so that the magnetic fluxes need a long time to reach those final steady values.

(9) The effect of the partial lamination of the yoke on the improvement of the transient response of the magnetic flux was numerically investigated. As a result, when the partial lamination was applied in the inner skin region about 3 *mm* out of the whole thickness 17.5 *mm* of the yoke, the transient response was enough improved to obtain the good transient commutation characteristics of the dc motor.

REFERENCES

Part I :

[1] Langsdorf, A. S. : 'Principles of Direct-Current Machines,' 6th ed., McGraw-Hill, New York, pp. 208-217(1959).

[2] Hirose, K., and T. Shimizu : 'Electric Machines I(in Japanese),' 2nd ed., OHM Sha, Tokyo, pp. 153-157(1963).

[3] The Institute of Electrical Engineers of Japan : 'Mercury Rectifiers(in Japanese),' 26th ed., I.E.E.J., Tokyo, pp. 306-331(1963).

[4] Aoki, S. : 'Speed Control of D.C. Motors and Application of Mercury Rectifiers Thereto(in Japanese),' Toshiba Review, Vol.15, No. 7, pp. 249-260(1936).

[5] Editorial Committee for SCR Handbook : 'SCR Handbook(in Japanese),' Maruzen, Tokyo, (1966).

[6] Miyairi, S. : 'Thyristor Applications Handbook(in Japanese),' Nikkan Kogyo Shinbun Sha, Tokyo, (1972).

[7] Yamamura, A., and S. Nishimura : 'Thyristor Applications Handbook(in Japanese),' OHM Sha, Tokyo, (1978).

[8] Ikeda, Y., M. Takeuchi, H. Matsushima, T. Toda, T. Nakagawa et al. : 'Recent Power Semi-Conductor Devices(Short Special Edition)(in Japanese),' J.I.E.E.J., Vol. 103, No. 1, pp. 1-26(1983).

[9] Nabae, A., Y. Yoshida, M. Kondo, F. Harashima, M. Zifuku et al. : 'Technical Trend of Recent Variable Speed Machines(Short Special Edition)(in Japanese),' ibid., Vol. 103, No. 9, pp. 869-941(1983).

[10] Sakata, H. : 'Thyristor Converter Controlled by Micro-Computer(in Japanese),' Memoirs of Japan Society for Power Electronics, Vol. 8, No. 50, pp. 80-93(1983).

[11] Yamanaka, T. : 'Inverter Control System for Electric Traction Motor(in Japanese),' ibid., Vol. 10, pp. 54-64(1985).

[12] Harris, L. D. :'Servomechanism Characteristics of D-C Motor Driven by Controlled Rectifiers,' A.I.E.E. Trans., Vol. 70, pp. 1582-1588(1951).

[13] Ishizaki, T., and S. Ishikawa : 'Dynamic Characteristics of DC Separately Excited Servomotor Driven by SCR(in Japanese),' J.I.E.E.J, Vol. 83, No. 7, pp. 1201-1206(1963).

[14] Nitta, K., Y. Okitsu, T. Suzuki, and Y. Kinouchi : 'Dynamic Characteristics of Separately Excited DC Motor Operated by a Thyristor Pulsating Power Supply(in Japanese),' ibid., Vol. 90, No. 8, pp. 1577-1584(1970).

[15] Takeuchi, T. : 'Characteristics of D.C. Motor Running Under Full-wave Rectifying Circuit(in Japanese),' ibid., Vol. 84, No. 7, pp. 1094-1103(1964).

[16] Hosono, I. : 'SCR Control of DC Motors(in Japanese),' Mitsubishi Giho, Vol. 37, No. 5, pp. 45-51(1963).

[17] Black, K. G. : 'The Effect of Rectifier Discontinuous Current on Motor Performance,' I.E.E.E. Trans. on AI, Vol. 83, No. 75, pp. 377-382(1964).

[18] Parrish, JR, E. A., and E. S. McVey : 'A Theoretical Model for Single-Phase Silicon Controlled Rectifier Systems,' I.E.E.E. on AC, Vol. AC-12, No. 5, pp. 577-579(1967).

[19] Parimelalagan, R., and V. Rajagopalan : 'Steady-State Investigations of Chopper-Fed DC Motor with Separate Excitation,' I.E.E.E. Trans. on IGA, Vol. IGA-7, No. 1, pp. 101-108(1971).

[20] Irie, H., T. Fujii, and T. Ishizaki : 'Controlling Characteristics of a Separately-excited D-C Motor Driven by a Thyristor Chopper(in Japanese),' J.I.E.E.J., Vol. 88, No. 4, pp. 675-683(1968).

[21] Inose, F. : 'On the Static Character of the Transistor Chopper(in Japanese),' ibid., Vol. 84, No. 7, pp. 1085-1093(1964).

[22] Yanase, A. : 'Running Characteristic of DC Motor Driven Chopper System(in Japanese),' ibid., Vol. 96-B, No. 10, pp. 489-496(1976).

[23] Zabar, Z., and A.Alexandrovitz : 'Guidelines on Adaptation of Thyristorized

Switch for Motor Speed Control,' I.E.E.E. on IECI, Vol. IECI-17, No. 1, pp. 10-13(1970)

[24] McMurray, W. : 'Silicon- Controlled Rectifier D-C to D-C Power Converters,' A.I.E.E. Trans., Vol. 83, pp. 198-203(1964).

[25] Irie, H. : 'Speed Control of Separately Excited DC Motor Controlled by Bilateral Chopper Circuit(in Japanese),' Memoirs of Japan Society for Power Electronics, Vol. 1, No. 3, pp. 21-26(1980).

[26] Togino, K. : 'Analysis of Electronic Servo-system Adapted to Numerically Controlled Machine-tool(4),' J.M.L. of Japan, Vol. 13, No. 6, pp. 274-280(1959).

[27] Hayashi, S. : 'Periodically Interrupted Electric Circuits,' Denki Shoin, Kyoto, (1961).

[28] Umoto, J., and T. Ando : 'Analysis of Separately Excited DC Motor Controlled by Single-Phase Combined Thyristor Bridge Rectifier Circuit(in Japanese),' Convention Records at the Annual Meeting in Kansai District of I.E.E.J., No. 3-4, (1968).

[29] Umoto, J., and T. Ando : 'Analysis of Dynamic Characteristics of DC Motor Controlled by Single-Phase Thyristor Rectifier Circuit(in Japanese),' Convention Records at the Annual Meeting of I.E.E.J., No. 452, (1968).

[30] Umoto, J., and T. Ando : 'Analysis of Time Constant of DC Motor Controlled by Single-Phase Half-Wave Rectifier Circuit(in Japanese),' ibid., No. 616, (1969).

[31] Umoto, J., S. Okabayashi, and T. Ando : 'Analysis of Dynamic Characteristics of DC Motor Controlled by Single-Phase Thyristor Rectifier Circuit(1)(in Japanese),' Convention Records at the Annual Meeting in Kansai District of I.E.E.J., No. G3-13, (1970).

[32] Umoto, J., S. Okabayashi, and T. Ando : 'Analysis of Dynamic Characteristics of DC Motor Controlled by Single-Phase Thyristor Rectifier Circuit(2)(in Japanese),' Convention Records at the Annual Meeting of I.E.E.J., No. 631,

(1971)

[33] Okabayashi, S., J. Umoto, and T. Ando : 'Analysis of Dynamic Characteristics of DC Motor Controlled by Single-Phase Thyristor Rectifier Circuit(3)(in Japanese),' ibid., No. 574, (1972)

[34] Umoto, J., A. Udo, and T. Ando : 'Analysis of Dynamic Characteristics of DC Motor Controlled by Single-Phase Thyristor Rectifier Circuit(4)(in Japanese),' Convention Records at the Annual Meeting in Kansai District of I.E.E.J., No. G3-13, (1973)

[35] Ando, T., N. Takata, and J. Umoto : 'Speed Control of Separately Excited DC Motor Controlled by Single-Phase Half-Wave Rectifier Circuit(in Japanese),' Convention Records at the Annual Meeting of I.E.E.J., No. 639, (1976).

[36] Ando, T., and J. Umoto : 'Dynamic Characteristics of a DC Motor Controlled by Single-Phase Half-Wave Thyristor Rectifier Circuit,' Memoirs of the Faculty of Engineering, Kyoto University, Vol. 34, Part 1, pp. 103-124(1972).

[37] Ando, T., and J. Umoto : 'Dynamic Characteristics of a DC Motor Controlled by Single-Phase Half-Wave Thyristor Rectifier Circuit(II),' ibid., Vol. 37, Part 3, pp. 141-154(1975).

[38] Ando, T. : 'Speed Control of Separately Excited DC Motor Controlled by Single-Phase Half-Wave Rectifier Circuit(in Japanese),' Memoirs of Japan Society for Power Electronics, Vol. 1, pp. 87-92(1976).

[39] Thaler, G. J., and W. A. Stein : 'Transfer Function and Parameter Evaluation for D-C Servomotors,' A.I.E.E. Trans., Vol. 75, pp. 410-416(1956).

[40] Mogi, A. : 'Synchros and Servomotors(in Japanese),' 3rd ed., Nikkan Kogyo Shinbun Sha, Tkyo, PP. 111-147(1966).

[41] Kondo, B. : 'Principles of Control Engineering(in Japanese),' 12th ed., Corona Sha, Tokyo, pp. 127-174(1977).

[42] Ishikawa, H. : 'An analysis of Sparkless Zone of DC Machine Driven by Rectifier Power Supply(in Japanese),' J.I.E.E.J., Vol. 85, No. 7, pp.

1218-1225(1965).

[43] Tazuki, O. : 'Direct Current Machines(in Japanese),' Tokyo Denki Daigaku Press, Tokyo, pp. 137-146(1969).

[44] Umoto, J., T. Dodo, and T. Ando : 'Analysis of Separately Excited DC Motor Controlled by Thyristor Chopper Circuit(in Japanese),' Convention Records at the Annual Meeting in Kansai District of I.E.E.J., No. G3-12, (1972).

[45] Ando, T., J. Umoto, and T. Ura : 'Transfer Function of Separately Excited DC Motor Controlled by Chopper Circuit(in Japanese),' Convention Records at the Annual Meeting of I.E.E.J., No. 950, (1977)

[46] Mori, S., T. Ando, and J. Umoto : 'Transfer Function of Separately Excited DC Motor Controlled by Thyristor Chopper Circuit(in Japanese),' ibid., No. 478, (1981).

[47] Mori, S., T. Ando, and J. Umoto : 'Transient Characteristic and Frequency response of DC Motor Controlled by Thyristor Chopper Circuit(in Japanese),' Convention Records at the Annual Meeting in Kansai District of I.E.E.J., No. G3-1, (1981).

[48] Ando, T., and J. Umoto : 'Dynamic Characteristics of Separately Excited DC Motor Controlled by Chopper Circuit(in Japanese),' Technical Group. Rotating Machines of I.E.E.J, Vol. RM-77-3, pp. 3-1 - 3-9(1977).

[49] Ando, T., S. Mori, and J. Umoto : 'Dynamic Characteristics of a DC Motor Controlled by Thyristor Chopper Circuit,' Memoirs of the Faculty of Engineering, Kyoto University, Vol. 44, Part 1, pp. 141-154(1982).

[50] Hosokawa, I., and H. Irie : 'Constant Voltage and Constant Speed Controls of DC Motor Driven by DC Chopper Circuit(in Japanese),' Memoirs of Japan Society for Power Electronics, Vol. 5, No. 35, pp. 45-54(1980).

Part II :

[1] Tazuki, O. : 'Direct Current Machines(in Japanese),' Tokyo Denki Daigaku Press, Tokyo, pp. 137-146, pp. 32-44(1969).

[2] Ishikawa, H. : 'An analysis of Sparkless Zone of DC Machine Driven by Rectifier Power Supply(in Japanese),' J.I.E.E.J., Vol. 85, No. 7, pp. 1218-1225(1965).

[3] Takatsuki, H., and K. Tsubotani : 'Improvement of Commutation Technique for DC Motor(Short Special Edition)(in Japanese),' ibid., Vol. 100, No. 3, pp. 187-194(1980).

[4] Carter, F. W. : 'Air-Gap Induction,' Electrical World and Engineer, Vol. 38, pp. 884-888(1901).

[5] Bewley, L. V. : 'Two-Dimensional Fields in Electrical Engineering,' 2nd ed., Dover Pub., New York, pp. 70-73, pp. 102-182, pp. 90-95(1963).

[6] Stevenson, A. R., and R. H. Parks : 'Graphical Determination of Magnetic Fields(Theoretical Considerations),' A.I.E.E., Vol. 46, pp. 112-135(1927).

[7] Kida, S. : 'Direct Current Machines(in Japanese),' Nikkan Kogyo Shinbun Sha, Tokyo, pp. 5-8, pp. 11-29(1966).

[8] Ahmed, S. V., and E. A. Erdelyi : 'Flux Distribution in DC Machines On-Load and Overloads,' I.E.E.E. Trans. on PAS, Vol. PAS-85, No. 9, pp. 960-966(1966).

[9] Erdelyi, E. A., E. F. Fuchs, and D. H. Binkley : 'Nonlinear Magnetic Field Analysis of DC Machines-Part III, Equipotential Plots Drawn by Computer,' I.E.E.E. Trans. on PAS, Vol. PAS-85, No. 7, pp. 1565-1583(1970).

[10] Chari, M. V. K., and P. Silvester : 'Finite-Element Analysis of Magnetically Saturated D-C Machines,' I.E.E.E. Trans. on PAS, Vol. PAS-90, No.8, pp. 2362-2372(1971).

[11] Rüdenberg, R. : 'Transient Performance of Electric Power Systems,' MaCgrow-Hill, New York, pp. 106-133(1950).

[12] Švajcr, J. : 'Transient Phenomena in Magnetic Circuits Having Components of Solid Ferromagnetic Material,' I.E.E.E. Trans. on MAG, Vol. MAG-10, No. 1, pp.54-59(1974).

[13] Sakabe, S., T. Nomura, and M. Iwamoto : 'Delay of Interpole Flux of DC Machines due to the Existence of Liner(in Japanese),' J.I.E.E.J., Vol. 97-B, No. 5, pp. 279-286(1977).

[14] Wagner, C. F. : 'Transients in Magnetic Systems,' Electrical Engineering, Vol. 53, No. 3, pp. 418-425(1934).

[15] Hannalla, A. Y., and D. C. Macdonald.: 'A Nodal Method for the Numerical Solution of Transient Field Problems in Electrical Machines,' I.E.E.E. Trans. on MAG, Vol. MAG-11, No. 5, pp. 1544-1546(1975).

[16] Dermerdash, N. A. : 'A New Approach for Determination of Eddy Current and Flux Penetration in Nonlinear Feromagnetic Materials,' I.E.E.E. Trans. on MAG, Vol. MAG-10, No. 3, pp. 682-685(1974).

[17] Smith, G. D. (Translated by Y. Fujikawa) : 'Numerical Solution of Partial Differential Equation,' 2nd ed., Science Sha, Tokyo, pp. 17-18(1975).

[18] Ando, T., and J. Umoto : 'Analysis of Transient Response of Magnetic Flux in Nonlinear Magnetic Circuit(in Japanese),' J.I.E.E.J., Vol. 100-B, No. 8, pp. 492-498(1980).

[19] Ando, T., and J. Umoto : 'Analysis of Transient Response of Magnetic Flux in Nonlinear Magnetic Circuit,' Memoirs of the Faculty of Engineering, Kyoto University, Vol. 42, Part 3, pp. 243-257(1980).

[20] Ando, T., and J. Umoto : 'Analysis of Transient Response of Magnetic Field by Nodal Method(in Japanese),' Convention Records at the Annual Meeting of I.E.E.J., No. 702(1980).

[21] Ando, T., and J. Umoto : 'Analysis of Transient Response of Magnetic Flux in DC Motor(in Japanese),' ibid., No. 779(1983).

[22] Ando, T., and J. Umoto : 'Analysis of Transient Distribution of Magnetic Flux in DC Motor(in Japanese),' Convention Records at the Annual Meeting in

Kansai of I.E.E.J., No. G3-62(1984).

[23] Ando, T., and J. Umoto : 'Transient Distribution of Magnetic Flux in DC Motor,' Memoirs of the Faculty of Engineering, Kyoto University, Vol. 43, Part 3, pp. 328-343(1981).

[24] Ando, T., and J. Umoto : 'Analysis of Transient Magnetic Flux in Interpole of DC Motor Considering Hysteresis Phenomenon,' Memoirs of the Faculty of Engineering, Kyoto University, Vol. 45, Part 4, pp. 51-67(1983).

[25] Ando, T., M. Takemura and J. Umoto : 'Analysis of Transient Response of Commutating Flux in DC Motor by Using Magnetic Circuit Model(in Japanese),' Convention Records at the Annual Meeting in Kansai of I.E.E.J., No. G3-2(1981).

[26] Ando, T., M. Takemura and J. Umoto : 'Analysis of Transient Response of Commutating Flux in DC Motor by Using Equivalent Magnetic Circuit Model(in Japanese),' Convention Records at the Annual Meeting of I.E.E.J., No. 770(1982).

[27] Ando, T., and J. Umoto : 'Analysis of Transient Magnetic Flux in Interpole of DC Motor Considering Hysteresis Phenomenon(in Japanese),' J.I.E.E.J, Vol. 104-B, No. 4, p. 262(1984).

[28] Langsdorf, A. S. : 'Principles of Direct-Current Machines,' 6th ed., McGraw-Hill, New York, pp. 267-301(1959).

[29] Matsuda, T. : 'Generalized Commutation Theory of Large DC Machines(in Japanese),' J.I.E.E.J, Vol. 98-B, No. 10, pp. 487-494(1974).

[30] Sakabe, S., T. Nomura and T. Iwamoto : 'Theory of Commutating Phenomena of DC Machines(in Japanese),' Mitsubishi Denki Giho, Vol. 51, No. 10, pp. 691-695(1977).

[31] Umoto, J., and S. Hayashi : 'An Analytical Method of Commutating Phenomena of DC Machines(in Japanese),' Convention Records at the Annual Meeting of I.E.E.J., No. 610(1961).

[32] Ando, T., S. Ueno, J. Umoto, H. Yamaguchi, and Y. Kawakami : 'Analysis of

Commutating Phenomenon in DC Motor with Wave Armature Winding(in Japanese),' Convention Records at the Annual Meeting in Kansai of I.E.E.J., No. G3A-22(1983).

[33] Ando, T., Y. Okuno, J. Umoto, and Y. Kawakami : 'Analysis of Commutating Phenomenon in DC Motor with Wave Armature Winding by Considering Shared Brush Current(in Japanese),' Convention Records at the Annual Meeting of I.E.E.J., No. 831(1985).

[34] Ando, T., J. Umoto and H. Takechi : 'Transient Response of Commutating Flux in DC Motor(in Japanese),' Convention Records at the Annual Meeting in Kansai of I.E.E.J., No. G3A-8(1982).

[35] Ando, T., K. Yoshida, J. Umoto, and T. Inoue : 'Analysis of Transient Response of Magnetic Flux in DC Motor(in Japanese),' ibid., No. G3A-21(1983).

[36] Ando, T., K. Yoshida, and J. Umoto : 'Analysis of Transient Response of Magnetic Flux in DC Motor(in Japanese),' Convention Records at the Annual Meeting of I.E.E.J., No. 759(1984).